

THE MINISTRY OF SCIENCE AND HIGHER EDUCATION OF THE RUSSIAN FEDERATION



ST. PETERSBURG STATE
POLYTECHNICAL UNIVERSITY
JOURNAL

Physics
and Mathematics

**VOLUME 14, No.1,
2021**

Peter the Great St. Petersburg
Polytechnic University
2021

**ST. PETERSBURG STATE POLYTECHNICAL UNIVERSITY JOURNAL.
PHYSICS AND MATHEMATICS**

JOURNAL EDITORIAL COUNCIL

A.I. Borovkov – vice-rector for perspective projects;
V.A. Glukhikh – full member of RAS;
D.A. Indeitsev – corresponding member of RAS;
A.I. Rudskoy – full member of RAS;
R.A. Suris – full member of RAS;
A.E. Zhukov – corresponding member of RAS.

JOURNAL EDITORIAL BOARD

V.K. Ivanov – Dr. Sci. (phys.-math.), prof., SPbPU, St. Petersburg, Russia, – editor-in-chief;
A.E. Fotiadi – Dr. Sci. (phys.-math.), prof., SPbPU, St. Petersburg, Russia, – deputy editor-in-chief;
V.M. Kapralova – Candidate of Phys.-Math. Sci., associate prof., SPbPU, St. Petersburg, Russia, – executive secretary;
V.I. Antonov – Dr. Sci. (phys.-math.), prof., SPbPU, St. Petersburg, Russia;
I.B. Bezprozvanny – Dr. Sci. (biology), prof., The University of Texas Southwestern Medical Center, Dallas, TX, USA;
A.V. Blinov – Dr. Sci. (phys.-math.), prof., SPbPU, St. Petersburg, Russia;
A.S. Cherepanov – Dr. Sci. (phys.-math.), prof., SPbPU, St. Petersburg, Russia;
D.V. Donetski – Dr. Sci. (phys.-math.), prof., State University of New York at Stony Brook, NY, USA;
D.A. Firsov – Dr. Sci. (phys.-math.), prof., SPbPU, St. Petersburg, Russia;
A.S. Kheifets – Ph.D., prof., Australian National University, Canberra, Australia;
O.S. Loboda – Candidate of Phys.-Math. Sci., associate prof., SPbPU, St. Petersburg, Russia;
J.B. Malherbe – Dr. Sci. (physics), prof., University of Pretoria, Republic of South Africa;
V.M. Ostryakov – Dr. Sci. (phys.-math.), prof., SPbPU, St. Petersburg, Russia;
V.E. Privalov – Dr. Sci. (phys.-math.), prof., SPbPU, St. Petersburg, Russia;
E.M. Smirnov – Dr. Sci. (phys.-math.), prof., SPbPU, St. Petersburg, Russia;
A.V. Solov'yov – Dr. Sci. (phys.-math.), prof., MBN Research Center, Frankfurt am Main, Germany;
A.K. Tagantsev – Dr. Sci. (phys.-math.), prof., Swiss Federal Institute of Technology, Lausanne, Switzerland;
I.N. Toptygin – Dr. Sci. (phys.-math.), prof., SPbPU, St. Petersburg, Russia;
E.A. Tropp – Dr. Sci. (phys.-math.), prof., SPbPU, St. Petersburg, Russia.

The journal is included in the List of leading peer-reviewed scientific journals and other editions to publish major findings of theses for the research degrees of Doctor of Sciences and Candidate of Sciences.

The publications are presented in the VINITI RAS Abstract Journal and Ulrich's Periodical Directory International Database.

The journal is published since 2008 as part of the periodical edition 'Nauchno-tekhnicheskie vedomosti SPb-GPU'.

The journal is registered with the Federal Service for Supervision in the Sphere of Telecom, Information Technologies and Mass Communications (ROSKOMNADZOR). Certificate ПИ № ФЦ77-52144 issued December 11, 2012.

The journal is distributed through the CIS countries catalogue, the «Press of Russia» joint catalogue and the «Press by subscription» Internet catalogue. The subscription index is **71823**.

The journal is in the **Web of Science** (Emerging Sources Citation Index) and the **Russian Science Citation Index** (RSCI) databases.

© Scientific Electronic Library (<http://www.elibrary.ru>).

No part of this publication may be reproduced without clear reference to the source.

The views of the authors may not represent the views of the Editorial Board.

Address: 195251 Politekhnicheskaya St. 29, St. Petersburg, Russia.

Phone: (812) 294-22-85.

<http://ntv.spbstu.ru/physics>

© Peter the Great St. Petersburg Polytechnic University, 2021

МИНИСТЕРСТВО НАУКИ И ВЫСШЕГО ОБРАЗОВАНИЯ РОССИЙСКОЙ ФЕДЕРАЦИИ



НАУЧНО-ТЕХНИЧЕСКИЕ ВЕДОМОСТИ

САНКТ-ПЕТЕРБУРГСКОГО ГОСУДАРСТВЕННОГО
ПОЛИТЕХНИЧЕСКОГО УНИВЕРСИТЕТА

Физико-математические
науки

Том 14, №1
2021

Санкт-Петербургский политехнический
университет Петра Великого
2021

**НАУЧНО-ТЕХНИЧЕСКИЕ ВЕДОМОСТИ САНКТ-ПЕТЕРБУРГСКОГО
ГОСУДАРСТВЕННОГО ПОЛИТЕХНИЧЕСКОГО УНИВЕРСИТЕТА.
ФИЗИКО-МАТЕМАТИЧЕСКИЕ НАУКИ**

РЕДАКЦИОННЫЙ СОВЕТ ЖУРНАЛА

Боровков А.И., проректор по перспективным проектам;

Глухих В.А., академик РАН;

Жуков А.Е., чл.-кор. РАН;

Индейцев Д.А., чл.-кор. РАН;

Рудской А.И., академик РАН;

Сулис Р.А., академик РАН.

РЕДАКЦИОННАЯ КОЛЛЕГИЯ ЖУРНАЛА

Иванов В.К., д-р физ.-мат. наук, профессор, СПбПУ, СПб., Россия, — главный редактор;

Фотиади А.Э., д-р физ.-мат. наук, профессор, СПбПУ, СПб., Россия, — зам. главного редактора;

Каприлова В.М., канд. физ.-мат. наук, доцент, СПбПУ, СПб., Россия — ответственный секретарь;

Антонов В.И., д-р физ.-мат. наук, профессор, СПбПУ, СПб., Россия;

Безпрозванный И.Б., д-р биол. наук, профессор, Юго-Западный медицинский центр
Техасского университета, Даллас, США;

Блинов А.В., д-р физ.-мат. наук, профессор, СПбПУ, СПб., Россия;

Донецкий Д.В., д-р физ.-мат. наук, профессор, университет штата Нью-Йорк в Стоуни-Брук, США;

Лобода О.С., канд. физ.-мат. наук, доцент, СПбПУ, СПб., Россия;

Малерб Й.Б., Dr.Sc. (Physics), профессор, университет Претории, ЮАР;

Остряков В.М., д-р физ.-мат. наук, профессор, СПбПУ, СПб., Россия;

Привалов В.Е., д-р физ.-мат. наук, профессор, СПбПУ, СПб., Россия;

Смирнов Е.М., д-р физ.-мат. наук, профессор, СПбПУ, СПб., Россия;

Соловьёв А.В., д-р физ.-мат. наук, профессор, Научно-исследовательский центр мезобионаносистем (MBN),
Франкфурт-на-Майне, Германия;

Таганцев А.К., д-р физ.-мат. наук, профессор, Швейцарский федеральный институт технологий,
Лозанна, Швейцария;

Топтыгин И.Н., д-р физ.-мат. наук, профессор, СПбПУ, СПб., Россия;

Тропп Э.А., д-р физ.-мат. наук, профессор, СПбПУ, СПб., Россия;

Фирсов Д.А., д-р физ.-мат. наук, профессор, СПбПУ, СПб., Россия;

Хейфец А.С., Ph.D. (Physics), профессор, Австралийский национальный университет,
Канберра, Австралия;

Черепанов А.С., д-р физ.-мат. наук, профессор, СПбПУ, СПб., Россия.

Журнал с 2002 г. входит в Перечень ведущих рецензируемых научных журналов и изданий, в которых должны быть опубликованы основные результаты диссертаций на соискание ученых степеней доктора и кандидата наук.

Сведения о публикациях представлены в Реферативном журнале ВИНИТИ РАН, в международной справочной системе «Ulrich's Periodical Directory».

С 2008 года выпускается в составе сериального периодического издания «Научно-технические ведомости СПб-ПУ».

Журнал зарегистрирован Федеральной службой по надзору в сфере информационных технологий и массовых коммуникаций (Роскомнадзор). Свидетельство о регистрации ПИ № ФС77-52144 от 11 декабря 2012 г.

Распространяется по Каталогу стран СНГ, Объединенному каталогу «Пресса России» и по Интернет-каталогу «Пресса по подписке». Подписной индекс 71823.

Журнал индексируется в базе данных **Web of Science** (Emerging Sources Citation Index), а также включен в базу данных «**Российский индекс научного цитирования**» (РИНЦ), размещенную на платформе Научной электронной библиотеки на сайте

<http://www.elibrary.ru>

При перепечатке материалов ссылка на журнал обязательна.

Точка зрения редакции может не совпадать с мнением авторов статей.

Адрес редакции и издательства:

Россия, 195251, Санкт-Петербург, ул. Политехническая, д. 29.

Тел. редакции (812) 294-22-85.

<http://ntv.spbstu.ru/physics>

© Санкт-Петербургский политехнический университет Петра Великого, 2021

Contents

Condensed matter physics

Lebedeva O.S., Lebedev N.G., Lyapkosoza I.A. <i>Elastic conductivity of germanene “arm-chair” nanoribbons with donor impurities.....</i>	8
Zelikman M.A. <i>Current configurations in the long Josephson contact in an external magnetic field.....</i>	21

Simulation of physical processes

Semenov A.S. <i>A microstructural model of ferroelectroelastic material with taking into account the defects’ evolution.....</i>	31
Sadin D.V., Golikov I.O., Shirokova E.N. <i>Testing of the hybrid large-particle method using two-dimensional Riemann problems.....</i>	55
Gataulin Ya.A., Smirnov E.M. <i>A flow in the blood vessel with a one-side stenosis: numerical study of the structure and local turbulization.....</i>	69

Atom physics and physics of clusters and nanostructures

Baranov M.A., Tsybin O.Yu., Velichko E.N. <i>Structured biomolecular films for microelectronics.....</i>	81
---	----

Mathematical physics

Anikonov D.S., Konovalova D.S. <i>The Duhamel-type integral for the initial boundary value problem.....</i>	95
--	----

Physical electronics

Bizyaev I.S., Gabdullin P.G., Gnuchev N.M., Arkhipov A.V. <i>Low-field electron emission from thin films of metals.....</i>	105
Golovitskii A.P., Korenyugin D.G. <i>Moderate and low pressure glow discharge in the gap between two eccentric tubes.....</i>	121

Nuclear physics

Tiba A., Egorov A.Yu., Berdnikov Ya.A., Lomasov V.N. <i>Copper-64 isotope production through the cyclotron proton irradiation of the natural-nickel target.....</i>	130
--	-----

Theoretical physics

Gorobey N.N., Lukyanenko A.S., Goltsev A.V. <i>The proper mass of the universe.....</i>	138
--	-----

Mathematics

Antonov V.I., Garbaruk V.V., Fomenko V.N. <i>Making a collective expert decision based on the Neumann – Pearson algorithm.....</i>	146
Timofeev S.V., Baenkhaeva A.V. <i>Mathematical modeling of information confrontation.....</i>	155

Mechanics

Frolova K.P. <i>Cross-property connections between Young's modulus and diffusion coefficient of two-phase composite.....</i>	167
---	-----

Содержание

Физика конденсированного состояния

Лебедева О.С., Лебедев Н.Г., Ляпкосова И.А. <i>Эластопроводимость кресельных германеновых нанолент с донорными дефектами</i>	8
Зеликман М.А. <i>Токовые конфигурации в длинном джозефсоновском контакте во внешнем магнитном поле</i>	21

Математическое моделирование физических процессов

Семенов А.С. <i>Микроструктурная модель сегнетоэластопругого материала с учетом эволюции дефектов</i>	31
Садин Д.В., Голиков И.О., Широкова Е.Н. <i>Тестирование гибридного метода крупных частиц на двумерных задачах Римана</i>	55
Гатаулин Я.А., Смирнов Е.М. <i>Численное исследование структуры и локальной турбулизации течения в кровеносном сосуде с односторонним стенозом</i>	69

Атомная физика, физика кластеров и наноструктур

Баранов М.А., Цыбин О.Ю., Величко Е.Н. <i>Структурированные биомолекулярные пленки для микроэлектроники</i>	81
---	----

Математическая физика

Аниконов Д.С., Коновалова Д.С. <i>Интеграл типа Дюамеля для начально-краевой задачи</i>	95
---	----

Физическая электроника

Бизяев И.С., Габдуллин П.Г., Гнучев Н.М., Архипов А.В. <i>Низкопороговая полевая эмиссия электронов тонкими пленками металлов</i>	105
Головицкий А.П., Кореньгин Д.Г. <i>Тлеющий разряд среднего и низкого давления в зазоре между двумя эксцентричными трубками</i>	121

Ядерная физика

Тиба А., Егоров А.Ю., Бердников Я.А., Ломасов В.Н. <i>Производство изотопа меди-64 путем облучения циклотронной мишени из природного никеля пучком протонов</i>	130
---	-----

Теоретическая физика

Горобей Н.Н., Лукьяненко А.С., Гольцев А.В. <i>Собственная масса Вселенной (статья на английском языке)</i>	138
---	-----

Математика

Антонов В.И., Гарбарук В.В., Фоменко В.Н. <i>Принятие коллективного экспертного решения на основе алгоритма Неймана – Пирсона</i>	146
Тимофеев С.В., Баенхаева А.В. <i>Математическое моделирование информационного противоборства</i>	155

Механика

Фролова К.П. <i>Соотношения между модулем Юнга и коэффициентом диффузии двухфазного материала.....</i>	167
---	-----

DOI: 10.18721/JPM.14101

UDC 538.915+975; 544.22.022.343; 544.225.22+25

ELASTIC CONDUCTIVITY OF GERMANENE “ARM-CHAIR” NANORIBBONS WITH DONOR IMPURITIES

O.S. Lebedeva^{1,2}, N.G. Lebedev¹, I.A. Lyapkoso²

¹ Volgograd State University,
Volgograd, Russian Federation;

² Volgograd State Agricultural University,
Volgograd, Russian Federation

In the article, results of theoretical calculations of the piezoresistance characteristics of impurity germanene nanoribbons (NR) of the “arm-chair” type with donor defects with various concentrations uniformly distributed in the crystal lattice of the nanomaterial have been presented and analyzed. Arsenic atoms were used as donor impurities. Investigations of the NR’s band structure were carried out in the frameworks of the Hubbard’s and Anderson’s models. The computation of the main characteristic of the piezoresistance effect, i.e., the longitudinal component of the elastic conductivity tensor was carried out using the Green’s function method within the framework of the same theoretical models. An analysis of the dependence of this characteristic on the tensile and compressive strains, the concentration of impurities and the nanoribbon width were carried out.

Keywords: band structure, stress-strain state, piezoresistance effect, elastic conductivity tensor

Citation: Lebedeva O.S., Lebedev N.G., Lyapkoso² I.A. Elastic conductivity of germanene “arm-chair” nanoribbons with donor impurities, St. Petersburg Polytechnical State University Journal. Physics and Mathematics. 14 (1) (2021) 8–20. DOI: 10.18721/JPM.14101

This is an open access article under the CC BY-NC 4.0 license (<https://creativecommons.org/licenses/by-nc/4.0/>)

ЭЛАСТОПРОВОДИМОСТЬ КРЕСЕЛЬНЫХ ГЕРМАНЕНОВЫХ НАНОЛЕНТ С ДОНОРНЫМИ ДЕФЕКТАМИ

О.С. Лебедева^{1,2}, Н.Г. Лебедев¹, И.А. Ляпкосова²

¹ Волгоградский государственный университет,
г. Волгоград, Российская Федерация;

² Волгоградский государственный аграрный университет,
г. Волгоград, Российская Федерация

В работе представлены и проанализированы результаты теоретических расчетов пьезорезистивных характеристик примесных германеновых нанолент кресельного типа (“arm-chair”) с донорными дефектами разной концентрации, однородно распределенными в кристаллической решетке наноматериала. В качестве донорных примесей использованы атомы мышьяка. Исследование зонной структуры нанолент проведено в рамках моделей Хаббарда и Андерсона. Вычисление основной характеристики пьезорезистивного эффекта – продольной компоненты тензора эластопроводимости выполнено в рамках тех же теоретических моделей с использованием метода функций Грина. Проанализированы зависимости указанной компоненты от относительной деформации растяжения и сжатия, концентрации примесей и ширины наноленты.

Ключевые слова: зонная структура, напряженно-деформированное состояние, пьезорезистивный эффект, тензор эластопроводимости



Ссылка при цитировании: Лебедева О.С., Лебедев Н.Г., Ляпкосова И.А. Эластопроводимость кресельных германеновых нанолент с донорными дефектами // Научно-технические ведомости СПбГПУ. Физико-математические науки. 2021. Т. 14. № 1. С. 8–20. DOI: 10.18721/JPM.14101

Статья открытого доступа, распространяемая по лицензии CC BY-NC 4.0 (<https://creativecommons.org/licenses/by-nc/4.0/>)

Introduction

One of the priority problems of condensed matter physics is obtaining of materials with preset properties and a possibility to control them. Since 2004, scientists have been synthesizing and studying carbon based nanomaterials (graphene, graphene nanoribbons) possessing practically important electronic, conductive, optical and mechanical properties which can expand the spectrum of their use [1 – 3].

The electronic properties of graphene nanoribbons are rather diverse and depend on the nature and concentration of impurities, applied external fields, mechanical strain, etc. Since the moment it was synthesized first in 2004, graphene became the object of most promising technologies of nanoelectromechanical systems for the development of nanoelectronic devices. It can replace silicon as a basis for transistors, cantilever for atomic force microscopy, chemical sensors, etc.

Despite its spectrum of unique properties, graphene is still not devoid of some drawbacks in terms of its practical use, e.g. it lacks band gap energy almost completely, which eliminates a possibility to close a graphene-based FET channel [4]. One of the priority solutions of this problem is the search for new non-carbon promising 2D materials with a structure similar graphene, but possessing a sufficient band gap.

In 2013, by means of computer choice among the materials with properties similar to graphene and a 2D-like structure, there were 92 promising analogues identified [5]. Forty of them were never proposed as a compound similar to graphene before, and their properties, including the conductive ones, remain poorly explored. Despite such an abundance of the selected alternatives that are promising in terms of creating a basis for nanoelectronic devices, their application is extremely limited by the problems of synthesis and interac-

tion with the substrate. Therefore, selection of analogues among actually synthesized nanomaterials from the “graphene family” and study of their piezoresistance properties is a relevant task of the first stage of work.

Predicted in 2009 and successfully synthesized in 2014, germanene should be regarded as one of the most promising nanomaterials of the “post-graphene era” [6 – 9].

Band gap and electronic properties of germanene are sensitive to external fields, mechanical strain and chemisorption [10, 11]. According to theoretical studies, the width of the germanene band gap equals approximately 24 meV ($E_g \approx 24$ meV), which by several orders of magnitude exceeds the one known for graphene ($E_g < 0.05$ meV). This expansion of the band gap allows using germanene in devices the work of which is based on field effects, such as transistors. It can be achieved either by applying external impact [12] or by means of intentional doping of a nanomaterial with acceptor and donor impurities of various concentrations. By combining mechanical strain/stress and varying the number of defects, we can create an effective mechanism of controlling the germanene band gap.

This paper is devoted to a theoretical study (and consequently, to a prediction) of the piezoresistance properties of the impurity germanene nanoribbons (NR): GeNRs.

Model of electronic structure of deformed impurity germanene nanoribbons

Geometric model of GeNRs is chosen based on the view of the two-dimensional hexagonal graphene layer. Fig. 1 shows a deformed unit cell of the germanene crystal lattice, where α denotes the angle between the primitive translation vectors \mathbf{a}_1 and \mathbf{a}_2 , while Δ_i is the interatomic spacing vector and a is the constant lattice of the

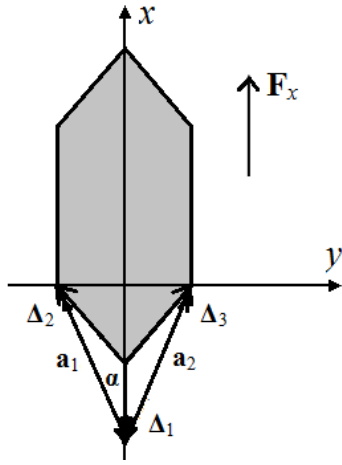


Fig. 1. Fragment of the arm-chair GeNR structure deformed by longitudinal tension of force \mathbf{F}_x :
 Δ_i ($i = 1, 2, 3$) – interatomic spacing vectors;
 $\mathbf{a}_1, \mathbf{a}_2$ – primitive translation vectors;
 α – angle between vectors \mathbf{a}_1 and \mathbf{a}_2

deformed GeNR ($a_1 = a_2 = a$). The length and width of the NR are measured along the Ox and Oy axes respectively.

Electronic spectrum of undeformed GeNRs in the frame of the strong coupling method and the nearest neighbors approximation can be presented in the following form [13]:

$$\varepsilon(\mathbf{k}) = \pm t_0 \left\{ 1 + 4 \cos \left(\frac{\mathbf{k}(\mathbf{a}_1 + \mathbf{a}_2)}{2} \right) \times \right. \\ \times \cos \left(\frac{\mathbf{k}(\mathbf{a}_1 - \mathbf{a}_2)}{2} \right) + \\ \left. + 4 \cos^2 \left(\frac{\mathbf{k}(\mathbf{a}_1 - \mathbf{a}_2)}{2} \right) \right\}^{1/2}, \quad (1)$$

where t_0 , eV, is the resonance or hopping integral ($t_0 = 1.47$ eV [6]); \mathbf{k} , cm^{-1} , is the wave vector; $\mathbf{a}_1, \mathbf{a}_2$, nm, are the primitive translation vectors.

The Fermi level in Eq. (1) is traditionally taken as 0 eV.

The direction of the $(\mathbf{a}_1 + \mathbf{a}_2)$ vector is called “arm-chair”, while the $(\mathbf{a}_1 - \mathbf{a}_2)$ vector has a “zig-zag” direction.

The condition of quantizing the wave vector \mathbf{k} along the NR width can be written as follows [13]:

$$3k_x R_0 = \frac{2\pi q}{N_x}, \quad q = 1, 2, \dots, N_x \quad (2)$$

For the arm-chair GeNRs, and

$$\sqrt{3}k_y R_0 = \frac{2\pi q}{N_y}, \quad q = 1, 2, \dots, N_y \quad (3)$$

for the zig-zag NRs.

Here, R_0 , nm, is the equilibrium interatomic spacing in the undeformed GeNR; k_x, k_y , cm^{-1} , are wave numbers in the Brillouin zone.

Fig. 1 demonstrates a geometric modification of the arm-chair GeNR lattice hexagon deformed by longitudinal tension of force \mathbf{F}_x .

Modeling of band structure of the deformed GeNRs is performed by means of transforming the parameters of the unit cell and the Brillouin zone. This procedure is described in detail in paper [15].

If we present the value of relative strain of the interatomic bond length R as $\delta = \Delta R/R_0$, where ΔR is the change of the equilibrium (Ge-Ge) bond length R_0 ($\Delta R = R - R_0$), then we can obtain the following expressions for the components of the wave vector [15]:

$$\frac{\mathbf{k}_x(\mathbf{a}_1 + \mathbf{a}_2)}{2} = k_x R_0 (1 + \delta)(1 + \cos \alpha), \\ \frac{\mathbf{k}_y(\mathbf{a}_1 - \mathbf{a}_2)}{2} = k_y R_0 (1 + \delta) \sin \alpha = \frac{\pi q}{n}, \\ q = 1, 2, \dots, n \quad (4)$$

for the arm-chair GeNR ($k_x \in$ the Brillouin zone);

$$\frac{\mathbf{k}_x(\mathbf{a}_1 + \mathbf{a}_2)}{2} =$$



$$= k_x R_0 \left[(1 + \delta) \cos \alpha + 1 - \delta \right] = \frac{\pi q}{n},$$

$$q = 1, 2, \dots, n, \quad (5)$$

$$\frac{\mathbf{k}_y (\mathbf{a}_1 - \mathbf{a}_2)}{2} = k_y R_0 (1 + \delta) \sin \alpha$$

for the zig-zag type GeNR ($k_y \in$ the Brillouin zone).

Tensile (compression) strain causes changes in the transverse dimensions of the GeNR, and consequently the chiral vector modulus [13] is modified in the following way:

$$C_h = C_{h0} (1 - \nu \delta),$$

$$C_{h0} = a_0 \sqrt{N_x^2 + N_y^2 + N_x N_y}, \quad (6)$$

where a_0 , nm, is a constant lattice of the undeformed GeNR, $a_0 = R_0$; N_x, N_y – integers defining the size and the type of the NR ($N_y = 0$ for the arm-chair type and $N_y = N_x$ the zig-zag type); ν is the Poisson's ratio taking values of 0.27 and 0.19 for the arm-chair and zig-zag type GeNRs, respectively.

We can evaluate angle α from relation (6) [15]:

$$\sin \alpha = \left(\frac{1 - \nu \delta}{1 + \delta} \right) \sin \alpha_0,$$

$$\cos \alpha = \sqrt{1 - \sin^2 \alpha}$$

for the arm-chair GeNR;

$$\cos \alpha = \frac{1}{(1 + \delta)} \times$$

$$\times \left[(1 - \nu \delta) (1 + \cos \alpha_0) - 1 + \delta \right],$$

$$\sin \alpha = \sqrt{1 - \cos^2 \alpha}$$

for the zig-zag GeNR.

Finally, the electronic spectrum of the deformed GeNRs takes the form [15]:

$$\varepsilon_a(\mathbf{k}) =$$

$$= \pm \gamma(\delta) \left\{ 1 \pm 4 \cos \left(\frac{\pi q}{n} \right) \times \right.$$

$$\times \cos [k_x R_0 (1 + \delta) (1 + \cos \alpha)] +$$

$$\left. + 4 \cos^2 \left(\frac{\pi q}{n} \right) \right\}^{\frac{1}{2}}, \quad (7)$$

$$\varepsilon_z(\mathbf{k}) =$$

$$= \pm \gamma(\delta) \left\{ 1 \pm 4 \cos [k_y R_0 (1 + \delta) \sin \alpha] \times \right. \quad (8)$$

$$\times \cos \left(\frac{\pi q}{n} \right) + 4 \cos^2 [k_y R_0 (1 + \delta) \sin \alpha] \left. \right\}^{\frac{1}{2}},$$

where $\gamma(\delta)$ is the resonance integral of the deformed GeNRs as a function of the relative strain δ ; subscripts “a” and “z” denote the spectra of the arm-chair and zig-zag type NRs, the $+/-$ symbols result from the fact that an NR unit cell contains for Ge atoms.

The electronic spectrum of the deformed GeNRs with no impurities, taking into account the Coulomb repulsion at one point, was calculated in the frame of the Hubbard's model [16], which is described in detail in paper [17]:

$$E(\mathbf{k}) = \frac{1}{2} [\varepsilon(\mathbf{k}) +$$

$$+ U \pm \sqrt{\varepsilon(\mathbf{k})^2 - 2\varepsilon(\mathbf{k})U(1 - 2n_{-\beta}) + U^2}], \quad (9)$$

where $\varepsilon(\mathbf{k})$ is the band structure of ideal NRs; U, J , is the energy of the Coulomb interaction at one point that is a semi-empirical method parameter of MNDO quantum chemistry [18], $n_{-\beta}$ is the number of electrons with opposite spin in the zone.

A comparative analysis of the depiction of the band structures $E(\mathbf{k})$ of Eq. (9) and $\varepsilon(\mathbf{k})$ of Eq. (7) for the arm-chair GeNR revealed no significant differences.

A quantitative evaluation of the energy band gap width of the semiconductor GeNR in case of longitudinal tensile (compression) strain showed its broadening (narrowing). The conduction band, as well as the valence band act in the same

manner. As a result, the density of electronic states in these zones increases (decreases). Such a behavior of the dispersion curves was observed during the study of achiral (arm-chair and zig-zag) carbon nanotubes [15, 17].

The gapless band structure of the conductive arm-chair GeNRs in case of longitudinal tension (compression) is also changed in the above described way. The only exclusion from the identical behavior is the nonoccurrence of band gaps in the spectra of such ribbons as they remain conductive.

Longitudinal tension of the conductive GeNRs also has no essential influence on the qualitative behavior of their band structure, while the band gap is absent at small strain.

Adding impurities in the crystalline structure of the GeNRs under consideration can facilitate the change in their piezoresistance as it is shown on example of graphene nanoribbons in paper [19], which will allow exerting intentional influence on their conductivity.

The calculation of the electronic spectrum of doped GeNRs was conducted using Anderson model [16]. This model consists in separate consideration of collective π -electrons and localized electron, the interaction between which is accounted for by means of introducing hybridization potential. The model is successfully adapted to the studies of the influence point defects (donor and acceptor) have on band structure of graphene nanoribbons [19].

The GeNR electronic spectrum in the frame of Anderson model has the following form [16]:

$$E(\mathbf{k}) = \frac{1}{2} [\varepsilon_i + \varepsilon(\mathbf{k}) \pm \sqrt{(\varepsilon_i - \varepsilon(\mathbf{k}))^2 + 36|V_{\text{GeD}}(\delta)|^2 \cdot x}], \quad (10)$$

where $\varepsilon(\mathbf{k})$, eV, is the band structure of an ideal (undoped) nanoribbon expressed by Eq. (7); ε_i , eV, is electron energy at the defect; $x = N_d/N$ is the concentration of impurities (N is the number of unit cells in the crystal, N_d is the number of defects); $V_{\text{GeD}}(\delta)$, eV, is the hybridization potential which consists in a matrix element of the energy of the crystal/point defect electron interaction

and is the function of the relative strain δ .

This paper considers such donor impurities of arsenic atoms as point defects. The electron energy at the defect can be evaluated as a difference of impurity/crystallite ionizing potential:

$$\begin{aligned} \varepsilon_i &= I_{\text{Ge}} - I_{\text{As}} = \\ &= (7.88 - 9.81) \text{ eV} = -1.93 \text{ eV}. \end{aligned}$$

The dependencies of the hopping integral $\gamma(\delta)$ and the hybridization potential $V_{\text{GeD}}(\delta)$ on the relative strain were calculated by means of the density functional theory method using the exchange–correlation energy functional B3LYP in the STO-3G basis sets [18]. For quantum chemical calculations, we considered a fragment of germanene surface the size of 6×6 unit cells (UC). Boundary unsaturated bonds were closed with monovalent hydrogen. A defect atom (As) was placed in the center of the constructed cluster to decrease the influence of the boundary atoms. We were modeling the deformation of the structure along the “arm-chair” direction by means of step-by-step freezing of germanium atoms at the opposite boundaries of the fragment. The obtained numerical values of the $\gamma(\delta)$ and $V_{\text{GeD}}(\delta)$ dependencies interpolated by the following analytical expressions:

$$\begin{aligned} \gamma &= \gamma_0 \exp(-1.9523R), \\ V_{\text{GeD}} &= V_0 \exp(-1.9523R), \\ R &= R_0(1 + \delta), \\ \gamma_0 &= 171.11 \text{ eV}, \\ V_0 &= 152.37 \text{ eV}. \end{aligned} \quad (11)$$

The equilibrium interatomic bond lengths in further calculations were assumed equal to $R_0 = 2.44 \text{ \AA}$; this value was obtained as a result of prior optimization of the geometric structure of the constructed germanene fragment using the above described density functional theory method.

Adding donor impurities of various concentrations to the system of undeformed GeNRs leads to a change in the band structure of the latter. Features of the energy spectrum of low-dimensional structures with donor nitrogen



atoms in the lattice are analyzed on the example of carbon nanotubes in paper [17]. The zone of impurity states in this case is localized in the proximity of the electron energy level at the defect ε_i and contains a local band gap which does not change the crystallite properties as a whole. As the impurity concentration increases, there is a greater change in the band structure of the carbon nanotubes, in particular, there is an increase in the local band gap. The described features of the electronic spectrum of the undeformed carbon nanotubes with impurities are verified by the general Anderson model theory [16].

Elastic conductivity of germanene nanoribbons with acceptor defects

According to the recommendation in book [20], determination of the elastic conductivity tensor of the two-dimensional crystalline structures can be written as

$$\begin{aligned} \frac{\Delta\sigma_{\xi\rho}}{\langle\sigma\rangle} &= M_{\xi\rho\chi\eta} \cdot \delta_{\chi\eta}, \\ \langle\sigma\rangle &= \frac{1}{2} \text{Sp}[\sigma] = \frac{\sigma_{xx} + \sigma_{yy}}{2}, \\ M_{\xi\rho\chi\eta} &= M_{\rho\xi\chi\eta} = M_{\rho\xi\eta\chi} = M_{\xi\rho\eta\chi}, \end{aligned} \quad (12)$$

where $\sigma_{\xi\rho}$ is the conductivity tensor; $\delta_{\chi\eta}$ is the strain tensor; $\xi, \rho, \chi, \eta = x, y$.

For a case of quasi-one-dimensional structures (for example, the arm-chair GeNR), the longitudinal component $M = M_{xxxx}$ of the fourth-rank elastic conductivity tensor can be expressed by the following formula:

$$M = \frac{\Delta\sigma}{\sigma_0} \frac{1}{\delta}, \quad (13)$$

where $\Delta\sigma$, S/m, is a change of the longitudinal component of the conductivity tensor due to strain; σ_0 , S/m, the longitudinal component σ_{xx} of the second-rank conductivity tensor of the undeformed arm-chair nanoribbons, $\Delta\sigma = \sigma - \sigma_0$ (σ , S/m, is the same component σ_{xx} of the deformed nanoribbons).

An expression for calculating the longitudinal component σ of the conductivity tensor of the

arm-chair GeNRs obtained in the frame of the Green – Kubo theory [21] using Green's function method and Hubbard model Hamiltonian [18] is presented in works [17, 19]:

$$\begin{aligned} \sigma &= 2 \frac{i\pi e^2}{k_B T V} \sum_{\mathbf{k}, \beta} \sum_{\mathbf{q}, \lambda} v(\mathbf{k}) v(\mathbf{q}) \langle n_{\mathbf{k}\beta} \rangle \times \\ &\times \left[\langle n_{\mathbf{q}\lambda} \rangle + \delta_{\mathbf{k}\mathbf{q}} \delta_{\beta\lambda} (1 - \langle n_{\mathbf{k}\beta} \rangle) \right], \end{aligned} \quad (14)$$

where V , m^3 , is the nanoribbon volume; T , K, is the absolute temperature; e , C, is the elementary charge; \mathbf{k}, \mathbf{q} are two-component wave vectors within the Brillouin zone (BZ); β, λ are the spin indices; $v(\mathbf{k})$, m/s, is the longitudinal component of the electron velocity vector in the Brillouin zone; $\langle n_{\mathbf{k}\beta} \rangle$ – is the average number of particles in a quantum state with the wave vector \mathbf{k} and spin β .

The average number of particles $\langle n_{\mathbf{k}\beta} \rangle$ is expressed by the Fermi – Dirac distribution function:

$$\langle n_{\mathbf{k}\beta} \rangle = \left[1 + \exp \left(\frac{\varepsilon(\mathbf{k}) - \mu}{k_B T} \right) \right]^{-1},$$

where k_B , J/K, is the Boltzmann constant; μ , J/mol, is the chemical potential which is found from a condition of distribution function normalization by a total number of N_e electrons in the system; this number is expressed as

$$\begin{aligned} N_e &= \sum_{\mathbf{k}, \beta} \langle n_{\mathbf{k}\beta} \rangle = \\ &= \sum_{\mathbf{k}, \beta} \left[1 + \exp \left(\frac{\varepsilon(\mathbf{k}) - \mu}{k_B T} \right) \right]^{-1}. \end{aligned}$$

The velocity vector is determined by means of a standard method using the electronic spectrum (10):

$$\mathbf{v}(\mathbf{k}) = \frac{1}{\hbar} \frac{\partial E(\mathbf{k})}{\partial \mathbf{k}}. \quad (15)$$

Table

Model parameter values used in the calculations

Parameter	Notation	Values
Number of UC along NR length width	N n	10 000 9, 10, 50, 100
Number of defects in NR	N_d	1, 10, 100, 1000
Relative tensile (compression) strain	δ	-0.10; -0.06; -0.04; -0.02; -0.01; 0.01; 0.02; 0.04; 0.06; 0.10
Equilibrium interatomic bond length (Ge-Ge), Å	R_0	2.44
Deformation temperature, K	T	300

Note: UC is the unit cell, NR is the nanoribbon.

This paper presents the results of studying the piezoresistance properties of the arm-chair GeNRs of various width and with different types of conductivity: n Arm, where n sets the number of unit cells (UC) along the ribbon width. The values of the parameters used in the calculations are summarized in the Table.

Dependencies of the longitudinal component M of the elastic conductivity tensor on the value of the relative strain δ calculated using Eq. (13), are presented in Figs. 2 and 3. The calculated points in the figures are marked by symbols and connected by lines.

We considered a case of the so-called half-filled band, i. e. each Ge atom gives one electron to the system, while each impurity As atom gives two. Therefore, the total number of electrons was calculated as $N_e = N \cdot n + N_d$.

As it follows from Fig. 2, a , the value of M from the conducting arm-chair 9Arm NR is positive at low concentration of the defects ($N_d = 1$) and negative at all other values of the concentration. All curves $M(\delta)$ for the conducting 9Arm NR with different concentrations show nonmonotonic decrease while the strain δ rises over the entire range of its values. The case of $N_d = 100$ is an exception, where the coefficient M exhibits monotonic growth in the domain of $\delta > 0$ (tensile strain).

Behavior of function $M(\delta)$ completely correlates with the changes in the band structure of the conducting impurity nanoribbons described above. An increase in the conduction band width leads to a decrease of the states density at the Fermi level with the growth of δ . However, the band gap occurring at the impurity level gets wider as the values N_d and δ grow. Therefore, as a result of the competition between these two effects, the conductivity of the nanoribbon decreases as a whole, which leads to the behavior of the component M described above for the cases of small concentration of impurities ($N_d = 1, 10$).

An increase in the impurities concentration leads to an interesting effect. In general, the numerical value of the coefficient M decreases with the growth of the concentration practically for all the calculated values of the relative strain δ . But at the concentration of $N_d = 100$, the dependence of $M(\delta)$ lies higher than that for the case of $N_d = 100$. Such a behavior of the value M is connected with the fact that due to thermal fluctuations the electrons fill the conduction band of the NR thus facilitating the conductivity growth. The increase of the donor impurities concentration raises the number of charge carriers in the conduction band. All these factors change the conductivity, the contribution to which is made by all filled

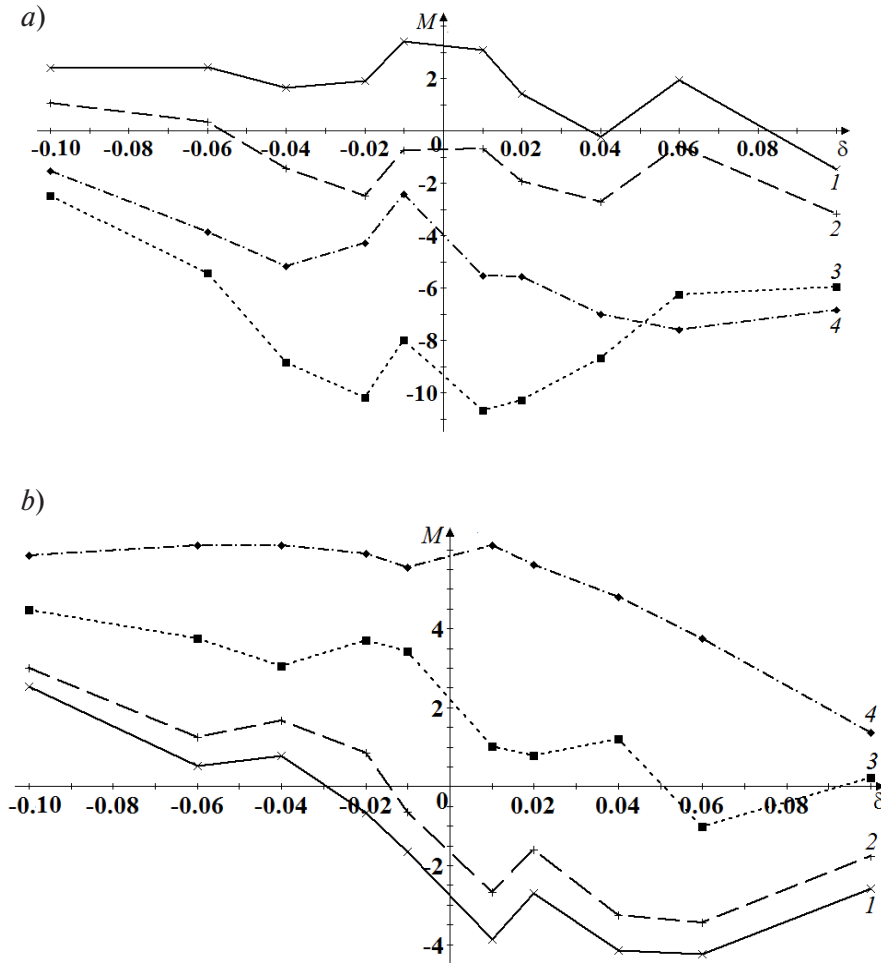


Fig. 2. Dependencies of the longitudinal component M of the elastic conductivity tensor of the arm-chair 9Arm GeNRs (a) and 10Arm GeNRs (b) (9 and 10 are the number of the UC along the width) on the value of the relative strain δ for various donor defect concentrations N_d : 1 (1), 10 (2), 100 (3), 1000 (4); The calculated points in the figures are marked by symbols and connected by lines

electronic states in the conduction band.

The dependence of $M(\delta)$ for the number of defects $N_d = 1000$ retains the general behavior trend of the NR 9Arm longitudinal component. The competition between two factor, in particular, the broadening of the band gap in the proximity of the impurity level due to defect concentration growth and the relative strain, and the increase in the number of free carriers, leads to a reduction of $M(\delta)$ in the domain of $\delta < 0$ (compression strain) and its rise in the domain of $\delta > 0$ (tensile strain).

In case of the semiconductor arm-chair GeNRs (10Arm, 50Arm, 100Arm), the behavior of the longitudinal component of the elastic con-

ductivity tensor M depends on the width of the nanoribbon studied. Thus, function $M(\delta)$ GeNR 10Arm monotonically decreases with the growth of the relative strain over the entire range of value δ (Fig. 2,b) for various values of the defects concentration ($N_d = 1, 10, 100, 1000$). Starting from $\delta = -0.1$, the value of M is positive for all values of N_d . The positive value is due to crystallite conductivity increasing along with the compression strain ($\delta < 0$) as a result of band gap narrowing and the number of the conduction band free carriers rising.

Then, for the case of small concentrations of the defects ($N_d = 1, 10$), the curves go into the negative value domain. As in the case of ideal

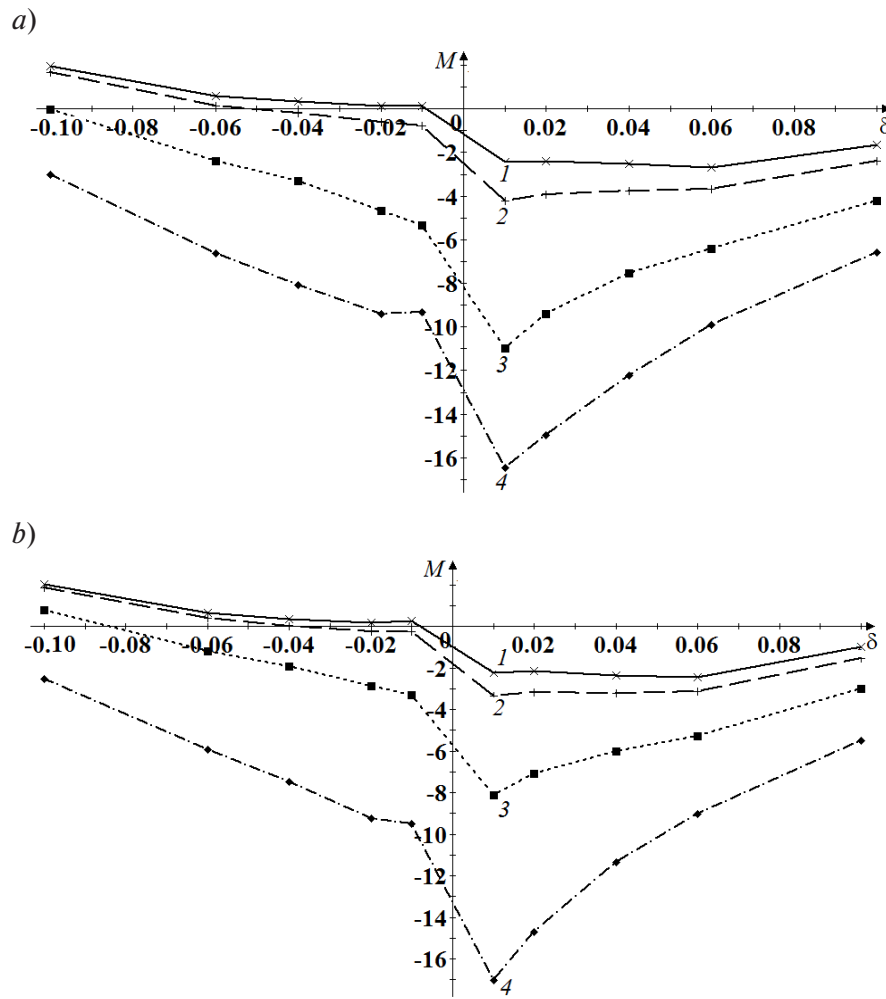


Fig. 3. Dependencies similar to the ones indicated in Fig. 2, but for 50Arm GeNRs (a) and 100Arm GeNRs (b) and the same concentration of donor defects N_d

GeNRs [12], it stems from the reduction of the conductivity along with the growth of strain δ . We can explain this effect with the broadening of the band gap E_g of the semiconductor NRs, which decreases the number of the filled electronic states in the conduction band.

The growth in the donor defects concentration ($N_d = 1, 10, 100, 1000$) in general does not change the behavior trend of the M value only increasing its numerical value.

The character of the functional dependence $M(\delta)$ changes for wide NRs of 50Arm and 100Arm. In the negative domain of δ (compression), we can observe the value of M GeNR 50Arm decreasing for all defects concentrations (Fig. 3,a). During the transition to the positive

strain (tensile) domain for the case of $N_d = 1$ the longitudinal component of the elastic conductivity tensor faces practically no changes until $\delta = 0.1$ ("plateau" domain), in the latter case we observe we see its growth. Further growth of the defects concentration ($N_d = 10, 100, 1000$) leads to dramatic rise of the M value in the tensile strain domain. Producing a wider ribbon (100Arm) results in a "plateau" for the case of $N_d = 10$ (Fig. 3,b) as well. Such an effect corresponds to the behavior of the band structure of the deformed semiconductor NRs. There is a competition between two factors. The first one is connected with the growth of the NR conductivity thanks to the increase in the number of free carriers in the conduction band cause by the donor



defects. The second factor consists in the blocked conductivity of the ribbon due to an increase of E_g along with the growth of δ .

In general, wider GeNR leads to a reduction of the band gap $E_g \sim 1/H$, where H – is the ribbon width. In turn, this increases the crystallite conductivity and, consequently, the numerical value of the coefficient M (Fig. 3, *b*).

The approach described above and the analytical algorithm were applied to the study of the piezoresistance properties of graphene nanoribbons with donor and acceptor impurities [19]. The comparison of the trends in the dependencies behavior $M(\delta)$ presented in this paper along with the literature data on piezoresistance properties of graphene nanoribbons showed a qualitative agreement of the obtained results. We should expect that the described properties are characteristic of the other graphene family structures as well.

Conclusion

A theoretical study of the piezoresistance of germanene nanoribbons of the “arm-chair” type with donor defects with different types of conductivity doped with point substitutional defects showed a number of

features of a qualitative and quantitative change of the longitudinal component of the elastic conductivity tensor M .

A study of the behavior and value of the constant M depending on the concentration of donor impurities, the geometric parameters of the nanoribbon (in particular, its width), the extent of the strain, demonstrates a complete picture of the change in the longitudinal conductivity of nanoribbons caused by mechanical tension and compression.

The sensitivity of the elastic conductivity tensor to the listed factors proves the possibility of effective control over the conductivity of germanene.

The obtained theoretical data can be proposed for quantitative calibration of nanoelectromechanical devices that function on the basis of the piezoresistance effect and have germanene nanoribbons as their primary structural material.

The study was financially supported by the Russian Foundation for Basic Research and the Administration of the Volgograd Oblast as part of scientific project No. 19-42-343001_r_mol_a (19-42-343001_p_mol_a).

REFERENCES

1. Morozov S.V., Novoselov K.S., Geim A.K., Electronic transport in graphene, *Phys. Usp.* 51 (7) (2008) 744–748.
2. Lozovik Yu.E., Merkulova S.P., Sokolik A.A., Collective electron phenomena in graphene, *Phys. Usp.* 51 (7) (2008) 727–744.
3. Chernozatonskii L.A., Sorokin P.B., Artukh A.A., New nanostructures based on graphene: physical and chemical properties and applications, *Russ. Chem. Rev.* 83 (2014) 251–279 (in Russian).
4. Lemme M.C., Current status of graphene transistors, *Solid State Phenomena.* 156 (October) (2009) 499–509.
5. Lebegue S., Bjoerkman T., Klintonberg M., et al., Two-dimensional materials from data filtering and *ab initio* calculations, *Physical Review X.* 3 (3) (2013) 031002.
6. Acun A., Zhang L., Bampoulis P., et al., Germanene: the germanium analogue of graphene, *Journal of Physics: Condensed Matter.* 27 (44) (2015) 443002.
7. Behzad S., Effect of uni-axial and bi-axial strains and vertical electric field on free standing buckled germanene, *Journal of Electron Spectroscopy and Related Phenomena.* 229 (December) (2018) 13–19.
8. Ould NE M.L., El Hachimi A.G., Boujnah M., et al., Comparative study of electronic and optical properties of graphene and germanene: DFT study, *Optik.* 158 (April) (2018) 693–698.
9. Kaloni T.P., Schwingenschlögl U., Stability of germanene under tensile strain, *Chemical Physics Letters.* 583 (17 September) (2013) 137–140.
10. Mortazavi B., Rahaman O., Makaremi M., et al., First-principles investigation of mechanical properties of silicene, germanene and stanene,

Physica E: Low-dimensional Systems and Nanostructures. 87 (March) (2017) 228–232.

11. **Kazemlou V., Phirouznia A.**, Influence of compression strains on photon absorption of silicene and germanene, Superlattices and Microstructures. 128 (April) (2019) 23–29.

12. **Lebedeva O.S., Lebedev N.G., Lyapkoso-va I.A.**, Elastic conductivity of silicene and germanene nanoribbons, St. Petersburg State Polytechnical University Journal. Physics and Mathematics. 12 (4) (2019) 38–49.

13. Physics of graphene, Edited by Aoki H., Dresselhaus M.S. (Nanoscience and Technology), Springer International Publishing, 2014.

14. **Landau L.D., Lifshitz E.M.**, Theory of elasticity, 2nd ed., Course of theoretical physics, Vol. 7, Pergamon Press, Oxford, 1981.

15. **Lebedeva O.S., Lebedev N.G.**, The influence of the stretching and compression deformations on the piezoresistance of the carbon nanotubes and graphene nanoribbons, St. Petersburg State Polytechnical University Journal. Physics and Mathematics. (1(189)) (2014) 26–34 (in Russian).

16. **Izyumov Ju.A., Chashhin N.I., Alekseev D.S.**, Teoriya sil'no korrelirovannykh sistem. Metod

proizvodjashhego funkcionala [The theory of strongly correlated systems. Method of generating functional], Reguljarnaja i Haoticheskaja Dinamika Publ., Moscow, 2006 (in Russian).

17. **Lebedeva O.S., Lebedev N.G.**, The piezoresistive effect in doped single-walled carbon nanotubes in the “Hubbard-I” approach, St. Petersburg State Polytechnical University Journal. (2 (195)) (2014) 149–161 (in Russian).

18. **Stepanov N.F.**, Kvantovaya mekhanika i kvantovaya khimiya [Quantum mechanics and quantum chemistry], Mir and Moscow State University Publishing, Moscow, 2001 (in Russian).

19. **Lebedeva O.S., Lebedev N.G., Lyapkosova I.A.**, The effect of isomorphic impurities on the elastic conductivity of Dirac structures, Journal of Physics: Condensed Matter. 32 (14) (2020) 145301.

20. **Bir G.L., Pikus G.E.**, Symmetry and strain-induced effects in semiconductors, John Wiley & Sons, Inc., New-York, 1974.

21. **Kvasnikov I.A.**, Termodinamika i statisticheskaja fizika. T. 4: Kvantovaja statistika [Thermodynamics and statistical physics, in 4 Vols., Vol. 4: Quantum Statistics], KomKniga Publ., Moscow, 2005.

Received 02.11.2020, accepted 25.01.2021.

THE AUTHORS

LEBEDEVA Olga S.

Volgograd State University

100, University Ave., Volgograd, 400062, Russian Federation

lebedeva_os@volsu.ru

LEBEDEV Nikolay G.

Volgograd State University

100, University Ave., Volgograd, 400062, Russian Federation

nikolay.lebedev@volsu.ru

LYAPKOSOVA Irina A.

Volgograd State Agricultural University

26, University Ave., 400002 Volgograd, Russian Federation

lyapkosovao_irina@mail.ru

СПИСОК ЛИТЕРАТУРЫ

1. **Морозов С.В., Новоселов К.С., Гейм А.К.** Электронный транспорт в графене // Успехи физических наук. 2008. Т. 178. № 7. С. 776–780.
2. **Лозовик Ю.Е., Меркулова С.П., Соко-**



- лик А.А. Коллективные электронные явления в графене // Успехи физических наук. 2008. Т. 178. № 7. С. 758–776.
3. Чернозатонский Л.А., Сорокин П.Б., Артюх А.А. Новые наноструктуры на основе графена: физико-химические свойства и приложения // Успехи химии. 2014. Т. 83. Вып. 3. С. 251–279.
4. Lemme M.C. Current status of graphene transistors // Solid State Phenomena. 2009. Vol. 156. October. Pp. 499–509.
5. Lebegue S., Bjoerkman T., Klintonberg M., Nieminen R.M., Eriksson O. Two-dimensional materials from data filtering and *ab initio* calculations // Physical Review X. 2013. Vol. 3. No. 3. P. 031002.
6. Acun A., Zhang L., Bampoulis P., Farmanbar M., van Houselt A., Rudenko A.N., Lingenfelder M., Brocks G., Poelsema B., Katsnelson M.I., Zandvliet H.J.W. Germanene: the germanium analogue of graphene // Journal of Physics: Condensed Matter. 2015. Vol. 27. No. 44. P. 443002.
7. Behzad S. Effect of uni-axial and bi-axial strains and vertical electric field on free standing buckled germanene // Journal of Electron Spectroscopy and Related Phenomena. 2018. Vol. 229. December. Pp. 13–19.
8. Ould NE M.L., El Hachimi A.G., Boujnah M., Benyoussef A., El Kenz A. Comparative study of electronic and optical properties of graphene and germanene: DFT study // Optik. 2018. Vol. 158. April. Pp. 693–698.
9. Kaloni T.P., Schwingenschlögl U. Stability of germanene under tensile strain // Chemical Physics Letters. 2013. Vol. 583. 17 September. Pp. 137–140.
10. Mortazavi B., Rahaman O., Makaremi M., Dianat A., Cunibert G., Rabczuk T. First-principles investigation of mechanical properties of silicene, germanene and stanene // Physica E: Low-dimensional Systems and Nanostructures. 2017. Vol. 87. March. Pp. 228–232.
11. Kazemlou V., Phirouznia A. Influence of compression strains on photon absorption of silicene and germanene // Superlattices and Microstructures. 2019. Vol. 128. April. Pp. 23–29.
12. Лебедева О.С., Лебедев Н.Г., Ляпкосова И.А. Эластопроводимость силициновых и германеновых нанолент // Научно-технические ведомости СПбГПУ. Физико-математические науки. 2019. Т. 12. № 4. С. 38–49.
13. Physics of graphene. Edited by Aoki H., Dresselhaus M.S. (Nanoscience and Technology). Switzerland: Springer International Publishing, 2014. 345 p.
14. Ландау Л.Д., Лифшиц Е.М. Курс теоретической физики в 10 тт. Т. VII. Теория упругости. М.: Наука, Гл. ред. физ.-мат. лит.-ры, 2003. 264 с.
15. Лебедева О.С., Лебедев Н.Г. Влияние растяжения и сжатия на пьезорезистивность углеродных нанотрубок и графеновых нанолент // Научно-технические ведомости СПбГПУ. Физико-математические науки. 2014. № 1 (189) С. 26–34.
16. Изюмов Ю.А., Чашин Н.И., Алексеев Д.С. Теория сильно коррелированных систем. Метод производящего функционала. М.: Регулярная и хаотическая динамика, 2006. 384 с.
17. Лебедева О.С., Лебедев Н.Г. Пьезорезистивный эффект в примесных однослойных углеродных нанотрубках в приближении «Хаббард-I» // Научно-технические ведомости СПбГПУ. 2014. № 2 (195). С. 149–161.
18. Степанов Н.Ф. Квантовая механика и квантовая химия. М.: Мир, 2001. 519 с.
19. Lebedeva O.S., Lebedev N.G., Lyapkoso I.A. The effect of isomorphic impurities on the elastic conductivity of Dirac structures // Journal of Physics: Condensed Matter. 2020. Vol. 32. No. 14. P. 145301.
20. Бир Г.Л., Пикус Г.Е. Симметрия и деформационные эффекты в полупроводниках. М.: Наука, 1972. 584 с.
21. Квасников И.А. Термодинамика и статистическая физика. В 4 тт. Т. 4. Квантовая статистика. М.: Комкнига, 2005. 352 с.

Статья поступила в редакцию 02.11.2020, принята к публикации 25.01.2021.

СВЕДЕНИЯ ОБ АВТОРАХ

ЛЕБЕДЕВА Ольга Сергеевна — кандидат физико-математических наук, ассистент Волгоградского государственного университета и доцент Волгоградского государственного аграрного университета, г. Волгоград, Российская Федерация.

400062, Российская Федерация, г. Волгоград, Университетский пр., 100

lebedeva_os@volsu.ru

ЛЕБЕДЕВ Николай Геннадьевич — доктор физико-математических наук, профессор Волгоградского государственного университета, г. Волгоград, Российская Федерация.

400062, Российская Федерация, г. Волгоград, Университетский пр., 100

nikolay.lebedev@volsu.ru

ЛЯПКОСОВА Ирина Александровна — кандидат сельскохозяйственных наук, доцент Волгоградского государственного аграрного университета, г. Волгоград, Российская Федерация.

400002, г. Волгоград, Университетский пр., 26

lyapkosova_irina@mail.ru



DOI: 10.18721/JPM.14102
UDC 538.945

CURRENT CONFIGURATIONS IN THE LONG JOSEPHSON CONTACT IN AN EXTERNAL MAGNETIC FIELD

M.A. Zelikman

Peter the Great St. Petersburg Polytechnic University,
St. Petersburg, Russian Federation

Current configurations in a periodically modulated long Josephson contact located in an external magnetic field are considered for values of the pinning parameter I greater than and less than the critical one (I_c). It is shown that, if $I > I_c$, the maximum value of the non-quenching current is determined by the contact length and does not depend on the value of the external magnetic field. In the case $I < I_c$, the critical current is determined by the value of the magnetic field at which the vortices begin to fill the entire length of the contact, and does not depend on the length of the contact. At the same time, with the growth of the external magnetic field, the critical value of the current decreases.

Keywords: long Josephson contact, magnetic field, undimmed current, vortices

Citation: Zelikman M.A., Current configurations in the long Josephson contact in an external magnetic field, St. Petersburg Polytechnical State University Journal. Physics and Mathematics. 14 (1) (2021) 21–30. DOI: 10.18721/JPM.14102

This is an open access article under the CC BY-NC 4.0 license (<https://creativecommons.org/licenses/by-nc/4.0/>)

ТОКОВЫЕ КОНФИГУРАЦИИ В ДЛИННОМ ДЖОЗЕФСОНОВСКОМ КОНТАКТЕ ВО ВНЕШНЕМ МАГНИТНОМ ПОЛЕ

М.А. Зеликман

Санкт-Петербургский политехнический университет Петра Великого,
Санкт-Петербург, Российская Федерация

Рассмотрены токовые конфигурации в периодически модулированном длинном джозефсоновском контакте, находящемся во внешнем магнитном поле, для значений параметра пиннинга I больше и меньше критического (I_c). Показано, что при $I > I_c$ максимальное значение незатухающего тока определяется длиной контакта и не зависит от величины внешнего магнитного поля. В случае $I < I_c$ критический ток определяется значением магнитного поля H_{\max} , при котором вихри начинают заполнять всю длину контакта, и не зависит от длины контакта. При этом с ростом внешнего магнитного поля критическое значение тока снижается.

Ключевые слова: длинный джозефсоновский контакт, магнитное поле, незатухающий ток, вихри

Ссылка при цитировании: Зеликман М.А. Токковые конфигурации в длинном джозефсоновском контакте во внешнем магнитном поле // Научно-технические ведомости СПбГПУ. Физико-математические науки. 2021. Т. 14. № 1. С. 21–30. DOI: 10.18721/JPM.14102

Статья открытого доступа, распространяемая по лицензии CC BY-NC 4.0 (<https://creativecommons.org/licenses/by-nc/4.0/>)

Introduction

The studies of the recent years brought us much closer to room-temperature superconductivity [1, 2]. Therefore, the problem of critical fields and currents, essential for practical application of superconductors, is now of utmost importance. For the classic superconductors, this problem is solved on the basis of Ginzburg – Landau equations. High-temperature superconductors (HTSC) are for the most part represented by granulated ceramics. They consist of adjoining granules separated by a dielectric. At the points where the granules touch each other, Josephson contacts are formed. All these Josephson contacts are nonlinear elements, which highly complicates the analysis of such media.

Moreover, the macrostructure of the HTSC is a cellular medium which leads to vortex pinning. Such complexities exclude the possibility of using Ginzburg – Landau equations to calculate current states in the HTSC. Other approaches have to be found to analyze currents in such media.

Recently, long Josephson contacts are in the focus of scientists' attention. On the one hand, this is connected with the possibility of developing artificial structures of such a type [3 – 5] that could allow testing theoretical predictions. At the present time, such structures in which the dielectric in the layer between the superconductors is replaced by a ferromagnetic are under study [6]. This keen interest to the indicated structures is also caused by the physical phenomena observed in them attributable to three-dimensional superconductors: the Meissner effect, emergence and interaction of vortices, vortex lattice formation, etc. Periodic modulating of a long Josephson contact allows us to study both the problems of vortex pinning, as well as the profile of the magnetic field penetrating the contact in a form of vortices. In this case, the mathematical problem is much simpler, than that for the three-dimensional superconductor, and can have an exact solution. Therefore, many works are devoted to the research of the long Josephson contacts

[7 – 12]. For example, papers [10, 11] considered a periodically modulated long contact placed into a constant external magnetic field parallel to the contact plane in case when the total current through the contact equals zero. Next, paper [12] presents a calculation of the current distribution in a contact with a given total current in a zero external magnetic field. However, in many cases the external field is not equal to zero, thus we should evaluate its influence on the superconductor current, in particular, on the critical current value.

The purpose of this study is to analyze a general case of a long Josephson contact with a non-dissipative supercurrent placed into an external magnetic field.

Problem setting

An artificial periodically modulated long Josephson contact (PMLJC) (Fig. 1, *a*) is a thin dielectric layer (plane xz) between two superconductors crossed by dielectric strips $2l$ thick along the axis y and d wide along the axis x ; the strips are parallel to each other, infinite along the axis z and are periodically located along the axis x , at a distance of L from each other. The external magnetic field, as well the axes of the vortices are directed along the axis z . Fig. 1, *b* depicts the structure of the artificially created PMLJC [3]. In the regions between the strips, the value of the phase jump φ between the sides of the contact is changing slowly in the coordinates, while it changes dramatically in the strip.

In Fig. 1, *a*, the value of the phase jump mean with respect to the k th region between the strips is denoted as φ_k . Assume the phase jump in the region closest to the contact boundary equals φ_1 , and as it advances deeper into the long contact the phase jumps is denoted as φ_2 , φ_3 , etc. The distribution of the φ_k values describes the steady-state current.

We should consider the penetration of the magnetic field in the presented model of the contact at zero and nonzero currents, as well as the processes in the absence of any external magnetic field.

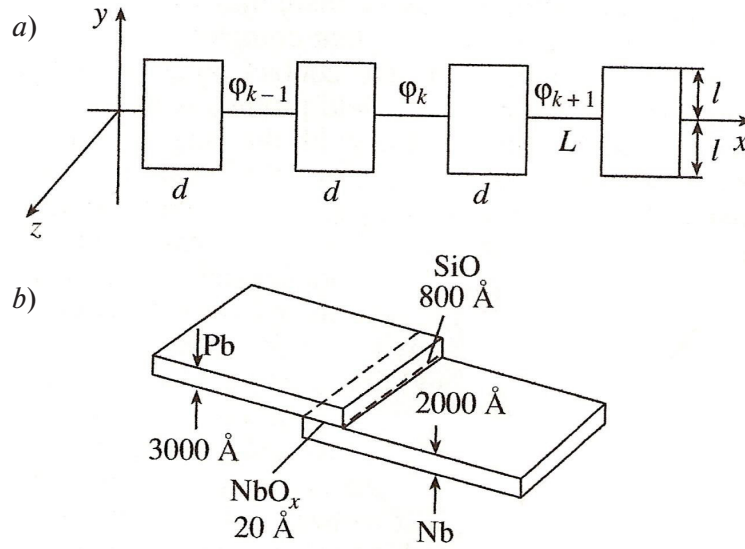


Fig. 1. Model of a periodically modulated long Josephson contact (a) and an example of the structure of such a contact created (b); φ_k — is the value of the phase jump mean with respect to the k^{th} region between the strips

Penetration of magnetic field in a PMLJC at zero total current

First, let us consider a case when the total current through the PMLJC equals zero. We should account for the fact that in the presence of pinning, the distribution of the phase jumps and currents throughout the contact is ambiguous. The cause of this ambiguity lies in the obvious “hysteresis” of the situation: the form of the established distribution configuration depends on the previous history of the PMLJC operation, i.e. on how the contact achieved this state. For example, if it was placed in any arbitrarily small field before the cool down and the transition into the superconducting state, then the magnetic fluxes will penetrate the inner cells of the contact as well. If it was placed in a magnetic field in the superconducting state, then at small fields, it will have the Meissner configuration, i.e. the field penetrates only a narrow boundary layer. There is an enormous range of variations.

Let us solve the problem for the case of adiabatic switching of the field. The contact is already in the superconducting state, while the external field H_e is slowly growing from the zero value.

Since the current is equal to zero and due

to symmetry, we can conclude that near both boundaries of the contact, the currents are distributed similarly, but have opposite directions.

At small values of H_e , there is the Meissner configuration near the contact boundary, when the φ_k values decrease as the number goes up and equal zero in the depth of the contact. At the same time, the magnetic field created by the boundary currents completely compensates the external one in the depth of the contact. Such a situation can take place until the external field reaches a certain maximum possible value H_s , moreover, up until the moment the Meissner state is stable [13]. In the Type-I superconductors, the limit of the indicated state is defined by the equality of the energies of the normal and the superconducting states taking into account the energy of the shielding currents. If the external field exceeds H_s , then the sample goes into a normal state. In the case of the Josephson contact under consideration, this reasoning is inapplicable.

It is interesting to learn how the contact behaves, when the external field exceeds the H_s value and the Meissner state is impossible. As it is known, when the pinning is absent, there would be a periodic sequence of vortices in the contact.

In this case, we need to account for the occurrence of the pinning. The authors of papers [10 – 12] demonstrated (including the authors of this article) that the character of the vortex picture depends on the value of the so-called pinning parameter [12]:

$$I = 4\pi\mu_0 j_c Lld / \Phi_0,$$

where j_c , A/m², is the critical current density of each point Josephson junction; Φ_0 , Wb, is the magnetic flux quantum; the sense of the geometric variables L, l, d is clear from Fig. 1.

At small values of the pinning parameter I , the situation is the same as with zero pinning, i.e. when the external field exceeds a certain value $H_{\max} > H_s$, vortices fill the entire contact from its boundary and to infinity. This is similar to the situation of the Type-II superconductor. At great values of the parameter I , with the growth of the field vortices advance from the boundary inside the contact, while the magnetic field in the depth of the contact remains equal to zero, i.e. the situation is similar to the Type-III superconductor behavior. On the basis of an approach developed in nonlinear dynamics [13, 14], paper [12] shows that there is a critical value of the pinning parameter $I_c = 0.9716$ which divides these two cases.

In the frame of works [10, 11], we calculated the magnetic field profile inside the contact based on the analysis of continuous configuration transformation which takes place in the direction of its energy decreasing (to be precise, Gibbs energy decreasing). The process of reconstructing the configuration is regarded as a continuous transformation of the currents and phase jumps distribution. As the external magnetic field increases gradually starting from zero, there is a continuous transformation of the transient current distribution. In addition, in some configuration regions the currents decrease, while in the other they rise, i.e. the vortices are not like hard particles “pushed” inside by the field, it is as if they are “flowing” inside the contact.

An algorithm proposed in papers [10, 11] allowed finding such a configuration, into which the Meissner state transits when the external field exceeds the H_s value to a small degree, and ob-

serving its development during any further growth of the field. This method answers the question of the state stability as well.

The calculations showed that there is such a critical value of the pinning parameter I_c in the range of 0.95–1.00 which divides two possible modes of the magnetic field penetrating the contact. This result correlates with the critical value of the pinning parameter $I_c = 0.9716$ found in papers [12 – 14]. In case of $I > I_c$, at any value of the external field there is a boundary current structure of finite length which completely compensates the external field in the depth of the contact. In our article [10], we present a detailed research of this case. In the depth of the contact, the magnetic field equals zero, at the border it decreases with the depth almost linearly, with some more or less considerable oscillations. Values of the slope coefficient are rational fractions that remain constant in the finite intervals of the parameter I . If a value of I goes beyond the upper limit of such an interval, the slope coefficient spikes and assumes the value of another rational fraction

As it was mentioned before, in the considered case of zero total current through the contact, the currents are distributed identically near both of its ends, but go in opposite directions. Moreover, the magnetic fields generated in the points symmetrical with respect to the middle of the contact are identical in value and direction.

Let us introduce normalized strength of the external field $h = H_e / H_0$, where $H_0 = \Phi_0 / \mu_0 S$ is a value of the external field at which one quantum of the magnetic flux Φ_0 passes through each cell with the area S . Then the magnetic field inside the m th cell can be calculated using the formula [10]:

$$h_m = (\varphi_{m+1} - \varphi_m) / 2\pi.$$

Fig. 2 presents magnetic field reliefs inside the contact for different values of the I parameter at certain values of the external normalized magnetic field h . The calculation was based on the assumption that right and left structures do not intersect, i.e. the contact length was considered infinite. If the length is finite, then the right and the left diagrams intersect, a recalculation should

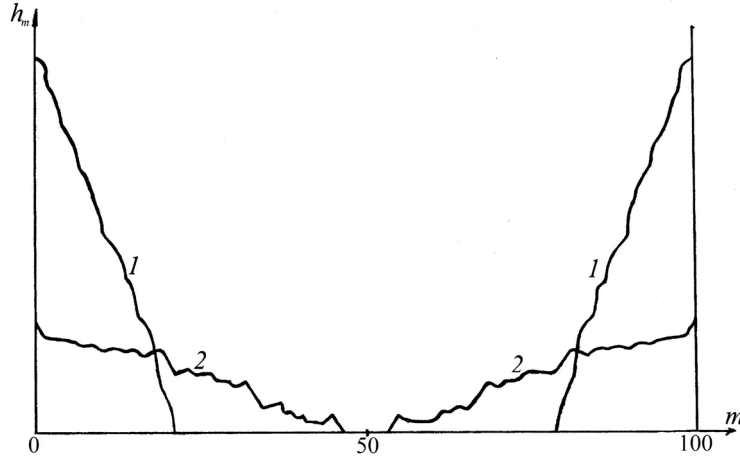


Fig. 2. Profiles of the magnetic field inside a long ($m = 100$) contact for two values of the pinning parameter: 5 and 2 (curves 1 and 2 respectively) at certain values of the external magnetic field (m is the cell number)

be made to account for that. However, in any case the picture is symmetrical, and the vortex system is at a standstill.

If $I < I_c$, then the boundary structure can only exist till the value of the external field $H_{\max}(I)$. At $H_e > H_{\max}$, the length of the boundary configuration, calculated by the method used in paper [10] (i.e. assuming infinite contact length), grows continuously in the process of the calculation. This means that the calculation process can have infinite duration, while the field penetrates the contact to infinite depth. For a detailed analysis of the $I < I_c$ case, we used the indicated method in paper [11] for the option of the limited contact length, as two symmetrical sequences of vortices coming from different ends of the contact must stop after they meet at its center.

Just as for $I > I_c$, in any case the picture is symmetrical, and the vortex system is at a standstill.

Nonzero current in the absence of the external magnetic field

At the zero external magnetic field, due to symmetry, one can argue that the currents are distributed in a similar manner near both ends and flow in the same direction. It results from the Ampère's circuital law that the field outside is expressed as

$$H = J/2b,$$

where J , A, is the total current through the contact; b , m, is the length of the contact along the axis z .

As in the "Penetration of magnetic field in a PMLJC at zero total current" section, we should find the configuration of the phase jump distribution in the boundary region minimizing Gibbs energy at the given fields on both sides of the contact (see this calculation in the aforementioned section). The critical value of the pinning parameter dividing the modes is the same, i.e. $I_c = 0.9716$. The difference in this case consists in the fact that the total current serves as the given parameter instead of the external magnetic field. If the value of the pinning parameter is less than critical ($I < I_c$), then the boundary structure can exist only till the external field value $H_{\max}(I)$, i.e. till the value of the total current

$$J_{\max}(I) = 2b H_{\max}(I).$$

However, the main difference of the option under study from the one in the aforementioned section lies in the fact that vortices at different ends of the contact have opposite orientations. Until the contact length is great enough for these vortex picture not to overlap (either at $I > I_c$ or at $I < I_c$ and $J < J_{\max}$), the whole configuration is static, the vortices are still. But, if the contact length is such that the pictures overlap, then in this region of overlap, the vortices of the oppo-

site orientations are attracted to one another and “annihilate”, i.e. are mutually eliminated. At the same time, the vortices that were contributing to the force holding the vortex configuration due to pinning disappear, and the picture stops being static. New vortices enter the overlap region, and the same happens to them as well. As the vortices move, the energy transfers into heat, and the currents stop being nondissipative.

The same phenomenon occurs, if $I < I_c$, but $J > J_{\max}$, when the vortex sequences from both sides tend to fill the entire length of the contact. These sequences have opposite orientations, and so they are mutually eliminated. They are replaced by new vortices, which motion leads to a transfer of the energy into heat.

Contact in external magnetic field at nonzero current

Let us consider a general case. A contact is in an external magnetic field which was switched on adiabatically, i.e. the magnetic field strength was growing slowly and monotonically from zero to H_e . After that, an external current is passing through the contact which is growing slowly and monotonically from zero to J . The resultant field outside the contact on one side (to be specific, let us say, the right one) equals $J + J/2b$, and on the other side is equal to $H_e - J/2b$.

Let us denote the vortex orientation in the right structure as positive, while the reverse one is negative. Again, we face the problem of calculating the boundary region configurations.

Case of $I > I_c$. Introduce dimensionless parameters

$$j = \frac{J}{bH_0}, l_{\text{cont}} = \frac{L_{\text{cont}}}{L + d},$$

where l_{cont} is the contact length expressed as the number of cells.

Fig. 3 shows the magnetic field profiles inside the contact for the case when it is long enough, so prior to switching the j current the boundary structures (in dashed lines) do not overlap. With the growth of the j current the situation inside the contact near its opposite ends starts to differ dramatically. On its right end, in the neighborhood

of which the field equals $H_e + J/2b$, the configuration corresponds the minimum of Gibbs energy at the adiabatic increase of the magnetic field from H_e to $H_e + J/2b$, i.e. the field linearly decreases with the depth into the contact starting from $H_e + J/2b$. The length of this boundary structure equals $(h + j/2)/k$ cells.

On the other end, the field was decreasing from H_e to $H_e - J/2b$, i.e. there was a counter motion of the external magnetic field. Therefore, due to hysteresis, the relief is no longer linear.

The following cases are possible.

1. If $j > 4h$, then $h - j/2 < -h$. In addition, the field subdues the pinning of the vortices already existing on the left end, as a result of which there is a vortex structure consisting of oppositely oriented vortices establishing on the left end (Fig. 3,a). The field profile on the left end of the contact is also linear, its length is equal to $(j/2 - h)/k$. If the contact length l_{cont} is less than the sum of the boundary structure lengths, in particular

$$(h + j/2)/k + (j/2 - h)/k = j/k,$$

then in their overlap region the oppositely oriented vortices are annihilated and replaced by new ones which cause the energy transfer into heat, and the currents stop being nondissipative.

2. If $2h < j < 4h$, then the vortices closest to the left end of the contact are negatively oriented, while the farthest are positively oriented (Fig. 3,b). In addition, the length of the negative part of the structure equals $(j/2 - h)/k$ cells. With the current growth, the right structure expands, but the vortices are not annihilated on the boundary with the left one, since they have the same orientation. The left configuration is shrinking under the pressure of the right one, and its vortices of the positive orientation are moving left and cancel out the negative ones. If the contact length is less than the sum of the lengths, i.e.

$$(h + j/2)/k + (j/2 - h)/k = j/k,$$

then all positive vortices of the left structure are eliminated, and the negative vortices of the left structure are cancelling out the positive vortices

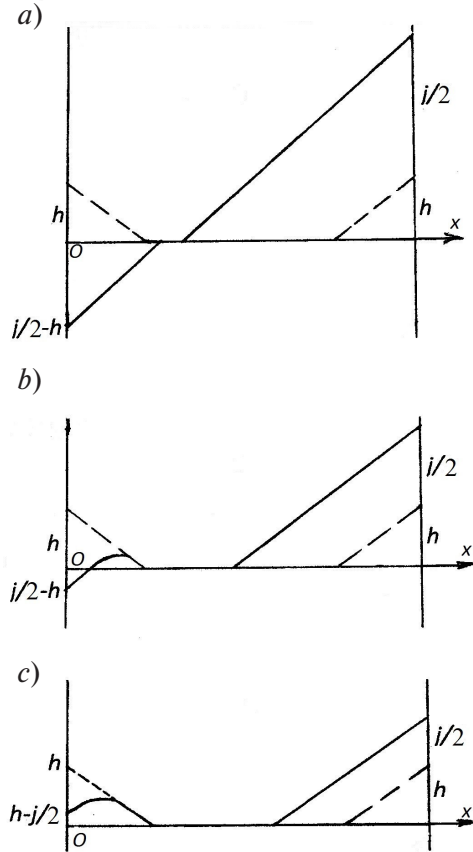


Fig. 3. Profiles of the magnetic field inside the long contact at the given external field h and different values of the current j : $j > 4h$ (a), $4h > j > 2h$ (b), $j < 2h$ (c). Dashed lines show the profiles prior to the current switching ($j = 0$)

of the right one. Again, we find ourselves in the situation considered in clause 1.

Generalizing cases 1 and 2, we draw a conclusion that the continuous vortices motion with the energy-heat transfer occurs if the following conditions are met: $j > kl_{cont}$, $j > 2h$, which can be written in a form

$$j > \max\{kl_{cont}, 2h\}. \quad (1)$$

This result includes the condition of the vortex picture motion $j > kl_{cont}$, obtained in paper [12], when $h = 0$.

3. If $h > j/2$ (Fig. 3,c), then both vortex structures are oriented identically, therefore there is no mutual annihilation in case of them overlapping. But there is a question whether the picture

is stationary or not. If the boundary structures intersect at nonzero current, then the forces acting on a point of their intersection from both sides are equal. With the current increasing, the right end force grows, while the left end one drops, as the left structure was obtained due to a decrease in the magnetic field strength. Therefore, the right structure is moving the left one to the left. At the same time, the left configuration shrinks to such a state at which the force of its counteraction is maximal. This state corresponds to a linear dependence of the magnetic field on the depth with the same coefficient k .

As a result, boundary profiles of the magnetic field of finite length establish at both ends. The sum of the boundary structure lengths equals

$$(h + j/2)/k + |h - j/2|/k = 2h/k \text{ cells.}$$

Fig. 4 demonstrates various possible cases. In case shown in Fig. 4,a, the structures don't intersect, the situation is stationary. In case presented in Fig. 4,b, the structures AFG and CMN would be at a standstill. We need to find whether the structures $DBFG$ and $BDMN$ would be at a standstill, and if the force exerted by $BDMN$ on $DBFG$ is sufficient to hold it at rest. It follows from the equilibrium of CMN that the force exerted by $BDMN$ is equal to the force of CBD , which in turn equals the ABD force. The latter compensates the $BDFG$ force, i.e. the $BDFG$ structure would be at rest. The same goes for the $BDMN$ structure. Similar consideration shows that in the case displayed in Fig. 4,c the structures are at a standstill as well.

However, in the case shown in Fig. 4,d (see its description below), there is no equilibrium, thus the vortices move right to left, and their energies transfer to heat.

Let us find such a ratio of parameters at which the situation d) occurs:

$$FG = h + j/2, MN = h - j/2, \\ FP = FG - MN = j.$$

It follows from $FP > RP$ that $j > kl_{cont}$. Taking account, that $h > j/2$, we come to a relation

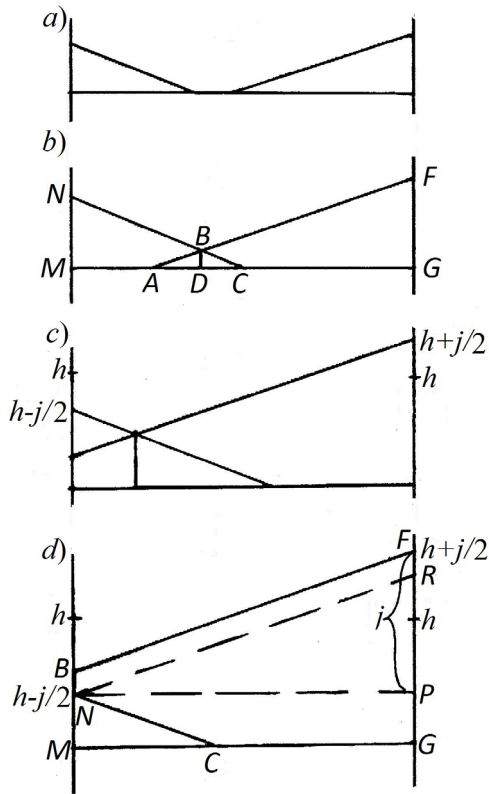


Fig. 4. Possible profiles of the normalized magnetic field strength in the contact. In the cases *a*, *b* and *c*, the structures are stationary; in the case *d* there is a right-to-left motion (letters denoting the points are introduced for convenience of reference in the text)

$$kl_{cont} < j < 2h. \quad (2)$$

By combining conditions (1) and (2), we obtain the condition for the nonstationary state at $I > I_c$:

$$j > kl_{cont}$$

(at any h).

Case of $I < I_c$. In case of the indicated condition, various situations may occur.

If $h + j/2 < h_s$, then there are Meissner configurations lining up at both ends. If the contact is not too short, they do not overlap and the picture is stationary.

However, if $h + j/2 < h_{max}$, then at the right end of the contact, a sequence of vortices forms that tends to seize the entire length of the contact. The left structure is either a Meissner configura-

tion, or a finite boundary structure, or a chain of vortices, which also tends to seize the whole contact. But, since the field strength at the right end is greater than that at the left one, then the left structure cannot counteract the push from the right, the vortices move right to left with their energy transferring into heat.

In another case, when the conditions

$$h_s < h + j/2 < h_{max},$$

$$h_s < h - j/2 < h_{max},$$

are simultaneously satisfied, there are structures of finite length at both ends.

Nevertheless, their lengths are not proportional to the field values in the neighborhood of the boundary, as it was in the case of $I > I_c$. One can analyze the behavior of the boundary structures depending on the ratio of the structure and contact lengths. However, since the range of the magnetic fields from h_s to h_{max} is rather narrow, then we can confidently neglect this situation and assert that the picture stops being stationary as soon as the greater field $H_e + J/2b$ exceeds the H_{max} value, i.e. $h + j/2 > h_{max}$.

In paper [12], at $h = 0$ the condition of the vortices motion has the form $j > 2h_{max}$, which is a subresult of the obtained formula.

We can consider the case of 3D Josephson medium in a similar manner with some suppositions [15].

Conclusion

Current configurations in a periodically modulated long Josephson contact located in an external magnetic field are considered for values of the pinning parameter I greater than and less than the critical one (I_c). The study is based on the results of an analysis of continuous configuration transformation which takes place in the direction of its energy decreasing (to be precise, Gibbs energy decreasing). The process of reconstructing the configuration is regarded as a continuous transformation of the currents and phase jumps distribution.

It is shown that, if $I > I_c$, the maximum value of the nondissipative current is determined by the contact length and does not depend on



the value of the external magnetic field. In case $I < I_c$, the critical current is determined by the value of the magnetic field H_{\max} at which the vortices begin to fill the entire length of the contact,

and does not depend on the length of the contact. At the same time, with the growth of the external magnetic field, the critical value of the current decreases.

REFERENCES

1. Drozdov A.P., Kong P.P., Minkov V.S., et al., Superconductivity at 250 K in lanthanum hydride under high pressures, *Nature*. 569 (7757) (2019) 528–531.
2. Somayazulu M., Ahart M., Mishra A.K., et al., Evidence for superconductivity above 260 K in lanthanum superhydride at megabar pressures, *Physical Review Letters*. 122 (2) (2019) 027001.
3. Golubov A.A., Serpuchenko I.L., Ustinov A.V., Dynamics of a Josephson fluxon in a long junction with inhomogeneities: theory and experiment, *Sov. Phys. JETP*. 67 (6) (1988) 1256–1264.
4. Paramonov M.E., Goldobin E.B., Koshelets V.P., Measurements of the linewidth of Josephson junction with injectors, *Journal of Radio Electronics*. (7) (2016) 1684–1719 (in Russian).
5. Revin L.S., Pankratov A.L., Masterov D.V., et al., Features of long YBCO Josephson junctions fabricated by preliminary topology mask, *IEEE Transactions on Applied Superconductivity*. 28 (7) (2018) 1100505.
6. Golovchanskiy I.A., Abramov N.N., Stolyarov V.S., et al., Ferromagnetic resonance with long Josephson junction, *Superconductor Science and Technology*. 30 (5) (2017) 054005.
7. Revin L.S., Pankratov A.L., Chiginev A.V., et al., Asymmetry of the velocity-matching steps in YBCO long Josephson junctions, *Superconductor Science and Technology*. 31 (4) (2018) 045002.
8. Rudenko E.M., Korotash I.V., Krakovnyy A.O., Bilogolovskyy M.O., Nonlinear dynamics of quantum vortices in long Josephson junctions, *Metallofiz. Noveishie Tekhnol.* 40 (10) (2018) 1273–1282 (in Ukrainian).
9. Nashaat M., Botha A.T., Shukrunov Yu.M., Devil's staircases in the IV characteristics of superconductor/ferromagnetic/superconductor Josephson junctions, *Physical Review. B*. 97 (22) (2018) 224514.
10. Zelikman M.A., Penetration of magnetic field into a long periodically modulated Josephson contact, *Technical Physics*. 54 (2) (2009) 197–203.
11. Zelikman M.A., Formation of a quasi-uniform sequence of vortices in a periodically modulated finite-length Josephson contact, *Technical Physics*. 54 (12) (2009) 1742.
12. Dorogovtzev S.N., Samuhin A.N., Magnetic flux penetration and critical current in long periodically modulated Josephson junction, *Europhysics Letters*. 25 (9) (1994) 693–698.
13. Meiss J.D., Symplectic maps, variational principles, and transport, *Reviews of Modern Physics*. 64 (3) (1992) 795–848.
14. Sagdeev R.Z., Usikov D.A., Zaslavsky G.M., Nonlinear physics: From the pendulum to turbulence and chaos, Harwood Academic Publishers, New Jersey, USA, 1988.
15. Zelikman M.A., Development of the Meissner state instability in an ordered 3D Josephson medium, *Technical Physics*. 54 (9) (2009) 1290–1300.

Received 29.10.2020, accepted 02.11.2020.

THE AUTHOR

ZELIKMAN Mark A.

Peter the Great St. Petersburg Polytechnic University

29 Politechnicheskaya St., St. Petersburg, 195251, Russian Federation

marzelik@mail.ru

СПИСОК ЛИТЕРАТУРЫ

1. Drozdov A.P., Kong P.P., Minkov V.S. et al. Superconductivity at 250 K in lanthanum hydride under high pressures // *Nature*. 2019. Vol. 569. No. 7757. Pp. 528–531.
2. Somayazulu M., Ahart M., Mishra A.K., Geballe Z.M., Baldini M., Meng Y., Struzhkin V.V., Hemley R.J. Evidence for superconductivity above 260 K in lanthanum superhydride at megabar pressures // *Physical Review Letters*. 2019. Vol. 122. No. 2. P. 027001.
3. Голубов А.А., Серпученко И.Л., Устинов А.В. Динамика джозефсоновского флюксона в длинном контакте с неоднородностями // *Журнал экспериментальной и теоретической физики*. 1988. Т. 94. № 6 (12). С. 297–311.
4. Парамонов М.Е., Голдобин Э.Б., Кошелев В.П. Измерение ширины линии джозефсоновского генератора с инжекторами // *Журнал радиоэлектроники*. 2016. № 7. С. 1684–1719.
5. Revin L.S., Pankratov A.L., Masterov D.V., Pavlov S.A., Chiginev A.V., Skorokhodov E.V. Features of long YBCO Josephson junctions fabricated by preliminary topology mask // *IEEE Transactions on Applied Superconductivity*. 2018. Vol. 28. No. 7. P. 1100505.
6. Golovchanskiy I.A., Abramov N.N., Stolyarov V.S., Emelyanova O.V., Golubov A.A., Ustinov A.V., Ryazanov V.V. Ferromagnetic resonance with long Josephson junction // *Superconductor Science and Technology*. 2017. Vol. 30. No. 5. P. 054005.
7. Revin L.S., Pankratov A.L., Chiginev A.V., Masterov D.V., Parafin A.E., Pavlov S.A. Asymmetry of the velocity-matching steps in YBCO long Josephson junctions // *Superconductor Science and Technology*. 2018. Vol. 31. No. 4. P. 045002.
8. Руденко Э.М., Коротах И.В., Краковный А.А., Белоголовский М.А. Нелинейная динамика квантовых вихрей в длинных джозефсоновских переходах // *Металлофизика и новейшие технологии*. 2018. Т. 40. № 10. С. 1273–1282 (на украинском языке).
9. Nashaat M., Botha A.T., Shukrunov Yu.M. Devil's staircases in the IV characteristics of superconductor/ferromagnetic/superconductor Josephson junctions // *Physical Review B*. Vol. 97. No. 22. P. 224514.
10. Зеликман М.А. Проникновение магнитного поля в длинный периодически модулированный джозефсоновский контакт // *Журнал технической физики*. 2009. Т. 79. № 2. С. 36–42.
11. Зеликман М.А. Установление квазиоднородной последовательности вихрей в периодически модулированном джозефсоновском контакте конечной длины // *Журнал технической физики*. 2009. Т. 79. № 12. С. 19–25.
12. Dorogovtzev S.N., Samuhin A.N. Magnetic flux penetration and critical current in long periodically modulated Josephson junction // *Europhysics Letters*. 1994. Vol. 25. No. 9. Pp. 693–698.
13. Meiss J.D. Symplectic maps, variational principles, and transport // *Reviews of Modern Physics*. 1992. Vol. 64. No. 3. Pp. 795–848.
14. Заславский Г.М., Сагдеев Р.З. Введение в нелинейную физику: от маятника до турбулентности и хаоса. М.: Наука, 1988. 368 с.
15. Зеликман М.А. Развитие неустойчивости мейсснеровского состояния в трехмерной упорядоченной джозефсоновской среде // *Журнал технической физики*. 2009. Т. 79. № 9. С. 47–57.

Статья поступила в редакцию 29.10.2020, принята к публикации 02.11.2020.

СВЕДЕНИЯ ОБ АВТОРЕ

ЗЕЛИКМАН Марк Аронович — доктор физико-математических наук, профессор кафедры физики Санкт-Петербургского политехнического университета Петра Великого, Санкт-Петербург, Российская Федерация.

195251, Российская Федерация, г. Санкт-Петербург, Политехническая ул., 29
marzelik@mail.ru

DOI: 10.18721/JPM.14103

UDC 539.3, 537.226.4

A MICROSTRUCTURAL MODEL OF FERROELECTROELASTIC MATERIAL WITH TAKING INTO ACCOUNT THE DEFECTS' EVOLUTION

A.S. Semenov

Peter the Great St. Petersburg Polytechnic University,
St. Petersburg, Russian Federation

For the description of the hysteresis behavior of ferroelectrics/ferroelastics under multiaxial combined electrical and/or mechanical loading, a thermodynamically consistent microstructural model of ferroelectroelastic material is proposed taking into account the presence and evolution of polar point defects. The model also takes into account multiphase composition, anisotropy of properties, domain structure, and dissipative motion of domain walls. The linear theory of the charged point defects evolution is proposed based on the free energy of defects in the quadratic form of the polarization vector and strain tensor of defects. The dependence of the hysteresis loop shift (due to internal field bias) on parameters of the free energy of defects is shown. Comparison of computation results with experimental curves of dielectric, mechanical, and electromechanical hysteresis for polycrystalline piezoelectric PZT PIC-151, BaTiO₃, single-crystal PMN-PZT and KTS doped with acceptor additives, showed a good agreement.

Keywords: polycrystalline piezoceramics, point defect, constitutive equation, hysteresis, finite element homogenization

Citation: Semenov A.S., A microstructural model of ferroelectroelastic material with taking into account the defects' evolution, St. Petersburg Polytechnical State University Journal. Physics and Mathematics. 14 (1) (2021) 31–54. DOI: 10.18721/JPM.14103

This is an open access article under the CC BY-NC 4.0 license (<https://creativecommons.org/licenses/by-nc/4.0/>)

МИКРОСТРУКТУРНАЯ МОДЕЛЬ СЕГНЕТОЭЛЕКТРОУПРУГОГО МАТЕРИАЛА С УЧЕТОМ ЭВОЛЮЦИИ ДЕФЕКТОВ

А.С. Семенов

Санкт-Петербургский политехнический университет Петра Великого,
Санкт-Петербург, Российская Федерация

Для описания гистерезисного поведения сегнетоэлектриков/сегнетоэластиков в условиях сложного многоосного комбинированного электрического и/или механического нагружения предложена термодинамически согласованная микроструктурная модель сегнетоэлектроупругого материала с учетом наличия и эволюции полярных точечных дефектов. Модель также учитывает многофазный состав, анизотропию свойств, доменную структуру и диссипативный характер движения доменных стенок. Предложена линейная теория эволюции заряженных точечных дефектов на основе выбора свободной энергии дефектов в виде квадратичной формы вектора поляризации и тензора деформации дефектов, уравнения эволюции которых получены на основе диссипативного неравенства. Установлена зависимость величины смещения петель гистерезиса от параметров свободной энергии дефектов. Сравнение результатов расчетов с экспериментальными кривыми диэлектрического, механического и электромеханического гистерезисов для легированных акцепторными добавками поликристаллической пьезокерамики PZT PIC-151, поликристаллического BaTiO₃, монокристаллических PMN-PZT и KTS показало хорошее совпадение.

Ключевые слова: поликристаллическая пьезокерамика, точечный дефект, определяющее уравнение, гистерезис, конечно-элементная гомогенизация, моделирование

Ссылка при цитировании: Семенов А.С. Микроструктурная модель сегнетоэлектростроупного материала с учетом эволюции дефектов // Научно-технические ведомости СПбГПУ. Физико-математические науки. 2021. Т. 14. № 1. С. 31–54. DOI: 10.18721/JPM.14103

Статья открытого доступа, распространяемая по лицензии CC BY-NC 4.0 (<https://creativecommons.org/licenses/by-nc/4.0/>)

Introduction

Ferroelectric piezoceramics (ferroelectroelastics) [1 – 3] are the most prominent example of active (smart) materials, finding wide practical applications as components of fuel injectors, nanopositioners, micromotors, scanning tunneling microscope drives, vibration dampers, piezoelectric transformers, memory cells, etc. The positioning accuracy, strength and durability of these devices can be assessed by developing refined models of ferroelastic materials [2, 4 – 12].

Point defects in the crystal lattice are a major influence on the evolution and motion of domain boundaries, the size and shape of hysteretic curves, switching times, and dielectric, piezoelectric and mechanical properties [1, 3, 13 – 16]. This is confirmed by numerous experiments performed for barium titanate (BaTiO₃) [15, 17, 18], PZT [19–21], PLZT [22], PMS-PZT [23], PMN-PZT [24], BNT-BT [25], KNN [26], TGS [1, 13], KTS [27]. However, modern models of ferroelastic materials do not directly account for the presence of defects and their evolution.

Point defects also considerably affect the degradation of electromechanical properties [16], either arising through cyclic electrical and/or mechanical stress (fatigue), or evolving over time in the absence of external mechanical and electrical loading (aging). The basic mechanisms behind fatigue and aging are similar in nature and are directly related to the presence and evolution of point defects.

Lattice defects can be both intrinsic and produced artificially during crystal growth by introducing acceptor or donor impurities, as well as by exposing the crystal to high-energy particles (including irradiation with X-rays, gamma rays, neutrons, and electrons) [13]. The presence of

spatially ordered polar defects with a given concentration makes it possible to generate an internal bias electric field in the crystal, preserving a stable monodomain state [13], to achieve large changes in the strain with a small change in the electric field [28]. This opens new prospects for deliberately modifying the electromechanical properties of ferroelastic materials by producing structural defects in controlled conditions, which is a method of domain engineering as a type of technological engineering.

In this regard, experimental and theoretical studies considering the influence of defects on the switching processes and motion of domain walls are a major focus.

The goal of this study is to develop and verify a thermodynamically consistent microstructural model of a ferroelastic material, accounting for the evolution of polar point defects, which allows describing the hysteretic behavior in mono- and polycrystalline ferroelastic materials under arbitrary scenarios of complex multiaxial combined electrical and/or mechanical loading.

We previously considered a microstructural model accounting for hard-switching point defects [11]. We further develop this approach in this study, including the option to change the orientation and concentration of dipolar point defects and the effect this has on the switching processes.

Defect-free model

The scleronomic microstructural model accounting for dissipative motion of domain walls in a single crystal was originally proposed in [5] by analogy with the model of crystal plasticity, and was further developed in [6 – 12]. The model was rigorously proved from a thermodynamic perspective and confirmed experimentally [5, 7 – 10].



The formulation of the constitutive equations is limited to the infinitesimal isothermal case. It is assumed that the strain tensor $\boldsymbol{\varepsilon}$ and the electric induction vector \mathbf{D} can be decomposed as the sum of linear (reversible) ($\boldsymbol{\varepsilon}^l$, \mathbf{D}^l) and permanent (similar to plastic) ($\boldsymbol{\varepsilon}^r$, \mathbf{P}^r) components:

$$\boldsymbol{\varepsilon} = \boldsymbol{\varepsilon}^l + \boldsymbol{\varepsilon}^r, \quad (1)$$

$$\mathbf{D} = \mathbf{D}^l + \mathbf{P}^r. \quad (2)$$

The linear relations corresponding to a linear piezoelectric material hold true for the reversible components:

$$\begin{cases} \boldsymbol{\varepsilon}^l = \boldsymbol{\varepsilon} - \boldsymbol{\varepsilon}^r = {}^4\mathbf{S}^E \cdot \boldsymbol{\sigma} + {}^3\mathbf{d}^T \cdot \mathbf{E}, \\ \mathbf{D}^l = \mathbf{D} - \mathbf{P}^r = {}^3\mathbf{d} \cdot \boldsymbol{\sigma} + \boldsymbol{\kappa}^\sigma \cdot \mathbf{E}. \end{cases} \quad (3)$$

These relations allow for the following reversible form:

$$\begin{cases} \boldsymbol{\sigma} = {}^4\mathbf{C}^D \cdot (\boldsymbol{\varepsilon} - \boldsymbol{\varepsilon}^r) - {}^3\mathbf{h}^T \cdot (\mathbf{D} - \mathbf{P}^r), \\ \mathbf{E} = -{}^3\mathbf{h} \cdot (\boldsymbol{\varepsilon} - \boldsymbol{\varepsilon}^r) + \boldsymbol{\beta}^e \cdot (\mathbf{D} - \mathbf{P}^r), \end{cases} \quad (4)$$

where ${}^4\mathbf{S}^E$ is the tensor of elastic compliance moduli of the crystal at constant electric field (4th-order), ${}^3\mathbf{d}$ is the tensor of piezoelectric moduli of the crystal (3rd-order), $\boldsymbol{\kappa}^\sigma$ is the dielectric constant tensor of the crystal at constant stresses (2nd-order). The tensors ${}^4\mathbf{C}^D$, ${}^3\mathbf{h}^T$, $\boldsymbol{\beta}^e$ are determined based on the tensors ${}^4\tilde{\mathbf{S}}^E$, ${}^3\tilde{\mathbf{d}}^T$, $\tilde{\boldsymbol{\kappa}}^\sigma$ by inverting the block matrix.

The processes of irreversible deformation and spontaneous polarization in piezoceramics are associated with potential sudden displacement of non-centrosymmetric atoms in the crystal lattice. $N = 6$ orientations of $\langle 001 \rangle$ spontaneous polarization (along positive and negative directions of the three crystallographic axes) occur in a tetragonal crystal, corresponding to six possible domain configurations and

$$M = N(N - 1) = 30$$

switching systems.

$N = 8$ orientations of $\langle 111 \rangle$ spontaneous polarization (along the directions of four main diagonals of the crystal cell) occur in a rhombo-

hedral single crystal, corresponding to 8 possible domain configurations and 56 switching systems. $N = 12$ orientations of $\langle 011 \rangle$ spontaneous polarization (along the diagonals of the crystal cell faces) occur in an orthorhombic single crystal corresponding to 12 possible domain configurations and 132 switching systems. The residual strain tensor and the residual polarization vector of the crystal can be written in this case as the sum of the contributions of individual domains:

$$\boldsymbol{\varepsilon}^r = \sum_{I=1}^N c_I \tilde{\boldsymbol{\varepsilon}}_I^r, \quad (5)$$

$$\mathbf{P}^r = \sum_{I=1}^N c_I \tilde{\mathbf{P}}_I^r, \quad (6)$$

where c_I is the volume fraction (concentration) of the I^{th} domain in the monocrystal, satisfying the constraints

$$0 \leq c_I \leq 1, \quad \sum_{I=1}^N c_I = 1. \quad (7)$$

The tildes in expressions (5), (6) represent the variables defined at the domain level. The tensors $\tilde{\boldsymbol{\varepsilon}}_I^r$ and vectors $\tilde{\mathbf{P}}_I^r$ are constant, determined by the values of spontaneous strain and polarization, as well as the geometry of the unit cell.

The single-crystal moduli ${}^4\mathbf{S}^E$, ${}^3\mathbf{d}$ and $\boldsymbol{\kappa}^\sigma$ are calculated based on the moduli ${}^4\tilde{\mathbf{S}}_I^E$, ${}^3\tilde{\mathbf{d}}_I$ and $\tilde{\boldsymbol{\kappa}}_I^\sigma$ of the individual domains using relations similar to (5) and (6):

$$\begin{aligned} {}^4\mathbf{S}^E &= \sum_{I=1}^N c_I {}^4\tilde{\mathbf{S}}_I^E, \quad {}^3\mathbf{d} = \sum_{I=1}^N c_I {}^3\tilde{\mathbf{d}}_I, \\ \boldsymbol{\kappa}^\sigma &= \sum_{I=1}^N c_I \tilde{\boldsymbol{\kappa}}_I^\sigma. \end{aligned} \quad (8)$$

The structure of the tensors ${}^4\tilde{\mathbf{S}}_I^E$, ${}^3\tilde{\mathbf{d}}_I$ and $\tilde{\boldsymbol{\kappa}}_I^\sigma$ depends on the type of the crystal lattice. The simplified approach that has gained wide recognition in practice [5, 6, 9], based on the isotropic approximation for the elastic compliance tensor ${}^4\tilde{\mathbf{S}}_I^E$ and the dielectric constant tensor $\tilde{\boldsymbol{\kappa}}_I^\sigma$, represents the tensors characterizing the linear behavior of the piezoelectric material domain as

$$\begin{aligned}
 {}^4\tilde{\mathbf{S}}_I^E &= \tilde{s}_1 \mathbf{1} \otimes \mathbf{1} + \tilde{s}_2 (\mathbf{1} \otimes \mathbf{1} + \mathbf{1} \otimes \mathbf{1}), \\
 {}^3\tilde{\mathbf{d}}_I &= \tilde{d}_{31} (\mathbf{p} \otimes \mathbf{1} - \mathbf{p} \otimes \mathbf{p} \otimes \mathbf{p}) + \\
 &\quad + \tilde{d}_{33} \mathbf{p} \otimes \mathbf{p} \otimes \mathbf{p} + \\
 &\quad + (1/2) \tilde{d}_{15} (\mathbf{1} \otimes \mathbf{p} + \mathbf{1} \otimes \mathbf{p} - 2\mathbf{p} \otimes \mathbf{p} \otimes \mathbf{p}), \\
 \tilde{\mathbf{K}}_I^\sigma &= \tilde{\mathbf{K}} \mathbf{1},
 \end{aligned} \tag{9}$$

using the symbols for direct and indirect dyadic products

$$\begin{aligned}
 (\mathbf{A} \otimes \mathbf{B})_{ijkl} &= A_{ij} B_{kl}, \\
 (\mathbf{A} \otimes \mathbf{B})_{ijkl} &= A_{ik} B_{jl}, \\
 (\mathbf{A} \otimes \mathbf{B})_{ijkl} &= A_{il} B_{jk}, \\
 (\mathbf{A} \otimes \mathbf{x})_{ijk} &= A_{ik} x_j,
 \end{aligned}$$

while $\mathbf{p} = \tilde{\mathbf{P}}_I^r / |\tilde{\mathbf{P}}_I^r|$ is the unit vector of the polarization direction of the domain.

According to equalities (9), the following 6 material constants are to be found to give the tensors ${}^4\tilde{\mathbf{S}}_I^E$, ${}^3\tilde{\mathbf{d}}_I$ and $\tilde{\mathbf{K}}_I^\sigma$:

$$\begin{aligned}
 \tilde{s}_1 &= -\tilde{v}/\tilde{E}, \\
 \tilde{s}_2 &= (1 + \tilde{v})/\tilde{E}, \tilde{d}_{31}, \tilde{d}_{33}, \tilde{d}_{15}, \tilde{\mathbf{K}}.
 \end{aligned}$$

Within the framework of the model assuming a transversely isotropic material [10], with the normal to the isotropy plane depending on the polarization direction, the expressions for the linear moduli ${}^4\tilde{\mathbf{S}}_I^E$, ${}^3\tilde{\mathbf{d}}_I$ and $\tilde{\mathbf{K}}_I^\sigma$ can be written in the following form [29]:

$$\begin{aligned}
 {}^4\tilde{\mathbf{S}}_I^E &= \tilde{s}_1 \mathbf{1} \otimes \mathbf{1} + \tilde{s}_2 (\mathbf{1} \otimes \mathbf{1} + \mathbf{1} \otimes \mathbf{1}) + \\
 &\quad + \tilde{s}_3 (\mathbf{1} \otimes \mathbf{p} \otimes \mathbf{p} + \mathbf{p} \otimes \mathbf{p} \otimes \mathbf{1}) + \\
 &\quad + \tilde{s}_4 (\mathbf{1} \otimes \mathbf{p} \otimes \mathbf{p} + \mathbf{p} \otimes \mathbf{p} \otimes \mathbf{1}) + \\
 &\quad + \tilde{s}_5 \mathbf{p} \otimes \mathbf{p} \otimes \mathbf{p} \otimes \mathbf{p}, \\
 {}^3\tilde{\mathbf{d}}_I &= \tilde{d}_{31} (\mathbf{p} \otimes \mathbf{1} - \mathbf{p} \otimes \mathbf{p} \otimes \mathbf{p}) + \tilde{d}_{33} \mathbf{p} \otimes \mathbf{p} \otimes \mathbf{p} + \\
 &\quad + (1/2) \tilde{d}_{15} (\mathbf{1} \otimes \mathbf{p} + \mathbf{1} \otimes \mathbf{p} - 2\mathbf{p} \otimes \mathbf{p} \otimes \mathbf{p}), \\
 \tilde{\mathbf{K}}_I^\sigma &= \tilde{\mathbf{K}}_{11} (\mathbf{1} - \mathbf{p} \otimes \mathbf{p}) + \tilde{\mathbf{K}}_{33} \mathbf{p} \otimes \mathbf{p},
 \end{aligned} \tag{10}$$

According to Eqs. (10), the following 10 material constants are to be found to give ${}^4\tilde{\mathbf{S}}_I^E$, ${}^3\tilde{\mathbf{d}}_I$ and $\tilde{\mathbf{K}}_I^\sigma$:

$$\tilde{s}_1, \tilde{s}_2, \tilde{s}_3, \tilde{s}_4, \tilde{s}_5, \tilde{d}_{31}, \tilde{d}_{33}, \tilde{d}_{15}, \tilde{\mathbf{K}}_{11}, \tilde{\mathbf{K}}_{33}.$$

The rate of change in the concentration of the I^{th} single-crystal domain is expressed in terms of summation over all switching systems of changes in the volume fraction of the I^{th} domain due to the inflow $\dot{c}^{J \rightarrow I}$ for switching domains from J to I and due to the outflow $\dot{c}^{I \rightarrow J}$ for switching from I to J :

$$\dot{c}_I = \sum_{\substack{J=1 \\ J \neq I}}^N (\dot{c}^{J \rightarrow I} - \dot{c}^{I \rightarrow J}). \tag{11}$$

A consequence of relations (5) and (11) is that the residual strain rates can be represented in the following form:

$$\begin{aligned}
 \dot{\boldsymbol{\varepsilon}}^r &= \sum_{I=1}^N \dot{c}_I \tilde{\boldsymbol{\varepsilon}}_I^r = \sum_{I=1}^N \sum_{\substack{J=1 \\ J \neq I}}^N (\dot{c}^{J \rightarrow I} - \dot{c}^{I \rightarrow J}) \tilde{\boldsymbol{\varepsilon}}_I^r = \\
 &= \sum_{I=1}^N \sum_{\substack{J=1 \\ J \neq I}}^N \dot{c}^{J \rightarrow I} \tilde{\boldsymbol{\varepsilon}}_I^r - \sum_{J=1}^N \sum_{\substack{I=1 \\ I \neq J}}^N \dot{c}^{J \rightarrow I} \tilde{\boldsymbol{\varepsilon}}_J^r = \\
 &= \sum_{I=1}^N \sum_{\substack{J=1 \\ J \neq I}}^N \dot{c}^{J \rightarrow I} (\tilde{\boldsymbol{\varepsilon}}_I^r - \tilde{\boldsymbol{\varepsilon}}_J^r).
 \end{aligned} \tag{12}$$

This implies the representation for the permanent strain rate tensor and a similarly derived expression for the polarization velocity vector:

$$\dot{\boldsymbol{\varepsilon}}^r = \sum_{I=1}^N \sum_{\substack{J=1 \\ J \neq I}}^N \dot{c}^{J \rightarrow I} \Delta \tilde{\boldsymbol{\varepsilon}}_{J \rightarrow I}^r, \tag{13}$$

$$\dot{\mathbf{P}}^r = \sum_{I=1}^N \sum_{\substack{J=1 \\ J \neq I}}^N \dot{c}^{J \rightarrow I} \Delta \tilde{\mathbf{P}}_{J \rightarrow I}^r, \tag{14}$$

where the tensors and vectors

$$\begin{aligned}
 \Delta \tilde{\boldsymbol{\varepsilon}}_{J \rightarrow I}^r &= \tilde{\boldsymbol{\varepsilon}}_I^r - \tilde{\boldsymbol{\varepsilon}}_J^r = \tilde{\boldsymbol{\mu}}_{J \rightarrow I} \tilde{\boldsymbol{\varepsilon}}_0^r, \\
 \Delta \tilde{\mathbf{P}}_{J \rightarrow I}^r &= \tilde{\mathbf{P}}_I^r - \tilde{\mathbf{P}}_J^r = \tilde{\boldsymbol{\beta}}_{J \rightarrow I} \tilde{P}_0^r
 \end{aligned}$$

are defined by constants characterizing the crystal lattice; $\tilde{\boldsymbol{\mu}}_{J \rightarrow I}$ and $\tilde{\boldsymbol{\beta}}_{J \rightarrow I}$ are the normalized Schmidt tensor and vector; $\tilde{\boldsymbol{\varepsilon}}_0^r$ and \tilde{P}_0^r are the spontaneous deformation and polarization, respectively.

The rates of change in the elastic, piezoelec-



tric, and dielectric moduli are determined similarly based on Eqs. (8) and (11):

$$\begin{aligned} {}^4\dot{\mathbf{S}}^E &= \sum_{I=1}^N \sum_{\substack{J=1 \\ J \neq I}}^N \dot{c}^{J \rightarrow I} \Delta {}^4\tilde{\mathbf{S}}_{J \rightarrow I}^E, \\ {}^3\dot{\mathbf{d}} &= \sum_{I=1}^N \sum_{\substack{J=1 \\ J \neq I}}^N \dot{c}^{J \rightarrow I} \Delta {}^3\tilde{\mathbf{d}}_{J \rightarrow I}, \\ \dot{\mathbf{k}}^\sigma &= \sum_{I=1}^N \sum_{\substack{J=1 \\ J \neq I}}^N \dot{c}^{J \rightarrow I} \Delta \tilde{\mathbf{k}}_{J \rightarrow I}^\sigma. \end{aligned} \quad (15)$$

The equations for calculating the kinematic variables $\dot{c}^{J \rightarrow I}$, which play a fundamental role in describing the switching processes, are introduced from the condition that the thermodynamic constraints are satisfied a priori.

Limiting the decomposition of the free energy (the Helmholtz thermodynamic potential) to terms not exceeding the second order of smallness, we obtain an expression for free energy as a quadratic form with respect to the reversible components of the strain tensor $\boldsymbol{\varepsilon}^I$ and the electric induction vector \mathbf{D}^I :

$$\begin{aligned} \psi &= (1/2) \boldsymbol{\varepsilon}^I \cdots {}^4\mathbf{C}^D \cdots \boldsymbol{\varepsilon}^I - \\ &- \mathbf{D}^I \cdot {}^3\mathbf{h} \cdots \boldsymbol{\varepsilon}^I + (1/2) \mathbf{D}^I \cdot \boldsymbol{\beta}^e \cdot \mathbf{D}^I. \end{aligned} \quad (16)$$

It is assumed that the free energy is a function of the reversible strain tensor $\boldsymbol{\varepsilon}^I$, the reversible electric displacement vector \mathbf{D}^I and a number of internal state variables c_I (that the moduli ${}^4\mathbf{C}^D$, ${}^3\mathbf{h}$, $\boldsymbol{\beta}^e$ depend on): $\psi(\boldsymbol{\varepsilon}^I, \mathbf{D}^I, c_I)$.

Substituting expression (16) for the free energy into the dissipative inequality

$$\delta = \boldsymbol{\sigma} \cdots \dot{\boldsymbol{\varepsilon}} + \mathbf{E} \cdot \dot{\mathbf{D}} - \dot{\psi} \geq 0 \quad (17)$$

yields a relation

$$\begin{aligned} \delta &= \left(\boldsymbol{\sigma} - \frac{\partial \psi}{\partial \boldsymbol{\varepsilon}^I} \right) \cdots \dot{\boldsymbol{\varepsilon}}^I + \left(\mathbf{E} - \frac{\partial \psi}{\partial \mathbf{D}^I} \right) \cdot \dot{\mathbf{D}}^I + \\ &+ \boldsymbol{\sigma} \cdots \dot{\boldsymbol{\varepsilon}}^r + \mathbf{E} \cdot \dot{\mathbf{P}}^r - \sum_{I=1}^N \frac{\partial \psi}{\partial c_I} \dot{c}_I \geq 0. \end{aligned} \quad (18)$$

A consequence of the independence of the change and $\dot{\boldsymbol{\varepsilon}}^I \dot{\mathbf{D}}^I$ when considering the linear in-

equality (18), are the following relations:

$$\boldsymbol{\sigma} = \frac{\partial \psi}{\partial \boldsymbol{\varepsilon}^I}, \quad (19)$$

$$\mathbf{E} = \frac{\partial \psi}{\partial \mathbf{D}^I}, \quad (20)$$

$$\begin{aligned} \delta &= \boldsymbol{\sigma} \cdots \dot{\boldsymbol{\varepsilon}}^r + \mathbf{E} \cdot \dot{\mathbf{P}}^r + \\ &+ (1/2) \boldsymbol{\sigma} \cdots {}^4\dot{\mathbf{S}}^E \cdots \boldsymbol{\sigma} + \mathbf{E} \cdot {}^3\dot{\mathbf{d}} \cdots \boldsymbol{\sigma} + \\ &+ (1/2) \mathbf{E} \cdot \dot{\mathbf{k}}^\sigma \cdot \mathbf{E} \geq 0. \end{aligned} \quad (21)$$

Inequalities (19) and (20) produce the constitutive equations (4). The proof that the sum $-\sum_{I=1}^N \frac{\partial \psi}{\partial c_I} \dot{c}_I$ can be substituted by the rates of change in the elastic, piezoelectric, and dielectric moduli during switching is considered in [11].

Substituting expressions (13)–(15) into relation (21) yields the expression

$$\delta = \sum_{I=1}^N \sum_{\substack{J=1 \\ J \neq I}}^N G^{J \rightarrow I} \dot{c}^{J \rightarrow I} \geq 0, \quad (22)$$

where the driving force $G^{J \rightarrow I}$, conjugate to $c^{J \rightarrow I}$, is given by the following equality:

$$\begin{aligned} G^{J \rightarrow I} &= \boldsymbol{\sigma} \cdots \Delta \tilde{\boldsymbol{\varepsilon}}_{J \rightarrow I}^r + \mathbf{E} \cdot \Delta \tilde{\mathbf{P}}_{J \rightarrow I}^r + \\ &+ (1/2) \boldsymbol{\sigma} \cdots \Delta {}^4\tilde{\mathbf{S}}_{J \rightarrow I}^E \cdots \boldsymbol{\sigma} + \\ &+ \mathbf{E} \cdot \Delta {}^3\tilde{\mathbf{d}}_{J \rightarrow I} \cdots \boldsymbol{\sigma} + (1/2) \mathbf{E} \cdot \Delta \tilde{\mathbf{k}}_{J \rightarrow I}^\sigma \cdot \mathbf{E}. \end{aligned} \quad (23)$$

One possible way to satisfy the non-negative dissipation condition (22) is to choose the equation for the evolution of $c^{J \rightarrow I}$ in the form

$$\dot{c}^{J \rightarrow I} = \begin{cases} B^{J \rightarrow I} \left(\frac{G^{J \rightarrow I}}{G_c^{J \rightarrow I}} \right)^n \left(\frac{c_J}{C_0} \right)^m, \\ G^{J \rightarrow I} \geq 0; \\ 0, G^{J \rightarrow I} < 0, \end{cases} \quad (24)$$

where $G^{J \rightarrow I} > 0$, $B^{J \rightarrow I} > 0$, $n > 0$, $m > 0$, $C_0 > 0$ are the material constants that determine the shape

of the hysteresis curves.

Introducing the last factor $(c_J / C_0)^m$ in Eq.(24) allows to describe the saturation effect and satisfy the constraints (7), since as the donor concentration is depleted, i.e., at $c^J \rightarrow 0$, the switching rate decreases, i.e., $\dot{c}^{J \rightarrow I} \rightarrow 0$, which ensures that the condition $c^J \geq 0$ is satisfied. The parameter $B^{J \rightarrow I}$ characterizes the viscosity of the material (in general, it is different for each switching system).

The evolution equation (24) corresponds to the rheonomic model without a switching threshold, which is similar to the nonlinear viscoelastic model. However, it can describe scleronomic behavior with a switching threshold for large values of n .

Model with defects

In this work, which is based on a micromechanically motivated phenomenological description [11], we assume that two additional internal variables are introduced to describe the electromechanical state of a real crystallite: the defect polarization vector \mathbf{P}^d and the defect strain tensor $\boldsymbol{\varepsilon}^d$. They serve as additional arguments of the free energy and evolution equations of the internal variables. Crystal polarization \mathbf{P}^d and its strain $\boldsymbol{\varepsilon}^d$, resulting from the appearance of point defects, are calculated by averaging within a representative volume of the crystal VRVC:

$$\begin{aligned} \mathbf{P}^d &= \frac{1}{V_{\text{RVC}}} \int_{V_{\text{RVC}}} \tilde{\mathbf{P}}^d dV, \\ \boldsymbol{\varepsilon}^d &= \frac{1}{V_{\text{RVC}}} \int_{V_{\text{RVC}}} \tilde{\boldsymbol{\varepsilon}}^d dV. \end{aligned} \quad (25)$$

The change in the dipole moment $\tilde{\mathbf{p}}^d$ during defect formation is determined by the expression (see [1]):

$$\tilde{\mathbf{p}}^d = \tilde{\mathbf{p}}^s + \sum_i \tilde{q}_i \Delta \tilde{\mathbf{r}}_i,$$

where $\tilde{\mathbf{p}}^s$ is the intrinsic dipole moment of the defect whose position does not coincide with the center of inversion; $\Delta \tilde{\mathbf{r}}_i$ is the displacement of charges \tilde{q}_i in the surrounding lattice due to the

defect emerging.

The distributions of the fields corresponding to the electric potential and the polarization vector of a fixed dipole, necessary for calculating the vector \mathbf{P}^d by Eq. (25), are described by the equations:

$$\tilde{\varphi}^d = -\tilde{\mathbf{p}}^d \cdot \nabla r^{-1} / 4\pi\epsilon_0 = \tilde{\mathbf{p}}^d \cdot \mathbf{r} r^{-3} / 4\pi\epsilon_0, \quad (26)$$

$$\begin{aligned} \tilde{\mathbf{P}}^d &= \tilde{\mathbf{p}}^d \cdot \nabla \nabla r^{-1} (\epsilon - \epsilon_0) / 4\pi\epsilon_0 = \\ &= -\tilde{\mathbf{p}}^d \cdot (\mathbf{1} - 3\mathbf{r}\mathbf{r}r^{-2}) r^{-3} (\epsilon - \epsilon_0) / 4\pi\epsilon_0, \end{aligned} \quad (27)$$

where \mathbf{r} is the radius vector originating from the point where the defect is located; r is its length; $\mathbf{1}$ is the unit tensor; ϵ, ϵ_0 are the dielectric constants of the material and vacuum.

If the crystal has a system of identically oriented polar defects, they produce volumetric polarization $\mathbf{P}^d = n\tilde{\mathbf{P}}^d$, where n is the number of defects per unit volume.

According to the continuum theory of point defects [30], the displacements in an unbounded body due to the point defects evolving (the defect is formed because a disproportionate sphere is either inserted into a spherical cavity or removed from it) and their corresponding strain have the form:

$$\tilde{\mathbf{u}}^d = -c \nabla r^{-1} = c \mathbf{r} r^{-3}, \quad (28)$$

$$\tilde{\boldsymbol{\varepsilon}}^d = -c \nabla \nabla r^{-1} = c (\mathbf{1} - 3\mathbf{r}\mathbf{r}r^{-2}) r^{-3}, \quad (29)$$

where $c = \Delta V / 4\pi$ is the defect power, ΔV is the change in the volume during insertion/removal.

It is assumed in formulating the constitutive equations that the quantities \mathbf{P}^d and $\boldsymbol{\varepsilon}^d$ that describe the influence of defects (the same as \mathbf{P}^r and $\boldsymbol{\varepsilon}^r$) accounting for the switching processes represent the contribution to the total spontaneous polarization and strain, and therefore the following decompositions are generally used instead of sums (1) and (2):

$$\boldsymbol{\varepsilon} = \boldsymbol{\varepsilon}^l + \boldsymbol{\varepsilon}^r + \boldsymbol{\varepsilon}^d, \quad (30)$$

$$\mathbf{D} = \mathbf{D}^l + \mathbf{P}^r + \mathbf{P}^d. \quad (31)$$



It is assumed that the free energy of a real crystal (containing defects) allows for decomposition:

$$\Psi = \Psi_{ideal} + \Psi_{defect}, \quad (32)$$

where $\Psi_{defect} = \Psi_{defect}(\mathbf{P}^d, \boldsymbol{\varepsilon}^d, \mathbf{P}^r, \boldsymbol{\varepsilon}^r)$ is the free energy due to formation of defects; $\Psi_{ideal} = \Psi_{ideal}(\mathbf{D}^l, \boldsymbol{\varepsilon}^l, c_l)$ is the reversible part of the free energy (16).

The value Ψ_{ideal} is determined by the quadratic form of the reversible components of induction \mathbf{D}^l and strain $\boldsymbol{\varepsilon}^l$:

$$\begin{aligned} \Psi_{ideal} = & (1/2) \boldsymbol{\varepsilon}^l \cdot {}^4\mathbf{C}^E \cdot \boldsymbol{\varepsilon}^l + \\ & + \mathbf{D}^l \cdot {}^3\mathbf{h} \cdot \boldsymbol{\varepsilon}^l + (1/2) \mathbf{D}^l \cdot {}^3\boldsymbol{\beta} \cdot \mathbf{D}^l. \end{aligned} \quad (33)$$

The arguments $\mathbf{P}^r, \boldsymbol{\varepsilon}^r$ in the function

$$\Psi_{defect} = \Psi_{defect}(\mathbf{P}^d, \boldsymbol{\varepsilon}^d, \mathbf{P}^r, \boldsymbol{\varepsilon}^r)$$

are introduced to account for the mutual influence of defects and domain walls.

Since this study is aimed at developing the linear theory of defects in ferroelastic materials, we can limit the decomposition of the free energy in a series to terms no higher than the second order of smallness. The most general expression for the free energy of defects has the following quadratic form:

$$\begin{aligned} \Psi_{defect} = & (1/2) \mathbf{P}^d \cdot \mathbf{Q}_P \cdot \mathbf{P}^d + \mathbf{P}^d \cdot {}^3\mathbf{Q}_{P\varepsilon} \cdot \boldsymbol{\varepsilon}^d + \\ & + (1/2) \boldsymbol{\varepsilon}^d \cdot {}^4\mathbf{Q}_\varepsilon \cdot \boldsymbol{\varepsilon}^d + \\ & + \mathbf{P}^d \cdot \mathbf{L}_P \cdot \mathbf{P}^r + \mathbf{P}^d \cdot {}^3\mathbf{L}_{P\varepsilon} \cdot \boldsymbol{\varepsilon}^r + \\ & + \mathbf{P}^r \cdot {}^3\mathbf{L}_{\varepsilon P} \cdot \boldsymbol{\varepsilon}^d + \boldsymbol{\varepsilon}^d \cdot {}^4\mathbf{L}_\varepsilon \cdot \boldsymbol{\varepsilon}^r, \end{aligned} \quad (34)$$

where $\mathbf{Q}_P, {}^3\mathbf{Q}_{P\varepsilon}, {}^4\mathbf{Q}_\varepsilon, \mathbf{L}_P, {}^3\mathbf{L}_{P\varepsilon}, {}^3\mathbf{L}_{\varepsilon P}, {}^4\mathbf{L}_\varepsilon$ are the tensors of the 2nd, 3rd and 4th ranks, characterizing the sensitivity of the material to the influence of defects. \mathbf{Q} -tensors are used in quadratic terms with respect to the quantities characterizing the defect state $\mathbf{P}^d, \boldsymbol{\varepsilon}^d$, and \mathbf{L} -tensors are used in linear terms.

Due to symmetry of the tensors $\boldsymbol{\varepsilon}^r$ and $\boldsymbol{\varepsilon}^d$,

$$\varepsilon_{ij}^r = \varepsilon_{ji}^r, \varepsilon_{ij}^d = \varepsilon_{ji}^d \quad (i, j = \overline{1, 3}),$$

The tensors ${}^3\mathbf{Q}_{P\varepsilon}, {}^3\mathbf{L}_{P\varepsilon}, {}^3\mathbf{L}_{\varepsilon P}, {}^4\mathbf{L}_\varepsilon, {}^4\mathbf{Q}_\varepsilon$ have symmetry

$$Q_{kij}^{P\varepsilon} = Q_{kji}^{P\varepsilon}, L_{kij}^{P\varepsilon} = L_{kji}^{P\varepsilon}, L_{kij}^{\varepsilon P} = L_{kji}^{\varepsilon P},$$

$$Q_{ijkl}^\varepsilon = Q_{jikl}^\varepsilon = Q_{ijlk}^\varepsilon, L_{ijkl}^\varepsilon = L_{jikl}^\varepsilon = L_{ijlk}^\varepsilon.$$

In addition, the tensors \mathbf{Q}_P and ${}^4\mathbf{Q}_\varepsilon$ have symmetry

$$Q_{ik}^P = Q_{ki}^P, Q_{ijkl}^\varepsilon = Q_{klij}^\varepsilon$$

because the left and right factors in expression (34) are identical.

The tensors \mathbf{L}_P and ${}^4\mathbf{L}_\varepsilon$ generally do not have such symmetry. It is only in the case of point defects tending to restore symmetry upon polarization switching [28, 31, 32], so that \mathbf{P}^d becomes co-directed with \mathbf{P}^r , and $\boldsymbol{\varepsilon}^d$ coaxial with $\boldsymbol{\varepsilon}^r$, that the tensors \mathbf{L}_P and ${}^4\mathbf{L}_\varepsilon$ have symmetry

$$L_{ik}^P = L_{ki}^P, L_{ijkl}^\varepsilon = L_{klij}^\varepsilon.$$

The above symmetry conditions allow reducing the number of independent components of the given tensors.

Within the framework of the transversely isotropic material model, the tensors

$$\mathbf{Q}_P, \mathbf{L}_P, {}^3\mathbf{Q}_{P\varepsilon}, {}^3\mathbf{L}_{P\varepsilon}, {}^3\mathbf{L}_{\varepsilon P}, {}^4\mathbf{Q}_\varepsilon, {}^4\mathbf{L}_\varepsilon,$$

appearing in Eq. (34) are expressed as

$$\begin{aligned} \mathbf{Q}_P &= Q_{11}^P (\mathbf{1} - \mathbf{p} \otimes \mathbf{p}) + Q_{33}^P \mathbf{p} \otimes \mathbf{p}, \\ \mathbf{L}_P &= L_{11}^P (\mathbf{1} - \mathbf{p} \otimes \mathbf{p}) + L_{33}^P \mathbf{p} \otimes \mathbf{p}, \\ {}^3\mathbf{Q}_{P\varepsilon} &= Q_{31}^{P\varepsilon} (\mathbf{p} \otimes \mathbf{1} - \mathbf{p} \otimes \mathbf{p} \otimes \mathbf{p}) + \\ &+ Q_{33}^{P\varepsilon} \mathbf{p} \otimes \mathbf{p} \otimes \mathbf{p} + \\ &+ (1/2) Q_{15}^{P\varepsilon} (\mathbf{1} \otimes \mathbf{p} + \mathbf{1} \otimes \bar{\mathbf{p}} - 2\mathbf{p} \otimes \mathbf{p} \otimes \mathbf{p}), \\ {}^3\mathbf{L}_{P\varepsilon} &= L_{31}^{P\varepsilon} (\mathbf{p} \otimes \mathbf{1} - \mathbf{p} \otimes \mathbf{p} \otimes \mathbf{p}) + \\ &+ L_{33}^{P\varepsilon} \mathbf{p} \otimes \mathbf{p} \otimes \mathbf{p} + \\ &+ (1/2) L_{15}^{P\varepsilon} (\mathbf{1} \otimes \mathbf{p} + \mathbf{1} \otimes \bar{\mathbf{p}} - 2\mathbf{p} \otimes \mathbf{p} \otimes \mathbf{p}), \\ {}^3\mathbf{L}_{\varepsilon P} &= L_{31}^{\varepsilon P} (\mathbf{p} \otimes \mathbf{1} - \mathbf{p} \otimes \mathbf{p} \otimes \mathbf{p}) + \\ &+ L_{33}^{\varepsilon P} \mathbf{p} \otimes \mathbf{p} \otimes \mathbf{p} + \end{aligned} \quad (35)$$

$$\begin{aligned}
 & + (1/2) L_{15}^{\varepsilon P} (\mathbf{1} \otimes \mathbf{p} + \mathbf{1} \bar{\otimes} \mathbf{p} - 2\mathbf{p} \otimes \mathbf{p} \otimes \mathbf{p}), \\
 & {}^4\mathbf{Q}_\varepsilon = Q_1^\varepsilon \mathbf{1} \otimes \mathbf{1} + Q_2^\varepsilon (\mathbf{1} \bar{\otimes} \mathbf{1} + \mathbf{1} \underline{\otimes} \mathbf{1}) + \\
 & + Q_3^\varepsilon (\mathbf{1} \otimes \mathbf{p} \otimes \mathbf{p} + \mathbf{p} \otimes \mathbf{p} \otimes \mathbf{1}) + \\
 & + Q_4^\varepsilon (\mathbf{1} \underline{\otimes} \mathbf{p} \otimes \mathbf{p} + \mathbf{p} \otimes \mathbf{p} \underline{\otimes} \mathbf{1}) + \\
 & + Q_5^\varepsilon \mathbf{p} \otimes \mathbf{p} \otimes \mathbf{p} \otimes \mathbf{p}, \quad (35) \\
 & {}^4\mathbf{L}_\varepsilon = L_1^\varepsilon \mathbf{1} \otimes \mathbf{1} + L_2^\varepsilon (\mathbf{1} \bar{\otimes} \mathbf{1} + \mathbf{1} \underline{\otimes} \mathbf{1}) + \\
 & + L_3^\varepsilon (\mathbf{1} \otimes \mathbf{p} \otimes \mathbf{p} + \mathbf{p} \otimes \mathbf{p} \otimes \mathbf{1}) + \\
 & + L_4^\varepsilon (\mathbf{1} \underline{\otimes} \mathbf{p} \otimes \mathbf{p} + \mathbf{p} \otimes \mathbf{p} \underline{\otimes} \mathbf{1}) + \\
 & + L_5^\varepsilon \mathbf{p} \otimes \mathbf{p} \otimes \mathbf{p} \otimes \mathbf{p},
 \end{aligned}$$

where \mathbf{p} is the vector of the unit normal to the isotropy plane defined by the polarization direction \mathbf{P}^r .

According to expressions (35), the following 23 material constants are to be found to give the tensors \mathbf{Q}_P , \mathbf{L}_P , ${}^3\mathbf{Q}_{P\varepsilon}$, ${}^3\mathbf{L}_{P\varepsilon}$, ${}^3\mathbf{L}_{\varepsilon P}$, ${}^4\mathbf{Q}_\varepsilon$, ${}^4\mathbf{L}_\varepsilon$:

$$\begin{aligned}
 & Q_{11}^P, Q_{33}^P, L_{11}^P, L_{33}^P, Q_{31}^{P\varepsilon}, Q_{33}^{P\varepsilon}, Q_{15}^{P\varepsilon}, \\
 & L_{31}^{P\varepsilon}, L_{33}^{P\varepsilon}, L_{15}^{P\varepsilon}, L_{31}^{\varepsilon P}, L_{33}^{\varepsilon P}, L_{15}^{\varepsilon P}, \\
 & Q_1^\varepsilon, Q_2^\varepsilon, Q_3^\varepsilon, Q_4^\varepsilon, Q_5^\varepsilon, \\
 & L_1^\varepsilon, L_2^\varepsilon, L_3^\varepsilon, L_4^\varepsilon, L_5^\varepsilon.
 \end{aligned}$$

In the isotropic case, the tensors \mathbf{Q}_P , \mathbf{L}_P , ${}^3\mathbf{Q}_{P\varepsilon}$, ${}^3\mathbf{L}_{P\varepsilon}$, ${}^3\mathbf{L}_{\varepsilon P}$, ${}^4\mathbf{Q}_\varepsilon$, ${}^4\mathbf{L}_\varepsilon$ allow for the following representation:

$$\begin{aligned}
 & \mathbf{Q}_P = Q^P \mathbf{1}, \\
 & \mathbf{L}_P = L^P \mathbf{1}, \\
 & \mathbf{Q}_{P\varepsilon} = {}^3\mathbf{L}_{P\varepsilon} = {}^3\mathbf{L}_{\varepsilon P} = {}^3\mathbf{0}, \quad (36) \\
 & {}^4\mathbf{Q}_\varepsilon = Q_1^\varepsilon \mathbf{1} \otimes \mathbf{1} + Q_2^\varepsilon (\mathbf{1} \bar{\otimes} \mathbf{1} + \mathbf{1} \underline{\otimes} \mathbf{1}), \\
 & {}^4\mathbf{L}_\varepsilon = L_1^\varepsilon \mathbf{1} \otimes \mathbf{1} + L_2^\varepsilon (\mathbf{1} \bar{\otimes} \mathbf{1} + \mathbf{1} \underline{\otimes} \mathbf{1}).
 \end{aligned}$$

Substituting Eqs. (30)–(32) into the definition of dissipation (17) yields an expression for the dissipative function accounting for the motion of domain walls, their interaction with defects, and defect formation processes:

$$\delta = \left(\boldsymbol{\sigma} - \frac{\partial \Psi_{ideal}}{\partial \boldsymbol{\varepsilon}^l} \right) \cdot \dot{\boldsymbol{\varepsilon}}^l + \left(\boldsymbol{\sigma} - \frac{\partial \Psi_{defect}}{\partial \boldsymbol{\varepsilon}^r} \right) \cdot \dot{\boldsymbol{\varepsilon}}^r +$$

$$\begin{aligned}
 & + \left(\boldsymbol{\sigma} - \frac{\partial \Psi_{defect}}{\partial \boldsymbol{\varepsilon}^d} \right) \cdot \dot{\boldsymbol{\varepsilon}}^d + \left(\mathbf{E} - \frac{\partial \Psi_{ideal}}{\partial \mathbf{D}^l} \right) \cdot \dot{\mathbf{D}}^l + \\
 & + \left(\mathbf{E} - \frac{\partial \Psi_{defect}}{\partial \mathbf{P}^r} \right) \cdot \dot{\mathbf{P}}^r + \left(\mathbf{E} - \frac{\partial \Psi_{defect}}{\partial \mathbf{P}^d} \right) \cdot \dot{\mathbf{P}}^d - \\
 & - (1/2) \boldsymbol{\sigma} \cdot {}^4\dot{\mathbf{S}}^E \cdot \boldsymbol{\sigma} - \mathbf{E} \cdot {}^3\dot{\mathbf{d}} \cdot \boldsymbol{\sigma} - \\
 & - (1/2) \mathbf{E} \cdot \dot{\boldsymbol{\kappa}}^\sigma \cdot \mathbf{E} \geq 0. \quad (37)
 \end{aligned}$$

Dissipation is absent upon change in linear reversible strain and electrical induction, so the differences

$$\boldsymbol{\sigma} - \frac{\partial \Psi_{ideal}}{\partial \boldsymbol{\varepsilon}^l}, \mathbf{E} - \frac{\partial \Psi_{ideal}}{\partial \mathbf{D}^l}$$

should become zero. It follows that the stress tensor and the electric field vector, satisfying the condition for non-negative dissipation, are defined by the relations:

$$\begin{cases} \boldsymbol{\sigma} = \frac{\partial \Psi_{ideal}}{\partial \boldsymbol{\varepsilon}^l} = {}^4\mathbf{C}^D \cdot (\boldsymbol{\varepsilon} - \boldsymbol{\varepsilon}^r - \boldsymbol{\varepsilon}^d) - \\ - {}^3\mathbf{h}^T \cdot (\mathbf{D} - \mathbf{P}^r - \mathbf{P}^d), \\ \mathbf{E} = \frac{\partial \Psi_{ideal}}{\partial \mathbf{D}^l} = -{}^3\mathbf{h} \cdot (\boldsymbol{\varepsilon} - \boldsymbol{\varepsilon}^r - \boldsymbol{\varepsilon}^d) + \\ + \boldsymbol{\beta}^\varepsilon \cdot (\mathbf{D} - \mathbf{P}^r - \mathbf{P}^d). \end{cases} \quad (38)$$

Notably, the last terms in brackets in system of equations (38) can be neglected in the vast majority of cases important for practice because the concentration of defects is assumed to be low.

Accounting for relations (38) in expression (37) yields the following expression for the dissipative function:

$$\begin{aligned}
 \delta = & \left(\boldsymbol{\sigma} - \frac{\partial \Psi_{defect}}{\partial \boldsymbol{\varepsilon}^r} \right) \cdot \dot{\boldsymbol{\varepsilon}}^r + \left(\boldsymbol{\sigma} - \frac{\partial \Psi_{defect}}{\partial \boldsymbol{\varepsilon}^d} \right) \cdot \dot{\boldsymbol{\varepsilon}}^d + \\
 & + \left(\mathbf{E} - \frac{\partial \Psi_{defect}}{\partial \mathbf{P}^r} \right) \cdot \dot{\mathbf{P}}^r + \left(\mathbf{E} - \frac{\partial \Psi_{defect}}{\partial \mathbf{P}^d} \right) \cdot \dot{\mathbf{P}}^d - \\
 & - (1/2) \boldsymbol{\sigma} \cdot {}^4\dot{\mathbf{S}}^E \cdot \boldsymbol{\sigma} - \mathbf{E} \cdot {}^3\dot{\mathbf{d}} \cdot \boldsymbol{\sigma} - \\
 & - (1/2) \mathbf{E} \cdot \dot{\boldsymbol{\kappa}}^\sigma \cdot \mathbf{E} \geq 0. \quad (39)
 \end{aligned}$$

Specific expressions of the evolution equa-



tions for the cases of hard-switching (frozen) and switchable (reorientable) defects, obtained from condition (39) for non-negative dissipation satisfied a priori for arbitrary loading scenarios, are given below.

Hard-switching defects. In the case of unchangeable (frozen, hard-switching) defects, when and $\mathbf{P}^d = \text{const}$ and $\boldsymbol{\varepsilon}^d = \text{const}$, Eq. (39) is simplified:

$$\delta = \left(\boldsymbol{\sigma} - \frac{\partial \Psi_{\text{defect}}}{\partial \boldsymbol{\varepsilon}^r} \right) \cdot \dot{\boldsymbol{\varepsilon}}^r + \left(\mathbf{E} - \frac{\partial \Psi_{\text{defect}}}{\partial \mathbf{P}^r} \right) \cdot \dot{\mathbf{P}}^r - \quad (40)$$

$$-(1/2) \boldsymbol{\sigma} \cdot {}^4 \dot{\mathbf{S}}^E \cdot \boldsymbol{\sigma} - \mathbf{E} \cdot {}^3 \dot{\mathbf{d}} \cdot \boldsymbol{\sigma} -$$

$$-(1/2) \mathbf{E} \cdot \dot{\mathbf{K}}^\sigma \cdot \mathbf{E} \geq 0.$$

Substituting expressions through $\dot{\boldsymbol{\varepsilon}}^r, \dot{\mathbf{P}}^r, {}^4 \dot{\mathbf{S}}^E, {}^3 \dot{\mathbf{d}}, \dot{\mathbf{K}}^\sigma$ in terms of $\dot{c}^{J \rightarrow I}$ (13)–(15) into Eq. (40) yields the representation

$$\delta = \sum_{I=1}^N \sum_{J=1}^N \left(G_{\text{ideal}}^{J \rightarrow I} - G_{\text{defect}}^{J \rightarrow I} \right) \dot{c}^{J \rightarrow I} \geq 0, \quad (41)$$

where $G_{\text{ideal}}^{J \rightarrow I}$ is calculated from Eq. (23) and $G_{\text{defect}}^{J \rightarrow I}$ is defined by the relation:

$$G_{\text{defect}}^{J \rightarrow I} = \frac{\partial \Psi_{\text{defect}}}{\partial \boldsymbol{\varepsilon}^r} \cdot \Delta \tilde{\boldsymbol{\varepsilon}}_{J \rightarrow I}^r + \quad (42)$$

$$+ \frac{\partial \Psi_{\text{defect}}}{\partial \mathbf{P}^r} \cdot \Delta \tilde{\mathbf{P}}_{J \rightarrow I}^r.$$

Representing the defect free energy Ψ_{defect} as a quadratic form (34), accounting for anisotropy and mutual influence from the formation of electric and mechanical defects, gives the following form for the expression for $G_{\text{defect}}^{J \rightarrow I}$ (42):

$$G_{\text{defect}}^{J \rightarrow I} = \mathbf{P}^d \cdot \mathbf{L}_P \cdot \Delta \tilde{\mathbf{P}}_{J \rightarrow I}^r + \mathbf{P}^d \cdot {}^3 \mathbf{L}_{Pe} \cdot \Delta \tilde{\boldsymbol{\varepsilon}}_{J \rightarrow I}^r + \quad (43)$$

$$+ \Delta \tilde{\mathbf{P}}_{J \rightarrow I}^r \cdot {}^3 \mathbf{L}_{eP} \cdot \boldsymbol{\varepsilon}^d + \boldsymbol{\varepsilon}^d \cdot {}^4 \mathbf{L}_e \cdot \Delta \tilde{\boldsymbol{\varepsilon}}_{J \rightarrow I}^r.$$

In the simplest case, when the free energy Ψ_{defect} is represented in the isotropic approximation (36), expression (43) is simplified to three terms containing only three scalar material parameters:

$$G_{\text{defect}}^{J \rightarrow I} = L^P \mathbf{P}^d \cdot \Delta \tilde{\mathbf{P}}_{J \rightarrow I}^r + \quad (44)$$

$$+ L_1 \text{tr} \boldsymbol{\varepsilon}^d \text{tr} \Delta \tilde{\boldsymbol{\varepsilon}}_{J \rightarrow I}^r + 2 L_2 \boldsymbol{\varepsilon}^d \cdot \Delta \tilde{\boldsymbol{\varepsilon}}_{J \rightarrow I}^r.$$

The evolution equation for $\dot{c}^{J \rightarrow I}$, unconditionally satisfying the condition (41) for non-negative dissipation, is taken in the following form:

$$\dot{c}^{J \rightarrow I} = \begin{cases} B^{J \rightarrow I} \left(\frac{G^{J \rightarrow I} - G_{\text{defect}}^{J \rightarrow I}}{G_c^{J \rightarrow I}} \right)^n \left(\frac{c_J}{C_0} \right)^m, \\ G^{J \rightarrow I} \geq G_{\text{defect}}^{J \rightarrow I}; \\ 0, G^{J \rightarrow I} < G_{\text{defect}}^{J \rightarrow I}. \end{cases} \quad (45)$$

The structure of Eq. (45) corresponds to the kinematic hardening model used in plasticity theory. The quantity $G_{\text{defect}}^{J \rightarrow I}$ governs the contribution of the domain switching system from J to I to the displacement of the hysteretic loop. The presence of point defects generates internal stress displacement fields $\boldsymbol{\sigma}_d$ and electric fields \mathbf{E}_d , which directly determine the shift in the hysteretic loop centers. As follows from expressions (43) and (23), generally speaking, the internal displacement fields for the defect free energy represented as a quadratic form (34) are linearly related to the deformation and polarization of the defects:

$$\boldsymbol{\sigma}_d = {}^4 \mathbf{L}_e^T \cdot \boldsymbol{\varepsilon}^d + {}^3 \mathbf{L}_{Pe}^T \cdot \mathbf{P}^d, \quad (46)$$

$$\mathbf{E}_d = {}^3 \mathbf{L}_{eP} \cdot \boldsymbol{\varepsilon}^d + \mathbf{L}_P^T \cdot \mathbf{P}^d.$$

The mathematical structure of the obtained expressions (46) for the internal displacement fields is similar to that of the constitutive equations for piezoelectrics (compare these expressions with Eq. (4) or (38)). In the case of invariable defects considered, the internal displacement fields remain constant.

A simplified formulation in the isotropic approximation (36) obtained by applying expressions (46) results in the absence of influence from cross terms:

$$\begin{aligned}\text{tr } \boldsymbol{\sigma}_d &= L_{tr}^\varepsilon \text{tr } \boldsymbol{\varepsilon}^d, \\ \text{dev } \boldsymbol{\sigma}_d &= L_{dev}^\varepsilon \text{dev } \boldsymbol{\varepsilon}^d, \\ \mathbf{E}_d &= L^P \mathbf{P}^d,\end{aligned}\quad (47)$$

where $L_{tr}^\varepsilon = 3L_1^\varepsilon + 2L_2^\varepsilon$, $L_{dev}^\varepsilon = 2L_2^\varepsilon$.

Using the microstructural model of ferroelastic material (42)–(45) with hard-switching defects and $\mathbf{P}^d = \text{const}$, $\boldsymbol{\varepsilon}^d = \text{const}$ allow describing the horizontal displacement of hysteretic loops.

Switchable defects. Defects resulting from external electrical/mechanical action or internal local inhomogeneous fields can evolve, which leads to changes in their characteristics (concentration, polarization direction, dipole moment, invariant). Kinetic models of the changes in the internal displacement field based on switching of the dipole defect orientation were considered in [15, 17, 33], as well as in [16, 34] based on the diffusion mechanism of charged particle migration. Below the introduction of the evolution equations within the phenomenological and microstructural approaches based on the use of the laws of thermodynamics is considered.

One of the simplest ways to satisfy the condition (39) for non-negative dissipation within the framework of the phenomenological model is to introduce the evolution equations where the change rates of the variables characterizing the defect state, $\dot{\boldsymbol{\varepsilon}}^d$ and $\dot{\mathbf{P}}^d$, are proportional to the corresponding driving forces:

$$\begin{aligned}\dot{\boldsymbol{\varepsilon}}^d &= {}^4\mathbf{B}_\varepsilon \cdot \left(\boldsymbol{\sigma} - \frac{\partial \Psi_{defect}}{\partial \boldsymbol{\varepsilon}^d} \right), \\ \dot{\mathbf{P}}^d &= \mathbf{B}_P \cdot \left(\mathbf{E} - \frac{\partial \Psi_{defect}}{\partial \mathbf{P}^d} \right),\end{aligned}\quad (48)$$

where ${}^4\mathbf{B}_\varepsilon$ and \mathbf{B}_P are constant tensors characterizing the relaxation properties (viscosity) of defects.

To ensure non-negative dissipation, it should be stipulated that the tensors ${}^4\mathbf{B}_\varepsilon$ and \mathbf{B}_P are positive definite:

$$\mathbf{x} \cdot {}^4\mathbf{B}_\varepsilon \cdot \mathbf{x} \geq 0; \quad \mathbf{y} \cdot \mathbf{B}_P \cdot \mathbf{y} \geq 0$$

for any 2nd-order tensors \mathbf{x} and vectors \mathbf{y} .

Then the dissipation induced by a change in the defect state will be a positive definite quadratic form:

$$\begin{aligned}\delta_d &= \left(\boldsymbol{\sigma} - \frac{\partial \Psi_{defect}}{\partial \boldsymbol{\varepsilon}^d} \right) \cdot {}^4\mathbf{B}_\varepsilon \cdot \left(\boldsymbol{\sigma} - \frac{\partial \Psi_{defect}}{\partial \boldsymbol{\varepsilon}^d} \right) + \\ &+ \left(\mathbf{E} - \frac{\partial \Psi_{defect}}{\partial \mathbf{P}^d} \right) \cdot \mathbf{B}_P \cdot \left(\mathbf{E} - \frac{\partial \Psi_{defect}}{\partial \mathbf{P}^d} \right).\end{aligned}\quad (49)$$

In the general case of representing the defect free energy Ψ_{defect} as a quadratic form (34), the evolution equations (48) take the form of linear inhomogeneous ordinary differential equations:

$$\begin{aligned}\dot{\mathbf{P}}^d &= \mathbf{B}_P \cdot \left(\mathbf{E} - \boldsymbol{\varepsilon}^d \cdot {}^3\mathbf{Q}_{P_\varepsilon}^T - \mathbf{P}^d \cdot \mathbf{Q}_P - \right. \\ &\quad \left. - \boldsymbol{\varepsilon}^r \cdot {}^4\mathbf{L}_{P_\varepsilon}^T - \mathbf{P}^r \cdot \mathbf{L}_P^T \right), \\ \dot{\boldsymbol{\varepsilon}}^d &= {}^4\mathbf{B}_\varepsilon \cdot \left(\boldsymbol{\sigma} - \boldsymbol{\varepsilon}^d \cdot {}^4\mathbf{Q}_\varepsilon - \mathbf{P}^d \cdot {}^3\mathbf{Q}_{P_\varepsilon} - \right. \\ &\quad \left. - \boldsymbol{\varepsilon}^r \cdot {}^4\mathbf{L}_\varepsilon^T - \mathbf{P}^r \cdot {}^3\mathbf{L}_{\varepsilon P} \right).\end{aligned}\quad (50)$$

To simplify analysis of the obtained equations, let us confine ourselves to the case of isotropic approximation:

$$\begin{aligned}\mathbf{B}_P &= B^P \mathbf{1}, \\ {}^4\mathbf{B}_\varepsilon &= B_1^\varepsilon \mathbf{1} \otimes \mathbf{1} + B_2^\varepsilon (\mathbf{1} \otimes \mathbf{1} + \mathbf{1} \otimes \mathbf{1}),\end{aligned}\quad (51)$$

where $B^P > 0$, $B_1^\varepsilon > 0$, $B_2^\varepsilon > 0$.

The representation of expression (51) in combination (36) yields, due to Eqs. (50), an uncoupled system of evolution equations with constant scalar coefficients:

$$\begin{aligned}\dot{\mathbf{P}}^d &= B^P (\mathbf{E} - Q^P \mathbf{P}^d - L^P \mathbf{P}^r), \\ \text{tr } \dot{\boldsymbol{\varepsilon}}^d &= B_{tr}^\varepsilon (\text{tr } \boldsymbol{\sigma} - Q_{tr}^\varepsilon \text{tr } \boldsymbol{\varepsilon}^d - L_{tr}^\varepsilon \text{tr } \boldsymbol{\varepsilon}^r), \\ \text{dev } \dot{\boldsymbol{\varepsilon}}^d &= B_{dev}^\varepsilon (\text{dev } \boldsymbol{\sigma} - Q_{dev}^\varepsilon \text{dev } \boldsymbol{\varepsilon}^d - L_{dev}^\varepsilon \text{dev } \boldsymbol{\varepsilon}^r),\end{aligned}\quad (52)$$

where

$$\begin{aligned}B_{tr}^\varepsilon &= 3B_1^\varepsilon + 2B_2^\varepsilon, \quad Q_{tr}^\varepsilon = 3Q_1^\varepsilon + 2Q_2^\varepsilon, \\ L_{tr}^\varepsilon &= 3L_1^\varepsilon + 2L_2^\varepsilon, \quad B_{dev}^\varepsilon = 2B_2^\varepsilon, \\ Q_{dev}^\varepsilon &= 2Q_2^\varepsilon, \quad L_{dev}^\varepsilon = 2L_2^\varepsilon\end{aligned}$$



are the material constants.

For arbitrary given $\mathbf{E}(t)$, $\mathbf{P}^r(t)$, $\boldsymbol{\sigma}(t)$, $\boldsymbol{\varepsilon}^r(t)$, the general solution of Eqs. (52) under initial conditions $\boldsymbol{\varepsilon}^d(0) = \boldsymbol{\varepsilon}_0^d$ and $\mathbf{P}^d(0) = \mathbf{P}_0^d$ takes the form

$$\begin{aligned} \mathbf{P}^d &= e^{-\frac{t}{\tau_p}} \mathbf{P}_0^d + B^P \int_0^t e^{-\frac{t-t'}{\tau_p}} \left(\mathbf{E}(t') - \right. \\ &\quad \left. - L^P \mathbf{P}^r(t') \right) dt', \\ \text{tr} \boldsymbol{\varepsilon}^d &= e^{-\frac{t}{\tau_\varepsilon^{\text{tr}}}} \text{tr} \boldsymbol{\varepsilon}_0^d + \\ &+ B_{\text{tr}}^\varepsilon \int_0^t e^{-\frac{t-t'}{\tau_\varepsilon^{\text{tr}}}} \left(\text{tr} \boldsymbol{\sigma}(t') - L_{\text{tr}}^\varepsilon \text{tr} \boldsymbol{\varepsilon}^r(t') \right) dt', \\ \text{dev} \boldsymbol{\varepsilon}^d &= e^{-\frac{t}{\tau_\varepsilon^{\text{dev}}}} \text{dev} \boldsymbol{\varepsilon}_0^d + \\ &+ B_{\text{dev}}^\varepsilon \int_0^t e^{-\frac{t-t'}{\tau_\varepsilon^{\text{dev}}}} \left(\text{dev} \boldsymbol{\sigma}(t') - L_{\text{dev}}^\varepsilon \text{dev} \boldsymbol{\varepsilon}^r(t') \right) dt', \end{aligned} \quad (53)$$

where the constants τ_p , $\tau_\varepsilon^{\text{tr}}$ and $\tau_\varepsilon^{\text{dev}}$, determining the relaxation times, are given by the expressions:

$$\begin{aligned} \tau_p &= \frac{1}{B^P Q^P}, \quad \tau_\varepsilon^{\text{tr}} = \frac{1}{B_{\text{tr}}^\varepsilon Q_{\text{tr}}^\varepsilon}, \\ \tau_\varepsilon^{\text{dev}} &= \frac{1}{B_{\text{dev}}^\varepsilon Q_{\text{dev}}^\varepsilon}. \end{aligned} \quad (54)$$

At constant values of $\boldsymbol{\sigma}$, $\boldsymbol{\varepsilon}^r$, \mathbf{E} , \mathbf{P}^r (under aging), the solution (53) is simplified:

$$\begin{aligned} \mathbf{P}^d &= e^{-\frac{t}{\tau_p}} \mathbf{P}_0^d + B^P \left(\mathbf{E} - L^P \mathbf{P}^r \right) \left(1 - e^{-\frac{t}{\tau_p}} \right), \\ \text{tr} \boldsymbol{\varepsilon}^d &= e^{-\frac{t}{\tau_\varepsilon^{\text{tr}}}} \text{tr} \boldsymbol{\varepsilon}_0^d + \\ &+ B_{\text{tr}}^\varepsilon \left(\text{tr} \boldsymbol{\sigma} - L_{\text{tr}}^\varepsilon \text{tr} \boldsymbol{\varepsilon}^r \right) \left(1 - e^{-\frac{t}{\tau_\varepsilon^{\text{tr}}}} \right), \\ \text{dev} \boldsymbol{\varepsilon}^d &= e^{-\frac{t}{\tau_\varepsilon^{\text{dev}}}} \text{dev} \boldsymbol{\varepsilon}_0^d + \\ &+ B_{\text{dev}}^\varepsilon \left(\text{dev} \boldsymbol{\sigma} - L_{\text{dev}}^\varepsilon \text{dev} \boldsymbol{\varepsilon}^r \right) \left(1 - e^{-\frac{t}{\tau_\varepsilon^{\text{dev}}}} \right). \end{aligned} \quad (55)$$

Thus, according to solution (55), the internal displacement fields $\boldsymbol{\sigma}_d$ and \mathbf{E}_d (47), proportion-

al to the calculated $\boldsymbol{\varepsilon}^d$ and \mathbf{P}^d , will increase over time under aging in the presence of primary polarization by the law $1 - \exp(-t/\tau)$, which is confirmed by numerous experimental data [15–17, 35] and theoretical studies based on alternative approaches [15–17, 33, 34, 36].

Given harmonically varying fields $\mathbf{E} = \mathbf{E}_0 \sin \omega t$ and stresses $\boldsymbol{\sigma} = \boldsymbol{\sigma}_0 \sin \omega t$, the solution (53) contains a term of the form $\exp(-t/\tau)$, which indicates that it is possible to describe the effect of decreasing internal displacement field under high-frequency harmonic action observed in the experiments [17, 36, 37].

It should be noted that the permanent strain $\boldsymbol{\varepsilon}^r$ and polarization \mathbf{P}^r are calculated within the framework of the proposed model similar to the case of hard-switching defects based on Eqs. (13)–(14) and (42)–(45).

Using the evolution equations of the phenomenological model for $\boldsymbol{\varepsilon}^d$ and \mathbf{P}^d in the form (48) allows us describing the horizontal shift of the hysteretic loop as a function of aging time.

The microstructural model of defect evolution accounts for the discrete nature of potential dipole defect orientations in accordance with the real configuration of oxygen vacancies in the unit crystal cell. In this case, by analogy with decompositions (5) and (6), the strain and polarization of defects are defined as the sum of the contributions of individual orientations:

$$\boldsymbol{\varepsilon}^d = \sum_{l=1}^L n_l \tilde{\boldsymbol{\varepsilon}}_l^d, \quad (56)$$

$$\mathbf{P}^d = \sum_{l=1}^L n_l \tilde{\mathbf{P}}_l^d, \quad (57)$$

where L is the number of possible defect orientations ($L = N = 6$ for perovskites with tetragonal symmetry in the polarized state), n_l is the density of dipole defects of a certain direction (coincides with the polarization orientation of the l^{th} domain for perovskites with tetragonal symmetry in the polarized state).

If we assume that the total defect density n_0 is unchanged, the density n_l satisfies the constraints:

$$0 \leq n_l \leq n_0, \sum_{l=1}^L n_l = n_0. \quad (58)$$

A thermal activation model of defect reorientation was proposed in [15, 17, 38], according to which the defect kinetics is described by a system of linear first-order differential equations:

$$\begin{aligned} \dot{n}_I &= -\sum_{J=1}^N a_0 \exp\left(-\frac{\Delta W_{I \rightarrow J}}{kT}\right) n_J = \\ &= -\sum_{J=1}^N a_{I \rightarrow J} n_J, \end{aligned} \quad (59)$$

where $\Delta W_{I \rightarrow J}$ is the activation energy upon switching from the I^{th} to the J^{th} defect location; $a_{I \rightarrow J}$ is the probability of dipole reorientation from I to J per unit time; T is the temperature; $k = 1.38 \cdot 10^{-23}$ J/K is the Boltzmann constant.

In the case of complex non-proportional multi-axial loading, model (59) can lead to violation of the dissipation inequality. Therefore, a thermodynamically consistent generalization is proposed in this paper based on the formalism described above in the section ‘Defect-free model’.

Instead of the evolution equation (59), it is proposed to use an equation similar in structure to Eq. (24):

$$\dot{n}^{J \rightarrow I} = \begin{cases} A^{J \rightarrow I} \left(\frac{H^{J \rightarrow I}}{H_c^{J \rightarrow I}} \right)^l \left(\frac{n_J}{n_0} \right)^q, \\ G_d^{J \rightarrow I} \geq 0; \\ 0, G_d^{J \rightarrow I} < 0; \end{cases} \quad (60)$$

where $A^{J \rightarrow I} > 0$, $H_c^{J \rightarrow I} > 0$, $l > 0$, $q > 0$, $n_0 > 0$ are the material constants.

The change rate in the concentration of the I^{th} case of defects is expressed based on the equality similar to (11):

$$\dot{n}_I = \sum_{\substack{J=1 \\ J \neq I}}^L (\dot{n}^{J \rightarrow I} - \dot{n}^{I \rightarrow J}).$$

The driving force $H^{J \rightarrow I}$, resulting from substituting the sums (56), (57) into expression (39) and conjugate to $n^{J \rightarrow I}$ is, in the context of equality

$$\begin{aligned} \delta_d &= \left(\boldsymbol{\sigma} - \frac{\partial \Psi_{defect}}{\partial \boldsymbol{\varepsilon}^d} \right) \cdot \dot{\boldsymbol{\varepsilon}}^d + \\ &+ \left(\mathbf{E} - \frac{\partial \Psi_{defect}}{\partial \mathbf{P}^d} \right) \cdot \dot{\mathbf{P}}^d = \sum_{I=1}^N \sum_{\substack{J=1 \\ J \neq I}}^N H^{J \rightarrow I} \dot{n}^{J \rightarrow I}, \end{aligned}$$

defined by the expression:

$$\begin{aligned} H^{J \rightarrow I} &= \left(\boldsymbol{\sigma} - \frac{\partial \Psi_{defect}}{\partial \boldsymbol{\varepsilon}^d} \right) \cdot \Delta \tilde{\boldsymbol{\varepsilon}}_{J \rightarrow I}^d + \\ &+ \left(\mathbf{E} - \frac{\partial \Psi_{defect}}{\partial \mathbf{P}^d} \right) \cdot \Delta \tilde{\mathbf{P}}_{J \rightarrow I}^d, \end{aligned} \quad (61)$$

where $\Delta \tilde{\boldsymbol{\varepsilon}}_{J \rightarrow I}^d = \tilde{\boldsymbol{\varepsilon}}_I^d - \tilde{\boldsymbol{\varepsilon}}_J^d$, $\Delta \tilde{\mathbf{P}}_{J \rightarrow I}^d = \tilde{\mathbf{P}}_I^d - \tilde{\mathbf{P}}_J^d$ are the material constants describing the change in the characteristics of the dipole defect upon change in the location of the oxygen vacancy in the crystal lattice.

Importantly, the relations

$$\boldsymbol{\sigma} - \frac{\partial \Psi_{defect}}{\partial \boldsymbol{\varepsilon}^d}, \mathbf{E} - \frac{\partial \Psi_{defect}}{\partial \mathbf{P}^d}.$$

act as the components in the expressions for the phenomenological model (48) and for the microstructural model (61).

The power dependence of $\dot{n}^{J \rightarrow I}$ on $H^{J \rightarrow I}$ in Eq. (60) can be obtained by introducing the assumption

$$\Delta W^{J \rightarrow I} = \Delta W_0^{J \rightarrow I} \left[1 - \left(\frac{H^{J \rightarrow I}}{H_c^{J \rightarrow I}} \right)^p \right]$$

in Eq. (59), using the condition that $H^{J \rightarrow I}$ is close to $H_c^{J \rightarrow I}$, based on the following transformation:

$$\begin{aligned} &\exp\left(-\frac{\Delta W^{J \rightarrow I}}{kT}\right) = \\ &= \exp\left\{-\frac{\Delta W_0^{J \rightarrow I}}{kT} \left[1 - \left(\frac{H^{J \rightarrow I}}{H_c^{J \rightarrow I}} \right)^p \right]\right\} = \end{aligned}$$



$$= \exp \left[\left(\frac{H^{J \rightarrow I}}{H_c^{J \rightarrow I}} \right)^p - 1 \right]^{\frac{\Delta W_0^{J \rightarrow I}}{kT}} \approx \left(\frac{H^{J \rightarrow I}}{H_c^{J \rightarrow I}} \right)^{\frac{p \Delta W_0^{J \rightarrow I}}{kT}}.$$

In the case of the defect free energy ψ_{defect} represented as the quadratic form (34), accounting for anisotropy and mutual influence of electric and mechanical processes of defect formation, the expression for $H^{J \rightarrow I}$ (61) takes the form:

$$\begin{aligned} H^{J \rightarrow I} = & (\boldsymbol{\sigma} - \boldsymbol{\varepsilon}^d \cdot {}^4\mathbf{Q}_\varepsilon - \mathbf{P}^d \cdot {}^3\mathbf{Q}_{P\varepsilon} - \\ & - \boldsymbol{\varepsilon}^r \cdot {}^4\mathbf{L}_\varepsilon^T - \mathbf{P}^r \cdot {}^3\mathbf{L}_{\varepsilon P}^T) \cdot \Delta \tilde{\boldsymbol{\varepsilon}}_{J \rightarrow I}^d + \\ & + (\mathbf{E} - \boldsymbol{\varepsilon}^d \cdot {}^3\mathbf{Q}_{P\varepsilon}^T - \mathbf{P}^d \cdot \mathbf{Q}_P - \\ & - \boldsymbol{\varepsilon}^r \cdot {}^4\mathbf{L}_{P\varepsilon}^T - \mathbf{P}^r \cdot \mathbf{L}_P^T) \cdot \Delta \tilde{\mathbf{P}}_{J \rightarrow I}^d. \end{aligned} \quad (62)$$

In the simplest case of the free energy ψ_{defect} represented in the isotropic approximation (36), equality (62) is simplified:

$$\begin{aligned} H^{J \rightarrow I} = & (\boldsymbol{\sigma} - Q_1^\varepsilon \mathbf{1} \text{tr} \boldsymbol{\varepsilon}^d - 2Q_2^\varepsilon \boldsymbol{\varepsilon}^d - \\ & - L_1^\varepsilon \mathbf{1} \text{tr} \boldsymbol{\varepsilon}^r - 2L_2^\varepsilon \boldsymbol{\varepsilon}^r) \cdot \Delta \tilde{\boldsymbol{\varepsilon}}_{J \rightarrow I}^d + \\ & + (\mathbf{E} - Q^P \mathbf{P}^d - L^P \mathbf{P}^r) \cdot \Delta \tilde{\mathbf{P}}_{J \rightarrow I}^d. \end{aligned} \quad (63)$$

Expression (63) does not account for the cross influence of mechanical and electric fields and contains the same 6 scalar material parameters

$$Q_1^\varepsilon, Q_2^\varepsilon, L_1^\varepsilon, L_2^\varepsilon, Q^P, L^P,$$

included in the equations of the phenomenological model (52).

The two models of defect evolution considered (the phenomenological one (48) – (52), without accounting for the specifics of dipole defect orientations) and the microstructural one (56) – (63), accounting for the discrete nature of potential dipole defect orientations in a unit cell) are both relaxation-type models, reflecting the system's tendency to equilibrium under external changes; they satisfy the condition for non-negative dissipation under arbitrary multi-axial loading.

Two-level homogenization method

Analyzing the behavior of polycrystalline ferro-piezoceramics, we can identify three characteristic structural levels: micro- (domain), meso- (crystallite), macro- (polycrystal). Furthermore, the relationships between the variables at different levels (two-level homogenization) should be established (Fig. 1).

The relationship between meso-level variables $\{\boldsymbol{\varepsilon}, \boldsymbol{\sigma}, \mathbf{D}, \mathbf{E}\}$ describing the behavior of the crystallite and micro-level variables $\{\tilde{\boldsymbol{\varepsilon}}, \tilde{\boldsymbol{\sigma}}, \tilde{\mathbf{D}}, \tilde{\mathbf{E}}\}$ describing the behavior of the domain is determined analytically in the framework of the Reiss approach by the equations:

$$\begin{aligned} \boldsymbol{\varepsilon} &= \frac{1}{V_{\text{RVC}}} \int_{V_{\text{RVC}}} \tilde{\boldsymbol{\varepsilon}} dV = \sum_{I=1}^N c_I \tilde{\boldsymbol{\varepsilon}}_I, \\ \boldsymbol{\sigma} &= \frac{1}{V_{\text{RVC}}} \int_{V_{\text{RVC}}} \tilde{\boldsymbol{\sigma}} dV \equiv \tilde{\boldsymbol{\sigma}}, \end{aligned} \quad (64)$$

$$\begin{aligned} \mathbf{D} &= \frac{1}{V_{\text{RVC}}} \int_{V_{\text{RVC}}} \tilde{\mathbf{D}} dV = \sum_{I=1}^N c_I \tilde{\mathbf{D}}_I, \\ \mathbf{E} &= \frac{1}{V_{\text{RVC}}} \int_{V_{\text{RVC}}} \tilde{\mathbf{E}} dV \equiv \tilde{\mathbf{E}}, \end{aligned} \quad (65)$$

where V_{RVC} is the representative volume of the crystallite (grain). The constitutive equations discussed in the previous two sections correspond to the meso-level and describe the behavior of the crystallite.

The relationship between macro-level variables $\{\bar{\boldsymbol{\varepsilon}}, \bar{\boldsymbol{\sigma}}, \bar{\mathbf{D}}, \bar{\mathbf{E}}\}$, describing the behavior of the polycrystal, and meso-level variables $\{\boldsymbol{\varepsilon}, \boldsymbol{\sigma}, \mathbf{D}, \mathbf{E}\}$ is defined by equations:

$$\bar{\boldsymbol{\varepsilon}} = \frac{1}{V_{\text{RVP}}} \int_{V_{\text{RVP}}} \boldsymbol{\varepsilon} dV, \quad \bar{\boldsymbol{\sigma}} = \frac{1}{V_{\text{RVP}}} \int_{V_{\text{RVP}}} \boldsymbol{\sigma} dV, \quad (66)$$

$$\bar{\mathbf{D}} = \frac{1}{V_{\text{RVP}}} \int_{V_{\text{RVP}}} \mathbf{D} dV, \quad \bar{\mathbf{E}} = \frac{1}{V_{\text{RVP}}} \int_{V_{\text{RVP}}} \mathbf{E} dV, \quad (67)$$

where V_{RVP} is the representative volume of the polycrystal.

To provide the most accurate account for the

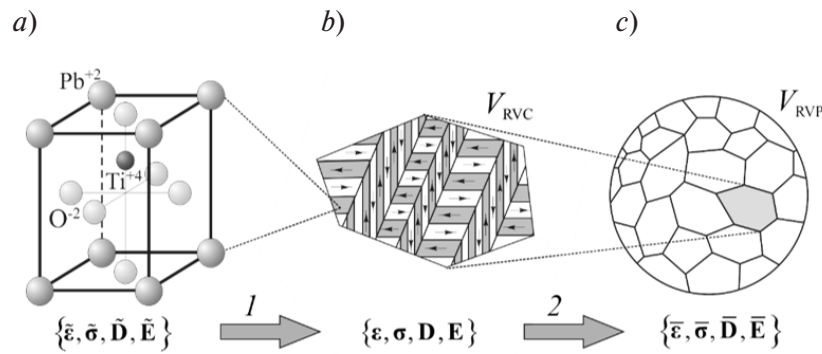


Fig. 1. Micro- (a), meso- (b) and macro- (c) levels in the structure of polycrystalline ferro-piezoceramics, as well as the corresponding levels (1, 2) of homogenization.

The figure shows unit cell/atoms (a), crystallite/domains (b), and polycrystal/crystallites (c);

V_{RVC} , V_{RVP} are the representative volumes of crystallite and polycrystal, respectively

mutual influence of differently oriented crystallites in a polycrystal, which considerably affects the hysteretic behavior of ferroelastic materials, averagings (66), (67) are performed in this study based on the finite-element homogenization method [8, 11].

Verification of the microstructural model with defects

The microstructural models of the material's ferroelastic behavior accounting for the evolution of defects proposed in the section 'Model with defects' have been implemented in the PANTOCRATOR finite-element (FE) software package [39, 40]. The package was used to carry out numerous computational experiments for various electromechanical loading scenarios of the representative volume of a polycrystal. The FE solutions of nonlinear coupled electromechanical boundary-value problems were obtained based on the vector potential formulation [40 – 42], making it possible to ensure convergence of iterative procedures for the nonlinear solution of the boundary-value problem at large integration steps, and the method of return mappings [40, 43], yielding high accuracy of integration of nonlinear differential-algebraic constitutive equations.

In order to verify the microstructural model, the computational results were compared with experimental data for different materials: BaTiO₃ [15, 18], PMN-PZT [24], PZT PIC151 [21], and KTS [27]. Poly- and single-crystalline

materials with tetragonal, rhombohedral, and orthorhombic structures were considered. The computational experiments for analyzing polycrystalline materials involved a representative volume of a polycrystal with a $3 \times 3 \times 3$ partition containing 216 crystallites (see details in [11]), offering a compromise between solution accuracy (less than 5% error) and the time for simulating a nonlinear boundary-value problem under multistep cyclic loading (3–4 h on Intel Core i9-9900K 3.6 GHz PC, 32 GB RAM for one loading cycle).

Fig. 2,a compares the results of FE modeling for the behavior of polycrystalline BaTiO₃ samples doped with Ni²⁺ (1% acceptor impurity) for defect-containing (subjected to aging at 45 °C for 15 min after pre-polarization) and defect-free materials, under cyclic electric loading with the amplitude $E_{\max} = 2$ MV/m and frequency $f = 1$ Hz, with the results of experiments in [15]. The model of material with a tetragonal structure with hard-switching polar defects (see Eqs. (44), (45)) with material constants for BaTiO₃ (see Table) was used in the computations. Computed curves for dielectric hysteresis (Fig. 2,a) demonstrate good agreement with the experimental results for both defect-containing and defect-free materials. The presence of ordered polar point defects generates an internal displacement field, consequently complicating the switching process and increasing the coercive field when the defect polarization direction coincides with the direction of the external elec-

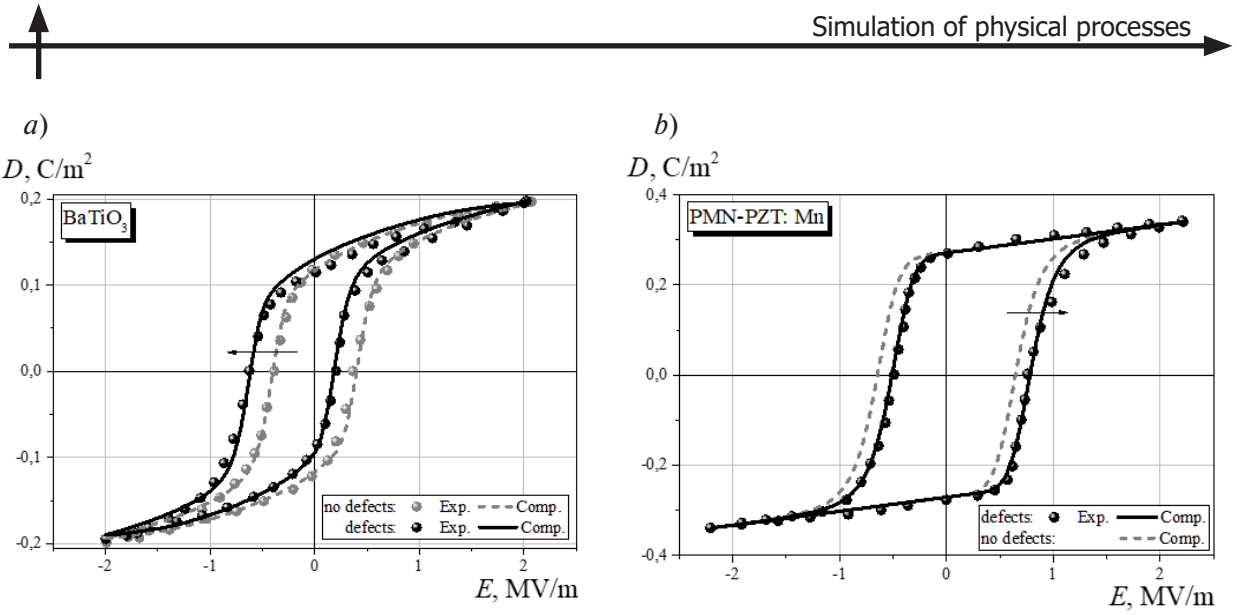


Fig. 2. FE-computations (lines) based on the material model accounting for absence or presence of polar point defects compared with experiments (symbols) for polycrystalline BaTiO_3 doped with Ni [15] (a) and monocrystalline PMN-PZT doped with Mn [24] (b)

tric field (i.e., at $E < 0$, $E_d = -0.22 \text{ MV/m}$ in this case) and facilitating back-switching and reducing the coercive field in the opposite direction of the electric field (i.e., at $E > 0$). As a result, the hysteric loop for the material with defects is shifted by E_d to the left (at $E_d < 0$) relative to the centrally symmetric hysteric loop of the defect-free material (see Fig. 2a). The shift in E_d is about one-third of the dielectric hysteresis loop width, or $0.68 E_c$.

Figure 2,b compares the simulated behavior of samples of single-crystal piezoelectric material $\text{Pb}(\text{Mg}_{1/3}\text{Nb}_{2/3})\text{O}_3$ - $\text{Pb}(\text{Zr,Ti})\text{O}_3$ (abbreviated as PMN-PZT) doped with Mn^{2+} (1 % acceptor impurity) with [001] orientation under cyclic loading by an electric field with an amplitude $E_{\text{max}} = 2.2 \text{ MV/m}$ and frequency $f = 1 \text{ Hz}$ with the experimental results in [24]. The model of material with a rhombohedral structure (see Eqs. (44), (45)) with the material constants (see Table) was used in the computations. The defect state is characterized by the value $E_d = +0.14 \text{ MV/m}^3$. The computed dielectric hysteresis curves (see Fig. 2,b) visually coincide with the experimental results. Because E_d is positive, the hysteric loop is shifted to the right with respect to the origin of coordinates. The shift is 0.12 of the loop width, or $0.24 E_c$.

Fig. 3 compares the behavior of polycrystalline ceramics



(abbreviated as PZT PIC151) in the initial state (during the first loading cycle) and after 10^9 cycles of electrical loading ($f = 50 \text{ Hz}$), obtained by FE modeling, with the experimental results in [21]. A model of a tetragonal/rhombohedral material (17%/83%) that satisfactorily describes the behavior of piezoceramics near the morphotropic phase boundary was used in the computations, accounting for the defects based on Eqs. (44), (45) with the material constants given in the Table. The defect state is characterized by the electric field value $E_d = -0.11 \text{ MV/m}^3$. Comparison of the computed dielectric hysteresis curves with the experimental results [21] shows good agreement (Fig. 3,a). The hysteric loop for material with defects shifts to the left by 0.11 of the loop width, or by $0.22 E_c$.

The accuracy of model prediction is somewhat lower for electromechanical hysteresis curves for PZT PIC151 material (see Fig. 3,b) than for dielectric hysteresis (see Fig. 3,a). However, the model behavior correctly reflects all the main trends in the hysteric loop when polar defects appear: its shift to the left ($E_d = -0.11 \text{ MV/m}^3 < 0$), an increase in the strain level in the right wing and a decrease in the left wing.

Fig. 4 compares the simulated results of mechanical behavior in samples of single crystal

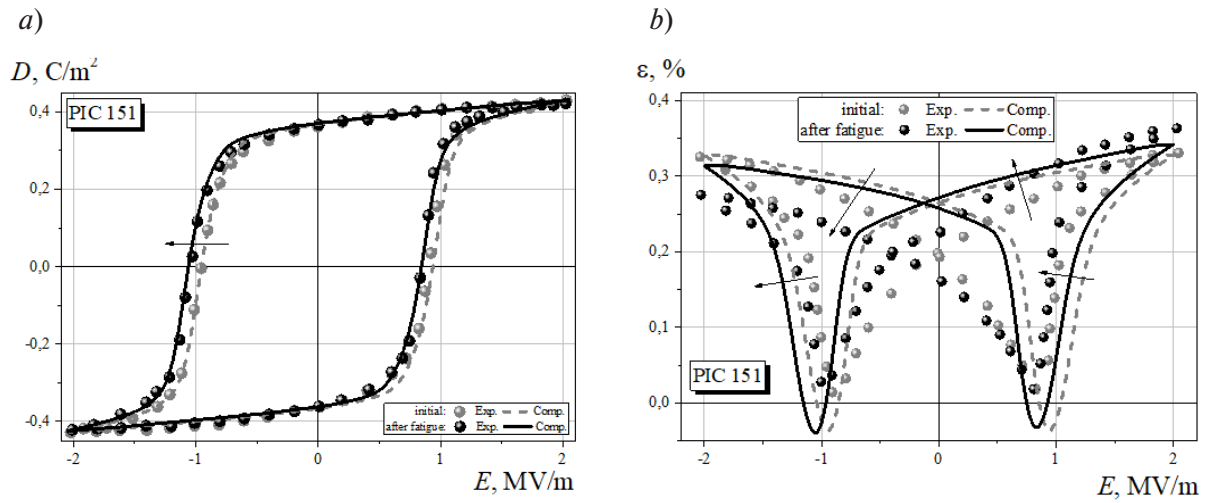


Fig. 3. FE-computations (lines) based on the model accounting for the presence of polar point defects compared with experiments [21] (symbols) for dielectric (a) and electromechanical (b) hysteresis in PZT PIC151 material before and after cyclic loading

Table

Material constants used in FE calculations

Quantity	Notation	Unit	Value for material			
			BaTiO ₃	PMN-PZT	PIC 151	KTS
Elastic modulus	\tilde{C}_{3333}^E	GPa	150	112	126	—
	\tilde{C}_{1133}^E		60.0	108	53.3	—
	\tilde{C}_{1313}^E		42.9	69	35.4	0.8
Dielectric permeability	$\tilde{\kappa}_{33}^\sigma$	nF/m	10.7	30,1	22	—
Piezoelectric modulus	\tilde{d}_{333}	pm/B	415	320	315	—
Spontaneous polarization and deformation	\tilde{P}_0	C/m ²	0.26	0.47	0.5/0.5	—
	$\tilde{\varepsilon}_0$	%	0.3	0.3	1.91/0.55	0.48
Critical driving force	G_c^{90}	MJ/m ³	0.088	—	0.5	—
	G_c^{71}		—	0.26	0.5	—
	G_c^{60}		—	—	—	0.003
Exponent of evolution equation	n	—	4	5	12	5
	m		2	2	1.5	8
Internal displacement field	E_d	MV/m	−0.22	+0.14	−0.11	—
	σ_d	MPa	—	—	—	+0.005

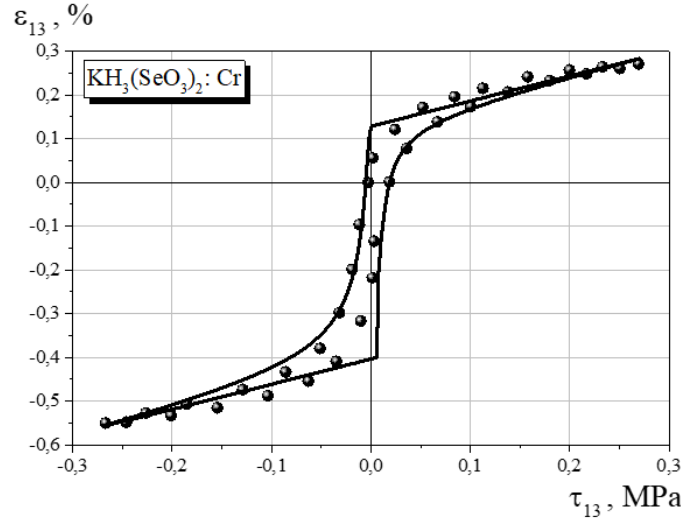


Fig. 4. Computed curves (lines) for mechanical hysteresis in monocrystalline $\text{KH}_3(\text{SeO}_3)_2$ doped with chromium ([001] orientation) compared with experiment [27] (symbols)

potassium trihydroselenite $\text{KH}_3(\text{SeO}_3)_2$, (abbreviated as KTS), doped with chromium (Cr^{3+}), under cyclic mechanical loading (twisting) with the amplitude $\tau_{13} = 0.27$ MPa and frequency $f = 0.01$ Hz at 206.6 K (Curie point $T_c = 211$ K) with the experimental results [27]. KTS is a pure ferroelastic with no ferroelectric properties. It undergoes a structural phase transition of the 2nd kind at $T_c = 211$ K (change of symmetry $mmm \rightarrow m/2$ from orthorhombic to monoclinic).

The model of material with an orthorhombic structure with hard-switching polar defects (44), (45) for material constants at the given temperature was used in the computations (see the Table). The computed dielectric hysteresis curves (Fig. 4) show satisfactory agreement with the experimental results. The hysteretic loop for the material with defects shifts to the right by the value σ_d ($\sigma_d > 0$). The shift is about a quarter of the mechanical hysteresis loop width, or $0.44 \sigma_c$.

The results presented above are based on the model with unchanging (hard-switching) defects (see Eqs. (44), (45)). This model makes it possible to adequately describe the hysteretic phenomena, provided that the defect reorientation time (see Eqs. (54)) greatly exceeds the load cycle time: $\tau_p \gg t_c$. Under these conditions, a more complex model with variable defects (see Eqs. (44), (45), (52)) leads to equivalent results. A

model with switchable defects should be used for small or comparable defect reorientation times, as well as under complex loading scenarios. This allows describing the evolution of defect polarization and deformation, as well as the time evolution of displacement fields.

The results obtained using the model with switchable defects (52) are shown in Fig. 5, illustrating the changes in the displacement field E_d under aging for 15 min in the absence of field ($E = 0$) after pre-polarization ($P^r \neq 0$) for barium titanate considered in the first example (see Fig. 2,a). Varying the parameter Q^p indicates that a result close to the experimental one is observed a $Q^p = 10^7$ m/F: $E_d \approx -0.22$ MV/m. The following parameter values were used in the computations:

$$B^p = 10^{-9} \text{ F/(m}\cdot\text{s)}, L^p = 3 \cdot 10^6 \text{ m/F}, \\ P^r = 0.26 \text{ C/m}^2.$$

Importantly, the curves presented in Fig. 5 show an initial exponential growth followed by a transition to the saturation mode, in accordance with the dependence

$$1 - \exp(-t/\tau_p). \quad (68)$$

A similar result is observed for the experimental data from [17] (see Fig. 5), [15] (see Figs. 2

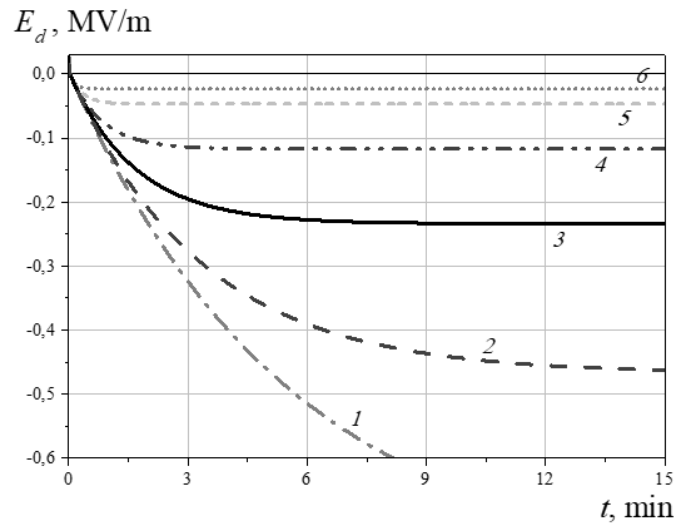


Fig. 5. Evolution of displacement field in BaTiO₃ under aging computed using the model with switchable defects (system of equations (52)) for different values of the parameter Q^P , Mm/F: 3 (1), 5 (2), 10 (3), 20 (4), 50 (5), 100 (6); corresponding values of τ_p , c: 333 (1), 200 (2), 100 (3), 50 (4), 20 (5), 10 (6)

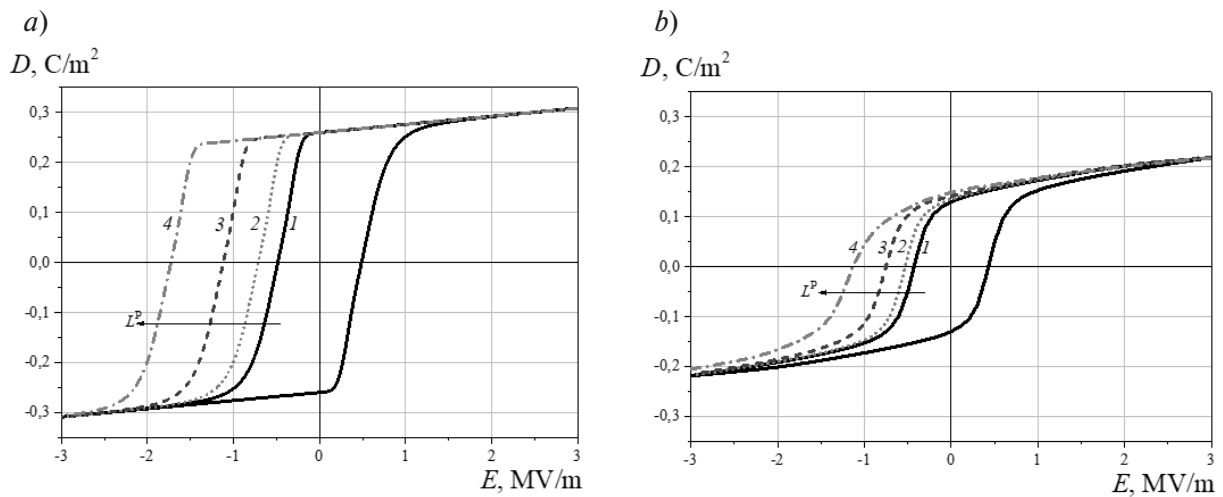


Fig. 6. Effect of L^P parameter value in the model with switchable defects (system of equations (52)) on horizontal loop displacements and dielectric hysteresis for single-crystalline (a) and polycrystalline (b) BaTiO₃; L^P values, Mm/F: 0 (1), 3 (2), 5 (3), 7 (4)

and 3), [16] (see Fig. 46 and Eq. (6)).

As can be seen from Fig. 5, saturation mode is observed at significant aging times, e.g., at $t > 5\tau_p$. A model with frozen defects (see formulas (44), (45)) is sufficient for describing the behavior of the material in this case.

The three constants of the phenomenological model, B^P , L^P and Q^P can be identified based on two experiments with different levels of constant

electrical action (under aging), by the curves describing the evolution of the displacement field, found from the first expression in system (55) and the third in (47):

$$E_d = L^P / Q^P (E - L^P P^r) (1 - e^{-t B^P Q^P}).$$

The relaxation time



$$\tau_P = \frac{1}{B^P Q^P}$$

is determined from the curve describing the evolution of the displacement field as the time to reach the level of 0.632 from the saturation level:

$$E_d(\tau_P)/E_d(\infty) = 1 - e^{-1} \approx 0.632.$$

The parameter L^P has a nonlinear effect on the magnitude of the displacement field E_d . Fig. 6 shows the computed dielectric hysteresis loops after aging for 15 min for single-crystalline and polycrystalline barium titanates, at different values of the parameter L^P . For clarity, Fig. 6 shows the initial (unshifted) hysteresis at $L^P = 0$ and only the descending (left-hand) branches of the hysteresis at $L^P \neq 0$. The width of the loop is virtually unchanged as L^P changes. There is a progressive shift of the hysteresis loop to the left with increasing L^P . The magnitude of the shift is proportional to the square of L^P :

$$E_d \sim P_0^r (L^P)^2 / Q^P.$$

The predictions of the phenomenological and microstructural models of the evolution of point defects under uniaxial proportional loading (see Eqs. (48) – (52) and (56) – (63), respectively) produce close results given an appropriate choice of material constants.

Conclusion

A thermodynamically consistent microstructural model of a ferroelastic material accounting for the evolution of polar point defects has been proposed to describe the hysteretic behavior of single- and polycrystalline ferroelastic materials under arbitrary scenarios of complex multiaxial combined electrical and/or mechanical loading. The model takes into account the multiphase composition (tetragonal, rhombohedral and orthorhombic phases and their mixtures), the anisotropy of properties, the domain structure and the dissipative nature of domain wall motion.

We have considered two statements of the defect evolution equations satisfying the thermody-

amic constraints:

phenomenological (excluding the peculiarities of dipole defect orientations);

microstructural (accounting for the discrete nature of possible orientations of the dipole defect in the unit cell).

Choosing the free energy of defects as a quadratic form of polarization and defect deformation, we have obtained the constitutive equations for the linear theory of evolution of charged point defects, satisfying the dissipative inequality at non-negative tensor coefficients.

The cases of switchable and frozen defects are considered separately.

We have investigated the influence of polar point defects on the switching processes, providing the dependence of the shift in the hysteretic loop on the free energy parameters of the defects.

The mutual influence of crystallites in a polycrystal is taken into account based on the two-level finite-element homogenization method used in calculations.

It is important to describe the presence and evolution of point defects in the model because they appear when donor or acceptor additives are used, which are widespread in modern piezoceramic materials to improve their performance characteristics, playing a major role in the degradation of properties during aging and fatigue.

Comparing the results computed by the proposed model and the experimental curves for dielectric, electromechanical, and mechanical hysteresis for polycrystalline PZT PIC-151 and BaTiO₃ and single-crystalline PMN-PZT and KTS doped with acceptor additives, we found good agreement.

The model can be further extended to the non-isothermal case, considering the non-quadratic free energy of defects, accounting for migration of different types of vacancies; an attempt can be made to describe the effect of de-aging under intense cyclic exposure. Furthermore, the model can be verified for the cases of lead-free piezoelectric and related materials.

This work was supported by RFBR Grant No. 19-08-01252.

REFERENCES

1. **Lines M.E., Glass A.M.**, Principles and application of ferroelectrics and related materials, Oxford University Press, Oxford, 1977.
2. **Belokon A.V., Skaliukh A.S.**, Matematicheskoye modelirovaniye neobratimyykh protsessov polyarizatsii [Mathematical modeling of irreversible polarization processes], Fizmatlit, Moscow, 2010 (in Russian).
3. **Smolenskiy G.A.**, Fizika segnetoelektricheskikh yavleniy [Physics of ferroelectric phenomena], Nauka, Leningrad, 1985 (in Russian).
4. **Landis C.M.**, Fully coupled, multi-axial, symmetric constitutive laws for polycrystalline ferroelectric ceramics, *J. Mech. Phys. Solids*. 50 (1) (2002) 127–152.
5. **Huber J.E., Fleck N.A., Landis C.M., McMeeking R.M.** A constitutive model for ferroelectric polycrystals, *J. Mech. Phys. Solids*. 47 (8) (1999) 1663–1697.
6. **Huber J.E., Fleck N.A.**, Multi-axial electrical switching of a ferroelectric: Theory versus experiment, *J. Mech. Phys. Solids*. 49 (4) (2001) 785–811.
7. **Liskowsky A.C., Semenov A.S., Balke H., McMeeking R.M.**, Finite element modeling of the ferroelectroelastic material behavior in consideration of domain wall motions, *MRS Online Proceedings Library Archive*. Vol. 881. Symposium CC – Coupled Nonlinear Phenomena Modeling and Simulation for Smart, Ferroic and Multiferroic Materials, Cambridge University Press, 2005, CC4.2.
8. **Semenov A.S., Balke H., Melnikov B.E.**, Simulation of polycrystalline piezoceramics by finite element homogenization, *Marine Intellectual Technologies*. (3, special issue) (2011) 106–112 (in Russian).
9. **Neumeister P., Balke H.**, Micromechanical modelling of remanent properties of morphotropic PZT, *J. Mech. Phys. Solids*. 59 (9) (2011) 1794–1807.
10. **Pathak A., McMeeking R.M.**, Three-dimensional finite element simulations of ferroelectric polycrystals under electrical and mechanical loading, *J. Mech. Phys. Solids*. 56 (2) (2008) 663–683.
11. **Semenov A.S.**, Micromechanical model of polycrystalline ferroelectroelastic material with account of defects, *J. Appl. Mech. Techn. Phys.* 60 (6) (2019) 1125–1140.
12. **Belov A.Y., Kreher W.S.**, Viscoplastic models for ferroelectric ceramics, *J. Eur. Ceram. Soc.* 25 (12) (2005) 2567–2571.
13. **Strukov B.A.**, Fazovyye perekhody v segnetoelektricheskikh kristallakh s defektami [Phase transitions in ferroelectric crystals with defects], *Sorosovskiy Obrazovatelnyy Zhurnal*. (12) (1996) 95–101 (in Russian).
14. **Lupascu D.C.**, Fatigue in ferroelectric ceramics and related issues, Springer, Heidelberg, 2004.
15. **Arlt G., Neumann H.**, Internal bias in ferroelectric ceramics: Origin and time dependence, *Ferroelectrics*. 87 (1) (1988) 109–120.
16. **Genenko Yu.A., Glaum J., Hoffmann M.J., Albe K.**, Mechanisms of aging and fatigue in ferroelectrics, *Mater. Sci. Eng. B*. 192 (February) (2015) 52–82.
17. **Neumann H., Arlt G.**, Dipole orientation in Cr-modified BaTiO₃ ceramics, *Ferroelectrics*. 76 (1) (1987) 303–310.
18. **Tan Y.Q., Zhang J.L., Wang C.L.**, Aging behaviours of CuO modified BaTiO₃ ceramics, *Adv. Appl. Ceram.* 113 (4) (2014) 223–227.
19. **Shur V.Y., Rummyantsev E.L., Nikolaeva E., et. al.**, Kinetics of fatigue in bulk ferroelectrics, *Proc. SPIE. Smart Structures and Materials*. SPIE. (2002) 1037–1039.
20. **Lupascu D., Rödel J.**, Fatigue in bulk lead zirconate titanate actuator materials, *Adv. Eng. Mater.* 7 (10) (2005) 882–898.
21. **Balke N., Lupascu D.C., Granzow T., Rödel J.**, Fatigue of lead zirconate titanate ceramics. I: Unipolar and DC loading, *J. Am. Ceram. Soc.* 90 (4) (2007) 1081–1087.
22. **Pike G.E., Warren W.L., Dimos D., et. al.**, Voltage offsets in (Pb, La) (Zr, Ti)O₃ thin films, *Appl. Phys. Lett.* 66 (4) (1995) 484.
23. **Du G., Liang R., Wang L., et. al.**, Linear temperature scaling of ferroelectric hysteresis in Mn-doped Pb(Mn_{1/3}Sb_{2/3})O₃-Pb(Zr,Ti)O₃ ceramics with internal bias field, *Appl. Phys. Lett.* 102



(14) (2013) 142903.

24. **Oh H.T., Lee J.Y., Lee H.Y.**, Mn-modified PMN-PZT $[\text{Pb}(\text{Mg}_{1/3}\text{Nb}_{2/3})\text{O}_3\text{-Pb}(\text{Zr,Ti})\text{O}_3]$ single crystals for high power piezoelectric transducers, *J. Korean Ceram. Soc.* 54 (2) (2017) 150–157.

25. **Luo Z., Glaum J., Granzow T., et. al.**, Bipolar and unipolar fatigue of ferroelectric BNT-based lead-free piezoceramics, *J. Am. Ceram. Soc.* 94 (2) (2011) 529–535.

26. **Wang H.-Q., Dai Y.-J., Zhang X.-W.**, Microstructure and hardening mechanism of $\text{K}_{0.5}\text{Na}_{0.5}\text{NbO}_3$ lead-free ceramics with CuO doping sintered in different atmospheres, *J. Am. Ceram. Soc.* 95 (4) (2012) 1182–1184.

27. **Gridnev S.A., Shuvalov L.A.**, The influence of real structure on switching processes and peculiarities of mechanical relaxation in proper ferroelastics $\text{KH}_3(\text{SeO}_3)_2$ and $\text{KD}_3(\text{SeO}_3)_2$, *Ferroelectrics*. 48 (1) (1983) 113–129.

28. **Ren X.**, Large electric-field-induced strain in ferroelectric crystals by point-defect-mediated reversible domain switching, *Nat. Mater.* 3 (2) (2004) 91–94.

29. **Semenov A.S., Melnikov B.E.**, Modelirovaniye protsessov neuprugogo deformirovaniya segnetoelastikov [Modeling the processes of inelastic deformation of ferroelastics], *Proceedings of the 7th International Scientific Symposium “Problems of Strength, Plasticity and Stability in the Solids Mechanics”*, December 16–17, 2010, TSTU Publishing, Tver (2011) 197–202 (in Russian).

30. **Eshelby J.D.**, *Kontinualnaya teoriya dislokatsiy* [Continual theory of dislocations], Publisher of Foreign Literature, Moscow, 1963 (in Russian).

31. **Zhang L. Erdem E., Ren X., Eichel R.-A.**, Reorientation of $(\text{Mn Ti}'' - \text{VO} \bullet \bullet) \times$ defect dipoles in acceptor-modified BaTiO_3 single crystals: An electron paramagnetic resonance study, *Appl. Phys. Lett.* 93 (20) (2008) 202901.

32. **Feng Z., Ren X.**, Aging effect and large recoverable electrostrain in Mn-doped KNbO_3 -based ferroelectrics, *Appl. Phys. Lett.* 91 (3) (2007) 032904.

33. **Erhart P., Träskelin P., Albe K.**, Formation and switching of defect dipoles in acceptor-doped

lead titanate: A kinetic model based on first-principles calculations, *Phys. Rev. B.* 88 (2) (2013) 024107.

34. **Genenko Y.A., Lupascu D.C.**, Drift of charged defects in local fields as aging mechanism in ferroelectrics, *Phys. Rev. B.* 75 (18) (2007) 184107.

35. **Lambeck P.V., Jonker G.H.**, The nature of domain stabilization in ferroelectric perovskites, *J. Phys. Chem. Solids*. 47 (5) (1986) 453–461.

36. **Lohkämper R., Neumann H., Arlt G.**, Internal bias in acceptor-doped BaTiO_3 ceramics: Numerical evaluation of increase and decrease, *J. Appl. Phys.* 68 (8) (1990) 4220–4224.

37. **Lambeck P.V., Jonker G.H.**, Ferroelectric domain stabilization in BaTiO_3 by bulk ordering of defects, *Ferroelectrics*. 22 (1) (1978) 729–731.

38. **Nowick A.S., Berry B.S.**, *Anelastic relaxation in crystalline solids*. Academic Press, New York, London, 1972.

39. **Semenov A.S.**, PANTOCRATOR – finite-element program specialized on the solution of non-linear problems of solid body mechanics, *Proceedings of the 5th International Conference “Assessment of Reliability of Materials and Structures: Problems and Solutions”*, October 14–17, 2003, SPb., SPbSPU, Polytechnical University Publishing, St. Petersburg (2003) 466–480.

40. **Semenov A.S., Liskowsky A.C., Balke H.**, Return mapping algorithms and consistent tangent operators in ferroelectroelasticity, *Int. J. Numer. Methods Eng.* 81 (10) (2010) 1298–1340.

41. **Landis C.M.**, A new finite-element formulation for electromechanical boundary value problems, *Int. J. Numer. Methods Eng.* 55 (5) (2002) 613–628.

42. **Semenov A.S., Kessler H., Liskowsky A., Balke H.**, On a vector potential formulation for 3D electromechanical finite element analysis, *Commun. Numer. Methods Eng.* 22 (5) (2006) 357–375.

43. **Semenov A.S., Liskowsky A.C., Neumeister P., et. al.**, Effective methods for solving nonlinear boundary value problems of ferroelectroelasticity, *Marine Intellectual Technologies*. (1) (2010) 56–61 (in Russian).

THE AUTHOR

SEMENOV Artem S.

Peter the Great St. Petersburg Polytechnic University

29 Politechnicheskaya St., St. Petersburg, 195251, Russian Federation

semenov.artem@gmail.com

СПИСОК ЛИТЕРАТУРЫ

1. **Лайнс М., Гласс А.** Сегнетоэлектрики и родственные им материалы. М.: Мир, 1981. 736 с.
2. **Белоконь А.В., Скалиух А.С.** Математическое моделирование необратимых процессов поляризации. М.: Физматлит, 2010. 325 с.
3. **Смоленский Г.А.** Физика сегнетоэлектрических явлений. Ленинград: Наука, 1985. 396 с.
4. **Landis C.M.** Fully coupled, multi-axial, symmetric constitutive laws for polycrystalline ferroelectric ceramics // J. Mech. Phys. Solids. 2002. Vol. 50. No. 1. Pp. 127–152.
5. **Huber J.E., Fleck N.A., Landis C.M., McMeeking R.M.** A constitutive model for ferroelectric polycrystals // J. Mech. Phys. Solids. 1999. Vol. 47. No. 8. Pp. 1663–1697.
6. **Huber J.E., Fleck N.A.** Multi-axial electrical switching of a ferroelectric: Theory versus experiment // J. Mech. Phys. Solids. 2001. Vol. 49. No. 4. Pp. 785–811.
7. **Liskowsky A.C., Semenov A.S., Balke H., McMeeking R.M.** Finite element modeling of the ferroelectroelastic material behavior in consideration of domain wall motions // MRS Online Proceedings Library Archive. Vol. 881. Symposium CC – Coupled Nonlinear Phenomena Modeling and Simulation for Smart, Ferroic and Multiferroic Materials. Cambridge University Press, 2005. CC4.2
8. **Семенов А.С., Бальке Х., Мельников Б.Е.** Моделирование поликристаллической пьезо-керамики методом конечно-элементной гомогенизации // Морские интеллектуальные технологии. 2011. № 3 (спецвыпуск). С. 106–112.
9. **Neumeister P., Balke H.** Micromechanical modelling of remanent properties of morphotropic PZT // J. Mech. Phys. Solids. 2011. Vol. 59. No. 9. Pp. 1794–1807.
10. **Pathak A., McMeeking R.M.** Three-dimensional finite element simulations of ferroelectric polycrystals under electrical and mechanical loading // J. Mech. Phys. Solids. 2008. Vol. 56. No. 2. Pp. 663–683.
11. **Семенов А.С.** Микромеханическая модель поликристаллического сегнетоэлектрoупругого материала с учетом дефектов // Прикладная механика и техническая физика. 2019. Т. 60. № 6. С. 173–191.
12. **Belov A.Y., Kreher W.S.** Viscoplastic models for ferroelectric ceramics // J. Eur. Ceram. Soc. 2005. Vol. 25. No. 12. Pp. 2567–2571.
13. **Струков Б.А.** Фазовые переходы в сегнетоэлектрических кристаллах с дефектами // Соросовский образовательный журнал. 1996. № 12. С. 95–101.
14. **Lupascu D.C.** Fatigue in ferroelectric ceramics and related issues. Heidelberg: Springer, 2004. 225 p.
15. **Arlt G., Neumann H.** Internal bias in ferroelectric ceramics: Origin and time dependence // Ferroelectrics. 1988. Vol. 87. No. 1. Pp. 109–120.
16. **Genenko Yu.A., Glaum J., Hoffmann M.J., Albe K.** Mechanisms of aging and fatigue in ferroelectrics // Mater. Sci. Eng. B. 2015. Vol. 192. Pp. 52–82.
17. **Neumann H., Arlt G.** Dipole orientation in Cr-modified BaTiO₃ ceramics // Ferroelectrics. 1987. Vol. 76. No. 1. Pp. 303–310.
18. **Tan Y.Q., Zhang J.L., Wang C.L.** Aging behaviours of CuO modified BaTiO₃ ceramics // Adv. Appl. Ceram. 2014. Vol. 113. No. 4. Pp. 223–227.
19. **Shur V.Y., Rumyantsev E.L., Nikolaeva E., Shishkin E., Baturin I., Shur A., Ozigul M.** Kinetics of fatigue in bulk ferroelectrics // Proc. SPIE. Smart Structures and Materials. SPIE. 2002. Vol. 80. No. 6. Pp. 1037–1039.
20. **Lupascu D., Rödel J.** Fatigue in bulk lead



zirconate titanate actuator materials // *Adv. Eng. Mater.* 2005. Vol. 7. No. 10. Pp. 882–898.

21. **Balke N., Lupascu D.C., Granzow T., Rödel J.** Fatigue of lead zirconate titanate ceramics. I: Unipolar and DC loading // *J. Am. Ceram. Soc.* 2007. Vol. 90. No. 4. Pp. 1081–1087.

22. **Pike G.E., Warren W.L., Dimos D., Tuttle B.A., Ramesh R., Lee J., Keramidas V.G., Evans Jr. J.T.** Voltage offsets in $(\text{Pb}, \text{La})(\text{Zr}, \text{Ti})\text{O}_3$ thin films // *Appl. Phys. Lett.* 1995. Vol. 66. No. 4. P. 484.

23. **Du G., Liang R., Wang L., Li K., Zhang W., Wang G., Dong X.** Linear temperature scaling of ferroelectric hysteresis in Mn-doped $\text{Pb}(\text{Mn}_{1/3}\text{Sb}_{2/3})\text{O}_3$ - $\text{Pb}(\text{Zr}, \text{Ti})\text{O}_3$ ceramic with internal bias field // *Appl. Phys. Lett.* 2013. Vol. 102. No. 14. P. 142903.

24. **Oh H.T., Lee J.Y., Lee H.Y.** Mn-modified PMN-PZT $[\text{Pb}(\text{Mg}_{1/3}\text{Nb}_{2/3})\text{O}_3$ - $\text{Pb}(\text{Zr}, \text{Ti})\text{O}_3]$ single crystals for high power piezoelectric transducers // *J. Korean Ceram. Soc.* 2017. Vol. 54. No. 2. Pp. 150–157.

25. **Luo Z., Glaum J., Granzow T., Jo W., Dittmer R., Hoffman M., Rödel J.** Bipolar and unipolar fatigue of ferroelectric BNT-based lead-free piezoceramics // *J. Am. Ceram. Soc.* 2011. Vol. 94. No. 2. Pp. 529–535.

26. **Wang H.-Q., Dai Y.-J., Zhang X.-W.** Microstructure and hardening mechanism of $\text{K}_{0.5}\text{Na}_{0.5}\text{NbO}_3$ lead-free ceramics with CuO doping sintered in different atmospheres // *J. Am. Ceram. Soc.* 2012. Vol. 95. No. 4. Pp. 1182–1184.

27. **Gridnev S.A., Shuvalov L.A.** The influence of real structure on switching processes and peculiarities of mechanical relaxation in proper ferroelastics $\text{KH}_3(\text{SeO}_3)_2$ and $\text{KD}_3(\text{SeO}_3)_2$ // *Ferroelectrics*. 1983. Vol. 48. No. 1. Pp. 113–129.

28. **Ren X.** Large electric-field-induced strain in ferroelectric crystals by point-defect-mediated reversible domain switching // *Nat. Mater.* 2004. Vol. 3. No. 2. Pp. 91–94.

29. **Семенов А.С., Мельников Б.Е.** Моделирование процессов неупругого деформирования сегнетоэластиков // *Материалы VII Международного научного симпозиума «Проблемы прочности, пластичности и устойчивости в механике деформируемого твердого тела»*. 16 – 17 декабря 2010 г., г. Тверь. Издание Тверского государственного технического университета (ТГТУ), 2011. С. 197–202.

30. **Эшелби Д.** Континуальная теория дислокаций. М.: Изд-во иностранной литературы, 1963. 248 с.

31. **Zhang L., Erdem E., Ren X., Eichel R.-A.** Reorientation of $(\text{Mn Ti}'' - \text{VO} \bullet \bullet) \times$ defect dipoles in acceptor-modified BaTiO_3 single crystals: An electron paramagnetic resonance study // *Appl. Phys. Lett.* 2008. Vol. 93. No. 20. P. 202901.

32. **Feng Z., Ren X.** Aging effect and large recoverable electrostrain in Mn-doped KNbO_3 -based ferroelectrics // *Appl. Phys. Lett.* 2007. Vol. 91. No. 3. P. 032904.

33. **Erhart P., Träskelin P., Albe K.** Formation and switching of defect dipoles in acceptor-doped lead titanate: A kinetic model based on first-principles calculations // *Phys. Rev. B*. 2013. Vol. 88. No. 2. P. 024107.

34. **Genenko Y.A., Lupascu D.C.** Drift of charged defects in local fields as aging mechanism in ferroelectrics // *Phys. Rev. B*. 2007. Vol. 75. No. 18. P. 184107.

35. **Lambeck P.V., Jonker G.H.** The nature of domain stabilization in ferroelectric perovskites // *J. Phys. Chem. Solids*. 1986. Vol. 47. No. 5. Pp. 453–461.

36. **Lohkämper R., Neumann H., Arlt G.** Internal bias in acceptor-doped BaTiO_3 ceramics: Numerical evaluation of increase and decrease // *J. Appl. Phys.* 1990. Vol. 68. No. 8. Pp. 4220–4224.

37. **Lambeck P. V., Jonker G.H.** Ferroelectric domain stabilization in BaTiO_3 by bulk ordering of defects // *Ferroelectrics*. 1978. Vol. 22. No. 1. Pp. 729–731.

38. **Nowick A.S., Berry B.S.** Anelastic relaxation in crystalline solids. New York, London: Academic Press, 1972. 694 p.

39. **Семенов А.С.** PANTOCRATOR – конечно-элементный программный комплекс, ориентированный на решение нелинейных задач механики // *Труды V Международной конференции «Научно-технические проблемы прогнозирования надежности и долговечности конструкций и методы их решения»*. 14 – 17 октября 2003 г., Санкт-Петербург, СПбГПУ. СПб.: Изд-во Политехнического ун-та, 2003. С. 466–480.

40. **Semenov A.S., Liskowsky A.C., Balke H.** Return mapping algorithms and consistent tan-

gent operators in ferroelectroelasticity // Int. J. Numer. Methods Eng. 2010. Vol. 81. No. 10. Pp. 1298–1340.

41. **Landis C.M.** A new finite-element formulation for electromechanical boundary value problems // Int. J. Numer. Methods Eng. 2002. Vol. 55. No. 5. Pp. 613–628.

42. **Semenov A.S., Kessler H., Liskowsky A., Balke H.** On a vector potential formulation for 3D

electromechanical finite element analysis // Commun. Numer. Methods Eng. 2006. Vol. 22. No. 5. Pp. 357–375.

43. **Семенов А.С., Лисковски А.Ч., Ноймайстер П., Бальке Х., Ле-Захаров С.А., Додонов П. А., Мельников Б.Е.** Эффективные методы решения нелинейных краевых задач сегнетоэлектростатической теории // Морские интеллектуальные технологии. 2010. № 1. С. 55–61.

Статья поступила в редакцию 20.08.2020, принята к публикации 20.12.2020.

СВЕДЕНИЯ ОБ АВТОРЕ

СЕМЕНОВ Артем Семенович — кандидат физико-математических наук, доцент Высшей школы механики и процессов управления, заведующий кафедрой сопротивления материалов Санкт-Петербургского политехнического университета Петра Великого, Санкт-Петербург, Российская Федерация.

195251, Российская Федерация, г. Санкт-Петербург, Политехническая ул., 29
Semenov.Artem@gmail.com



DOI: 10.18721/JPM.14104
UDC 519.6:533.6.011

TESTING OF THE HYBRID LARGE-PARTICLE METHOD USING TWO-DIMENSIONAL RIEMANN PROBLEMS

D.V. Sadin, I.O. Golikov, E.N. Shirokova

Military Space Academy named after A.F. Mozhaysky,
St. Petersburg, Russian Federation

The full potential of the hybrid large-particle method using the known and new Riemann problems in two-dimensional domains has been studied. The method includes a space-time second-order approximation for smooth solutions. Using the artificial viscosity nonlinear correction and the convective fluxes hybridization maintained monotonicity of solutions. Centrally symmetrical problems with a complex shock-wave structure and with the development of instability on the contact boundary were studied in details. The test calculations demonstrated high resolution, low dissipation, and stability of the method.

Keywords: hybrid large-particle method, two-dimensional Riemann problems, high resolution

Citation: Sadin D.V., Golikov I.O., Shirokova E.N., Testing of the hybrid large-particle method using two-dimensional Riemann problems, St. Petersburg Polytechnical State University Journal. Physics and Mathematics. 14 (1) (2021) 55–68. DOI: 10.18721/JPM.14104

This is an open access article under the CC BY-NC 4.0 license (<https://creativecommons.org/licenses/by-nc/4.0/>)

ТЕСТИРОВАНИЕ ГИБРИДНОГО МЕТОДА КРУПНЫХ ЧАСТИЦ НА ДВУМЕРНЫХ ЗАДАЧАХ РИМАНА

Д.В. Садин, И.О. Голиков, Е.Н. Широкова

Военно-космическая академия имени А.Ф. Можайского,
Санкт-Петербург, Российская Федерация

Изучены возможности гибридного метода крупных частиц с использованием известных и новых задач Римана в двумерных областях. Метод обладает вторым порядком аппроксимации по пространству и времени на гладких решениях. Монотонность решений обеспечивается нелинейной коррекцией искусственной вязкости и гибридизацией конвективных потоков. Детально исследованы центрально-симметричные задачи со сложной ударно-волновой структурой и развитием неустойчивости на контактной границе. Тестовые расчеты продемонстрировали высокую разрешающую способность, малую диссипативность и устойчивость метода.

Ключевые слова: гибридный метод крупных частиц, двумерные задачи Римана, разрешающая способность

Ссылка при цитировании: Садин Д.В., Голиков И.О., Широкова Е.Н. Тестирование гибридного метода крупных частиц на двумерных задачах Римана // Научно-технические ведомости СПбГПУ. Физико-математические науки. 2021. Т. 14. № 1. С. 55–68. DOI: 10.18721/JPM.14104

Статья открытого доступа, распространяемая по лицензии CC BY-NC 4.0 (<https://creativecommons.org/licenses/by-nc/4.0/>)

Introduction

Computational fluid dynamics has been experiencing rapid development in the recent decades. It is intensified by the development of research and commercial software packages for computation and justification of parameters of technical devices used in various engineering processes, at different stages of production, for instance, in the aircraft, aerospace and energy industries.

To date, there are a number of approaches to discrete modelling retaining monotonicity and having an increased order of approximation for the computation of gas-dynamic fluxes. Such computations are based on an accurate or approximate solution to breakdown of discontinuity (Godunov type schemes [1–3]); total variation diminishing (TVD) schemes [4–6]); weighted essentially non-oscillatory (WENO) schemes at variable templates [7–9]; hybrid algorithms [10–12], compact schemes [13–15], etc.

Along with the trend of building schemes of fourth, fifth and higher orders of approximation [8, 9, 15], discrete models of second-order approximation are still relevant for a wide variety of problems [16–20]. For example, a sufficiently detailed discussion of such schemes can be found in paper [19], which is developing monotonic upstream-centered scheme (MUSCL approach) with the use of various quasi-one-dimensional schemes of reconstruction.

A hybrid large-particle method was proposed to solve the problems of multiphase media dynamics based on a scheme of customizable dissipative properties (CDP2), which changes the approximation order depending on the smoothness of solutions [21, 22]. However, applied problems often contain domains of both “pure” gas and heterogeneous mixture fluxes with disperse phase. Therefore, the proposed method should be universal and demonstrate high resolution and monotonicity in these two case. It is essential that the new numerical method is verified using a series of test problems in a wide range of flux parameters. It was previously verified using standard one and two-dimensional test problems [23–25].

The advantages of the method over known

schemes that take into account characteristic properties of conservation laws lies in extension of the class of problems with equations of both hyperbolic and mixed types with imaginary characteristics components. The algorithm of the hybrid large-particle method can be successfully applied in solving traditionally complex computational problems such as formation of artificial boundary layer or fictitious Mach stem, occurrence of rarefaction shock wave, carbuncle instability in hypersonic flow regimes, which are characteristic of Godunov type schemes [26]. The method’s algorithm is simple and has a good ration of dissipative and dispersive properties. For example, in a test with double Mach reflection, the hybrid large-particle method prevails over popular HLLC (Harten – Lax – van Leer contact [27]) and WENO5 [11] schemes with respect to eddy resolution (see comparison of the schemes in article [25]).

The present paper verifies computational properties (monotonicity, dissipativity, eddy resolution) of the hybrid large-particle method with a space-time second-order approximation [28] for Riemann problem solvers in two-dimensional domains. The results are compared with the basic method [29] and solutions based on modern schemes of increased approximation order [15, 30]. We consider the issues of numerical reproduction of complex shock wave and vortex structures in detail.

The cited papers solve the test problems using Euler equation. For the purpose of correct comparison, we present our calculations in an inviscid problem formulation. This is due to the need for justification of grid resolution for a correct solution of Navier-Stokes equation with a set Reynolds number, when scheme viscosity becomes significantly less than the physical one [8].

Hybrid large-particle method

Main equations. Consider conservation laws of calorically perfect gas in a form of Euler equations:

$$\frac{\partial \mathbf{q}}{\partial t} + \nabla_d \mathbf{G} + \nabla_d \mathbf{F} = 0, \quad (1)$$



$$\mathbf{q} = [\rho, \rho \mathbf{v}, \rho E]^T, \quad \mathbf{G} = [\rho \mathbf{v}, \rho \mathbf{v} \mathbf{v}, \rho E \mathbf{v}]^T,$$

$$\mathbf{F} = [0, p, p \mathbf{v}]^T, \quad \nabla_d = \text{diag}(\nabla \cdot, \nabla, \nabla \cdot),$$

where ρ , \mathbf{v} , p , E are density, velocity vector with components u and v , pressure, total gas energy per unit mass; \mathbf{q} , \mathbf{G} , \mathbf{F} are conservative, flux, gradient and deformation values, respectively; t is time.

Eq. (1) are written in dimensionless form for the required functions

$$\rho' = \rho / \Theta_0, \quad p' = p / P_0,$$

$$u' = u / \sqrt{P_0 / \Theta_0}, \quad v' = v / \sqrt{P_0 / \Theta_0},$$

with respect to some dimensional constants Θ_0 , P_0 .

Coordinates are related to the characteristic linear dimension of the problem statement domain

$$x' = x / L, \quad y' = y / L,$$

while dimensionless time is determined as

$$t' = t / (L \sqrt{\Theta_0 / P_0}).$$

In Eq. (1) and further in the statements of the problems, the primes are omitted.

The closing equation has the form

$$p = (\gamma - 1) \rho (E - \mathbf{v}^2 / 2),$$

where γ is a ratio of specific heats.

Method implementation. Let us write the hybrid large-particle method with CDP2 using a finite volume formulation in an orthogonal uniformly spaced grid [28].

The schemes are formulated with a split into Lagrange (0), Euler and final (1) stages, without limiting the generality in the one-dimensional case:

$$\mathbf{q}_n^{(0)} = \mathbf{q}_n^k - (\mathbf{F}_{n+1/2}^k - \mathbf{F}_{n-1/2}^k) \tau / h, \quad (2)$$

$$\mathbf{q}_n^{(1)} = \mathbf{q}_n^{(0)} - (\mathbf{G}_{n+1/2}^{(0)} - \mathbf{G}_{n-1/2}^{(0)}) \tau / h. \quad (3)$$

For an increase up to the second order approximation with respect to time, we use a correcting step:

$$\mathbf{q}_n^{(2)} = 0,5(\mathbf{q}_n^k + \mathbf{q}_n^{(1)}) - 0,5(\mathbf{F}_{n+1/2}^{(1)} - \mathbf{F}_{n-1/2}^{(1)}) \tau / h, \quad (4)$$

$$\mathbf{q}_n^{k+1} = \mathbf{q}_n^{(2)} - 0,5(\mathbf{G}_{n+1/2}^{(2)} - \mathbf{G}_{n-1/2}^{(2)}) \tau / h, \quad (5)$$

where $\tau = t^{k+1} - t^k$ is a time step (t^k — time layer); h is mesh size with its center x_n and boundaries

$$x_{n\pm 1/2} = x_n \pm h/2.$$

If we determine the values at the mesh boundaries as arithmetic mean in the centers of adjacent meshes, we obtain non-dissipative, but absolutely unstable second-order approximation scheme. In the basic method of large particles, fluxes are calculated considering their directions by means of first-order schemes [29].

Non-linear method correction. To ensure stability and monotonicity of the method retaining the second-order accuracy for smooth solutions, we use non-linear correction of gradient and deformation values $\mathbf{F}_{n\pm 1/2}$ and $\mathbf{G}_{n\pm 1/2}$.

At the Lagrange stage (2), we add into scheme

$$\tilde{\mathbf{F}}_{n\pm 1/2} = [0, \tilde{p}_{n\pm 1/2}, \tilde{p}_{n\pm 1/2} u_{n\pm 1/2}^k]^T$$

non-linear scalar artificial viscosity

$$\tilde{p}_{n\pm 1/2} = p_{n\pm 1/2}^k + [1 - \Psi_v(r_{n\pm 1/2})] Q_{n\pm 1/2},$$

where $Q_{n\pm 1/2}$ is common linear dissipation, for example, Landshoff type one; $\Psi_v(r_{n\pm 1/2})$ is viscosity limiter with a slope ratio parameter $r_{n\pm 1/2}$.

Parameter $r_{n\pm 1/2}$ is calculated under the condition

$$r_{n+1/2} = \begin{cases} (u_n^k - u_{n-1}^k) / (u_{n+1}^k - u_n^k), \\ \text{if } (u_{n+1}^k - u_n^k)(p_{n+1}^k - p_n^k) \geq 0; \\ (u_{n+2}^k - u_{n+1}^k) / (u_{n+1}^k - u_n^k), \\ \text{or else.} \end{cases}$$

Smooth solutions retain the second order of approximation:

$$r_{n\pm 1/2} \rightarrow 1 \Rightarrow \psi_v(r_{n\pm 1/2}) \rightarrow 1 \Rightarrow$$

$$\tilde{\mathbf{F}}_{n\pm 1/2} \rightarrow \mathbf{F} + O(h^2).$$

At the Euler and final stages (3), we calculate primitive variables $\phi = \{\rho, u, E\}$ with the use of hybrid non-linear correction (weighted by flux limiter ψ_f of additive combination of upwind and central approximation) with accuracy $O(h^2)$ for smooth solutions:

$$\hat{\phi}_{n+1/2} = \begin{cases} \phi_{n+1/2}^+ & \text{if } u_{n+1/2}^{(0)} \geq 0, \\ \phi_{n+1/2}^- & \text{or else;} \end{cases}$$

$$\phi_{n+1/2}^+ = \left[\left(1 - \psi_f(r_{n+1/2}^+) \right) \phi_n^{(0)} + \psi_f(r_{n+1/2}^+) \phi_{n+1/2}^{(0)} \right];$$

$$\phi_{n+1/2}^- = \left[\left(1 - \psi_f(r_{n+1/2}^-) \right) \phi_{n+1}^{(0)} + \psi_f(r_{n+1/2}^-) \phi_{n+1/2}^{(0)} \right];$$

$$r_{n+1/2}^+ = \frac{\phi_n^{(0)} - \phi_{n-1}^{(0)}}{\phi_{n+1}^{(0)} - \phi_n^{(0)}},$$

$$r_{n+1/2}^- = \frac{\phi_{n+2}^{(0)} - \phi_{n+1}^{(0)}}{\phi_{n+1}^{(0)} - \phi_n^{(0)}}.$$

Then, numerical mass fluxes

$$\hat{M}_{n\pm 1/2}^{(0)} = \hat{\rho}_{n\pm 1/2}^{(0)} u_{n\pm 1/2}^{(0)} \tau,$$

of momentum $\hat{u}_{n\pm 1/2}^{(0)} \hat{M}_{n\pm 1/2}^{(0)}$ and energy $\hat{E}_{n\pm 1/2}^{(0)} \hat{M}_{n\pm 1/2}^{(0)}$ are formed and we determine the required functions:

$$\rho^{(1)} = \rho^{(0)} + \left(\hat{M}_{n-1/2}^{(0)} - \hat{M}_{n+1/2}^{(0)} \right) / h,$$

$$u_n^{(1)} = \left[\rho_n^{(0)} u_n^{(0)} + \left(\hat{u}_{n-1/2}^{(0)} \hat{M}_{n-1/2}^{(0)} - \hat{u}_{n+1/2}^{(0)} \hat{M}_{n+1/2}^{(0)} \right) / h \right] / \rho_n^{(1)},$$

$$E_n^{(1)} = \left[\rho_n^{(0)} E_n^{(0)} + \left(\hat{E}_{n-1/2}^{(0)} \hat{M}_{n-1/2}^{(0)} - \hat{E}_{n+1/2}^{(0)} \hat{M}_{n+1/2}^{(0)} \right) / h \right] / \rho_n^{(1)}.$$

Functions of limited TVD type are fit to use for non-linear correction of viscosity and fluxes. Further we use the following limiters:

$$\psi(r) = \begin{cases} \max[\min(r, 1), 0] \\ (\text{MM} - \text{Minmod}), \\ (r + |r|) / (1 + r) \\ (\text{VL} - \text{Van Leer}), \\ \max[\min(2r, 1), \min(r, 2), 0] \\ (\text{SB} - \text{Superbee}), \end{cases}$$

which we will denote using subscripts, for example, $\psi_{v, \text{MM}}$ is minmod viscosity limiter.

Experience of computations showed that the limiters provide the hybrid large-particle method with numerical dissipation in the order of its level increasing: SB, VL, MM.

At the correcting step (4), (5) computing formulae of numerical gradients, deformation capacity and convection are similar to the presented ones with the substitution of the superscripts of k with the notation (1), (0) with the notation (2), (1) with the notation $(k + 1)$. The hybrid large-particle method globally has aggregated second-order space-time approximation $O(h^2 + \tau^2)$ for smooth solutions.

Method stability. The time step is determined under the convergence condition by Courant – Friedrichs – Lewy (CFL):

$$\tau^k = \text{CFL} \frac{h}{\max_{\forall n} (|u_n^k| + a_n^k)},$$

where CFL is a fixed Courant number, a_n^k is the speed of sound.

Numerical experiments allowed us to justify stability threshold of the hybrid large-particle method as $\text{CFL} < 0.7$. The Courant number is set in the calculations of the paper taking into ac-



count reliability and accuracy of the algorithm: CFL = 0.4.

Computational results and their discussion

The considered test problems serve to verify the properties of numerical methods to reproduce shock waves, rarefaction waves, contact discontinuities and vortex structures in two-dimensional domain.

Tests 3, 4 and 12. Out of the great variety of two-dimensional Riemann problems, let us consider tests 3, 4 and 12 [30]. Further, assume that the gas is perfect with ratio of specific heats $\gamma = 1.4$. The problems are solved till time point T squared

$$(x, y) \in (0, 1) \times (0, 1),$$

which is divided by lines $x = 1/2$ and $y = 1/2$ into four quadrants.

In each quadrant, there are constant initial conditions set in dimensionless form (see Table).

We performed the calculations using the hybrid large-particle method in a uniformly spaced grid 400×400 with flux $\psi_{f,VL}$ and viscosity $\psi_{v,VL}$ limiters (VL – van Leer, tests 3 and 12), and test

4 – $\psi_{f,VL}$, $\psi_{v,MM}$ (MM – Minmod). We set soft boundary conditions of extrapolation at the outer boundaries.

The exact solutions for these problems are unknown. Numerical solutions are shown in Fig. 1 as contour lines of density and velocity vectors (arrows). For the purpose of correct comparison, the lines of the density level correspond to the ones presented in paper [30].

The problems under consideration cover fluxes with Mach (Fig. 1, *e, f*) and double Mach reflections (Fig. 1, *d*), as well as configurations with closely located contact discontinuities along the larger side of the “lens” (see Fig. 1, *e, f*). For tests 3 and 12, there are additional diagonal vorticity jets. In paper [30], the authors pay attention to an artifact in test problem 12 which can be more or less attributed to all difference scheme under consideration: there is an entropy trace in the place of the initial discontinuity in the process of its decay and further calculation.

The indicated computational problem reveals itself in a number of other test problems. It is explained by the fact that the initial error occurs in a short time interval of the establishment (“smearing”) of the computational profile of the shock

Constant initial conditions in computations for the three tests

Table

Position in quadrants	Parameter	Parameter value in the test and in the quadrants					
		Test 3, $T = 0,30$		Test 4, $T = 0,25$		Test 12, $T = 0,25$	
		Upper	Lower	Upper	Lower	Upper	Lower
Left	p	0.3000	0.0290	0.3500	1.1000	1.0000	1.0000
	ρ	0.5323	0.1380	0.5065	1.1000	1.0000	0.8000
	u	1.2060	1.2060	0.8939	0.8939	0.7276	0.0000
	v	0.0000	1.2060	0.0000	0.8939	0.0000	0.0000
Right	p	1.5000	0.3000	1.1000	0.3500	0.4000	1.0000
	ρ	1.5000	0.5323	1.1000	0.5065	0.5313	1.0000
	u	0.0000	0.0000	0.0000	0.0000	0.0000	0.0000
	v	0.0000	1.2060	0.0000	0.8939	0.0000	0.7276

Notations: p, ρ are dimensionless pressure and density; u, v are dimensionless components of velocity vector \mathbf{v} ; T is dimensionless time point till which the problems were being solved.

Note. 1. Square $0,1 \times 0,1$ is divided into four quadrants. 2. The numbers of tests correspond to the ones used in paper [30].

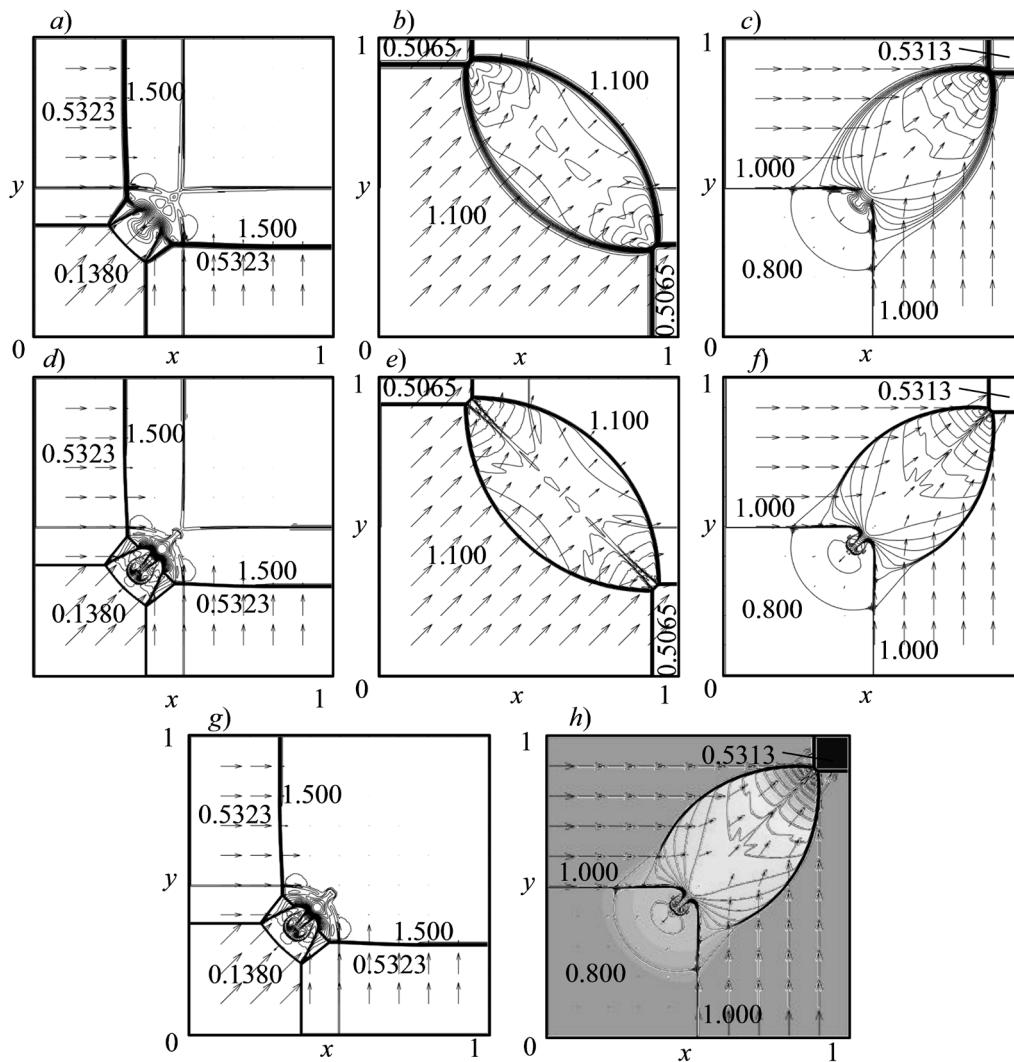


Fig. 1. Results of numerical solution to Riemann problems in two-dimensional domains using the basic large particle method ($a - c$) and the hybrid method ($d - h$) with tests [30]: 3 (a, d, g), 4 (b, e) and 12 (c, f, h).

For test 3, we obtained 32 contour lines of density from 0.16 to 1.71; for tests 4 and 12, respectively, 29 contour lines from 0.52 to 1.92 and 30 contour lines from 0.54 to 1.70; g is a solution with correction of the initial error;

h is a solution compared with WENO5 from paper [30]; arrows show velocity vectors.

wave and stays in the form of an entropy trace [31]. This numerical defect can be eliminated by means of resetting the gas-dynamic parameters in the cocurrent stream after the shock wave in several time steps prior to the initial values (see the example of computations in Fig. 1, g). Let us pay attention to the fact that in test 12, in a small domain the numerical size of a stationary tangential contact discontinuity, we can observe density fluctuations.

The hybrid large-particle method (Fig. 1, $d-f$) demonstrates significant improvements in

terms of reproduction accuracy of flux structures with respect to the basic method [29] (Fig. 1, $a-c$) and the first-order approximation Godunov's scheme [32]. The CDP2 algorithm in the tests outperforms the cited method of adaptive viscosity [16] and the method of piecewise parabolic reconstruction [18] in terms of resolution. The computational results are in good agreement with the best schemes presented in paper [30].

For example, in Fig. 1, h , there is a direct comparison with a five-order accuracy WENO5 scheme: a lower layer on top of which we laid over



an upper layer with the computational results of the hybrid CDP2 method. Note, that the contour lines of density almost exactly coincide in the entire range of the lay-over. The CDP2 scheme computations are in good agreement with bicom-pact schemes with conservative monotization [15] (these test results were not published, but kindly provided by the authors for comparison).

Tests A, B, C and D. To verify efficiency of the hybrid large-particle method, in particular the level of its dissipative properties and the capability to detect instabilities on the contact boundary, we are interested in two-dimensional Riemann problems with central symmetry, for example a well-known test with cylindrical gas propagation into infinite undisturbed environment (explosion problem) [30] – test *A*. In addition, let us consider three other modified problems: tests *B*, *C* and *D*. Test problem *B* formulates propagation into unlimited non-flow gas out of a high pressure domain of square section, while tests *C* and *D* are the previously described problems in space limited by solid walls.

Due to central symmetry, we perform the computations in the upper right quadrant in a uniformly spaced grid 400×400 with the limiters of flux $\psi_{f,VL}$ and viscosity $\psi_{v,SB}$. To eliminate (minimize) the influence of the outer boundaries in the cases of *A* and *B*, the computational grid is expanded to a size of 500×500 . The infinity was simulated by means of expanding the grid by 100 meshes with the mesh step progressing to the right and upwards in compliance with the law

$$h'_{n+1} = h'_n + 0.1h,$$

so that in the time of the computation, the disturbances do not reach the outer boundaries.

The boundary conditions for tests *C* and *D* are standard reflection conditions at the walls. At the initial time in a circle (cases *A* and *C*) and square (cases *B* and *D*), we set density $\rho_i = 1$ and pressure $p_i = 1$, while outside of these domains their values equal $\rho_0 = 0.125$ and $p_0 = 0.1$. We made an allowance that the gas in the entire definition domain is stationary. We assume the size of the computational domain along the coordinate axes to be unit

$$(x, y) \in (0, 1.5) \times (0, 1.5),$$

the circle radius and half the length of the square equal $4/15$.

For visual representation of the computational results in the form of numerical schlieren images, we use nonlinear function of density gradient:

$$s_{i,j} = \exp \left(-k \frac{|\nabla \rho_{i,j}|}{\max_{\forall i,j} |\nabla \rho_{i,j}|} \right),$$

where i, j are the numbering of meshes along x and y respectively; $\nabla \rho_{i,j}$ is a density gradient; k is a customizing coefficient for quality (contrast) display of the flux phenomena.

Fig. 2 shows numerical schlieren images of the density gradient function for the problems of gas propagation into infinite space for sequential points of dimensionless time 0.2, 1.1, 1.3 и 3.2 (the upper row displays the initial high pressure domain as a circle, and the lower one – as a square). After the decay of the initial discontinuity, the following phenomena are formed: shock wave s_1 , contact discontinuity c moving from the center; rarefaction wave w (case *A*) or two waves w_1 and w_2 (case *B*) moving to the center. In the course of time, there is a secondary circle-shaped (Fig. 2, *b, c*) or almost square-shaped (Fig. 2, *f, g*) curved wave s_2 formed converging to the coordinate origin. At the interface of gases denoted by letter c , there is a discontinuity forming. After focusing of the curved wave s_2 , a shock wave s_3 interacting with the contact boundary c is reflected from the symmetry center (Fig. 2, *d, h*). A comparison of the numerical solution (Fig. 2, *d*) with the results of paper [30] proves lesser dissipativity of the CDP2 scheme in the problems with the development of instability at the contact boundary.

Papers [3, 30] discuss the influence of the disturbed (step) initial boundary of the circle on the instability development. As the computations show, even a smoothed contact discontinuity is not stable. In this sense, we are interested in test *B*, in which the contact boundary (square) in the initial point of time coincides with the mesh faces. In this case, the distur-

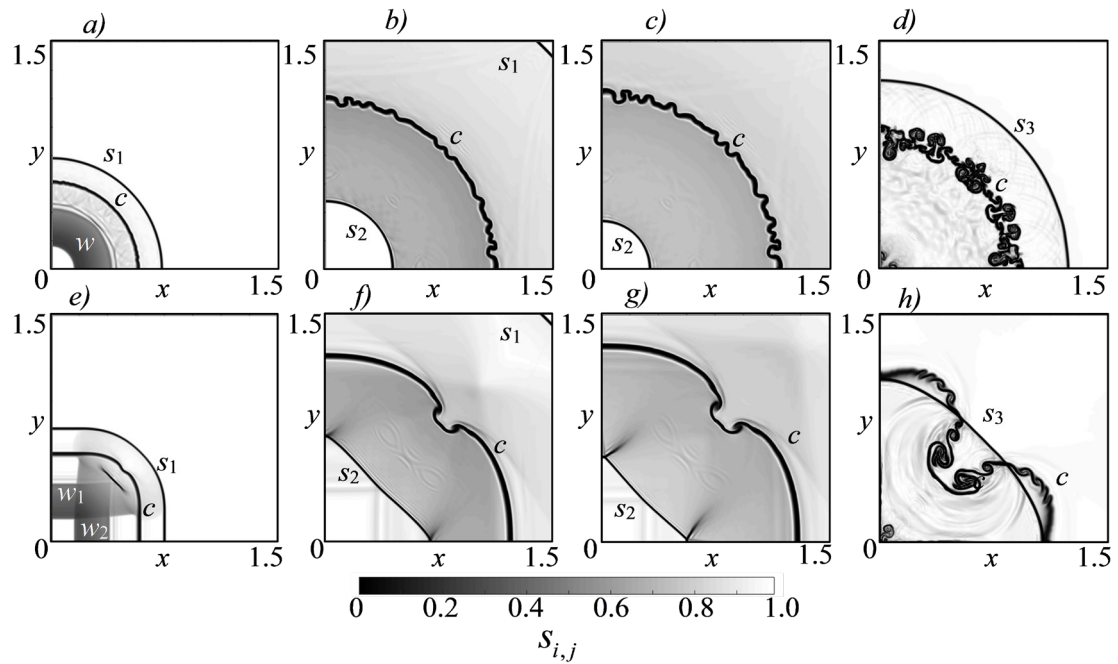


Fig. 2. Numerical schlieren images of the density gradient function in sequential points of time: 0.2 (a, e), 1.1 (b, f), 1.3 (c, g) and 3.2 (d, h).

Tests A (a–d) and B (e–h) were used.

Grid size is 400×400 ; c is the contact boundary; s_1, s_3 are shock waves; s_2 is a curved wave, w, w_1, w_2 are rarefaction waves.

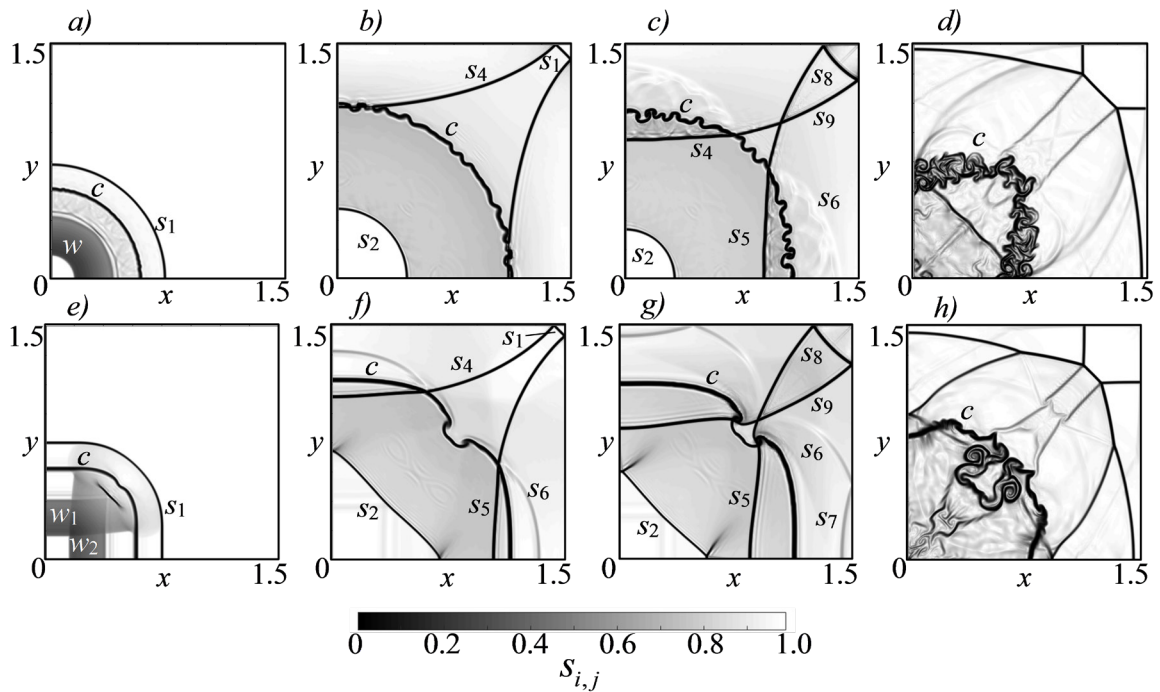


Fig. 3. Numerical schlieren images of the density gradient function in sequential points of time: 0.2 (a, e), 1.1 (b, f), 1.3 (c, g) and 3.2 (d, h).

Tests C (a – d) and D (e – h) were used.

Grid size is 400×400 ; c is the contact boundary; s_1-s_9 are shock waves; w, w_1, w_2 are rarefaction waves.

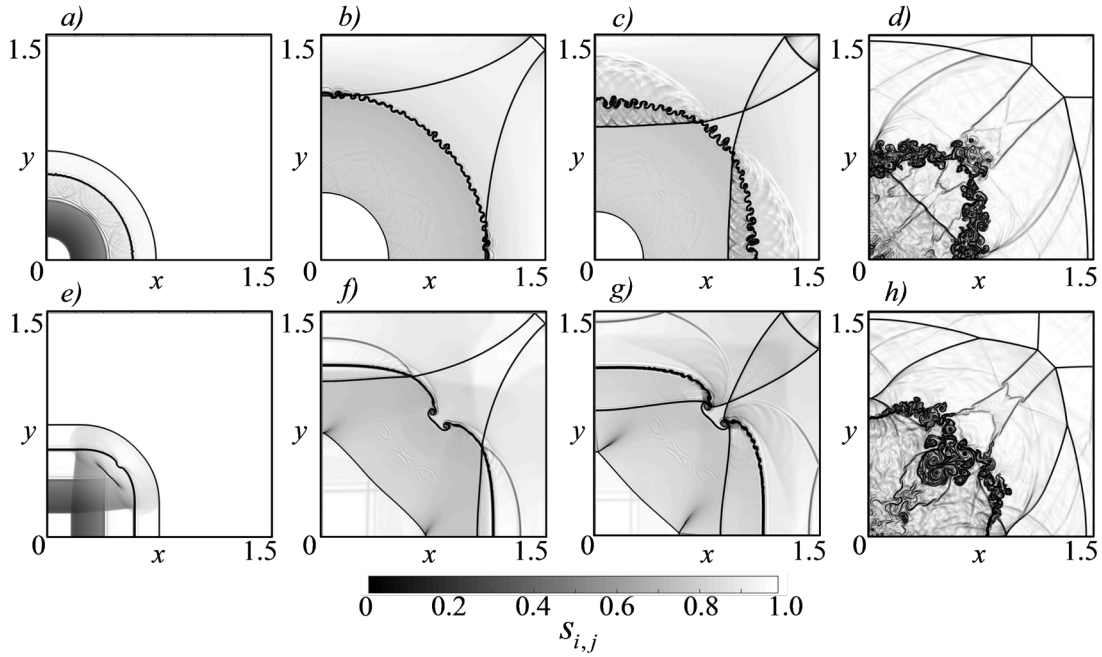


Fig. 4. Numerical schlieren images of the density gradient function in sequential points of time identical to those presented in Fig. 3, but obtained with a grid size of 800×800

bances begin developing from the peaks of the square domain, and then spread along the whole gas-gas interface (Fig. 2, *h*).

Possible solutions of the problems in bounded space (*C* and *D*) for the time points above have a “richer” configuration of gas fluxes and are shown in Fig. 3. The beginning of the propagation at $t_1 = 0.2$ does not differ from the considered cases (Fig. 2, *a*, *e*) as the shock front s_1 did not reach the walls. In the subsequent time points $t_2 = 1.1$ and $t_3 = 1.3$, structures that include shock waves are formed: s_4 reflected from the wall, propagated s_5 , and s_6 reflected from the contact boundary, secondary reflected s_7 , focused s_8 , and s_9 formed after a collision of bow waves. From this point on, at $t_4 = 3.2$, the gas flux is accompanied by multiple interactions of the shock waves with the walls, between each other and with the contact boundary as turbulence begins to develop.

To explain a physical mechanism of the instability development and vortices formation at the contact boundary, let us consider a transfer equa-

tion for vorticity $\omega = \nabla \times \mathbf{v}$:

$$\frac{d\omega}{dt} = \frac{\nabla \rho \times \nabla p}{\rho^2} + (\omega \cdot \nabla) \mathbf{v} - \omega (\nabla \cdot \mathbf{v}),$$

where d/dt is a derivative along the vorticity trajectory.

At the initial time point, $\omega = 0$. It follows from the presented equation that the cause of the vortices generation lies in the incongruence of the gradients of pressure and density

$$(\nabla \rho \times \nabla p) / \rho^2 \neq 0$$

(baroclinic effect).

This effect is especially prominent in multiple interactions of shock waves reflected from the walls with the contact boundary, with secondary vortices forming and turbulence developing (see Fig. 3, 4, *d* and *h*).

To verify the convergence, as well the influence of the grid resolution on the formation of vortices, we performed a computation with a grid

of meshes half the size of the initial one. The results for cases *C* and *D* are shown in Fig. 4. An overlay of numeric fields (figures not provided) obtained in different grids proves practical coincidence of the shock wave lines and their conjugating in triple points. Vortical elements are displayed in great detail in such a detailed grid, while the computations agree with each other well due to the stochastic nature in the mean sense.

Conclusion

We considered a class of difference schemes with customizable dissipative properties and a split by physical processes: the hybrid large-particle method of a space-time second-order approximation for smooth solutions. The method was verified using well-known Riemann problems in two-dimensional domains which have

reliable numerical solutions.

The results showed a significant improvement in the accuracy of reproducing flux structures in comparison with the basic hybrid large-particle method. We demonstrated high competitiveness of the proposed algorithm when comparing it to the modern schemes of an increased approximation order.

The paper provides a detailed study of the method efficiency in new test problems with multiple interactions of the shock waves with the contact boundary, channel walls, as well as instability development.

The hybrid large-particle method proved to have high resolution both in shock configuration domains and regions of vortex structures.

The proposed test problems could be used for verification in other difference schemes.

REFERENCES

1. **Godunov S.K.**, A difference method for numerical calculation of discontinuous solutions of the equations of hydrodynamics, *Matematicheskii Sbornik*. 47 (89) (3) (1959) 271–306 (in Russian).
2. **Kolgan V.P.**, *Primeneniye printsipa minimalnykh znacheniy proizvodnykh k postroyeniyu konechno-raznostnykh skhem dlya rascheta razryvnykh resheniy gazovoy dinamiki* [An application of the minimal derivative values concept to construction of the finite-difference schemes for calculating the discontinuous solutions of gasdynamics], *Uchenyye Zapiski TsAGI*. 3 (6) (1972) 68–77 (in Russian).
3. **Toro E.F.**, *Riemann solvers and numerical methods for fluid dynamics*, Springer-Verlag, Berlin, Heidelberg, 2009.
4. **Harten A.**, High resolution schemes for hyperbolic conservation laws, *J. Comput. Phys.* 49 (3) (1983) 357–393.
5. **Sweby P.K.**, High-resolution schemes using flux limiters for hyperbolic conservation laws, *SIAM J. Numer. Anal.* 21 (5) (1984) 995–1011.
6. **Hirsch C.**, *Numerical computation of internal and external flows*, Vol. 2, Computational methods for inviscid and viscous flows, John Wiley & Sons, New York, 1990.
7. **Jiang G.-S., Shu C.-W.**, Efficient implementation of weighted ENO schemes, *J. Comp. Phys.* 126 (1) (1996) 202–228.
8. **Shi J., Zhang Y.-T., Shu C.-W.**, Resolution of high order WENO schemes for complicated flow structures, *J. Comp. Phys.* 186 (2) (2003) 690–696.
9. **Evstigneev N.M.**, On the construction and properties of WENO schemes order five, seven, nine, eleven and thirteen. Part 2. Numerical examples, *Computer Research and Modeling*. 8 (6) (2016) 885–910 (in Russian).
10. **Fedorenko R.P.**, The application of difference schemes of high accuracy to the numerical solution of hyperbolic equations, *USSR Comput. Math. and Math. Phys.* 2 (6) (1963) 1355–1365.
11. **Liu X., Zhang S., Zhang H., Shu C.-W.**, A new class of central compact schemes with spectral-like resolution II: Hybrid weighted nonlinear schemes, *J. Comp. Phys.* 284 (1 March) 133–154.
12. **Lobanov A.I., Mirov F.Kh.**, Hybrid difference scheme under generalized approximation condition in the space of undetermined coefficients, *Comput. Math. and Math. Phys.* 58 (8) (2018) 1270–1279.
13. **Tolstykh A.I.**, On families of compact fourth- and fifth-order approximations involving the inversion of two-point operators for equations with con-



vective terms, *Comput. Math. and Math. Phys.* 50 (5) (2010) 848–861.

14. **Shen Y.-Q., Zha G.-C.**, Generalized finite compact difference scheme for shock/complex flow field interaction, *J. Comp. Phys.* 230 (12) (2011) 4419–4436.

15. **Bragin M.D., Rogov B.V.**, Conservative limiting method for high-order bcompact schemes as applied to systems of hyperbolic equations, *Appl. Num. Math.* 151 (May) (2020) 229–245.

16. **Popov I.V., Fryazinov I.V.**, Calculations of two-dimensional test problems by the method of adaptive viscosity, *Math. Models Comput. Simul.* 2 (6) (2010) 724–732.

17. **Karabasov S.A.**, On the power of second-order accurate numerical methods for model problems of gas- and hydrodynamics, *Math. Models Comput. Simul.* 3 (1) (2011) 92–112.

18. **Bulat P.V., Volkov K.N.**, Solution of two-dimensional Riemann problems using the method of piecewise parabolic reconstruction, *J. Eng. Phys. Thermophys.* 90 (3) (2017) 525–534.

19. **Kolesnik E.V., Smirnov E.M.**, Testing of various schemes with quasi-one-dimensional reconstruction of gasdynamic variables in the case of unstructured-grid calculations, *St. Petersburg Polytechnic University Journal. Physics and Mathematics.* 10 (3) (2017) 123–139.

20. **Chizhonkov E.V.**, On second-order accuracy schemes for modeling of plasma oscillations, *Numerical Methods and Programming.* 21 (1) (2020) 115–128 (in Russian).

21. **Sadin D.V.**, TVD scheme for stiff problems of wave dynamics of heterogeneous media of non-hyperbolic nonconservative type, *Comput. Math. and Math. Phys.* 56 (12) (2016) 2068–2078.

22. **Sadin D.V.**, Schemes with customizable dissipative properties as applied to gas-suspensions flow simulation, *Matem. Mod.* 29 (12) (2017) 89–104 (in Russian).

23. **Sadin D.V., Davidchuk V.A.**, Comparison of a modified large-particle method with some high resolution schemes. One-dimensional test prob-

lems, *Numerical Methods and Programming.* 20 (2) (2019) 138–146 (in Russian).

24. **Sadin D.V., Belyayev B.V., Davidchuk V.A.**, Comparison of a modified large-particle method with some high resolution schemes. Two-dimensional test problems, *Numerical Methods and Programming.* 20 (3) (2019) 337–345 (in Russian).

25. **Sadin D.V.**, Analysis of dissipative properties of a hybrid large-particle method for structurally complicated gas flows, *Computer Research and Modeling.* 12 (4) (2020) 757–772 (in Russian).

26. **Tagirova I.Yu., Rodionov A.V.**, Application of the artificial viscosity for suppressing the carbuncle phenomenon in Godunov-type schemes, *Mathematical Models and Computer Simulations.* 8 (3) (2016) 249–262.

27. **Balsara D.S.**, A two-dimensional HLLC Riemann solver for conservation laws: Application to Euler and magneto hydrodynamic flows, *J. Comput. Phys.* 231 (22) (2012) 7476–7503.

28. **Sadin D.V.**, A modification of the large-particle method to a scheme having the second order of accuracy in space and time for shockwave flows in a gas suspension, *Bulletin of the South Ural State University. Ser. Mathematical Modelling, Programming & Computer Software (Bulletin SUSU MMCS).* 12 (2) (2019) 112–122 (in Russian).

29. **Belotserkovskii O.M., Davydov Yu.M.**, A non-stationary “Coarse particle” method for gas-dynamical computations, *URSS Comp. Math. and Math. Phys.* 11 (1) (1971) 241–271.

30. **Liska R., Wendroff B.**, Comparison of several difference schemes on 1D and 2D test problems for the Euler equations, *SIAM J. Sci. Comp.* 25 (3) (2003) 995–1017.

31. **Woodward P., Colella P.**, The numerical simulation of two-dimensional fluid flow with strong shocks, *J. Comp. Phys.* 54 (1) (1984) 115–173.

32. **Brio M., Zakharian A.R., Webb G.M.**, Two-dimensional Riemann solver for Euler equations of gas dynamics, *J. Comp. Phys.* 167 (1) (2001) 177–195.

Received 28.10.2020, accepted 26.11.2020.

THE AUTHORS

SADIN Dmitriy V.

Military Space Academy named after A.F. Mozhaysky

13, Zhdanovskaya St., St. Petersburg, 197198, Russian Federation

sadin@yandex.ru

GOLIKOV Igor O.

Military Space Academy named after A.F. Mozhaysky

13, Zhdanovskaya St., St. Petersburg, 197198, Russian Federation

igira55@yandex.ru

SHIROKOVA Elena N.

Military Space Academy named after A.F. Mozhaysky

13, Zhdanovskaya St., St. Petersburg, 197198, Russian Federation

shirokelen-78@mail.ru

СПИСОК ЛИТЕРАТУРЫ

1. Годунов С.К. Разностный метод численного расчета разрывных решений гидромеханики // Математический сборник. 1959. Т. 47 (89). № 3. С. 271–306.
2. Колган В.П. Применение принципа минимальных значений производных к построению конечно-разностных схем для расчета разрывных решений газовой динамики // Ученые записки ЦАГИ. 1972. Т. 3. № 6. С. 68–77.
3. Toro E.F. Riemann solvers and numerical methods for fluid dynamics. Berlin, Heidelberg: Springer-Verlag, 2009. 724 p.
4. Harten A. High resolution schemes for hyperbolic conservation laws // Journal of Computational Physics. 1983. Vol. 49. No. 3. Pp. 357–393.
5. Sweby P.K. High-resolution schemes using flux limiters for hyperbolic conservation laws // SIAM Journal of Numerical Analysis. 1984. Vol. 21. No. 5. Pp. 995–1011.
6. Hirsch C. Numerical computation of internal and external flows. Vol. 2. Computational methods for inviscid and viscous flows. New York: John Wiley & Sons, 1990. 691 p.
7. Jiang G.-S., Shu C.-W. Efficient implementation of weighted ENO schemes // Journal of Computational Physics. 1996. Vol. 126. No. 1. Pp. 202–228.
8. Shi J., Zhang Y.-T., Shu C.-W. Resolution of high order WENO schemes for complicated flow structures // Journal of Computational Physics. 2003. Vol. 186. No. 2. 690–696.
9. Евстигнеев Н.М. О построении и свойствах WENO-схем пятого, седьмого, девятого, одиннадцатого и тринадцатого порядков. Часть 2. Численные примеры // Компьютерные исследования и моделирование. 2016. Т. 8. № 6. 885–910.
10. Федоренко Р.П. Применение разностных схем высокой точности для численного решения гиперболических уравнений // Журнал вычислительной математики и математической физики. 1962. Т. 2. № 6. С. 1122–1128.
11. Liu X., Zhang S., Zhang H., Shu C.-W. A new class of central compact schemes with spectral-like resolution II: Hybrid weighted nonlinear schemes // Journal of Computational Physics. 2015. Vol. 284. 1 March. Pp. 133–154.
12. Лобанов А.И., Милов Ф.Х. Гибридная разностная схема с обобщенным условием аппроксимации. Анализ в пространстве неопределенных коэффициентов // Журнал вычислительной математики и математической физики. 2018. Т. 58. № 8. С. 73–82.
13. Толстых А.И. О семействах компактных аппроксимаций 4-го и 5-го порядков с обращением двухточечных операторов для уравнений с конвективными членами // Журнал вычислительной математики и математической физики.



ки. 2010. Т. 50. № 5. С. 894–907.

14. **Shen Y.-Q., Zha G.-C.** Generalized finite compact difference scheme for shock/complex flow field interaction // *Journal of Computational Physics*. 2011. Vol. 230. No. 12. Pp. 4419–4436.

15. **Bragin M.D., Rogov B.V.** Conservative limiting method for high-order bcompact schemes as applied to systems of hyperbolic equations // *Applied Numerical Mathematics*. 2020. Vol. 151. May. Pp. 229–245.

16. **Попов И.В., Фрязинов И.В.** Расчеты двумерных тестовых задач методом адаптивной искусственной вязкости // *Математическое моделирование*. 2010. Т. 22. № 5. С. 57–66.

17. **Карабасов С.А.** О возможностях методов второго порядка аппроксимации на примере модельных задач газо- и гидродинамики // *Математическое моделирование*. 2010. Т. 22. № 7. С. 93–120.

18. **Булат П.В., Волков К.Н.** Решение двумерных задач Римана при помощи метода кусочно-параболической реконструкции // *Инженерно-физический журнал*. 2017. Т. 90. № 3. С. 558–568.

19. **Колесник Е.В., Смирнов Е.М.** Тестирование различных схем с квазиодномерной реконструкцией газодинамических переменных при расчетах на неструктурированных сетках // *Научно-технические ведомости СПбГПУ. Физико-математические науки*. 2017. Т. 10. № 3. С. 123–139.

20. **Чижонков Е.В.** О схемах второго порядка точности для моделирования плазменных колебаний // *Вычислительные методы и программирование*. 2020. Т. 21. № 1. С. 115–128.

21. **Садин Д.В.** TVD-схема для жестких задач волновой динамики гетерогенных сред негиперболического неконсервативного типа // *Журнал вычислительной математики и математической физики*. 2016. Т. 56. № 12. С. 2098–2109.

22. **Садин Д.В.** Схемы с настраиваемыми диссипативными свойствами для численного моделирования течений газа и газовзвесей // *Математическое моделирование*. 2017. Т. 29. № 12. С. 89–104.

23. **Садин Д.В., Давидчук В.А.** Сравнение модифицированного метода крупных частиц с некоторыми схемами высокой разрешающей

способности. Одномерные тесты // *Вычислительные методы и программирование*. 2019. Т. 20. № 2. С. 138–146.

24. **Садин Д.В., Беляев Б.В., Давидчук В.А.** Сравнение модифицированного метода крупных частиц с некоторыми схемами высокой разрешающей способности. Двумерные тесты // *Вычислительные методы и программирование*. 2019. Т. 20. № 3. С. 337–345.

25. **Садин Д.В.** Анализ диссипативных свойств гибридного метода крупных частиц для структурно сложных течений газа // *Компьютерные исследования и моделирование*. 2020. Т. 12. № 4. С. 757–772.

26. **Тагирова И.Ю., Родионов А.В.** Применение искусственной вязкости для борьбы с карбункул-неустойчивостью в схемах типа Годунова // *Математическое моделирование*. 2015. Т. 27. № 10. С. 47–64.

27. **Balsara D.S.** A two-dimensional HLLC Riemann solver for conservation laws: Application to Euler and magnetohydrodynamic flows // *Journal of Computational Physics*. 2012. Vol. 231. No. 22. Pp. 7476–7503.

28. **Садин Д.В.** Модификация метода крупных частиц до схемы второго порядка точности по пространству и времени для ударно-волновых течений газовзвесей // *Вестник Южно-Уральского государственного университета. Сер. Математическое моделирование и программирование*. 2019. Т. 12. № 2. С. 112–122.

29. **Белоцерковский О.М., Давыдов Ю.М.** Нестационарный метод “крупных частиц” для газодинамических расчетов // *Журнал вычислительной математики и математической физики*. 1971. Т. 11. № 1. С. 182–207.

30. **Liska R., Wendroff B.** Comparison of several difference schemes on 1D and 2D test problems for the Euler equations // *SIAM Journal on Scientific Computing*. 2003. Vol. 25. No. 3. Pp. 995–1017.

31. **Woodward P., Colella P.** The numerical simulation of two-dimensional fluid flow with strong shocks // *Journal of Computational Physics*. 1984. Vol. 54. No. 1. Pp. 115–173.

32. **Brio M., Zakharian A.R., Webb G.M.** Two-Dimensional Riemann Solver for Euler Equations of Gas Dynamics // *Journal of Computational Physics*. 2001. Vol. 167. No. 1. Pp. 177–195.

Статья поступила в редакцию 28.10.2020, принята к публикации 26.11.2020.

СВЕДЕНИЯ ОБ АВТОРАХ

САДИН Дмитрий Викторович — доктор технических наук, профессор Военно-космической академии имени А.Ф. Можайского, Санкт-Петербург, Российская Федерация.

197198, Российская Федерация, г. Санкт-Петербург, Ждановская ул., 13
sadin@yandex.ru

ГОЛИКОВ Игорь Олегович — кандидат технических наук, доцент Военно-космической академии имени А.Ф. Можайского, Санкт-Петербург, Российская Федерация.

197198, Российская Федерация, г. Санкт-Петербург, Ждановская ул., 13
igira55@yandex.ru

ШИРОКОВА Елена Николаевна — кандидат химических наук, преподаватель Военно-космической академии имени А.Ф. Можайского, Санкт-Петербург, Российская Федерация.

197198, Российская Федерация, г. Санкт-Петербург, Ждановская ул., 13
shirokelen-78@mail.ru



DOI: 10.18721/JPM.14105
UDC 532.542.4

A FLOW IN THE BLOOD VESSEL WITH A ONE-SIDE STENOSIS: NUMERICAL STUDY OF THE STRUCTURE AND LOCAL TURBULIZATION

Ya.A. Gataulin, E.M. Smirnov

Peter the Great St. Petersburg Polytechnic University,
St. Petersburg, Russian Federation

In the paper, the LES results of a flow by using a model of the blood vessel with a one-side 70% stenosis, at a Reynolds number of 1803, have been presented. The Germano – Lilly model was applied to subgrid viscosity evaluation. A jet-like zone and a recirculation one were found to stand out just behind the stenosis, and a pair of secondary-flow vortices forms being within each of them. Instabilities of the mixing layer initiated the flow turbulence with formation of vortex structures of different scales at the boundary between the reverse flow zone and the jet. These structures filled the whole cross-section of the vessel about the flow attachment point. Turbulent shear stresses were significant in magnitude only at a flow section of about four-caliber length. Further downstream, the flow relaminarised.

Keywords: blood flow, stenosis, turbulence, numerical simulation, large eddy simulation

Citation: Gataulin Ya.A., Smirnov E.M., A flow in the blood vessel with a one-side stenosis: numerical study of the structure and local turbulization, St. Petersburg Polytechnical State University Journal. Physics and Mathematics. 14 (1) (2021) 69–80. DOI: 10.18721/JPM.14105

This is an open access article under the CC BY-NC 4.0 license (<https://creativecommons.org/licenses/by-nc/4.0/>)

ЧИСЛЕННОЕ ИССЛЕДОВАНИЕ СТРУКТУРЫ И ЛОКАЛЬНОЙ ТУРБУЛИЗАЦИИ ТЕЧЕНИЯ В КРОВЕНОСНОМ СОСУДЕ С ОДНОСТОРОННИМ СТЕНОЗОМ

Я.А. Гатаулин, Е.М. Смирнов

Санкт-Петербургский политехнический университет Петра Великого,
Санкт-Петербург, Российская Федерация

В статье представлены результаты расчетов течения в модели кровеносного сосуда с односторонним стенозом 70 % при числе Рейнольдса, равном 1803. Численное решение получено методом моделирования крупных вихрей по динамической модели Джермано – Лилли для оценки подсеточной вязкости. Установлено, что непосредственно за стенозом в потоке выделяются 2 зоны: струйного течения и обширная рециркуляционная, а в каждой присутствует пара вихрей вторичного течения. Неустойчивости слоя смешения на границе струи и зоны обратного течения инициируют турбулизацию потока с образованием разномасштабных вихревых структур. Последние заполняют все поперечное сечение сосуда в окрестности точки присоединения. Турбулентные напряжения значительны по величине лишь на участке длиной около четырех калибров. Вниз по потоку течение реламинаризируется.

Ключевые слова: кровоток, стеноз, турбулентность, численное моделирование, метод моделирования крупных вихрей

Ссылка при цитировании: Гатаулин Я.А., Смирнов Е.М. Численное исследование структуры и локальной турбулизации течения в кровеносном сосуде с односторонним стенозом // Научно-технические ведомости СПбГПУ. Физико-математические науки. 2021. Т. 14. № 1. С. 69–80. DOI: 10.18721/JPM.14105

Introduction

Modern computational fluid dynamics (CFD) offers the broadest range of tools for simulating blood flow in various segments of the vascular bed. Laminar flow is established in small and medium-sized vessels, where the Reynolds number Re does not exceed 1000. We considered the spatial structure of laminar flow in carotid artery models, including the case of stenotic vessels (persistent narrowing of its lumen), in several earlier studies [1 – 3]. However, the flow behind the stenosis in large blood vessels is characterized by higher values of the Reynolds number and is particularly difficult to compute. The flow behind the stenosis in such vessels actually turns out to be cyclically transient, since it is locally turbulent during a period in the cardiac cycle, remaining completely laminar for the rest of the cycle. Developing approaches to simulation of the turbulence occurring locally holds the key to obtaining sufficiently reliable predictions.

Turbulent flows in stenotic vessels are traditionally computed using models based on the Reynolds-Averaged Navier – Stokes equations (RANS) [4 – 7]. It was established that RANS models are capable of providing good agreement between the computed field of averaged velocity and the measured data; however, the predictions obtained for some turbulence characteristics that are interesting for biomedical applications turn out to have very low quality.

Direct Numerical Simulation (DNS) [8 – 11] and eddy-resolving models (including primarily Large Eddy Simulation or LES) [12 – 15] have become widely popular in recent years for improving the quality of numerical analysis of turbulent flows in stenotic vessels. All components of unsteady vortex motion are completely resolved within the DNS method, which means that the computational costs for obtaining a numerical solution are high, rapidly increasing with an increase in the Reynolds number. The much less expensive LES method only numerically reproduces sufficiently large eddies, which are

characterized by energy transfer, while eddies of a smaller scale are simulated using subgrid-scale models (SGS).

Most of the applied computations by the LES method are carried out using the classical Smagorinsky model introducing subgrid-scale turbulent viscosity. This model was developed assuming a sufficiently developed turbulence, which for practical applications is reduced to the condition that the subgrid-scale viscosities be considerably higher than the molecular ones. The Smagorinsky model with a constant empirical coefficient C_s in the formula for calculating the subgrid-scale viscosity is ill-suited for flows with a transient nature of motion (from laminar to turbulent).

Germano et al. [16] expanded the capabilities of the Smagorinsky algebraic model, in particular for the case of transient flows, developing the so-called dynamic model, where the coefficient C_s is not given but calculated based on the expression obtained by applying a double filtering procedure to the velocity field. Lilly [17] later proposed a modification of the dynamic model, important for practical applications, which consists in cutting off the locally negative values of the coefficient C_s at zero. The Germano-Lilly dynamic model was successfully applied in [14] for LES computations of transient regimes in statistically two-dimensional pulsatile flow in a channel with local one-sided narrowing (stenosis model) by 50%; the peak values of the Reynolds number reached 2000; the periodic boundary conditions were imposed in the third direction.

This paper presents numerical analysis for transient three-dimensional flow of an incompressible viscous fluid in a blood vessel model with unilateral stenosis of 70% at a constant flow rate corresponding to the Reynolds number $Re = 1803$.

The geometry of the stenosis is identical to one of the cases described in the recent experimental work [18], using digital tracer imaging (Particle Image Velocimetry, PIV) to measure the characteristics of pulsatile flow (with a peak value of



$Re = 1803$). Simulations using the CFD software package ANSYS CFX 18.2 were performed based on the large eddy simulation method with the Germano – Lilly dynamic model for computing the subgrid-scale viscosity.

Problem statement and computational aspects

The geometric model of the vessel with unilateral stenosis (Fig. 1) is borrowed from the experimental study [18]. The vessel beyond the boundaries of the stenosis is a tube with the diameter D . Let us introduce the Cartesian coordinate system x, y, z , whose origin is located in the section with the narrowest lumen; the z axis is directed along the vessel, and the y axis is directed towards the non-stenotic (provisionally upper) wall. The geometry of the stenosis that is symmetrical about the central longitudinal plane $x = 0$ is described by the following formulas:

$$\begin{aligned} \frac{d(z)}{D} &= \left(1 - \frac{S}{200}\right) - \frac{S}{200} \cos\left(\frac{2z\pi}{L}\right), \\ &-\frac{L}{2} \leq z \leq \frac{L}{2}; \\ \frac{c(z)}{D} &= 1 - \frac{d(z)}{2D}, \quad -\frac{L}{2} \leq z \leq \frac{L}{2}, \end{aligned}$$

where d is the local lumen diameter in the stenotic region, L is the length of the stenosis, s is the coordinate of the lumen center along the axis y (counted from the lower wall, as adopted here and below),

$$S = (1 - d_{\min}/D) \cdot 100 \%$$

(d_{\min} is the minimum local diameter d).

In the case considered, $S = 45\%$, $L = 2D$, while the area of the narrowest section in the stenotic region is 30.25% of the cross-sectional area of the tube beyond the stenosis, i.e., the stenosis amounts to 69.75% (70% rounded off).

The flow in this model of a blood vessel at $Re = 1803$ was computed by the LES method using the Germano – Lilly dynamic model [16, 17]. The computational domain included a stenotic region, an inlet section with the length of $5D$ and an outlet section with the length of $20D$; the latter is sufficient for eliminating any significant influence of the outlet boundary condition on the flow near the stenosis.

The computations were carried out using the general-purpose 'finite-volume' CFD code ANSYS CFX, version 18.2. This software tool operates with dimensional values.

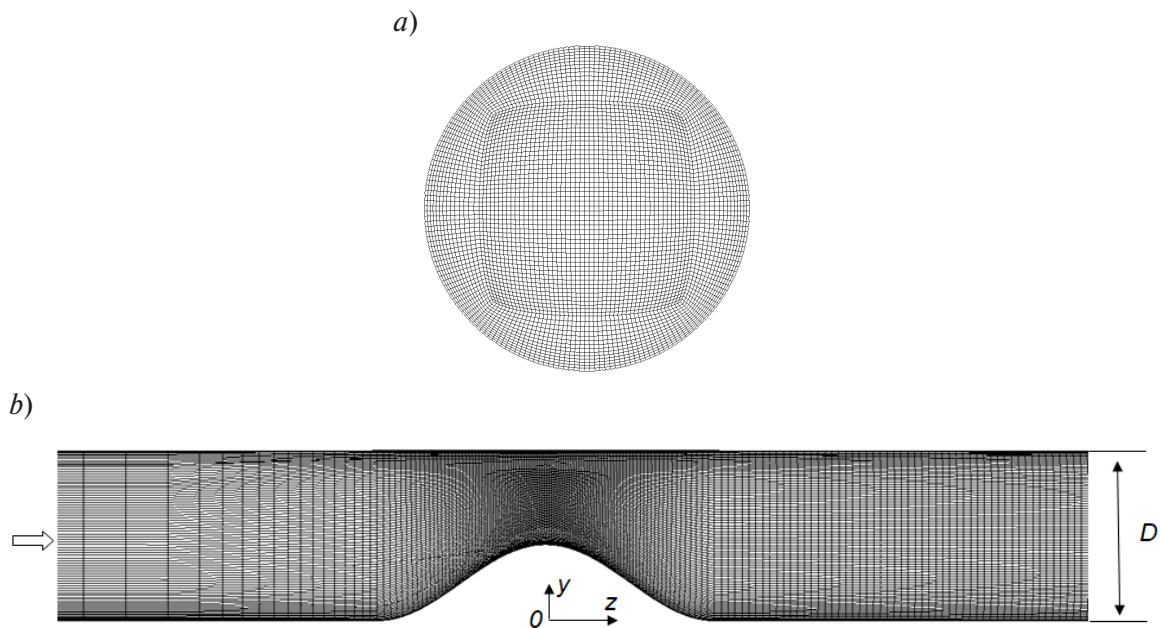


Fig. 1. View of computational mesh in transverse (a) and longitudinal (b) sections of the vessel with stenosis

Table

Computational parameters and their values

Parameter	Notation	Unit of measurement	Value
Vessel diameter (beyond stenosis)	D	mm	10
Mean flow velocity (beyond stenosis)	V_b	m/s	0.627
Fluid density	ρ	kg/m ³	1000
Dynamic viscosity coefficient	μ	Pa·s	0.003478
Reynolds number	$Re = \rho V_b D / \mu$		1803

The set of defining dimensional parameters of the problem is given in the table. The Reynolds number is computed from these parameters.

A parabolic velocity distribution was given at the inlet to the computational domain, which corresponds to the Poiseuille solution for developed laminar flow in a circular tube; constant pressure and 'soft' conditions for the velocity were imposed at the outlet. No-slip conditions were imposed on the walls.

The ICEM CFD program was used to construct a computational *O-grid* mesh consisting of hexahedral elements (Fig. 1). The longitudinal mesh spacing was uniform in the stenotic region and throughout the entire outlet section, amounting to $0.04D$, while the maximum transverse spacing was $0.02D$. The longitudinal spacing at the inlet section gradually decreased to $0.04D$ approaching the stenotic region. The total number of elements in the mesh was about 4.5 million.

A central scheme with second-order accuracy was used in the computations for approximating the convective terms in the equations of motion. A three-layer Euler scheme was used to advance in time. The time step was 0.0002 s, which ensured local Courant numbers less than unity in the entire computational domain.

The sample used to obtain the averaged flow characteristics was accumulated over a time of $1050t_s$, where t_s is the time scale of the problem ($t_s = D/V_b$); the previous time interval, covering about $600t_s$, was sufficient for statistically steady flow to be established, starting from a zero velocity field.

The simulations were performed on the Poly-

technic RSC Tornado cluster of the Polytechnic Supercomputer Center (<http://www.scc.spbstu.ru>). The problem was run on 18 dual-core nodes (Intel (R) Xeon (R) E5 2697v3) and parallelized to 450 cores; the full simulation took about a week of real time (76,000 core hours).

Results and discussion

A peculiarity of the simulated flow is the presence of a laminar-turbulent transition behind the stenosis. To illustrate this, the Q -criterion isosurface was constructed in Fig. 2,*a* [19], with the colors corresponding to the local values of the velocity modulus; this allows visualizing the region where turbulent vortical structures with different scales evolve due to hydrodynamic instabilities. The latter are characteristic for jet-like shear flow.

Fig. 2 also shows two isosurfaces of the time-averaged longitudinal velocity component. One of these surfaces (see Fig. 2,*b*), plotted for the value $V_z = 3.2V_b = 2$ m/s, illustrates the dimensions of the region with pronounced jet flow. The other one (Fig. 2,*c*), corresponding to the value $V_z = -0.002V_b$, shows two zones of recirculation flow behind the stenosis: an extensive one (about $5D$ -long) immediately behind the stenosis, and a very small one, located near the opposite wall at a distance of about $4D$ from the center of the stenosis. A small separation zone is also formed before the stenosis.

The fields of time-averaged velocity components in three cross sections of the vessel model are shown in Fig. 3. Evidently, the jet formed in the stenotic region, whose local velocities are relatively high (exceeding the mean flow rate $V_b = 0.627$ m/s beyond the stenosis by up to 4

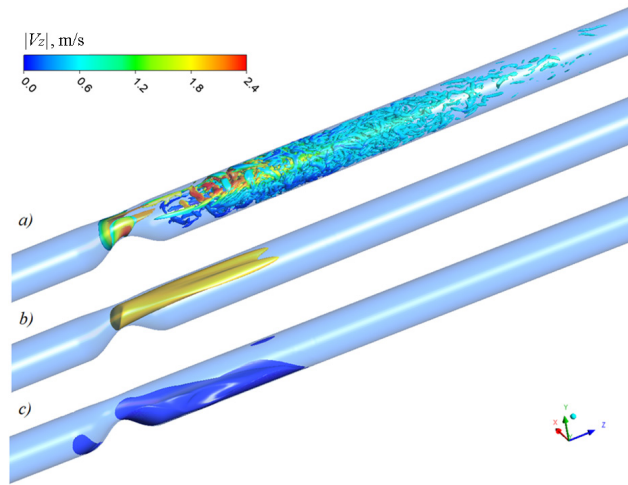


Fig. 2. Flow structures in stenotic vessel, visualized by constructing a Q -criterion isosurface ($Q = 0,06 \text{ s}^{-2}$) (a); two isosurfaces of averaged longitudinal velocity V_z taking the values $3,2V_b$ (b) and $-0,002V_b$ (c)

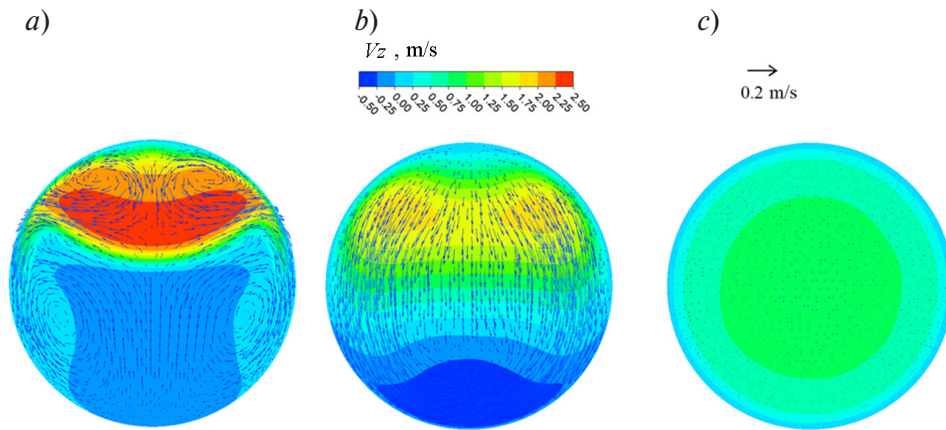


Fig. 3. The time-averaged field of longitudinal velocity component with the field of transverse velocity vectors superimposed on it in three sections of the vessel model: $z/D = 2$ (a), 4 (b), 10 (c)

times), is also characterized by the presence of a fairly intense transverse (secondary) flow in the form of a vortex pair (see Fig. 3,a). In fact, this pair, similar to Dean vortices in curved tubes, develops in the anterior part of the stenosis, where the flow occurs along curved streamlines following the geometry of the stenosis. In turn, the vortex pair developing in the stenosis induces a secondary flow (with opposite circulation) in the backflow zone behind the stenosis, also leading to bifurcation of the jet downstream (see Fig. 2,b and 3,b). The averaged transverse flow almost completely degenerates at a distance less than $10D$ from the center of the stenosis, and the

distribution of the averaged longitudinal velocity regains an axisymmetric 'tubular' shape, with the maximum velocity in the center of the vessel (see Fig. 3,c).

The field of averaged longitudinal velocity in the central longitudinal section (in the plane of symmetry) is shown in Fig. 4,a. It can be seen here and in Fig. 3,b that the maximum velocity of the backflow section in the main recirculation zone is comparable in magnitude with the mean flow rate V_b beyond the stenosis.

A high-gradient shear layer (mixing layer) is formed at the boundary of the jet and the recirculation zone; the phenomena characteristic for this

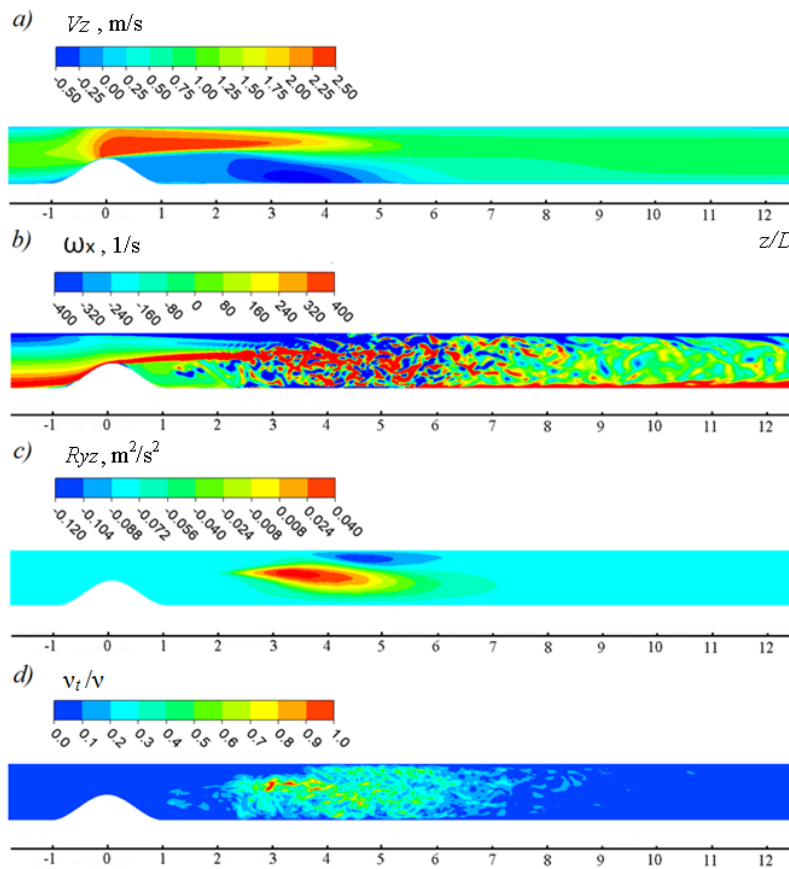


Fig. 4. Computed fields in the symmetry plane of the vessel: time-averaged longitudinal velocity (a), instantaneous value of x -component of vorticity (b), Reynolds shear stress $R_{yz} = R_{yz} = -\overline{V'_y V'_z}$ (c), instantaneous value of the ratio of subgrid-scale vortex to molecular viscosity (d)

layer are caused by the Kelvin – Helmholtz instability. Visualization for the instantaneous field of the x -component of the vorticity vector (Fig. 4,b) indicates that the Kelvin – Helmholtz instability and other hydrodynamic instabilities appearing in the presence of backflow and secondary flows generate turbulent flow with three-dimensional vortical structures of different scales evolving. These structures fill the entire cross section of the vessel in the neighborhood of the attachment point. However, the flow becomes relaminarized further downstream. It can be seen from Figs. 2,a and 4,b that as the distance from the stenosis increases, small-scale structures quickly disappear from the spectrum of pulsatile flow, while the remaining vortical structures with lower intensity stretch along the flow.

Fig. 4,c shows the field of values for one of

the components of the Reynolds stress tensor computed from the numerically resolved components of pulsatile motion (marked with a prime; the overbar corresponds to averaging over time). It can be seen that the turbulent shear stress $R_{yz} = R_{yz} = -\overline{V'_y V'_z}$, playing a predominant role in extracting kinetic energy from the main flow, is significant in magnitude only at several calibers in the neighborhood of the attachment point, namely, at $2.5 < z/D < 6.5$. This is in agreement with the measurement data given in [18] for the generation rate of turbulent kinetic energy at the moment of the highest flow rate.

Determining the level of subgrid-scale kinematic viscosity predicted in our computations by the Germano – Lilly dynamic model gives the instantaneous field of the ratio of the subgrid-scale

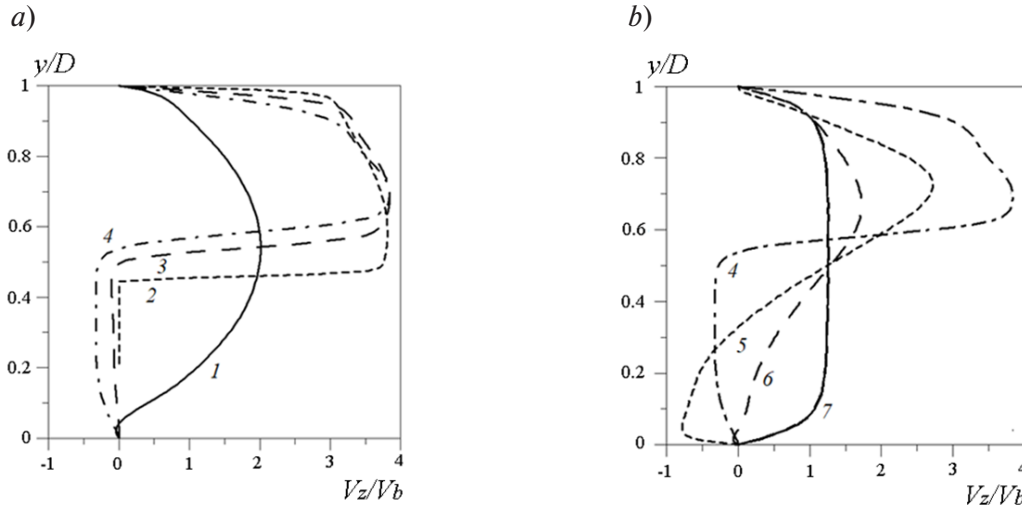


Fig. 5. Profiles of time-averaged longitudinal velocity in the symmetry plane, in different sections of the stenotic vessel; a): $z/D = -1$ (1), 0 (2), 1 (3), 2 (4); b): $z/D = 2$ (4), 4 (5), 5 (6), 10 (7)

vortex to molecular viscosity, shown in Fig. 4,*d*. We can conclude from these data that the contribution of subgrid-scale viscosity to dissipative effects in the given flow configuration, with $Re = 1803$, is again significant only in the region covering several calibers in the neighborhood of the attachment point; moreover, even the ratio ν_t/ν is less than unity even in this region.

Fig. 5 shows the profiles of the time-averaged longitudinal component of velocity in the symmetry plane, normalized to the value of the mean flow velocity V_b for several cross sections of the flow in the stenotic region (two graphs are given for clarity). As the flow in the first half of the stenotic region is strongly accelerated, a flow core that is nearly homogeneous evolves in the center of the stenosis, with relatively thin high-gradient shear layers forming at the boundaries of the core (see Fig. 5,*a*). The upper part of the flow core is already largely smeared two calibers away from the center of the stenosis ($z/D = 2$); this is mainly due to convective transfer of low-velocity fluid from the wall, responsible for the above-mentioned secondary flow in the form of a vortex pair (see Fig. 3,*a*). At the same time, the high-gradient layer at the lower boundary is very pronounced up to this section. The nature of the velocity profiles is drastically different in the sections $z/D = 4$ and 5, located further downstream (Fig. 6,*b*): their central part

is characterized by very moderate velocity gradients (see Fig. 5,*b*). The velocity profile related to the section $z/D = 10$ is a good illustration for the consequences of the mixing action of turbulent structures 'residing' in the neighborhood of the attachment point and some distance away from it: an almost axisymmetric central flow region develops as a result of this mixing (see also Fig. 3,*c*), with velocities close to mean flow rate, along with a boundary layer (gradually increasing in thickness with distance from the given section).

Longitudinal distributions of the time-averaged skin friction coefficient on the lower and upper walls of the vessel (in the symmetry plane) are shown in Fig. 6. The skin friction coefficient was calculated by the formula

$$C_f = \tau_w / (\rho V_b^2 / 2),$$

where τ_w is the modulus of the skin shear stress vector on the wall.

To identify the backflow zones, the values of the skin friction coefficient shown in the graphs were computed taking into account the sign of the longitudinal component τ_{wz} of the surface stress vector.

The skin friction coefficient is very high, exceeding the value of 0.00887 obtained for the flow before this region by almost 50 times. The

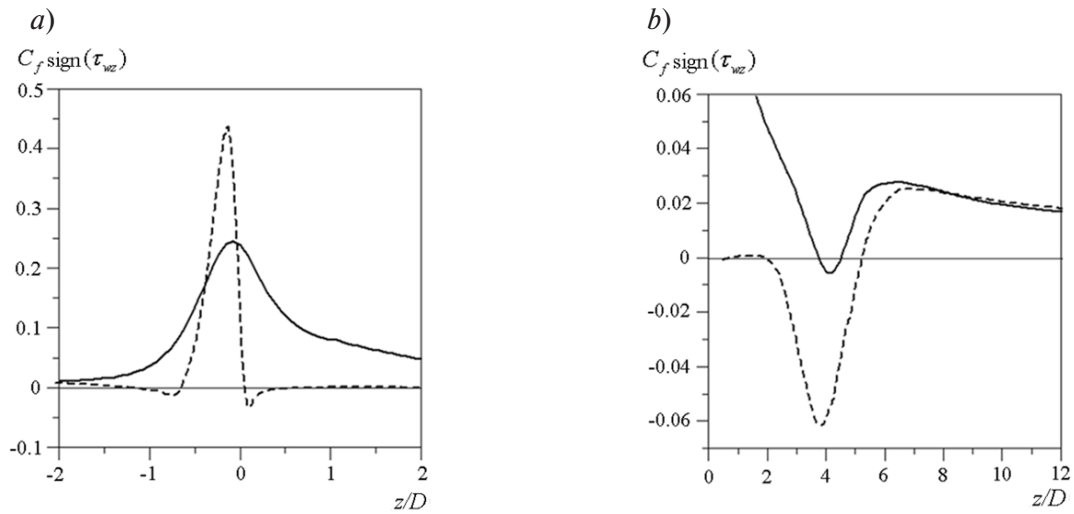


Fig. 6. Longitudinal changes in the time-averaged skin friction coefficient in the stenotic region (a) and behind it (b); data are given for the upper (solid line) and lower (dashes) walls

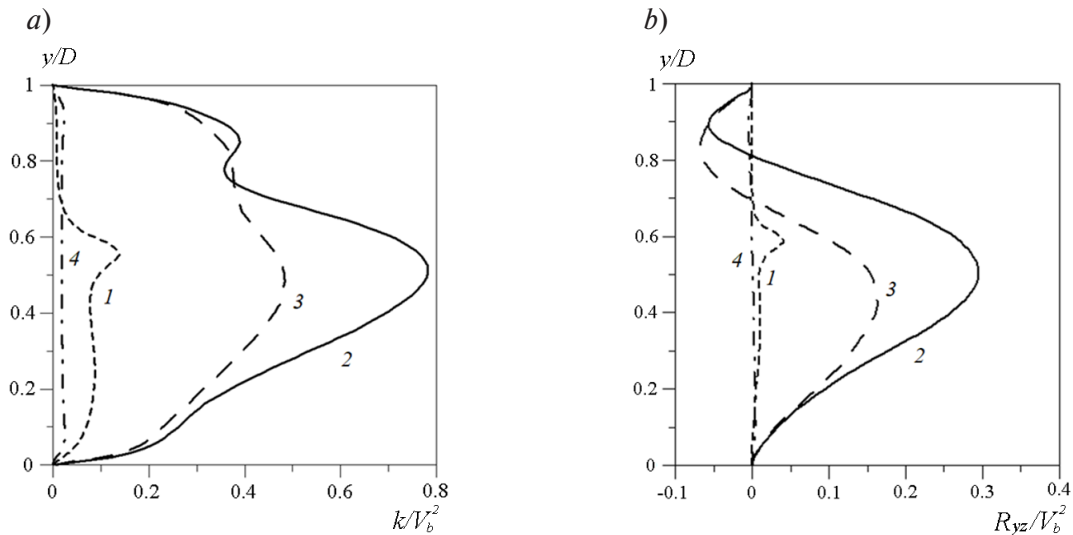


Fig. 7. Normalized profiles of turbulent kinetic energy of turbulence k (a) and Reynolds stress R_{yz} (b) in symmetry plane of the vessel for 4 sections located in the region behind the stenosis: $z/D = 2$ (1), 4 (2), 5 (3), 10 (4)

values of C_f with the largest magnitude in the backflow zone are 7 times higher than those before the stenotic region. According to the computations performed, the attachment point of the flow in the symmetry plane is located at a distance $L_r = 5.3D$ from the center of the stenosis. This value is fairly close to the experimental estimate $L_r \cong 4.5D$, which follows from the data given in [18]. These data were obtained for the position of the attachment point during pulsa-

tile flow, with the Reynolds numbers lying in the range 1000 – 1800.

Fig. 7 shows the profiles of two turbulence characteristics for four sections located behind the stenosis: turbulent kinetic energy k and the Reynolds stress R_{yz} ; both are computed (for the symmetry plane) from the numerically resolved components of pulsatile motion and are normalized to the square of the mean flow rate. Notably, the turbulent kinetic energy in the sections



$z/D = 4$ and 5 is close in order of magnitude to the specific kinetic energy of the flow entering the stenotic region. The positions of the peak values of Reynolds stress and turbulent kinetic energy practically coincide for each of these cross sections, while the ratios $R_{yz,peak}/k_{peak}$ are approximately 0.38 and 0.35 for the cross sections $z/D = 4$ and 5 respectively.

Furthermore, it seems interesting to compare the value of the numerically resolved R_{yz} and simulated (subgrid-scale) turbulent stresses for these cross sections. The latter can be assessed by multiplying the characteristic subgrid-scale viscosity by the maximum value of the velocity gradient, estimated from the profiles shown in Fig. 5. According to the data in Fig. 4, *d*, the molecular viscosity can be taken as the characteristic value of subgrid-scale viscosity. As a consequence, the estimated value of $\tau_{SGS}/V_b^2 \cong 0.005$, which is only $2 - 3\%$ of the level of numerically resolved turbulent stresses.

The quantities k and R_{yz} decrease rapidly with distance from the sections $z/D = 4$ and 5 . The profiles of both quantities have local maxima at $y/D \cong 0.6$ for the section $z/D = 2$: on the one hand, the average velocity profile here is characterized by large gradients (Fig. 5) and, on the other hand, the manifestation of hydrodynamic instabilities is fairly pronounced (see Fig. 4, *b*).

Conclusion

We have applied large eddy simulation with the Germano – Lilly dynamic model of subgrid-scale viscosity for numerical study of substantially three-dimensional flow developing at a Reynolds number $Re = 1803$ in a blood vessel with unilateral stenosis of 70% . The computations performed revealed the following peculiarities of the flow.

The averaged motion in the region behind stenosis is characterized by the presence of two zones with recirculation flow: an extensive one developing directly behind the stenosis, and a small one, located near the opposite wall of vessel.

As a jet with relatively high local velocities is generated in the stenotic region, rather intense secondary flow also develops, taking the form of a pair of vortices, similar to Dean vortices in curved tubes. In turn, the vortex pair evolving in the stenosis induces secondary backflow behind the stenosis, also leading to bifurcation of the jet.

The cross flow is almost completely degenerate at a distance of less than 10 calibers (diameters of the vessel) from the stenosis. A high-gradient mixing layer forms at the boundary between the jet and the backflow zone. The hydrodynamic instabilities inherent to this layer generate turbulence in the flow, with three-dimensional vortical structures of different scales forming, which fill the entire cross-section of vessel in the neighborhood of the attachment point, located at a distance of approximately five calibers from the center of stenosis.

Shear turbulent stresses only have substantial values in the zone with the size of about 4 calibers in the neighborhood of the attachment point. The flow is relaminarized downstream.

We believe that applying the LES method is bound to improve the quality of predicting the characteristics of turbulence developing during blood flow through stenotic regions of the vascular bed, and, as a consequence, provide more reliable data of interest for biomedicine.

This study was financially supported by the Russian Science Foundation, grant No. 19-73-30003.

REFERENCES

1. Gataulin Ya.A., Zaitsev D.K., Smirnov E.M., et al., Weakly swirling flow in a model of blood vessel with stenosis: Numerical and experimental study, St. Petersburg State Polytechnical University Journal. Physics and Mathematics. (4(230)) (2015) 36–47.
2. Gataulin Ya.A., Zaitsev D.K., Smirnov E.M.,
- Yukhnov A.D., Numerical study of spatial-temporal evolution of the secondary flow in the models of a common carotid artery, St. Petersburg State Polytechnical University Journal. Physics and Mathematics. (4(253)) (2016) 48–55.
3. Gataulin Ya.A., Zaitsev D.K., Smirnov E.M.,

Yukhnev A.D., Structure of unsteady flow in the spatially curved model of the common carotid artery with stenosis: A numerical study, *Russian Journal of Biomechanics*. 23 (1) (2019) 58–66.

4. **Ghalichi F., Farzan G., Deng X., et al.**, Low Reynolds number turbulence modeling of blood flow in arterial stenosis, *Biorheology*. 35 (4, 5) (1998) 281–294.

5. **Varghese S.S., Frankel S.H.**, Numerical modeling of pulsatile turbulent flow in stenotic vessels, *Journal of Biomechanical Engineering*. 125 (4) (2003) 445–460.

6. **Lee T.S., Liao W., Low H.T.**, Numerical study of physiological turbulent flows through series arterial stenosis, *International Journal for Numerical Methods in Fluids*. 46 (3) (2004) 315–344.

7. **Li M.X., Beech-Brandt J.J., John L.R., et al.**, Numerical analysis of pulsatile blood flow and vessel wall mechanics in different degrees of stenosis, *Journal of Biomechanics*. 40 (16) (2007) 3715–3724.

8. **Sherwin S.J., Blackburn H.M.**, Three-dimensional instabilities and transition of steady and pulsatile flows in an axisymmetric stenotic flows, *Journal of Fluid Mechanics*. 533 (25 June) (2005) 297–327.

9. **Blackburn H.M., Sherwin S.J.**, Instability modes and transition of pulsatile stenotic flow: pulse-period dependence, *Journal of Fluid Mechanics*. 573 (February) (2007) 57–88.

10. **Varghese S.S., Frankel S.H., Fischer P.F.**, Direct numerical simulation of stenotic flows. Part 1. Steady flow, *Journal of Fluid Mechanics*. 582 (10 July) (2007) 253–280.

11. **Varghese S.S., Frankel S.H., Fischer P.F.**,

Direct numerical simulation of stenotic flows. Part 2. Pulsatile flow, *Journal of Fluid Mechanics*. 582 (10 July) (2007) 281–318.

12. **Mittal R., Simmons S.P., Udaykumar H.S.**, Application of large-eddy simulation to the study of pulsatile flow in a modelled arterial stenosis, *Journal of Biomechanical Engineering*. 123 (4) (2001) 325–332.

13. **Mittal R., Simmons S.P., Najjar F.**, Numerical study of pulsatile flow in a constricted channel, *Journal of Fluid Mechanics*. 485 (25 May) (2003) 337–378.

14. **Molla M.M., Paul M.C., Roditi G.**, LES of additive and non-additive pulsatile flows in a model arterial stenosis, *Computer Methods in Biomechanics and Biomedical Engineering*. 13 (1) (2010) 105–120.

15. **Paul M.C., Molla M.M.**, Investigation of physiological pulsatile flow in a model arterial stenosis using large-eddy and direct numerical simulations // *Applied Mathematical Modelling*. 36 (9) (2012) 4393–4413.

16. **Germano M., Piomelli U., Moin P., Cabot W.H.**, A dynamic subgrid-scale eddy viscosity model, *Physics of Fluids*. 3 (7) (1991) 1760–1765.

17. **Lilly D.K.**, A proposed modification of the Germano subgrid-scale closure method, *Physics of Fluids*. 4 (3) (1992) 633–635.

18. **Choi W., Park J.H., Byeon H., Lee S.J.**, Flow characteristics around a deformable stenosis under pulsatile flow condition, *Physics of Fluids*. 30 (1) (2018) 011902.

19. **Jeong J., Hussain F.**, On the identification of a vortex, *Journal of Fluid Mechanics*. 285 (25 February) (1995) 69–94.

Received 29.12.2020, accepted 10.02.2021.

THE AUTHORS

GATAULIN Yakov A.

Peter the Great St. Petersburg Polytechnic University

29 Politechnicheskaya St., St. Petersburg, 195251, Russian Federation

yakov_gataulin@mail.ru

SMIRNOV Evgeny M.

Peter the Great St. Petersburg Polytechnic University

29 Politechnicheskaya St., St. Petersburg, 195251, Russian Federation

smirnov_em@spbstu.ru



СПИСОК ЛИТЕРАТУРЫ

1. Гатаулин Я.А., Зайцев Д.К., Смирнов Е.М., Федорова Е.А., Юхнев А.Д. Расчетно-экспериментальное исследование слабо закрученного течения в модели сосуда со стенозом // Научно-технические ведомости СПбГПУ. Физико-математические науки. 2015. № 4 (230). С. 36–47.
2. Гатаулин Я.А., Зайцев Д.К., Смирнов Е.М., Юхнев А.Д. Численное исследование пространственно-временной эволюции вторичного течения в модели общей сонной артерии // Научно-технические ведомости СПбГПУ. Физико-математические науки. 2016. № 4 (253). С. 48–55.
3. Гатаулин Я.А., Зайцев Д.К., Смирнов Е.М., Юхнев А.Д. Структура нестационарного течения в пространственно-извитой модели общей сонной артерии со стенозом: численное исследование // Российский журнал биомеханики. 2019. Т. 23. № 1. С. 69–78.
4. Ghalichi F., Farzan G., Deng X., Champlain A.D., Douville Y., King M., Guidoin R. Low Reynolds number turbulence modeling of blood flow in arterial stenoses // Biorheology. 1998. Vol. 35. No. 4, 5. Pp. 281–294.
5. Varghese S.S., Frankel S.H. Numerical modeling of pulsatile turbulent flow in stenotic vessels // Journal of Biomechanical Engineering. 2003. Vol. 125. No. 4. Pp. 445–460.
6. Lee T.S., Liao W., Low H.T. Numerical study of physiological turbulent flows through series arterial stenoses // International Journal for Numerical Methods in Fluids. 2004. Vol. 46. No. 3. Pp. 315–344.
7. Li M.X., Beech-Brandt J.J., John L.R., Hoskins P.R., Easson W.J. Numerical analysis of pulsatile blood flow and vessel wall mechanics in different degrees of stenoses // Journal of Biomechanics. 2007. Vol. 40. No. 16. Pp. 3715–3724.
8. Sherwin S.J., Blackburn H.M. Three-dimensional instabilities and transition of steady and pulsatile flows in an axisymmetric stenotic flows // Journal of Fluid Mechanics. 2005. Vol. 533. 25 June. Pp. 297–327.
9. Blackburn H.M., Sherwin S.J. Instability modes and transition of pulsatile stenotic flow: pulse-period dependence // Journal of Fluid Mechanics. 2007. Vol. 573. February. Pp. 57–88.
10. Varghese S.S., Frankel S.H., Fischer P.F. Direct numerical simulation of stenotic flows. Part 1. Steady flow // Journal of Fluid Mechanics. 2007. Vol. 582. 10 July. Pp. 253–280.
11. Varghese S.S., Frankel S.H., Fischer P.F. Direct numerical simulation of stenotic flows. Part 2. Pulsatile flow // Journal of Fluid Mechanics. 2007. Vol. 582. 10 July. Pp. 281–318.
12. Mittal R., Simmons S.P., Udaykumar H.S. Application of large-eddy simulation to the study of pulsatile flow in a modelled arteria stenosis // Journal of Biomechanical Engineering. 2001. Vol. 123. No. 4. Pp. 325–332.
13. Mittal R., Simmons S.P., Najjar F. Numerical study of pulsatile flow in a constricted channel // Journal of Fluid Mechanics. 2003. Vol. 485. 25 May. Pp. 337–378.
14. Molla M.M., Paul M.C., Roditi G. LES of additive and non-additive pulsatile flows in a model arterial stenosis // Computer Methods in Biomechanics and Biomedical Engineering. 2010. Vol. 13. No. 1. Pp. 105–120.
15. Paul M.C., Molla M.M. Investigation of physiological pulsatile flow in a model arterial stenosis using large-eddy and direct numerical simulations // Applied Mathematical Modelling. 2012. Vol. 36. No. 9. Pp. 4393–4413.
16. Germano M., Piomelli U., Moin P., Cabot W.H. A dynamic subgrid-scale eddy viscosity model // Physics of Fluids. 1991. Vol. 3. No. 7. Pp. 1760–1765.
17. Lilly D.K. A proposed modification of the Germano subgrid-scale closure method // Physics of Fluids. 1992. Vol. 4. No. 3. Pp. 633–635.
18. Choi W., Park J.H., Byeon H., Lee S.J. Flow characteristics around a deformable stenosis under pulsatile flow condition // Physics of Fluids. 2018. Vol. 30. No. 1. P. 011902.
19. Jeong J., Hussain F. On the identification of a vortex // Journal of Fluid Mechanics. 1995. Vol. 285. 25 February. Pp. 69–94.


СВЕДЕНИЯ ОБ АВТОРАХ

ГАТАУЛИН Яков Александрович — математик, заместитель директора Института прикладной математики и механики по научно-исследовательской работе студентов Санкт-Петербургского политехнического университета Петра Великого, Санкт-Петербург, Российская Федерация.

195251, Российская Федерация, г. Санкт-Петербург, Политехническая ул., 29
yakov_gataulin@mail.ru

СМИРНОВ Евгений Михайлович — доктор физико-математических наук, профессор Высшей школы прикладной математики и вычислительной физики Санкт-Петербургского политехнического университета Петра Великого, Санкт-Петербург, Российская Федерация.

195251, Российская Федерация, г. Санкт-Петербург, Политехническая ул., 29
smirnov_em@spbstu.ru



Atom physics and physics of clusters and nanostructures

DOI: 10.18721/JPM.14106

UDC 53.093, 53.096, 57.031, 57.033, 57.038

STRUCTURED BIOMOLECULAR FILMS FOR MICROELECTRONICS

M.A. Baranov, O.Yu. Tsybin, E.N. Velichko

Peter the Great St. Petersburg Polytechnic University,
St. Petersburg, Russian Federation

In order to develop the technology for dehydration of biomolecular films with specified parameters under an electrostatic field (EF), the structures of dehydrated films obtained from aqueous solutions of albumin molecules and deposited on solid glass substrates in the EF have been studied, dehydration conditions being varied. The resulting structures were examined under a microscope (with recording the micrographs) in the light passing through the films and in the one reflected from the substrates. An analysis of the micrographs made it possible to reveal characteristic inhomogeneities arising in the films and recognize their main types. The optimal regions of parameters in which the film production modes were predominantly realized were found. For the first time, a "bubble" model for interpretation of the spatially inhomogeneous structure of dehydrated biomolecular films was put forward. In the model, the processes conditioned by dissolved gases in the initial solutions were taken into account.

Keywords: self-organized structure, biomolecular film, microelectronics, biological molecule, electrochemistry, biosensor

Citation: Baranov M.A., Tsybin O.Yu., Velichko E.N., Structured biomolecular films for microelectronics, St. Petersburg Polytechnical State University Journal. Physics and Mathematics. 14 (1) (2021) 81–94. DOI: 10.18721/JPM.14106

This is an open access article under the CC BY-NC 4.0 license (<https://creativecommons.org/licenses/by-nc/4.0/>)

СТРУКТУРИРОВАННЫЕ БИОМОЛЕКУЛЯРНЫЕ ПЛЕНКИ ДЛЯ МИКРОЭЛЕКТРОНИКИ

М.А. Баранов, О.Ю. Цыбин, Е.Н. Величко

Санкт-Петербургский политехнический университет Петра Великого,
Санкт-Петербург, Российская Федерация

С целью разработки технологии дегидратации биомолекулярных пленок с заданными параметрами в электростатическом поле (ЭП), исследованы структуры дегидратированных пленок, полученных из водных растворов молекул альбумина и осажденных на твердых стеклянных подложках в ЭП; при этом варьировались условия дегидратации. Полученные структуры изучены под микроскопом (с регистрацией микрофотографий) в проходящем через пленки свете и отраженном от подложек. Анализ микрофотографий позволил выявить характерные неоднородности, возникающие в пленке, и выделить их основные типы. Определены оптимальные области параметров, в которых режимы получения пленок преимущественно реализуются. Впервые для интерпретации пространственно-неоднородной структуры дегидратированных биомолекулярных пленок предложена «пузырьковая» модель, в которой учитываются процессы, обусловленные растворенными газами в исходных растворах.

Ключевые слова: самоорганизованная структура, биомолекулярная пленка, микроэлектроника, биологическая молекула, электрохимия, биосенсор

Ссылка при цитировании: Баранов М.А., Цыбин О.Ю., Величко Е.Н. Структурированные биомолекулярные пленки для микроэлектроники // Научно-технические ведомости СПбГПУ. Физико-математические науки. 2021. Т. 14. № 1. С. 81–94. DOI: 10.18721/JPM.14106

Статья открытого доступа, распространяемая по лицензии CC BY-NC 4.0 (<https://creativecommons.org/licenses/by-nc/4.0/>)

Introduction

Electronic devices incorporating organic layers on solid surfaces have rapidly gained importance in science and technology [1 – 13]. Studies and applications of polymer films (including protein, organic single-layer and multilayer) on solid substrates are diverse, combining physics, chemistry, materials science, biology, medicine, electronics, nanoscale engineering, etc. Biomolecular films are in demand for the protein production technologies, human genome sequencing, protein research, and in many other areas, ranging from food technologies to environmental problems [14 – 21].

Processes leading to chaotic or ordered inhomogeneities have been uncovered through implementations of technologies for synthesizing films on substrates [1 – 8]. For example, spatial inhomogeneities can evolve on the film surface, forming patterns of different size, order, morphology and complexity. Such patterns contain thin straight and curved lines dividing sections of the structure, ordered geometric shapes of bulges and depressions near the surface, as well as protrusions, grooves and cracks of varying depths, in particular those with long-range spatial order [4, 5]. Spiral, radial, circular cracks, etc., were observed in thin films. Some forms can be repetitive and stable; they are likely associated with some peculiar physicochemical properties observed in the films and their potential applications. For example, medical studies have established that the structure of patterns on dried samples of human blood, saliva, and tears can be used to diagnose diseases [6 – 8].

Isothermal dehydration can be an efficient and flexible method for incorporating biomolecular films in micro- and nanoelectronics; however, the nature of the inhomogeneities emerging and possible ways to eliminate them have not been fully understood yet [22 – 24].

The goal of the study consists in developing

a technology for dehydration of biomolecular films with the given parameters at room and elevated temperatures under an applied electrostatic field, which are good candidates for microelectronics.

Isothermal dehydration method

The technology for removing water from a previously prepared solution (evaporation, dehydration, drying) is based on fundamental physical principles. Evaporation of atoms and molecules is described by the Clausius – Clapeyron reaction, essentially yielding a channel for loss of neutral particles:

$$n_a = bT^{1/2} \exp(-l_a/kT),$$

where n_a is the number of particles evaporating from a unit area per unit of time; l_a , J, is the work done during evaporation of a particle; T , K, is the temperature; k , J/K, is the Boltzmann constant; b , $K^{-1/2}$, is the thermal evaporation rate.

The mass transport of water from liquid surfaces is influenced by temperature, composition of the gas phase, activity of surface substances, bulk rheological properties and kinetics of vapor transport and heat flux through the surface, as well as the geometry of experimental conditions [25 – 27].

Film seems to have an optimal geometry for experiments developing the theory of evaporation from the surface, as it is characterized by small thickness in comparison with the other two dimensions. Isothermal processes in such objects make it possible to simplify their analysis. When self-organized structuring of the surface of a dehydrated biomolecular film on a substrate is caused by evaporation of the solvent at a constant temperature, stable patterns (including periodic ones) with widely varying morphologies appear on the film; the characteristic size of the patterns depends on the initial film thickness.



The heterogeneity of surface coatings arising through dehydration is caused by interfacial dynamic instability due to surface tension gradients, called the Marangoni instability [28, 29]. The main factors, namely the surface tension force and the viscous friction force, change along with varying temperature and amount of solvent.

As biological fluids have complex compositions, and there is a variety of physical, chemical, mechanical and other processes, the mechanisms behind the formation of different patterns induced by spontaneous evaporation are still poorly understood. The patterns observed are very intricate, so analytical formulas or a single model can hardly account for all the details of their formation [30]. The mechanism governing the growth of logarithmic spiral cracks is associated with a stress front propagating in a specific direction [31].

The pattern is affected by the structure of the substrate [32], temperature and humidity conditions, and the electric and magnetic fields applied to the objects during dehydration.

Ref. [33] reported on drying droplets of laponite gel (Laponite RD, a synthetic layered silicate) under an applied radial electric field. This created reproducible patterns that depended on the strength, direction and time of exposure to the electric field. As the electric field was applied, patterns on the film appeared after a certain amount of energy was dissipated.

Active electronic and physical properties of thin biomolecular films were discovered by impedance measurements and theoretical fluctuation studies [34, 35]. Such properties can be depend on the periodic structure of the films, which was revealed by optical measurements and methods of non-equilibrium thermodynamics [36, 37].

Correlations were found between the dynamics of protein film formation and the ionic component concentration in the initial solution, which made it possible to link the evolving processes with polarization of the sample's molecules (their electrical nature) [38, 39]. The effect of an electric field on protein (polypeptide) biomolecular films is a crucial problem for microelectronics; however, data on the subject are scarce in the literature.

It is known that biomolecular electrical conductivity is provided by different kinds of charge carriers, electrons and protons in molecules, playing a major role in the processes that govern the biological world; this type of conductivity can be implemented in electronic devices. Recent studies have substantiated the theoretical foundations of biomolecular electronics and ionics, proving that it can offer viable technologies [9, 10]. Remarkable strides have been made in producing biomolecular materials in the form of film metamaterials, which can maintain ion and electron currents over millimeter ranges in microelectronic devices. The structure of biomolecular metamaterials determines the electrical impedance over a wide frequency range, as well as the characteristics of electronic devices incorporating such materials.

We experimentally studied the spatial structure of dehydrated protein films obtained from an aqueous albumin solution on a dielectric substrate during isothermal drying at varying concentrations of the initial solutions, temperatures, and constant electric fields applied with the strengths ranging from zero to approximately 1 V/cm. We tested large molecules that can serve as good candidates for micro- and nanoelectronics during dehydration of solutions for the first time ever.

Method

Albumin protein (Human albumin) from Biotest Pharma GmHb (Dreieich, Germany) was used in the experiments. An aqueous solution with an initial concentration of 20% (200 g/L) was prepared from albumin. Working samples with a volume of 2 ml, each with concentrations of 2, 5, and 10%, were prepared from the primary solution for each experiment. The samples were placed in glass Petri dishes 20 mm in diameter.

Fig. 1 shows a schematic view of the experimental setup for studying the spatial structure of protein films dehydrated in a thermostat under an applied electric field. The setup contained a flat capacitor with fixed plate-shaped coatings (F. Pl.) made of stainless steel with the dimensions of 100×100 mm; the distance between the plates was 20 mm. Experimental solu-

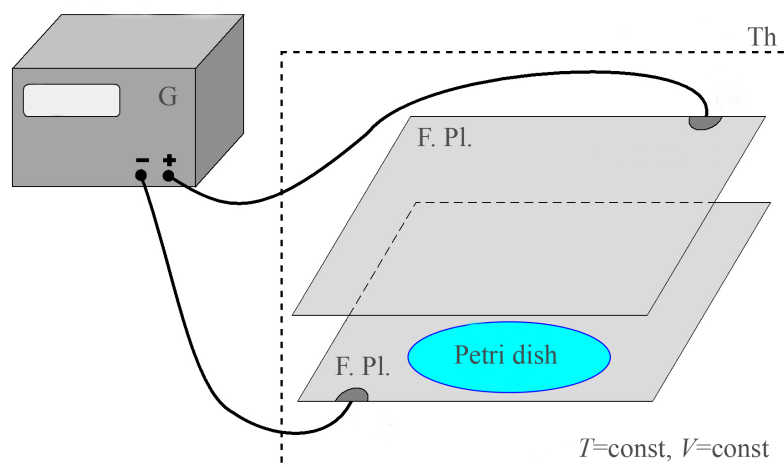


Fig. 1. Schematic representation of the experimental setup used for studies of the spatial structure of the protein film during its dehydration in an electric field: G – electric field generator; Th – thermostat; F. Pl. – fixed capacitor plates; Petri dish – Petri dish with aqueous solution

tion samples in a Petri dish were placed between the plates in an electric field (with a strength of 0; 0.5; 1.2; 5.0 V/cm) and put into a thermostat (Th) (at temperatures of 293, 298, 303, 308 and 313 K) for a dehydration period, which varied widely, from one hour or longer. A TC-1/80-SPU thermostat with forced air circulation was used to dry the films. The humidity in the thermostat chamber was $20 \pm 1\%$.

Images of the films were recorded in transmitted light using an Olympus CX 43 optical microscope and a USB camera. We used an Altami UHCCD05000KPA camera with a resolution of 1280×980 , a SONY ICX282AQ sensor, and a PlanC N microscope lens with a $40\times$ magnification, an aperture of 0.10, and 24-bit depth. The spectral range was 380 – 650 nm.

All micrographs in this paper were recorded on a common scale. The average thickness of the obtained samples was $200 \pm 10 \mu\text{m}$ with the measuring probe positioned on the sample in the center and at the edge of the cuvette.

Experimental results

Fig. 2 shows images of spatio-temporal structures in albumin protein films obtained at different strengths of the applied uniform electric

field. Spatially periodic images were observed, containing thin dark straight lines delimiting individual regions, as well as transparent disks with circular or spiral boundaries.

After albumin films were dried, the typical sizes and densities of the disks and spirals changed with varying external conditions. The height h of disks and spirals was about $100 \mu\text{m}$, corresponding to the film thickness H from $h \ll H$ to $h \approx H$. As the surface was quasi-periodically filled with such regions, the film acquired spatial ordering, exhibiting pronounced properties of a metamaterial. The main structural elements observed in Fig. 2 and below are represented by two types of patterns:

- segments dividing straight and curved lines;
- a network of disk granules.

All images in Fig. 2 have the same scale; a scale bar ($300 \mu\text{m}$) is given in the first image. The dividing segments are likely due to are caused by folds and higher density regions in the structure of the film obtained. Compact small-sized disk granules, transparent or bounded by circular and spiral dark walls are observed in the regions between straight lines (see Fig. 2). The spiral structures around the disks are similar to those described in the literature [40, 41]. A similar study

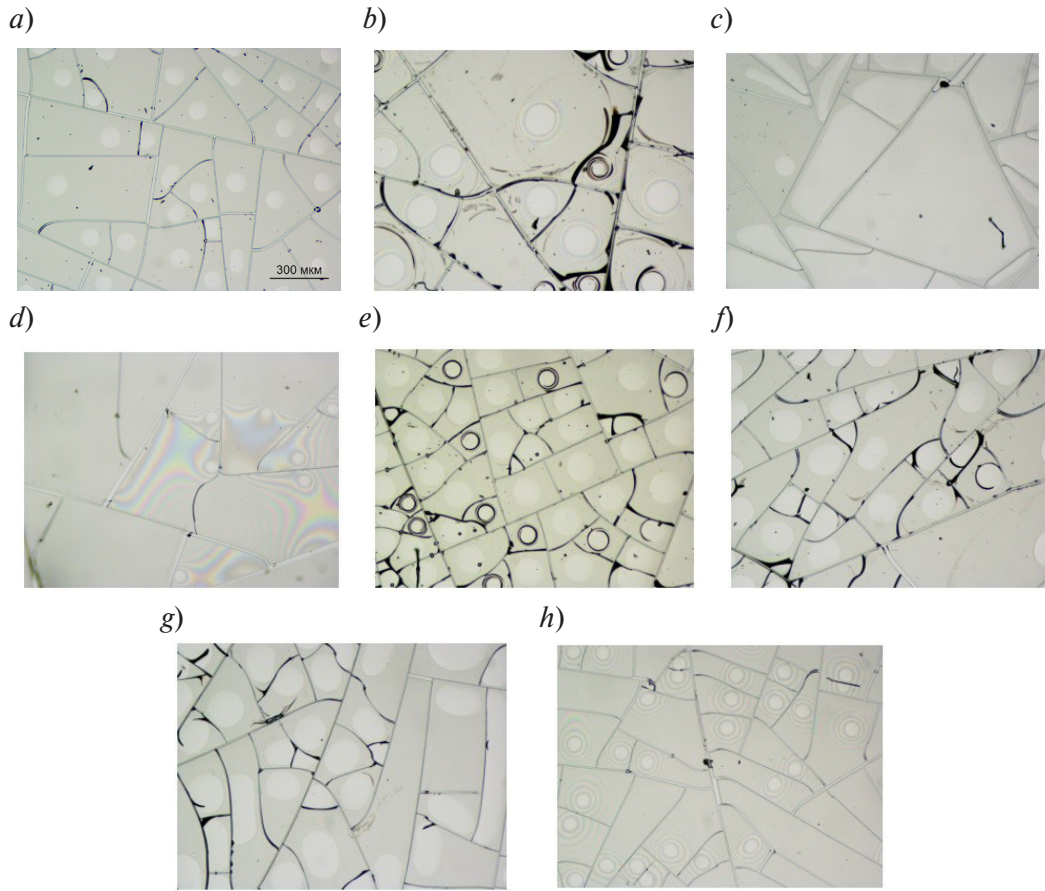


Fig. 2. Micrographs of protein films obtained at different albumin solution concentrations (2% (*a – d*) and 5% (*e – h*)) and electric field strengths, V/cm: 0.5 (*a, e*), 1, 0 (*b, f*), 2.0 (*c, g*), 5.0 (*d, h*); dehydration temperature $T = 310$ K

[41] obtained Newton's interference rings during sample drying. The authors attribute this to delamination of the film with an air gap growing between the sample and the glass substrate. Similar structures were also formed in our experiments. The same as in [41], they can be associated with diffraction of light by air bubbles and subsequent interference.

Spiral formation was linked to thermomechanical stresses, growth dynamics, and osmotic pressure in [40] and studies. To analyze the growth dynamics, we recorded the results of isothermal dehydration of protein films at different times, monitoring the film cracking process. Fig. 3 shows photographs (with a scale bar) of the inhomogeneities formed with a time step of 1 s. The finer details coincide in all images, which means that the processes are slow and fast changes are not observed.

Thermomechanical stresses and adhesion to the substrate depended on the mass of residual water, which was determined by weighing. The resulting dependence of the water mass on the protein concentration in the initial solution is shown in Fig. 4.

The dependence (Fig. 4) decreases smoothly as the initial concentration of albumin is increased to 15% (wt.%). The film was strongly bonded to the substrate in these conditions. The film became unstable with poor adhesion to the substrate at an initial albumin concentration of about 20% or higher. Comparing our results with the numerical data given in [42], we can analyze the dependence of free energy for dry film on the mass of residual water, as well as stability and adhesion of the films. However, such analysis is not given here as it would be beyond the scope of this study.

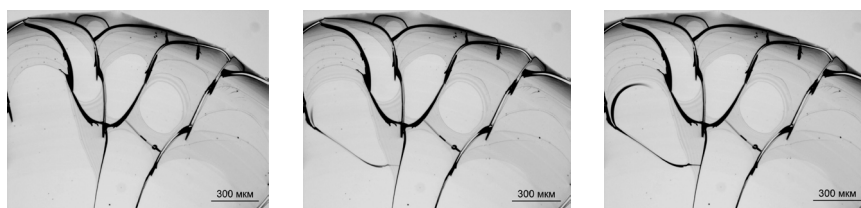


Fig. 3. Images of film inhomogeneities at different time moments with a step of 0.25 s. The first image corresponds to 10 s after the object removal from the thermostat

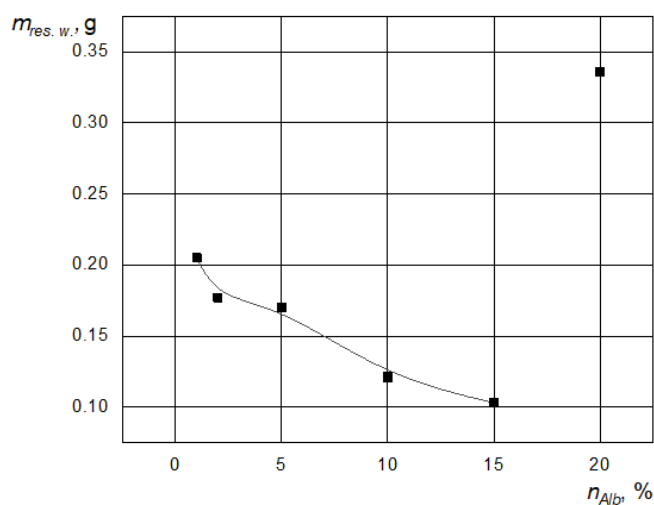


Fig. 4. Dependence of residual water mass in dehydrated albumin films on albumin concentration in the initial solution

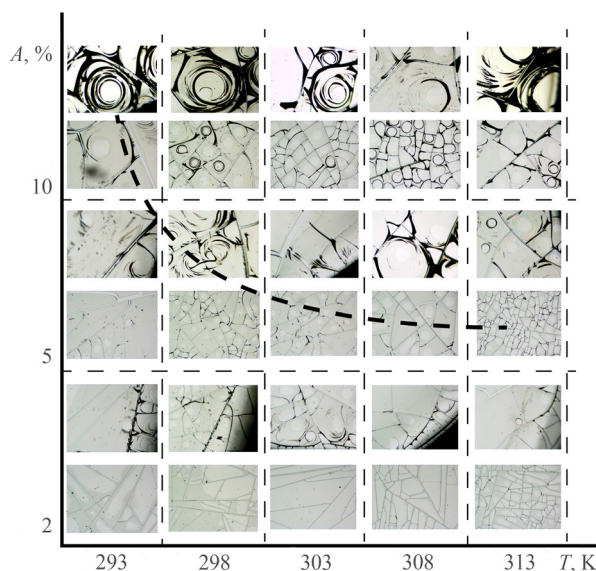


Fig. 5. Images of spatial structures in albumin protein films obtained at different initial concentrations of albumin protein solution (determined by the mass of components and plotted along the ordinate) and dehydration temperatures. The dotted curve shows the approximate border of the regionb with increased surface density of disk structures (the region lies above the curve)

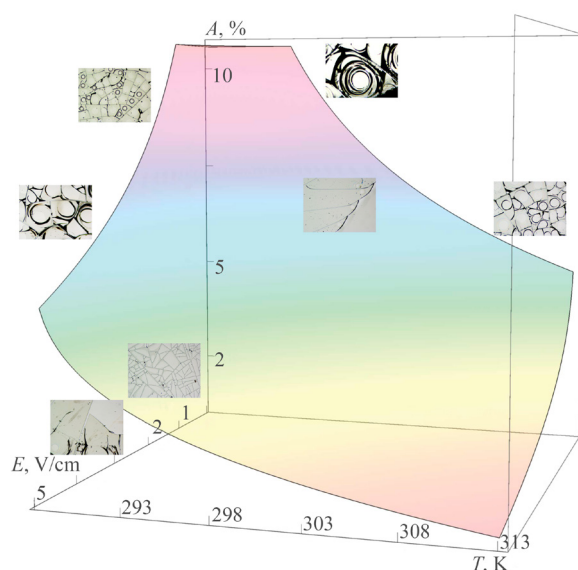


Fig. 6. Curved surface (obtained experimentally) separating the regions of increased and decreased concentrations of helical structures in dehydrated films of albumin protein as a function of initial solution concentration, dehydration temperature, and strength of the applied electric field

Fig. 5 shows the images of spatial structure for albumin protein films at different values dehydration temperatures and initial concentrations of albumin protein in the working sample.

Changes in temperature and concentration of albumin protein in the sample during dehydration had a joint effect on the disk granule structures evolving. Microscopic granules changed from transparent disks to those with circular or spiral boundaries under some conditions. The increase in the surface density and the total area of the spiral forms became more pronounced with higher concentrations of the initial solution in the working sample. More stable films and smoother lines dividing the surface regions were produced with higher dehydration temperatures. The dashed curve in Fig. 5 separates the region with increased surface density of disk structures, including circular and spiral forms (the latter lie mainly above the curve).

Fig. 6 shows an experimentally obtained curved surface separating regions with increased and decreased concentrations of disk (including circular and spiral) structures in dehydrated albumin films. This surface is given as a function of three parameters: the initial concentration of the solution, the dehydration temperature, and the

strength of the applied external electric field. The spiral structures generally did not appear in the region lying below this surface. The quality of the films was assessed in this region by the observed division into regions with rectilinear or curved boundaries.

Increased concentrations of transparent disk granules, circular and spiral structures were observed in the films at sufficiently high initial concentrations of the solution, dehydration temperatures, and external electric field strengths. These results provide an insight into the nature of the physical processes occurring at the stage of film dehydration, making it possible to formulate the models explaining their evolution.

Discussion

The data given in Fig. 6 can serve as a basis for developing model representations of the physical processes occurring. We believe that the model propose should link the formation of spherical cavities (bubbles) with the reduced density of particles in solution films at the dehydration stage. It is likely that small volumes of air released from the solution act as such particles. Indeed, the phenomenon of bubble formation can be explained by taking into account the presence

of dissolved air in the initial working sample at atmospheric pressure. Outward signs indicate that this is similar to internal vaporization during liquid heating. However, quantitative analysis suggests more complex dependences on the parameters of the processes, which have not been sufficiently studied.

As water molecules evaporate, the boundaries of the film approach each other and the dissolved air is compressed, which leads to formation of gas bubbles. The bubbles appear as transparent disks in micrographs of the films (obtained in transmitted light). Due to high values of viscosity forces of the solution and surface tension, migration of bubbles is slow, and some of them remain bounded in the dehydrated film. As air escapes to the film surface, the protein mass may be stretched at the boundary of the channel in which the air bubble moves, with such stretching leading to a compacted a circular state.

The simple model we propose can qualitatively characterize the processes of formation of the observed structures by taking into account the presence of dissolved air in the film but requires a more complete quantitative description. In our opinion, this model is more adequate than those suggested earlier. It is proposed for the first time. A uniform bubble size distribution speaks in favor of our model. In addition, the model takes into account the physical processes of dissolution (absorption) and release of gases in liquids. The average bubble diameter is much smaller (by an order of magnitude or more) than the film thickness. Exfoliation of film sections from the substrate cannot be uniform in surface and shape, and, moreover, cannot be reproduced for different substrates in different measurement modes. Considering the processes associated with dissolved air turns out to be sufficient to interpret the results obtained, making it possible to ignore secondary physical effects.

Escape of air bubbles to the surface of the film can explain not only the disk shape of the patterns formed but also the spiral shapes evolving, which complements or even replaces the traditional thermomechanical model [43].

A spatially inhomogeneous film can form in an electric field under the action of nonstationary

temperature and vapor-gas mechanical stresses, as well as external electrostatic pressure under lateral and spatial charge redistribution.

The measurement results (Fig. 6) indicate that the external electrostatic field has a pronounced effect. Indeed, the pressure of the electric field on the surface due to polarization of protein and water molecules is proportional to the square of the electric field strength E :

$$\frac{F}{S} = \varepsilon \varepsilon_0 \sigma E^2,$$

where F , N, is the local value of the force acting on the region S (m^2); E , V/m, is the strength of the electrostatic field; ε is the relative dielectric constant of the film substance in the corresponding phase state; ε_0 , F/m, is the dielectric constant ($\varepsilon_0 = 8.85 \cdot 10^{-12}$ F/m); σ , S/m, is the specific electrical conductivity.

The component of the electric field E normal to the film surface can induce a lateral charge redistribution in the volume of the liquid phase due to the appearance of a concentration gradient of ions and the potential they generate. The dielectric constant ε_0 produces a nonuniform disjoining pressure. In addition to thermomechanical effects, this pressure can increase the film deformation, leading to the formation of lines with higher density separating individual regions of the surface. Notably, however, the general effect of the electrostatic field is much more complex.

The polarizing electric field in an aqueous solution is proportional to the concentration of protein impurity ions, and the mobility of impurity ions is proportional to the process temperature. An increase in the impurity concentration and temperature lead to an increase in the ion current density and, accordingly, in the lateral and spatial charge redistribution. Lateral and spatial charge redistribution includes electrophoretic migration in the volume at the liquid phase stage, as well as induced surface charges at the transition stage to the solid phase.

Conclusion

We have considered the structure of dehy-



drated films obtained from aqueous solution of albumin molecules on a solid glass surface at an elevated temperature and under an applied external electrostatic field. Solutions of large molecules that appear to be suitable candidates for microelectronic technologies were tested for dehydration for the first time ever. The initial concentration of molecular solution, temperature conditions, and the strength of the electrostatic field applied were varied during dehydration. The method for studying the obtained films consisted in recording micrographs in the light transmitted through the film and reflected from the substrate. Analysis of the images revealed characteristic inhomogeneities of two main types in the films:

- regions separated by thin lines,
- microscopic disk-shaped granules (including those with pronounced circular or spiral boundaries), distributed over the surface.

As a result, we have found the parameter ranges for the conditions in which either the first or the second type of inhomogeneities evolves.

We have proposed a novel 'bubble' model for interpreting the spatially inhomogeneous structure of dehydrated biomolecular films accounting for the processes produced by dissolved gases in the initial solution.

The structure of the protein films synthesized apparently correlates with temperature conditions, the concentration of biomolecules in the initial solution and the applied electric field, which are characteristic for the studied dehydration processes. This provides insights into the thermomechanical and electrical nature of some of these processes.

The effects of dissolved gases and the bubble mechanism should also be taken into account in descriptions of the processes occurring in films prepared by other methods, for example, Langmuir – Blodgett or layer-by-layer deposition.

The proposed dehydration mechanism is at the stage of supercomputer and experimental verification. The data can be used to develop technologies for producing high-quality films with specific parameters, in particular, for microelectronics applications.

Acknowledgments

We would like to express our gratitude to Alexey Skvortsov (Doctor of Physical and Mathematical Sciences, Professor of Peter the Great St. Petersburg Polytechnic University) for valuable discussions regarding the subject of this study.

The study was carried out within the framework of State Task for Basic Research (code 0784-2020-0025).

REFERENCES

1. **Biswas A., Bayer I.S., Biris A.S., et al.**, Advances in top-down and bottom-up surface nanofabrication: Techniques, applications & future prospects, *Advances in Colloid and Interface Science*. 170 (1-2) (2012) 2–27.
2. **Krishnan V., Sakakibara K., Mori T., et al.**, Manipulation of thin film assemblies: recent progress and novel concepts, *Current Opinion in Colloid & Interface Science*. 16 (6) (2011) 459–469.
3. **Moores B., Hane F., Eng L., Leonenko Z.**, Kelvin probe force microscopy in application to biomolecular films: frequency modulation, amplitude modulation, and lift mode, *Ultramicroscopy*. 110 (6) (2010) 708–711.
4. **Golbraikh E., Rapis E.G., Moiseev S.S.**, On the crack pattern formation in a freely drying protein film, *Technical Physics*. 48 (10) (2003) 1333–1337.
5. **Yakchno T.A.**, Sodium chloride crystallization from drying drops of albumin-salt solutions with different albumin concentrations, *Technical Physics*. 60 (11) (2015) 1601–1608.
6. **Shatokhina S.N., Shabalin V.N.**, Morfologiya biologicheskikh zhidkostey – novoye napravleniye v klinicheskoy meditsine [Morphology of biological fluids is a new trend in clinical medicine], *Almanac of Clinical Medicine*. (6) (2003) 404–422 (in Russian).
7. **Shatokhina S.N., Zakharova N.M., Dedova M.G., et al.**, Morphological marker of tumor progression in laryngeal cancer, *Problems in Oncology*. 59 (2) (2013) 66–70 (in Russian).

8. **Shatokhina S.N., Aleksandrin V.V., Shatokhina I.S., et al.**, A marker of cerebral ischemia in solid state structures of blood serum // *Bulletin of Experimental Biology and Medicine*. 164 (3) (2018) 366–370.
9. **Velichko E.N., Tsybin O.Yu.**, *Biomolekulyarnaya elektronika. Vvedeniye [Biomolecular electronics. Introduction]*, Polytechnic University Publishing, St. Petersburg, 2011 (in Russian).
10. **Amdursky N., Glowacki E. D., Meredith P.**, Macroscale biomolecular electronics and ionics, *Advanced Materials*. 31 (3) (2019) 1802221.
11. **Iost R.M., Crespilho F.N.**, Layer-by-layer self-assembly and electrochemistry: applications in biosensing and bioelectronics, *Biosensors and Bioelectronics*. 31 (1) (2012) 1–10.
12. **Siqueira Jr. J.R., Caseli L., Frank N., et al.**, Immobilization of biomolecules on nanostructured films for biosensing, *Biosensors and Bioelectronics*. 25 (6) (2010) 1254–1263.
13. **Iost R.M., Madurro J.M., Brito-Madurro A.G., et al.**, Strategies of nano-manipulation for application in electrochemical biosensors, *International Journal of Electrochemical Science*. 6 (7) (2011) 2965–2997.
14. **Szott L.M., Horbett T.A.**, Protein interactions with surfaces: Computational approaches and repellency, *Current Opinion in Chemical Biology*. 15 (5) (2011) 683–689.
15. **Yoneda J.S., Miles A.J., Araujo A.P.U., Wallace B.A.**, Differential dehydration effects on globular proteins and intrinsically disordered proteins during film formation, *Protein Science*. 26 (4) (2017) 718–726.
16. **Xin S., Li X., Wang Q., et al.**, Novel layer-by-layer structured nanofibrous mats coated by protein films for dermal regeneration, *Journal of Biomedical Nanotechnology*. 10 (5) (2014) 803–810.
17. **Haynie D.T., Zhang L., Rudra J.S., et al.**, Polypeptide multilayer films, *Biomacromolecules*. 6 (6) (2005) 2895–2913.
18. **Zhang X., Crivoi A., Duan F.**, Three-dimensional patterns from the thin film drying of amino acid solutions, *Scientific Reports*. 5 (2015) 10926.
19. **Ferreira C.O., Carla A. Nunes C.A., et al.**, Characterization of chitosan-whey protein films at acid pH, *Food Research International*. 42 (7) (2009) 807–813.
20. **Golbraikh E., Rapis E.G., Moiseev S.S.**, On the crack pattern formation in a freely drying protein film, *Technical Physics*. 48 (10) (2003) 1333–1337.
21. **Iost R.M., Silva W.C., Madurro J.M., et al.**, Electrochemical nano (bio) sensors: advances, diagnosis and monitoring of diseases, *Frontiers in Bioscience*. 3E (2) (2011) 663–689.
22. **Kovalchuk M.V., Boikova S., Dyakova Yu.A., et al.**, Structural characteristics of lysozyme Langmuir layers grown on a liquid surface from an oligomeric mixture formed during the early stages of lysozyme crystallization, *Thin Solid Films*. 677 (1 May) (2019) 13–21.
23. **Boikova A.S., D'yakova Yu.A., Il'ina K.B., et al.**, Fabrication of multilayer films on the basis of lysozyme protein and precipitant (iodide and potassium) ions on a silicon substrate by the modified Langmuir–Schaefer method, *Crystallography Reports*. 63 (5) (2018) 719–723.
24. **Kovalchuk M.V., Boikova A.S., D'yakova Yu.A., et al.**, Modification of Langmuir–Schaefer method for fabrication of ordered protein films, *Crystallography Reports*. 62 (4) (2017) 632–638.
25. **Bellich B., Elisei E., Heyd R., et al.**, Isothermal dehydration of thin films, *Journal of Thermal Analysis and Calorimetry*. 121 (3) (2015) 963–973.
26. **Guvendiren M., Yang S., Burdick J.A.**, Swelling-induced surface patterns in hydrogels with gradient crosslinking density, *Advanced Functional Materials*. 19 (19) (2009) 3038–3045.
27. **Heyd R., Rampino A., Bellich B., et al.**, Isothermal dehydration of thin films of water and sugar solutions, *The Journal of Chemical Physics*. 140 (12) (2014) 124701.
28. **Zhu J.L., Shi W.Y., Feng L., Bénard** – Marangoni instability in sessile droplet evaporating at constant contact angle mode on heated substrate, *International Journal of Heat and Mass Transfer*. 134 (May) (2019) 784–795.
29. **Li P., Chao Y.**, Marangoni instability of self-wetting films modulated by chemical reactions flowing down a vertical fibre, *Chemical Engineering Science*. 227 (14 December) (2020) 115936.
30. **Gao M.N., Huang X.F., Zhao Y.P.**, Formation of wavy-ring crack in drying droplet of protein solutions, *Science China Technological Sciences*.



61 (7) (2018) 949–958.

31. **Néda Z., Leung K.-t., Józsa L., Ravasz M.**, Spiral cracks in drying precipitates, *Physical Review Letters*. 88 (9) (2002) 095502.

32. **Liu T., Luo H., Ma J., et al.**, Surface roughness induced cracks of the deposition film from drying colloidal suspension, *The European Physical Journal*, E. 39 (2) (2016) 24.

33. **Khatun T., Dutta T., Tarafdar S.**, Crack formation under an electric field in droplets of laponite gel: Memory effect and scaling relations, *Langmuir*. 29 (50) (2013) 15535–15542.

34. **Baranov M., Rodion S., Alekseenko A.**, Optical and electrical properties of protein films, *Proceedings of the 2018 IEEE International Conference on Electrical Engineering and Photonics (EExPolytech)*, Saint Petersburg, Russia, 22–23 October 2018, IEEE Catalog Number: CF-P18R49-POD (2018) 186–188.

35. **Bibi F., Villain M., Guillaume C., et al.**, A review: origins of the dielectric properties of proteins and potential development as biosensors, *Sensors*. 16 (8) (2016) 1232.

36. **Baranov M.A., Alekseenko A.P., Velichko E.N.**, Study of electric properties of self-assembled films of albumin during their dehydration, *Journal of Physics: Conference Series*, IOP Publishing. 1124 (3) (2018) 031013.

37. **Galus S., Lenart A.**, Optical, mechanical, and moisture sorption properties of whey protein edible films, *Journal of Food Process Engineering*. 42 (6) (2019) e13245.

38. **Velichko E., Zezina T., Baranov M., et al.**, Dynamics of polypeptide cluster dipole moment for nano communication applications, In the book:

“Internet of Things, Smart Spaces, and Next Generation Networks and Systems”, *Proceedings of the 18th International Conference, NEW2AN, and 11th Conference, ruSMART 2018*, St. Petersburg, Russia, August 27–29, 2018, Edited by O. Galinina, S. Andreev, S. Balandin, E. Koucheryavy, Springer, Cham, Switzerland (2018) 675–682.

39. **Velichko E., Zezina T., Cheremiskina A., Tsybin O.**, Nano communication device with embedded molecular films: effect of electromagnetic field and dipole moment dynamics, In the book: “Internet of Things, Smart Spaces, and Next Generation Networks and Systems”, *Proceedings of the 15th International Conference, NEW2AN 2015, and 8th Conference, ruSMART 2015*, St. Petersburg, Russia, August 26–28, 2015, Edited by S. Balandin, S. Andreev, E. Koucheryavy, Springer, Cham, Switzerland (2015) 765–771.

40. **Gao M.N., Huang X.F., Zhao Y.P.**, Formation of wavy-ring crack in drying droplet of protein solutions, *Science China Technological Sciences*. 61 (7) (2018) 949–958.

41. **Lazarus V., Pauchard L.**, From craquelures to spiral crack patterns: influence of layer thickness on the crack patterns induced by desiccation, *Soft Matter*. 7 (6) (2011) 2552–2559.

42. **Velichko E.N., Baranov M.A., Mostepanenko V.M.**, Change of sign in the Casimir interaction of peptide films deposited on a dielectric substrate, *Modern Physics Letters, A*. 35 (3) (2020) 2040020.

43. **Fortier D., Shur Yu., Jorgenson T., et al.**, Self-organization of ice-wedge systems during their formation and degradation, In the book: *Abstracts of the AGU Fall Meeting 2019, 9–13 December 2019, San Francisco, USA*. Abstract C13E-1359.

Received 02.11.2020, accepted 25.01.2021.

THE AUTHORS

BARANOV Maksim A.

Peter the Great St. Petersburg Polytechnic University

29 Politechnicheskaya St., St. Petersburg, 195251, Russian Federation

baranovma1993@gmail.com

TSYBIN Oleg Yu.

Peter the Great St. Petersburg Polytechnic University

29 Politechnicheskaya St., St. Petersburg, 195251, Russian Federation

oleg.tsybin@gmail.com

VELICHKO Elena N.

Peter the Great St. Petersburg Polytechnic University

29 Politechnicheskaya St., St. Petersburg, 195251, Russian Federation

velichko-spbstu@yandex.ru

СПИСОК ЛИТЕРАТУРЫ

1. Biswas A., Bayer I.S., Biris A.S., et al. Advances in top-down and bottom-up surface nanofabrication: techniques, applications & future prospects // *Advances in Colloid and Interface Science*. 2012. Vol. 170. No. 1-2. Pp. 2–27.
2. Krishnan V., Sakakibara K., Mori T., Hill J.P., Ariga K. Manipulation of thin film assemblies: recent progress and novel concepts // *Current Opinion in Colloid & Interface Science*. 2011. Vol. 16. No. 6. Pp. 459–469.
3. Moores B., Hane F., Eng L., Leonenko Z. Kelvin probe force microscopy in application to biomolecular films: frequency modulation, amplitude modulation, and lift mode // *Ultramicroscopy*. 2010. Vol. 110. No. 6. Pp. 708–711.
4. Гольбрайх Е., Рапис Е.Г., Моисеев С.С. О формировании узора трещины в свободно высыхающей пленке водного раствора белка // *Журнал технической физики*. 2003. Т. 73. № 10. С. 116–121.
5. Яхно Т.А. Кристаллизация хлорида натрия из высыхающих капель белково-солевых растворов с разным содержанием белка // *Журнал технической физики*. 2015. Т. 85. № 11. С. 30–37.
6. Шатохина С.Н., Шабалин В.Н. Морфология биологических жидкостей — новое направление в клинической медицине // *Альманах клинической медицины*. 2003. № 6. С. 404–422.
7. Шатохина С.Н., Захарова Н.М., Дедова М.Г., Самбулов В.И., Шебалин В.Н. Морфологический маркер прогрессии новообразования при раке гортани // *Вопросы онкологии*. 2013. Т. 59. № 2. С. 66–70.
8. Шатохина С.Н., Александрин В.В., Шатохина И.С., Кубатиев А.А., Шабалин В.Н. Маркер ишемии головного мозга в твердофазных структурах сыворотки крови // *Бюллетень экспериментальной биологии и медицины*. 2017. Т. 164. № 9. С. 351–355.
9. Величко Е.Н., Цыбин О.Ю. Биомолекулярная электроника. Введение. СПб.: Изд-во Политехнического ун-та, 2011. 256 с.
10. Amdursky N., Glowacki E.D., Meredith P. Macroscale biomolecular electronics and ionics // *Advanced Materials*. 2019. Vol. 31. No. 3. P. 1802221.
11. Iost R.M., Crespihlo F.N. Layer-by-layer self-assembly and electrochemistry: applications in biosensing and bioelectronics // *Biosensors and Bioelectronics*. 2012. Vol. 31. No. 1. Pp. 1–10.
12. Siqueira Jr. J.R., Caseli L., Frank N. Crespihlo F.N., Zucolotto V., Osvaldo N., Oliveira O.N. Immobilization of biomolecules on nanostructured films for biosensing // *Biosensors and Bioelectronics*. 2010. Vol. 25. No. 6. Pp. 1254–1263.
13. Iost R.M., Madurro J.M., Brito-Madurro A.G., Nantes I.L., Caseli L., Crespihlo F.N. Strategies of nano-manipulation for application in electrochemical biosensors // *International Journal of Electrochemical Science*. 2011. Vol. 6. No. 7. Pp. 2965–2997.
14. Szott L.M., Horbett T.A. Protein interactions with surfaces: Computational approaches and repellency // *Current Opinion in Chemical Biology*. 2011. Vol. 15. No. 5. Pp. 683–689.
15. Yoneda J.S., Miles A.J., Araujo A.P.U., Wallace B.A. Differential dehydration effects on globular proteins and intrinsically disordered proteins during film formation // *Protein Science*. 2017. Vol. 26. No. 4. Pp. 718–726.
16. Xin S., Li X., Wang Q., Huang R., Xu X., Lei Z., Deng H. Novel layer-by-layer structured nanofibrous mats coated by protein films for dermal regeneration // *Journal of Biomedical Nanotechnology*. 2014. Vol. 10. No. 5. Pp. 803–810.
17. Haynie D.T., Zhang L., Rudra J.S., Zhao W., Zhong Y., Palath N. Polypeptide multilayer films // *Biomacromolecules*. 2005. Vol. 6. No. 6. Pp. 2895–2913.



18. **Zhang X., Crivoi A., Duan F.** Three-dimensional patterns from the thin film drying of amino acid solutions // *Scientific Reports*. 2015. Vol. 5. P. 10926.
19. **Ferreira C.O., Carla A. Nunes C.A., Delgadillo I., Lopes-da-Silva J.A.** Characterization of chitosan-whey protein films at acid pH // *Food Research International*. 2009. Vol. 42. No. 7. Pp. 807–813.
20. **Гольбрайх Е., Рапис Е.Г., Моисеев Е.С.** О формировании узора трещины в свободно высыхающей пленке водного раствора белка // *Журнал технической физики*. 2003. Т. 73. № 10. С. 116–121.
21. **Iost R.M., Silva W.C., Madurro J.M., Brito-Madurro A.G., Ferreira L.S., Crespilho F.N.** Electrochemical nano (bio) sensors: advances, diagnosis and monitoring of diseases // *Frontiers in Bioscience*. 2011. Vol. 3E. No. 2. Pp. 663–689.
22. **Kovalchuk M.V., Boikova S., Dyakova Yu.A., et al.** Structural characteristics of lysozyme Langmuir layers grown on a liquid surface from an oligomeric mixture formed during the early stages of lysozyme crystallization // *Thin Solid Films*. 2019. Vol. 677. 1 May. Pp. 13–21.
23. **Бойкова А.С., Дьякова Ю.А., Ильина К.Б., Марченкова М.А., Серегин А.Ю., Просеков П.А., Волковский Ю.А., Писаревский Ю.В., Ковальчук М.В.** Получение многослойных пленок на основе белка лизоцима и ионов осадителя (йода и калия) на кремниевой подложке модифицированным методом Ленгмюра — Шеффера // *Кристаллография*. 2018. Т. 63. № 5. С. 703–707.
24. **Ковальчук М.В., Бойкова А.С., Дьякова Ю.А., Марченкова М.А., Ополченцев А.М., Писаревский Ю.В., Просеков П.А., Серегин А.Ю.** Модификация метода Ленгмюра — Шеффера для получения упорядоченных белковых пленок // *Кристаллография*. 2017. Т. 62. № 4. С. 650–656.
25. **Bellich B., Elisei E., Heyd R., Saboungi M.-L., Cesàro A.** Isothermal dehydration of thin films // *Journal of Thermal Analysis and Calorimetry*. 2015. Vol. 121. No. 3. Pp. 963–973.
26. **Guvendiren M., Yang S., Burdick J.A.** Swelling-induced surface patterns in hydrogels with gradient crosslinking density // *Advanced Functional Materials*. 2009. Vol. 19. No. 19. Pp. 3038–3045.
27. **Heyd R., Rampino A., Bellich B., Elisei E., Cesàro A., Saboungi M.-L.** Isothermal dehydration of thin films of water and sugar solutions // *The Journal of Chemical Physics*. 2014. Vol. 140. No. 12. P. 124701.
28. **Zhu J.L., Shi W.Y., Feng L.** Bénard–Marangoni instability in sessile droplet evaporating at constant contact angle mode on heated substrate // *International Journal of Heat and Mass Transfer*. 2019. Vol. 134. May. Pp. 784–795.
29. **Li P., Chao Y.** Marangoni instability of self-rewetting films modulated by chemical reactions flowing down a vertical fibre // *Chemical Engineering Science*. 2020. Vol. 227. 14 December. P. 115936.
30. **Gao M.N., Huang X.F., Zhao Y.P.** Formation of wavy-ring crack in drying droplet of protein solutions // *Science China Technological Sciences*. 2018. Vol. 61. No. 7. Pp. 949–958.
31. **Néda Z., Leung K.-t., Józsa L., Ravasz M.** Spiral cracks in drying precipitates // *Physical Review Letters*. 2002. Vol. 88. No. 9. P. 095502.
32. **Liu T., Luo H., Ma J., Xie W., Wang Y., Jing G.** Surface roughness induced cracks of the deposition film from drying colloidal suspension // *The European Physical Journal. E*. 2016. Vol. 39. No. 2. P. 24.
33. **Khatun T., Dutta T., Tarafdar S.** Crack formation under an electric field in droplets of laponite gel: Memory effect and scaling relations // *Langmuir*. 2013. Vol. 29. No. 50. Pp. 15535–15542.
34. **Baranov M., Rodion S., Alekseenko A.** Optical and electrical properties of protein films // *Proceedings of the 2018 IEEE International Conference on Electrical Engineering and Photonics (EExPolytech)*. Saint Petersburg, Russia, 22–23 October 2018. IEEE Catalog Number: CF-P18R49-POD, 2018. Pp. 186–188.
35. **Bibi F., Villain M., Guillaume C., Sorli B., Gontard N.** A review: origins of the dielectric properties of proteins and potential development as biosensors // *Sensors*. 2016. Vol. 16. No. 8. P. 1232.
36. **Baranov M.A., Alekseenko A.P., Velichko E.N.** Study of electric properties of self-assembled films of albumin during their dehydration // *Journal of Physics: Conference Series*. IOP Publishing,

2018. Vol. 1124. No. 3. P. 031013.

37. **Galus S., Lenart A.** Optical, mechanical, and moisture sorption properties of whey protein edible films // Journal of Food Process Engineering. 2019. Vol. 42. No. 6. P. e13245.

38. **Velichko E., Zezina T., Baranov M., Nepomnyashchaya E., Tsybin O.** Dynamics of polypeptide cluster dipole moment for nano communication applications // “Internet of Things, Smart Spaces, and Next Generation Networks and Systems”, Proceedings of the 18th International Conference, NEW2AN, and 11th Conference, ruSMART 2018, St. Petersburg, Russia, August 27–29, 2018. Edited by O. Galinina, S. Andreev, S. Balandin, E. Koucheryavy. Switzerland: Springer, Cham, 2018. Pp. 675–682.

39. **Velichko E., Zezina T., Cheremiskina A., Tsybin O.** Nano communication device with embedded molecular films: effect of electromagnetic field and dipole moment dynamics // “Internet of Things, Smart Spaces, and Next Generation Networks and Systems”, Proceedings of the 15th International Conference, NEW2AN 2015, and 8th Conference,

ruSMART 2015, St. Petersburg, Russia, August 26–28, 2015. Edited by S. Balandin, S. Andreev, E. Koucheryavy. Switzerland: Springer, Cham, 2015. Pp. 765–771.

40. **Gao M.N., Huang X.F., Zhao Y.P.** Formation of wavy-ring crack in drying droplet of protein solutions // Science China Technological Sciences. 2018. Vol. 61. No. 7. Pp. 949–958.

41. **Lazarus V., Pauchard L.** From craquelures to spiral crack patterns: influence of layer thickness on the crack patterns induced by desiccation // Soft Matter. 2011. Vol. 7. No. 6. Pp. 2552–2559.

42. **Velichko E.N., Baranov M.A., Mostepanenko V.M.** Change of sign in the Casimir interaction of peptide films deposited on a dielectric substrate // Modern Physics Letters A. 2020. Vol. 35. No. 3. P. 2040020.

43. **Fortier D., Shur Yu., Jorgenson T., Kanevskiy M.Z., Jones B.M., Jones K.W.** Self-organization of ice-wedge systems during their formation and degradation // Abstracts of the AGU Fall Meeting 2019. 9–13 December 2019, San Francisco, USA. Abstract C13E-1359.

Статья поступила в редакцию 02.11.2020, принята к публикации 25.01.2021.

СВЕДЕНИЯ ОБ АВТОРАХ

БАРАНОВ Максим Александрович — ассистент Высшей школы прикладной физики и космических технологий Санкт-Петербургского политехнического университета Петра Великого, Санкт-Петербург, Российская Федерация.

195251, Российская Федерация, г. Санкт-Петербург, Политехническая ул., 29
baranovma1993@gmail.com

ЦЫБИН Олег Юрьевич — доктор физико-математических наук, профессор Высшей инженерно-физической школы Санкт-Петербургского политехнического университета Петра Великого, Санкт-Петербург, Российская Федерация.

195251, Российская Федерация, г. Санкт-Петербург, Политехническая ул., 29
oleg.tsybin@gmail.com

ВЕЛИЧКО Елена Николаевна — кандидат технических наук, доцент, директор Высшей школы прикладной физики и космических технологий Санкт-Петербургского политехнического университета Петра Великого, Санкт-Петербург, Российская Федерация.

195251, Российская Федерация, г. Санкт-Петербург, Политехническая ул., 29
velichko-spbstu@yandex.ru

DOI: 10.18721/JPM.14107
UDC 517.946

DUHAMEL-TYPE INTEGRAL FOR THE INITIAL BOUNDARY VALUE PROBLEM

D.S. Anikonov, D.S. Konovalova

Sobolev Institute of Mathematics,
Novosibirsk, Russian Federation

The paper considers an initial boundary value problem for the wave equation for the case of three spatial variables. The definition of a generalized solution has been introduced and the theorem of unique existence has been proved. A new formula was proposed, being an analog of the well-known Duhamel integral. The most part of the paper is devoted to the analysis of differential properties of the solution. In particular, the authors indicated a possibility of discontinuity of the second partial time derivative on a certain hyperplane and pointed out its jump value as well. This property allowed us to set the inverse problem of determining the coefficient of the equation and propose an algorithm for solving it under the condition of non-zero internal action on a 2D subset. In this case, the known data were considered to be the values of a fixed oscillating point's position at every moment of time.

Keywords: wave equation, Duhamel integral, inverse problem, descent method, Cauchy problem

Citation: Anikonov D.S., Konovalova D.S., Duhamel-type integral for the initial boundary value problem, St. Petersburg Polytechnical State University Journal. Physics and Mathematics. 14 (1) (2021) 95–104. DOI: 10.18721/JPM.14107

This is an open access article under the CC BY-NC 4.0 license (<https://creativecommons.org/licenses/by-nc/4.0/>)

ИНТЕГРАЛ ТИПА ДЮАМЕЛЯ ДЛЯ НАЧАЛЬНО-КРАЕВОЙ ЗАДАЧИ

Д.С. Аниконов, Д.С. Коновалова

Институт математики им. С.Л. Соболева СО РАН,
г. Новосибирск, Российская Федерация

В работе рассматривается начально-краевая задача для волнового уравнения для случая трех пространственных переменных. Вводится определение обобщенного решения и доказывается теорема существования и единственности. Предложена новая формула, являющаяся аналогом известного интеграла Дюамеля. Большая часть статьи посвящена анализу дифференциальных свойств решения. В частности, указано на возможность разрыва второй частной производной по времени на некоторой гиперплоскости и приведена величина ее разрыва. Это свойство позволило поставить обратную задачу об определении коэффициента уравнения и предложить алгоритм ее решения при условии ненулевого внутреннего воздействия на некотором двумерном подмножестве. При этом известными данными считались значения положения фиксированной колеблющейся точки в каждый момент времени.

Ключевые слова: волновое уравнение, интеграл Дюамеля, обратная задача, метод спуска, задача Коши

Ссылка при цитировании: Аниконов Д.С., Коновалова Д.С. Интеграл типа Дюамеля для начально-краевой задачи // Научно-технические ведомости СПбГПУ. Физико-математические науки. 2021. Т. 14. № 1. С. 95–104. DOI: 10.18721/JPM.14107

Статья открытого доступа, распространяемая по лицензии CC BY-NC 4.0 (<https://creativecommons.org/licenses/by-nc/4.0/>)

Introduction

The paper considers the hyperbolic equation

$$\frac{\partial^2 u(x, t)}{\partial t^2} - a^2 \Delta_x u(x, t) = f(x, t), \quad (1)$$

$$x = (x_1, x_2, x_3), \quad x_3 > 0, \quad t > 0,$$

together with the initial and boundary data

$$u(x, 0) = \frac{\partial}{\partial t} u(x, 0) = 0, \quad (2)$$

$$u(x_1, x_2, 0, t) = 0.$$

The direct (initial boundary value) problem lies in finding the function $u(x, t)$ from Eq. (1) and conditions (2), when $a > 0, f(x, t)$ are known.

Our paper proves the theorem of unique existence of the solution for the initial boundary value problem and proposes a formula for its solution never presented before. The formula can be regarded as a generalization of Duhamel integral.

Recall that classic Duhamel integral is the solution to Cauchy problem when there is neither a constraint on variable x_3 nor, respectively, any boundary condition. The most specific feature of our formula is the use of discontinuous function under the integral. The obtained formula also allows us to pose and solve the inverse problem of finding the coefficient of equation (1).

Moreover, the study conclusions are applied to a special case of two spatial variables, when functions $u(x, t), f(x, t)$ depend only on the variables (x_2, x_3, t) , which can be considered to be a realization of the descent.

The classic theory of mixed problems is presented for example in articles [1–3] for a case of bounded domain of spatial variables. In a multidimensional case, the known results for unbounded domains are included in book [3], where the known data is additionally assumed as finite which for a bounded time interval allows us to resolve the problem into the already studied case of the bounded domain.

Our conclusions for the direct problem are regarded as a generalization of the classic results. There are numerous papers published by various authors and devoted to this research direc-

tion. With no pretense of any extensive review, we indicated only several of them, for instance, papers [4 – 16]. As to the inverse problem of this paper, we noted only the papers by other authors [17 – 23] most similar to our direction or research.

Notations, definitions and direct problem statement

Let us introduce the following notations:

$$G^+ = \{(x_1, x_2, x_3, t), -\infty < x_1, x_2 < \infty, x_3 > 0, t > 0\},$$

$$G^- = \{(x_1, x_2, x_3, t), -\infty < x_1, x_2 < \infty, x_3 < 0, t > 0\},$$

$$G_1^+ = \{(x, t) \in G^+, at > x_3\},$$

$$G_2^+ = \{(x, t) \in G^+, at < x_3\},$$

$$G_1^- = \{(x, t) \in G^-, at > -x_3\},$$

$$G_2^- = \{(x, t) \in G^-, at < -x_3\};$$

define a unit sphere in a three-dimensional space as Ω , and its elements as $\omega = (\omega_1, \omega_2, \omega_3)$, which using spherical angles are written as

$$\omega_1 = \sin \gamma \cos \varphi,$$

$$\omega_2 = \sin \gamma \sin \varphi, \quad \omega_3 = \cos \gamma,$$

$$0 \leq \gamma \leq 2\pi, \quad 0 \leq \varphi \leq \pi.$$

For first derivatives of arbitrary function $\psi(\xi_1, \dots, \xi_n)$ with respect to ξ_i , except for the traditional notations, we also use $\partial_i \psi(\xi_1, \dots, \xi_n)$. The left-hand side of Eq. (1) is denoted as $L_a u$.

We follow the existing tradition, when $C^p(G)$ denotes a set of functions possessing all partial derivatives up to and including order p continuous in domain G , while a set of such functions pos-



sessing continuous extensions of all derivatives at the domain boundary is denoted as $C^p(\overline{G})$. Let us assume that $f(x, t) \in C^2(G^+)$.

Consider function $F(x, t)$ equal to $f(x, t)$ for $x_3 \geq 0$ and $-f(x, t)$ for $x_3 < 0$. Let us denote restriction of function $x_3 < 0$ on closed set G^+ using $F^+(x, t)$, and on set G^- using $F^-(x, t)$. Note that function $F(x, t)$ turns out to be, generally speaking, discontinuous, when $x_3 = 0$.

We search for the generalized solution of problem (1), (2) in the next class of functions:

$$u(x, t) \in C^1(\overline{G^+}), u(x, t) \in C^2(\overline{G_1^+}),$$

$$u(x, t) \in C^2(\overline{G_2^+}),$$

i.e. function $u(x, t)$ is the solution to Eq. (1) in the classic sense in domains G_1^+, G_2^+ , while at the border between them it turns continuous with its first derivatives. Note that continuity of second derivatives on hyperplane $x_3 = at$ is not intended.

Differential properties of the Duhamel-type integral

Consider the following integral:

$$U(x, t) = \frac{1}{4\pi} \int_0^t \tau \int_{\Omega} F(x + a\tau\omega, t - \tau) d\omega d\tau. \quad (3)$$

The following statement is true.

Lemma 1. *A function defined by Eq. (3) belongs to the following classes:*

$$U(x, t) \in C^1(\overline{G^+}), U(x, t) \in C^2(\overline{G_1^+}),$$

$$U(x, t) \in C^2(\overline{G_2^+}).$$

Proof. Suppose $(x, t) \in G_1^+$. First, let us find derivatives of function $U(x, t)$ with respect to t . Let us present $U(x, t)$ as a sum

$$U(x, t) = I_1(x, t) + I_2(x, t) + I_3(x, t),$$

$$I_1(x, t) =$$

$$= \frac{1}{4\pi} \int_0^{x_3/a} \tau \int_{\Omega} F^+(x + a\tau\omega, t - \tau) d\omega d\tau, \quad (4)$$

$$I_2(x, t) = \frac{1}{4\pi} \int_{x_3/a}^t \tau \int_0^{2\pi} \int_0^{\alpha(x_3, \tau)} F^+(x +$$

$$+ a\tau\omega(\gamma, \varphi), t - \tau) \sin \varphi d\varphi d\gamma d\tau, \quad (5)$$

$$I_3(x, t) = \frac{1}{4\pi} \int_{x_3/a}^t \tau \int_0^{2\pi} \int_{\alpha(x_3, \tau)}^{\pi} F^-(x +$$

$$+ a\tau\omega(\gamma, \varphi), t - \tau) \sin \varphi d\varphi d\gamma d\tau, \quad (6)$$

where $\alpha(x_3, \tau) = \arccos(-x_3 / a\tau)$.

Let us differentiate each of the Eqs. (4) – (6) with respect to t :

$$\frac{\partial I_1(x, t)}{\partial t} =$$

$$= \frac{1}{4\pi} \int_0^{x_3/a} \tau \int_{\Omega} \partial_4 F^+(x + a\tau\omega, t -$$

$$- \tau) d\omega d\tau, \quad (7)$$

$$\frac{\partial^2 I_1(x, t)}{\partial t^2} =$$

$$= \frac{1}{4\pi} \int_0^{x_3/a} \tau \int_{\Omega} \partial_4 \partial_4 F^+(x + a\tau\omega, t -$$

$$- \tau) d\omega d\tau, \quad (8)$$

$$\frac{\partial I_2(x, t)}{\partial t} =$$

$$= \frac{t}{4\pi} \int_0^{2\pi} \int_0^{\alpha(x_3, t)} F^+(x + a\tau\omega(\gamma, \varphi), 0) \times$$

$$\times \sin \varphi d\varphi d\gamma + \quad (9)$$

$$+ \frac{1}{4\pi} \int_{x_3/a}^t \tau \int_0^{2\pi} \int_0^{\alpha(x_3, t)} \partial_4 F^+(x + a\tau\omega(\gamma, \varphi), t - \tau) \times$$

$$\times \sin \varphi d\varphi d\gamma d\tau,$$

$$\frac{\partial^2 I_2(x, t)}{\partial t^2} =$$

$$= \frac{1}{4\pi} \int_0^{2\pi} \int_0^{\alpha(x_3, t)} F^+(x + a\tau\omega(\gamma, \varphi), 0) \times$$

$$\begin{aligned}
 & \times \sin \varphi d\varphi d\gamma + \\
 & + \frac{t}{4\pi} \int_0^{2\pi} F^+ \left(x + at\omega(\gamma, \alpha(x_3, t)), 0 \right) \times \\
 & \times \sin \alpha(x_3, t) \frac{\partial}{\partial t} \alpha(x_3, t) d\gamma + \\
 & + \frac{t}{4\pi} \int_0^{2\pi} \int_0^{\alpha(x_3, t)} \text{grad}_x F^+ \left(x + at\omega(\gamma, \varphi), 0 \right) \times \\
 & \times a\omega(\gamma, \varphi) \sin \varphi d\varphi d\gamma + \\
 & + \frac{t}{4\pi} \int_0^{2\pi} \int_0^{\alpha(x_3, t)} \partial_4 F^+ \left(x + at\omega(\gamma, \varphi), 0 \right) \times \\
 & \times \sin \varphi d\varphi d\gamma + \\
 & + \frac{1}{4\pi} \int_{x_3/a}^t \tau \int_0^{2\pi} \int_0^{\alpha(x_3, t)} \partial_4 \partial_4 F^+ \left(x + a\tau\omega(\gamma, \varphi), t - \tau \right) \times \\
 & \times \sin \varphi d\varphi d\gamma d\tau,
 \end{aligned} \tag{10}$$

$$\begin{aligned}
 & \frac{\partial I_3(x, t)}{\partial t} = \\
 & = \frac{t}{4\pi} \int_0^{2\pi} \int_{\alpha(x_3, t)}^{\pi} F^- \left(x + at\omega(\gamma, \varphi), 0 \right) \times \\
 & \times \sin \varphi d\varphi d\gamma + \\
 & + \frac{1}{4\pi} \int_{x_3/a}^t \tau \int_0^{2\pi} \int_{\alpha(x_3, t)}^{\pi} \partial_4 F^- \left(x + a\tau\omega(\gamma, \varphi), t - \tau \right) \times \\
 & \times \sin \varphi d\varphi d\gamma d\tau,
 \end{aligned} \tag{11}$$

$$\begin{aligned}
 & \frac{\partial^2 I_3(x, t)}{\partial t^2} = \\
 & = \frac{1}{4\pi} \int_0^{2\pi} \int_{\alpha(x_3, t)}^{\pi} F^- \left(x + at\omega(\gamma, \varphi), 0 \right) \times \\
 & \times \sin \varphi d\varphi d\gamma + \\
 & + \frac{t}{4\pi} \int_0^{2\pi} F^- \left(x + at\omega(\gamma, \alpha(x_3, t), 0) \sin \alpha(x_3, t) \right) \times \\
 & \times \left(-\frac{\partial}{\partial t} \alpha(x_3, t) \right) d\gamma + \\
 & + \frac{t}{4\pi} \int_0^{2\pi} \int_{\alpha(x_3, t)}^{\pi} \text{grad}_x F^- \left(x + at\omega(\gamma, \varphi), 0 \right) \times \\
 & \times a\omega(\gamma, \varphi) \sin \varphi d\varphi d\gamma +
 \end{aligned} \tag{12}$$

$$\begin{aligned}
 & + \frac{t}{4\pi} \int_0^{2\pi} \int_{\alpha(x_3, t)}^{\pi} \partial_4 F^- \left(x + at\omega(\gamma, \varphi), 0 \right) \times \\
 & \times \sin \varphi d\varphi d\gamma + \\
 & + \frac{1}{4\pi} \int_{x_3/a}^t \tau \int_0^{2\pi} \int_{\alpha(x_3, t)}^{\pi} \partial_4 \partial_4 F^- \left(x + a\tau\omega(\gamma, \varphi), t - \tau \right) \times \\
 & \times \sin \varphi d\varphi d\gamma d\tau.
 \end{aligned} \tag{12}$$

Now, consider the case of $(x, t) \in G_2^+(x_3 > at)$:

$$\begin{aligned}
 & \frac{\partial U(x, t)}{\partial t} = \\
 & = \frac{t}{4\pi} \int_{\Omega} F^+ \left(x + at\omega, 0 \right) d\omega + \\
 & + \frac{1}{4\pi} \int_0^t \tau \int_{\Omega} \partial_4 F^+ \left(x + at\omega, t - \tau \right) d\omega d\tau,
 \end{aligned} \tag{13}$$

$$\begin{aligned}
 & \frac{\partial^2 U(x, t)}{\partial t^2} = \\
 & = \frac{1}{4\pi} \int_{\Omega} F^+ \left(x + at\omega, 0 \right) d\omega + \\
 & + \frac{t}{4\pi} \int_{\Omega} \text{grad}_x F^+ \left(x + at\omega, 0 \right) a\omega d\omega + \\
 & + \frac{t}{4\pi} \int_{\Omega} \partial_4 F^+ \left(x + at\omega, 0 \right) d\omega + \\
 & + \frac{1}{4\pi} \int_0^t \tau \int_{\Omega} \partial_4 \partial_4 F^+ \left(x + at\omega, t - \tau \right) d\omega d\tau.
 \end{aligned} \tag{14}$$

By adding up right-hand sides of Eqs. (7), (9), (11) and letting $t \rightarrow x_3/a$, we see that the limit value of this sum coincides with the limit value of the right-hand side of Eq. (13). Thus, we show that partial derivative $\partial U(x, t) / \partial t$ is continuous at $at = x_3$.

Moreover, using the indicated equations it is easy to show the continuity of $\partial_4 U(x, t)$ for $(x, t) \in \bar{G}^+$.

To analyze the second partial derivative of function $U(x, t)$ with respect to t , we use Eqs. (8), (10), (12), which result in continuity of $\partial_4 \partial_4 U(x, t)$ for $(x, t) \in \bar{G}^+$.

Now, consider derivatives of $U(x, t)$ with respect to x_3 . Suppose $(x, t) \in G_1^+$. Then



$$\begin{aligned} \frac{\partial I_1(x, t)}{\partial x_3} = & \\ = & \frac{x_3}{4\pi a^2} \int_{\Omega} F^+(x + x_3 \omega, t - x_3/a) d\omega + \quad (15) \\ & + \frac{1}{4\pi} \int_0^{x_3/a} \tau \int_{\Omega} \partial_3 F^+(x + x_3 \omega, t - \tau) d\omega d\tau, \end{aligned}$$

$$\begin{aligned} \frac{\partial^2 I_1(x, t)}{\partial x_3^2} = & \\ = & \frac{1}{4\pi a^2} \int_{\Omega} F^+(x + x_3 \omega, t - x_3/a) d\omega + \\ & + \frac{x_3}{4\pi a^2} \int_{\Omega} \text{grad} F^+(x + x_3 \omega, t - x_3/a) \eta d\omega + \quad (16) \\ & + \frac{x_3}{4\pi a^2} \int_{\Omega} \partial_3 F^+(x + x_3 \omega, t - x_3/a) d\omega + \\ & + \frac{1}{4\pi} \int_0^{x_3/a} \tau \int_{\Omega} \partial_3 \partial_3 F^+(x + a\tau \omega, t - \tau) d\omega d\tau, \end{aligned}$$

where $\eta = (\omega_1, \omega_2, 1 + \omega_3, -1/a)$;

$$\begin{aligned} \frac{\partial I_2(x, t)}{\partial x_3} = & \\ = & -\frac{x_3}{4\pi a^2} \int_{\Omega} F^+(x + x_3 \omega, t - x_3/a) d\omega + \\ & + \frac{1}{4\pi a} \int_0^t \int_0^{2\pi} F^+(x + a\tau \omega(\gamma, \alpha(x_3, \tau)), t - \quad (17) \\ & - \tau) d\gamma d\tau + \\ & + \frac{1}{4\pi} \int_0^t \tau \int_0^{2\pi} \int_0^{\alpha(x_3, \tau)} \partial_3 F^+(x + a\tau \omega(\gamma, \varphi), t - \\ & - \tau) d\varphi d\gamma d\tau, \end{aligned}$$

$$\begin{aligned} \frac{\partial^2 I_2(x, t)}{\partial x_3^2} = & \\ = & -\frac{1}{4\pi a^2} \int_{\Omega} F^+(x + x_3 \omega, t - x_3/a) d\omega - \\ & - \frac{x_3}{4\pi a^2} \int_{\Omega} \text{grad} F^+(x + x_3 \omega, t - \quad (18) \end{aligned}$$

$$\begin{aligned} & -x_3/a) \eta d\omega - \frac{1}{4\pi a^2} \times \\ & \times \int_0^{2\pi} F^+(x + x_3 \omega(\gamma, \alpha(x_3, x_3/a)), t - \\ & - x_3/a) d\gamma - \frac{1}{4\pi a} \times \\ & \times \int_0^t \int_0^{2\pi} \frac{\partial}{\partial x_3} F^+(x + a\tau \omega(\gamma, \alpha(x_3, \tau)), t - \\ & - \tau) d\gamma d\tau - \frac{x_3}{4\pi a^2} \times \quad (18) \\ & \times \int_{\Omega} \partial_3 F^+(x + x_3 \omega, t - x_3/a) d\omega + \\ & + \frac{1}{4\pi} \int_0^t \tau \int_0^{2\pi} \partial_3 F^+(x + a\tau \omega(\gamma, \alpha(x_3, \tau)), t - \\ & - \tau) \frac{\partial \alpha(x_3, \tau)}{\partial x_3} d\gamma d\tau + \frac{1}{4\pi} \times \\ & \times \int_0^t \tau \int_0^{2\pi} \int_0^{\alpha(x_3, \tau)} \partial_3 \partial_3 F^+(x + a\tau \omega(\gamma, \varphi), t - \\ & - \tau) d\varphi d\gamma d\tau, \end{aligned}$$

$$\begin{aligned} \frac{\partial I_3(x, t)}{\partial x_3} = & \\ = & -\frac{1}{4\pi a} \int_0^t \int_0^{2\pi} F^-(x + a\tau \omega(\gamma, \alpha(x_3, \tau)), t - \\ & - \tau) d\gamma d\tau + \frac{1}{4\pi} \times \quad (19) \\ & \times \int_0^t \int_0^{2\pi} \int_0^{\pi} \partial_3 F^-(x + a\tau \omega(\gamma, \varphi), t - \\ & - \tau) d\varphi d\gamma d\tau, \end{aligned}$$

$$\begin{aligned} \frac{\partial^2 I_3(x, t)}{\partial x_3^2} = & \\ = & \frac{1}{4\pi a^2} \int_0^{2\pi} F^-(x + x_3 \omega(\gamma, \alpha(x_3, x_3/a)), t - \\ & - \tau) d\gamma - \frac{1}{4\pi a} \times \quad (20) \end{aligned}$$

$$\begin{aligned} & \times \int_{x_3/a}^t \int_0^{2\pi} \frac{\partial}{\partial x_3} F^-(x + a\tau\omega(\gamma, \alpha(x_3, \tau)), t - \\ & \quad - \tau) d\gamma d\tau + \frac{1}{4\pi} \times \\ & \times \int_{x_3/a}^t \int_0^{2\pi} \int_{\alpha(x_3, \tau)}^{\pi} \partial_3 \partial_3 F^-(x + a\tau\omega(\gamma, \varphi), t - \\ & \quad - \tau) d\varphi d\gamma d\tau. \end{aligned} \quad (20)$$

While computing derivatives of $U(x, t)$ with respect to x_3 , we repeatedly used equation $\alpha(x_3, x_3/a) = \pi$ which allowed for some simplification of the obtained expressions.

For $(x, t) \in G_2^+$, the computations of derivatives with respect to x_3 are simple:

$$\begin{aligned} & \frac{\partial U(x, t)}{\partial x_3} = \\ & = \frac{1}{4\pi} \int_0^t \tau \int_{\Omega} \partial_3 F^+(x + a\tau\omega, t - \tau) d\omega d\tau, \end{aligned} \quad (21)$$

$$\begin{aligned} & \frac{\partial^2 U(x, t)}{\partial x_3^2} = \\ & = \frac{1}{4\pi} \int_0^t \tau \int_{\Omega} \partial_3 \partial_3 F^+(x + a\tau\omega, t - \tau) d\omega d\tau. \end{aligned} \quad (22)$$

Let us add up right-hand sides of Eqs. (15), (17), (19) and find the limit of the indicated sum, when $t \rightarrow x_3/a$. Despite the cumbersome expressions, the required limit turns out to be equal to the right-hand side of Eq. (21), which proves the continuity of the first derivative $U(x, t)$ with respect to x_3 at set G^+ . This property combined with the previously proved continuity of the derivative $U(x, t)$ with respect to t allows us to conclude that $U(x, t) \in C^1(G^+)$.

Formulae for other derivatives containing differentiation with respect to x_1, x_2 are obtained in a similar manner, but have a simpler form. It follows from these formulae as well as from a simple analysis of the right-hand sides of Eqs. (18), (20), (22) that $U(x, t)$ belongs to the classes of $C^2(G_1^+)$, $C^2(G_2^+)$.

This proves lemma 1.

Lemma 2. *Second partial derivative of function $U(x, t)$ with respect to t may have a discontinuity of the first kind when $x_3 = at$, while its jump is given by the formula*

$$\begin{aligned} & \lim_{t \rightarrow x_3/a+0} \partial_4 \partial_4 U(x, t) - \lim_{t \rightarrow x_3/a-0} \partial_4 \partial_4 U(x, t) = \\ & = -f(x_1, x_2, 0, 0). \end{aligned} \quad (23)$$

P r o o f. Consider a sum of right-hand sides of Eqs. (8), (10) and (12). The limit of the obtained expression is significantly reduced due to equations

$$t = x_3/a, \quad \alpha(x_3, x_3/a) = \pi,$$

$$\omega(\gamma, \alpha(x_3, x_3/a)) = (0, 0, -1).$$

Moreover, some integrals become zero, and others are simplified. By subtracting from the thus obtained sum the right-hand sides of Eq. (14) at $t = x_3/a$, we come to formula (23).

This proves lemma 2.

Main results

Theorem. *There is a unique generalized solution to problem (1), (2).*

P r o o f. Let us complete the definition of function $F(x, t)$ with zero for $t < 0$. Then the integral in the right-hand side of Eq. (3), considered for all $x \in R^3$, is a convolution of function $F(x, t)$ with a fundamental solution of the wave Eq. (1). Therefore, it is a solution of this equation in the class of generalized functions (Schwartz distributions) (see paper [1, p. 224]). Also note that this integral is a regular generalized function and, thanks to the proved properties of function $U(x, t)$ (lemma 1), has classic continuous derivatives up to the second order in domains G_1^+, G_2^+ . Thus, the equation

$$L_a(U(x, t)) = f(x, t)$$

is valid, when $(x, t) \in G_1^+, (x, t) \in G_2^+$.

Now, let us pay attention to equalities (2). The boundary conditions $U(x_1, x_2, 0, t)$ follows from the oddity of function $F(x, t)$ with respect to x_3 and the symmetry of the integration domain at $x_3 =$



$= 0$. As function $U(x, t)$ in domain G_2^+ coincides with classic Duhamel integral, then the initial conditions in equalities (2) are satisfied as well. These conclusions, combined with the properties indicated in lemma 2, allow us to regard function $U(x, t)$ as the required solution to the problem. To correlate the notations, all is left is to assume $U(x, t) = u(x, t)$.

The uniqueness of the solution results from the uniqueness of the solution to the Cauchy problem for Eq. (1) in the class of generalized functions.

The theorem is proved.

Let us further demonstrate the method of descent traditionally used in the Cauchy problem. Suppose now the right-hand side of Eq. (1) does not depend, for example, on variable x_1 . Then, formula (3) is written as

$$u(x_2, x_3, t) = \frac{1}{4\pi} \int_0^t \tau \int_{\Omega} F(x_2 + a\tau\omega_2, x_3 + a\tau\omega_3, t - \tau) d\omega d\tau. \quad (24)$$

As Eq. (24) is a special case of formula (3), then all the conclusions for the problem (1), (2) are valid in this case as well, with the details easy to deduct from the presented study. This method of descent could be further used to obtain the already known formula semibounded string.

Eq. (23) allows us to state the inverse problem and propose an algorithm for its solution. Suppose for a certain fixed vector

$$(x_1, x_2, x_3), x_3 > 0$$

there is a defined function

$$u(x_1, x_2, x_3, t) = h(t).$$

We need to find coefficient a . Assuming the condition

$$f(x_1, x_2, 0, 0) \neq 0$$

is satisfied, let us consider the value of the second derivative $h''(t)$.

It results from lemma 2 that $h''(t)$ has a unique discontinuity in a certain point $t_0 = ax_3$, which provides the required value $a = t_0/x_3$.

Conclusion

As we have already stated, this article is aimed at generalization of classic results which due a number of constraints are not always adequate for applied problems. Therefore, the main purpose of our study is to expand the possibilities of practical introduction of theoretical conclusions.

The paper considers a case of three spatial variables. However, thanks to the method of descent the achieved results are applicable to description of the oscillating process with respect to not only three-dimensional volumes, but also two-dimensional domains, such as a membrane.

The obtained formula is a new result, as classic Duhamel integral for a classic solution to the wave equation was previously used only for the Cauchy problem and was only applied to smooth functions of class C^2 .

In addition, existence of an explicit formula allowed us to set and solve an inverse problem of determining the coefficient of the wave equation characterizing oscillating medium.

The study was also carried out for the purpose of possible application of the obtained results to other generalizations.

REFERENCES

1. **Vladimirov V.S.**, Equations of mathematical physics, Mir Publishing, Moscow, 1984.
2. **Il'in V.A.**, The solvability of mixed problems for hyperbolic and parabolic equations, Russian Mathematical Surveys. 15 (2) (1960) 85–142.
3. **Ladyzhenskaya O.A.**, Smeshannaya zadacha dlya giperbolicheskogo uravneniya [The mixed problem for hyperbolic equation], Gostekhizdat, Moscow, 1953.
4. **Kirichenko S.V., Pul'kina L.S.**, A problem

with nonlocal initial data for one-dimensional hyperbolic equation, *Russian Mathematics*. 58 (9) (2014) 13–21.

5. **Moiseev E.I., Kholomeyeva A.A., Frolov A.A.**, Boundary displacement control for the oscillation process with boundary conditions of damping type for a time less than critical, *Itogi Nauki i Tekhniki, Ser. Sovrem. Mat. Pril., Temat. Obz.* 160 (2019) 74 – 84 (in Russian).

6. **Kulikovskii A.G., Sveshnikova E.I., Chugainova A.P.**, Mathematical methods for studying discontinuous solutions of nonlinear hyperbolic systems of equations, *Lektsionnyye Kursy NOC, Vol. 16, Steklov Mathematical Institute of RAS, Moscow, 2010* (in Russian).

7. **Filippov A.F.**, Differential equations with discontinuous righthand sides, *Control systems*, Edited by Arscott F.M., Springer Nature, Switzerland AG. (1988).

8. **Anikonov D.S., Kovtanyuk A.E., Prokhorov I.V.**, Transport equation and tomography, *VSP (Inverse and Ill-Posed Problems Series)*, Utrecht, Boston, Köln, Tokyo, 2002.

9. **Petrova G., Popov B.**, Linear transport equations with μ -monotone coefficients, *Journal of Mathematical Analysis and Applications*. 2001. 260 (2) (2001) 307–324.

10. **Bouchut F., Jame F.**, One-dimensional transport equations with discontinuous coefficients, *Nonlinear Analysis: Theory, Methods and Applications*. 32 (7) (1998) 891–933.

11. **Driscoll T.A., Fornberg B.**, Block pseudospectral methods for Maxwell's equations. II: Two-dimensional, discontinuous-coefficient case, *SIAM Journal on Scientific Computing*. 21 (3) (1999) 1146–1167.

12. **Durdiev D.K.**, Obratnaya zadacha opredeleniya dvukh koeffitsientov v odnom integrodifferentsial'nom volnovom uravnenii [An inverse problem for determining two coefficients in the one integro-differential wave equation], *Siberian Journal of Industrial Mathematics*. 12 (3) (2009) 28–40 (in Russian).

13. **Tadmor E.**, Local error estimates for discontinuous solutions of nonlinear hyperbolic equations, *SIAM Journal on Numerical Analysis*. 28 (4) (1991) 891–906.

14. **Derevtsov E.Yu., Maltseva S.V., Svetov I.E.**,

Mathematical models and algorithms for reconstruction of singular support of functions and vector fields by tomographic data, *Eurasian Journal of Mathematical and Computer Applications*. 3 (4) (2015) 4–44.

15. **Konovalova D.S.**, Localization of the discontinuity line of the right-hand side of a differential equation, *Journal of Applied and Industrial Mathematics*. 10 (1) (2016) 97–105.

16. **Kazantsev S.G.**, Singular value decomposition for the cone-beam transform in the ball, *Journal of Inverse and Ill-Posed Problems*. 23 (2) (2015) 173–185.

17. **Valitov I.R., Kozhanov A.I.**, Obratnyye zadachi dlya giperbolicheskikh uravneniy: sluchay neizvestnykh koeffitsiyentov, zavisyashchikh ot vremeni [Inverse problems for hyperbolic equations: the case of unknown time coefficients], *Bulletin of the Novosibirsk State University, Series "Mathematics, Mechanics, Computer Science"*. 6 (1) (2006) 3–18.

18. **Safifullova R.R.**, Inverse problem for the second order hyperbolic equation with unknown time dependent coefficient, *Bulletin of the South Ural State University. Series "Mathematical Modeling, Programming & Computer Software"*. 6 (4) (2013) 73–86 (in Russian).

19. **Anikonov D.S., Konovalova D.S.**, Direct and inverse problems for a wave equation with discontinuous coefficients, *St. Petersburg Polytechnical University Journal. Physics and Mathematics*. 11 (2) (2018) 61–71.

20. **Voronin A.F.**, Inverse and direct problems for the first-kind equation in convolutions on a semidirect, *Siberian Electronic Mathematical Reports*. 14 (2017) 1456–1462 (in Russian).

21. **Derevtsov E.Y.**, Ob odnom obobshchenii eksponentsialnogo lucheвого preobrazovaniya v tomografii [On a generalization of exponential ray transformation in tomography], *Siberian Journal of Pure and Applied Mathematics*. 18 (4) (2018) 29–41 (in Russian).

22. **Derevtsov E.Y., Maltseva S.V., Svetov I.E.**, Determination of discontinuities of a function in a domain with refraction from its attenuated ray transform, *Journal of Applied and Industrial Mathematics*. 12 (4) (2018) 619–641.

23. **Svetov I.E., Polyakova A.P., Maltseva S.V.**,

The method of approximate inverse for ray transform operators on two-dimensional symmetric m -tensor fields, *Journal of Applied and Industrial Mathematics*. 13 (1) (2019) 157–167.

Received 21.08.2020, accepted 27.10.2020.

THE AUTHORS

ANIKONOV Dmitry S.

Sobolev Institute of Mathematics

4 Acad. Koptug Ave., Novosibirsk, 630090, Russian Federation

anik@math.nsc.ru

KONOVALOVA Dina S.

Sobolev Institute of Mathematics

4 Acad. Koptug Ave., Novosibirsk, 630090, Russian Federation

dsk@math.nsc.ru

СПИСОК ЛИТЕРАТУРЫ

1. **Владимиров В.С.** Уравнения математической физики. М.: Наука, 1981. 512 с.
2. **Ильин В.А.** О разрешимости смешанных задач для гиперболического и параболического уравнений // *Успехи математических наук*. 1960. Т. 15. № 2 (92). С. 97–154.
3. **Ладыженская О.А.** Смешанная задача для гиперболического уравнения. М.: Государственное издательство технико-теоретической литературы, 1953. 279 с.
4. **Кириченко С.В., Пулькина Л.С.** Задача с нелокальными начальными данными для одномерного гиперболического уравнения // *Известия вузов. Математика*. 2014. № 9. С. 17–26.
5. **Моисеев Е.И., Холомеева А.А., Фролов А.А.** Граничное управление смещением процессом колебаний при граничном условии типа торможения за время, меньшее критического // *Материалы международной конференции “International Conference on Mathematical Modelling in Applied Sciences “ICMMAS-17”*. Санкт-Петербургский политехнический университет, 24–28 июля 2017 г. Итоги науки и техники. Сер. Современная математика и ее приложения. Тематические обзоры. 2019. Т. 160. С. 74–84.
6. **Куликовский А.Г., Свешникова Е.И., Чугайнова А.П.** Математические методы изучения разрывных решений нелинейных гиперболических систем уравнений // *Лекционные курсы НОЦ. Вып. 16. М.: Изд. Математического института им. В.А. Стеклова РАН, 2010. 122 с.*
7. **Филиппов А.Ф.** Дифференциальные уравнения с разрывной правой частью. М.: Наука. Гл. ред. физ.-мат. лит.-ры, 1985. 255 с.
8. **Аниконов Д.С., Ковтаниук А.Е., Прохоров И.В.** Использование уравнения переноса в томографии. М.: «Логос», 2000. 223 р.
9. **Petrova G., Popov B.** Linear transport equations with μ -monotone coefficients // *Journal of Mathematical Analysis and Applications*. 2001. Vol. 260. No. 2. Pp. 307–324.
10. **Bouchut F., Jame F.** One-dimensional transport equations with discontinuous coefficients // *Nonlinear Analysis: Theory, Methods and Applications*. 1998. Vol. 32. No. 7. Pp. 891–933.
11. **Driscoll T.A., Fornberg B.** Block pseudospectral methods for Maxwell’s equations. II: Two-dimensional, discontinuous-coefficient case // *SIAM Journal on Scientific Computing*. 1999. Vol. 21. No. 3. Pp. 1146–1167.
12. **Дурдиев Д.К.** Обратная задача определения двух коэффициентов в одном интегродифференциальном волновом уравнении // *Сибирский журнал индустриальной математики*. 2009. Т. 12. № 3 (39). С. 28–40.

13. **Tadmor E.** Local error estimates for discontinuous solutions of nonlinear hyperbolic equations // *SIAM Journal on Numerical Analysis*. 1991. Vol. 28. No. 4. Pp. 891–906.
14. **Derevtsov E.Yu., Maltseva S.V., Svetov I.E.** Mathematical models and algorithms for reconstruction of singular support of functions and vector fields by tomographic data // *Eurasian Journal of Mathematical and Computer Applications*. 2015. Vol. 3. No. 4. Pp. 4–44.
15. **Коновалова Д.С.** Локализация линии разрывов правой части дифференциального уравнения // *Сибирский журнал индустриальной математики*. 2016. Т. 19. № 1 (65). С. 62–72.
16. **Kazantsev S.G.** Singular value decomposition for the cone-beam transform in the ball // *Journal of Inverse and Ill-Posed Problems*. 2015. Vol. 23. No. 2. Pp. 173–185.
17. **Валитов И.Р., Кожанов А.И.** Обратные задачи для гиперболических уравнений: случай неизвестных коэффициентов, зависящих от времени // *Вестник Новосибирского государственного университета. Сер. Математика, механика, информатика*. 2006. Т. 6. № 1. С. 3–18.
18. **Сафиуллова Р.Р.** Обратная задача для гиперболического уравнения второго порядка с неизвестным коэффициентом, зависящим от времени // *Вестник Южно-Уральского государственного университета. Сер. Математическое моделирование и программирование*. 2013. Т. 6. № 4. С. 73–86.
19. **Аниконов Д.С., Коновалова Д.С.** Прямая и обратная задачи для волнового уравнения с разрывными коэффициентами // *Научно-технические ведомости СПбГПУ. Физико-математические науки*. 2018. Т. 11. № 2. С. 61–71.
20. **Воронин А.Ф.** Обратная и прямая задачи для уравнения первого рода в свертках на полупрямой // *Сибирские электронные математические известия*. 2017. Т. 14. С. 1456–1462.
21. **Деревцов Е.Ю.** Об одном обобщении экспоненциального лучевого преобразования в томографии // *Сибирский журнал чистой и прикладной математики*. 2018. Т. 18. № 4. С. 29–41.
22. **Деревцов Е.Ю., Мальцева С.В., Светов И.Е.** Определение разрывов функции, заданной в области с рефракцией, по ее экспоненциальному лучевому преобразованию // *Сибирский журнал индустриальной математики*. 2018. Т. 21. № 4 (76). С. 51–74.
23. **Светов И.Е., Полякова А.П., Мальцева С.В.** Метод приближенного обращения для операторов лучевых преобразований, действующих на двумерные симметричные m -тензорные поля // *Сибирский журнал индустриальной математики*. 2019. Т. 22. № 1. С. 104–115.

Статья поступила в редакцию 21.08.2020, принята к публикации 27.10.2020.

СВЕДЕНИЯ ОБ АВТОРАХ

АНИКОНОВ Дмитрий Сергеевич — доктор физико-математических наук, заведующий лабораторией Института математики имени С.Л. Соболева СО РАН, г. Новосибирск, Российская Федерация. 630090, Российская Федерация, г. Новосибирск, пр. Академика Коптюга, 4
anik@math.nsc.ru

КОНОВАЛОВА Дина Сергеевна — кандидат физико-математических наук, старший научный сотрудник Института математики им. С.Л. Соболева СО РАН, г. Новосибирск, Российская Федерация. 630090, Российская Федерация, г. Новосибирск, пр. Академика Коптюга, 4
dsk@math.nsc.ru

DOI: 10.18721/JPM.14108

UDC 537.533.2, 598.9

LOW-FIELD ELECTRON EMISSION FROM THIN FILMS OF METALS

I.S. Bizyaev, P.G. Gabdullin, N.M. Gnuchev, A.V. Arkhipov

Peter the Great St. Petersburg Polytechnic University,
St. Petersburg, Russian Federation

The paper presents an experimental study of the low-threshold field electron emission from thin films of metals (Mo, W, Zr, Ni and Ti) deposited on silicon substrates by magnetron sputtering. Several samples of such films having effective thickness in the range 6 – 10 nm were capable of room-temperature electron emission in electric field with macroscopic intensity as low as a few kV/mm. Optimized thermofield treatment procedure further improved their emission properties reducing the threshold field by several times. AFM study revealed a correlation between film's emission properties and their surface topography. At the same time, no equally pronounced correlation of the emissivity with other characteristics of coatings (including the sort of the metal and the silicon substrate conductivity type) was detected. Results of the study witness in favor of two-temperature (or hot-electron) emission mechanism for the investigated coatings.

Keywords: field emission, thin film, atomic force microscopy, hot-electron emission

Citation: Bizyaev I.S., Gabdullin P.G., Gnuchev N.M., Arkhipov A.V., Low-field electron emission from thin films of metals, St. Petersburg Polytechnical State University Journal. Physics and Mathematics. 14 (1) (2021) 105–120. DOI: 10.18721/JPM.14108

This is an open access article under the CC BY-NC 4.0 license (<https://creativecommons.org/licenses/by-nc/4.0/>)

НИЗКОПОРОГОВАЯ ПОЛЕВАЯ ЭМИССИЯ ЭЛЕКТРОНОВ ТОНКИМИ ПЛЕНКАМИ МЕТАЛЛОВ

И.С. Бизяев, П.Г. Габдуллин, Н.М. Гнучев, А.В. Архипов

Санкт-Петербургский политехнический университет Петра Великого,
Санкт-Петербург, Российская Федерация

В работе экспериментально исследованы эмиссионные свойства тонких пленок нескольких металлов (Mo, Ni, W, Ti и Zr), нанесенных на кремниевые подложки методом магнетронного распыления. При эффективной толщине 6 – 10 нм, многие образцы пленок показали способность эмитировать электроны при комнатной температуре в поле с макроскопической напряженностью порядка единиц В/мкм. Оптимизированная процедура термополевой обработки позволяла дополнительно активировать их эмиссионные свойства, снижая эмиссионный порог в несколько раз. Была выявлена корреляция эмиссионных свойств пленок с топографией их поверхности, определяемой методом атомно-силовой микроскопии (АСМ). При этом выраженной корреляции эмиссионной способности с прочими характеристиками покрытий (в том числе с видом металла и типом проводимости подложки) обнаружено не было. Полученные экспериментальные результаты свидетельствуют в пользу двухтемпературной («горячелектронной») модели эмиссионного механизма для изученных покрытий.

Ключевые слова: полевая эмиссия, тонкая пленка, атомно-силовая микроскопия, эмиссия горячих электронов

Ссылка при цитировании: Бизяев И.С., Габдуллин П.Г., Гнучев Н.М., Архипов А.В. Низкопороговая полевая эмиссия электронов тонкими пленками металлов // Научно-технические ве-

Introduction

One of the attractive applications of nanostructured materials is their use as a part of cold (non-heated) cathodes of electronic devices. Currently, in practice, most often are used either metal (or silicon) tips or carbon nanotubes and similar fibers [1 – 5]. However, many researchers believe that cold emitters of electrons that do not have sharp points – with a relatively smooth emitter boundary [3 – 9] – are also promising, even though no practically competitive systems of this type have been proposed so far.

In one of the experimental types of cold cathodes studied since the 1960s [10 – 13], a nanostructured metal (or carbon) film on a dielectric substrate was used as the main element. The film is actually a set of microscopic metal (or carbon) islands. The current in the film between the electrodes deposited on top of it flows as a result of the tunneling transfer of electrons through the gaps separating the islands. In this case, electroluminescence and electron emission into the vacuum are observed. The mechanism of such emission has not been definitively determined, but, according to the most popular model [13 – 15], it includes the following processes:

- hot electrons are emitted,
- the electronic subsystem of the islands is heated by the current injected into them,
- high electron temperature is maintained as a result of violation of the energy exchange between the electrons and the lattice, the last effect being characteristic of nanoscale objects.

The validity of this model was confirmed by the observation of emission while using non-current methods of pumping electron energy into islands – in particular, under the influence of infrared (IR) radiation [13, 16].

Another type of experimental samples possessing cold emission was studied in [17 – 19]. It was shown that carbon “nano-island” films on silicon substrates are able to emit electrons at room

temperature in sufficiently weak electrostatic fields (the macroscopic field intensity was about 1 V/m) and without any additional effects, such as surface current excitation. At the same time, there were neither areas with low work function, nor high-aspect elements of topography (points, fibers, etc.) on the surface.

To describe the emissivity of such films, we proposed a model [20, 21], which is largely similar to the hot electron model described above. The assumption of slow relaxation of hot carriers in nanostructures is also used in this model, but it is assumed that this slowness is a result of the peculiarities of the electronic structure of sp^2 -hybridized carbon [22, 23].

The primary goal of this paper was to test experimentally the validity of the latter assumption. It was necessary to determine whether the cold electron emission in macroscopic electric field strength of about 1 V/m (without other external influences, such as the flow of surface current or IR irradiation) is possible only for carbon island films, or it will also be observed in case of metal films of similar structures.

Experimental

The samples of metal films were deposited on naturally oxidized substrates of doped silicon by magnetron sputtering using a HEX unit manufactured by Mantis Deposit (Great Britain). The substrates were pre-cleaned by ultrasonic treatment in an acetone solution. Then they were installed on the slide table of the growth chamber and subjected to additional thermal cleaning at a temperature of about 150 °C and residual gases pressure of 10^{-3} Pa. Before spraying the coating, the magnetron target was also cleaned: the substrates were covered with a special screen during the first five minutes of the sprayer operation. The capabilities of the installation made it possible to conduct the metal deposition process at a residual gas pressure of about 10^{-4} Pa, to regulate the dep-



osition rate (from 0.13 to 1.0 Å/s) and the temperature of the substrates (from room temperature to 250 °C). The effective ("nominal") coating thickness was monitored by quartz microweights.

The emission properties of the samples were tested in an experimental apparatus assembled on the basis of a TCH-2 vacuum installation at a residual gas pressure of about 10^{-7} Pa. The device contained six identical sections and allowed parallel testing of the corresponding number of samples. Each of them was fixed on a separate object table equipped with a direct-glow heater, thanks to which the temperature of the sample could be adjusted in the range from the room temperature to 600 °C. The electric field was created in a planar gap of 0.6 mm wide between the sample and the end face of a cylindrical anode with a diameter of 6 mm.

After installing a batch of samples in the device and pre-pumping it, they were decontaminated by heating up to 150 °C. Further, the procedure of thermal field activation of the emission properties of coatings, developed earlier in the course of experiments with nanocarbon emitters, could be carried out [24]. For metal films, the parameters of the procedure were optimized by the selection method.

When measuring the emission characteristics, a slowly varying voltage was applied between the sample and the anode, up to a maximum value of 4.5 kV from a controlled high-voltage source. The time intervals of its rise and fall (linear in time) were 35 s, which corresponds to a frequency of 14 mHz. The voltage $U(t)$ and the emission current $I(t)$ were recorded by a digital oscilloscope and used to obtain the emission characteristics $I(U)$.

The samples of the coatings that passed the emission tests were studied using an atomic force microscope (AFM) of NanoDST Pacific Nanotechnology (USA) in so-called semi-contact (CloseContact) mode. This made it possible to determine the "true" topography of the surface with absolute values of the normal coordinate in the course of operational measurements under non-vacuum conditions, with minimal influence of the adsorbed layers of atmospheric gases and water on the measurement results. However, to

remove an excessively dense layer of volatile substances, some samples were heated in air up to a temperature above 100 °C for 2 hours before performing AFM measurements. In addition to AFM, in some cases, a MIAIA3 Tescan scanning electron microscope (SEM) (Czech Republic) with the possibility of EMF analysis of the surface elemental composition was used.

The choice of the set of experimental methods used in the described primary experiments made it possible to conduct rapid testing of a large number of samples that differed in the material of metal coatings, their thickness, the parameters of the deposition processes and the type of substrate.

Experimental results

Emission properties of the samples and the possibility of their activation.

Experiments with the samples of metal coatings on silicon substrates confirmed the ability of some of these samples to emit electrons in an electric field with a macroscopic strength E (defined as the ratio of the applied voltage to the width of the field gap) of the order of units V/μm. The measured emission characteristics (Fig. 1) were usually exponential in the "straight" $I(U)$ coordinates and were well approximated by the linear dependence in the Fowler-Nordheim coordinates

$$\ln(I/U^2) = f(1/U),$$

This is considered to be a confirmation of the field (tunnel) nature of the emission mechanism.

As for the previously studied nanocarbon materials [24], the emissivity of metal films could be activated by applying the following thermal-field treatment procedure.

An electric field of low intensity (about 1 V/m) was applied to the sample, and the sample was heated at a rate of about 5 °C/min until an emission current of 100 nA appeared; or, in the absence of a field, until the temperature of 600 °C was reached (the point at which the thermal emission current appeared).

For many coatings, the auto-emission current appeared and began to increase over time

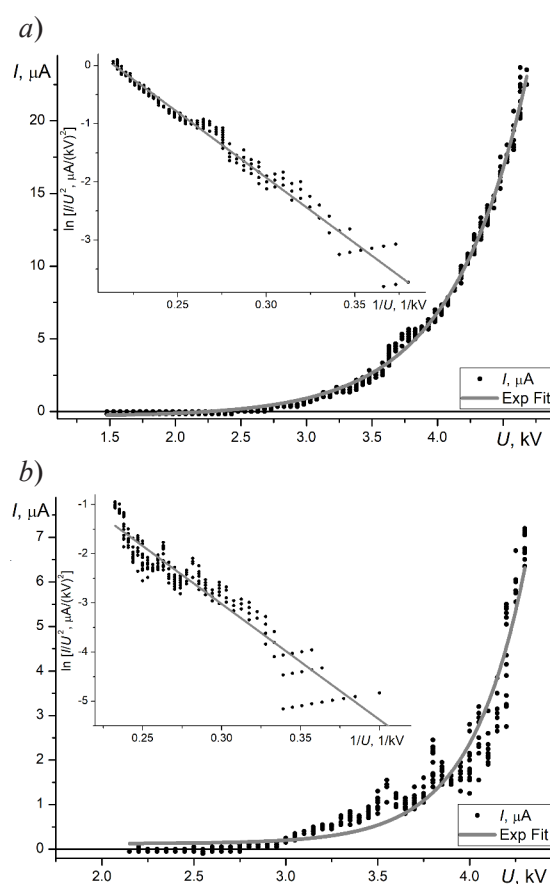


Fig.1. Emission characteristics of Mo (a) and Zr (b) film samples with an effective thickness of 6 nm. The insets show the same dependencies in Fowler – Nordheim coordinates

at a temperature of about 300 °C. After reaching the current value of 100 nA, the field strength was being gradually reduced, the current being kept at the specified value; at the same time the heating of the sample stopped, and, as the result, the sample slowly cooled to room temperature, while the value of the emission current at 100 nA level was still maintained (for this purpose, the voltage applied to the field gap was specially selected).

Due to the application of the described procedure to the samples with the best emission properties, the voltage level required to get the current of a given value was reduced several times. Attempts to simplify the procedure, for example, to activate the sample without applying an electric field, but only by temperature action, or to turn off the field during the cooling of the activated samples, were unsuccessful. Their result was invariably the loss of the emissivity of the studied structures.

The table summarizes the results of experiments on the influence of various parameters of thin metal films on their emissivity. The following sections of the article are devoted to a more complete description of them.

The emissivity of the samples (the best of the corresponding series) is characterized in the table by two values. One of them is the threshold value of the macroscopic field strength E_{th} , which was determined by the moment of the appearance of a current equal to about 100 nA. The other is the maximum value of the current I_{max} , which could be taken from the sample area located opposite the anode (its diameter was 6 mm).

Comparison of the emission properties of thin films of different metals. To determine the effect of the coating material on emission, samples of films of five different metals were made: molybdenum, zirconium, nickel, tungsten and titanium, having the same nominal thickness d_{nom} (given in



Table

The main parameters of the studied films and their emission properties

Experiment No.	Material		Deposition rate, Å/s	E_{th} , V/μm	I_{max} , mA
	Of the coating (d_{nom} , nm)	of the substrate			
1	Mo (6)	KDB 10	0.2	3.0	2.2
	Zr (6)		0.5	4.3	8.0
	Ni (6)		1.0	5.0	2.6
	W (6)		1.0	not determined	
	Ti (6)		0.2	no emission	
2	Mo (6)	Si + 200 nm of oxide	1.0	no emission	
	Mo (8)				
3	Mo (4)	KDB 10	0.2	4.8	0.05
	Mo (6)	KEF 7.5		3.0	2.20
	Mo (4)			4.0	0.15
	Mo (6)			6.4	0.03
4	Mo (2)	KDB 10	0.2	no emission	
	Mo (4)			not determined	
	Mo (6)			3.0	2.2
	Mo (8)		1.0	3.2	12
	Mo (10)			4.0	25
	Mo (20)			no emission	
5	Mo (6) № 1	KDB 10	0.13	3.2	4.16
	Mo (6) № 2		1.0	4.2	23.70
	Mo (6) № 3*			3.6	1.53

Designations: d_{nom} – nominal thickness of the metal film; KDB – boron-doped, hole-conducting silicon; KEF – phosphorus-doped silicon with electronic conductivity. Figures 7.5 or 10 mean the resistivity of the substrate, expressed in ohms per centimeter; E_{th} – the threshold electric field strength (determined by the moment of appearance of the current, equal to about 100 nA), I_{max} – the maximum emission current obtained.

Notes. The substrate temperature was 100 °C; the only exception was sample No. 3* in experiment 5, for which it was equal to 150°C.

the table in parentheses, in nm). A summary of the results of the comparison is also presented in the table.

The best emissivity was shown by the samples of molybdenum coatings (see Fig. 1,a). As a result, most of the experiments in this work were carried out with molybdenum films. Almost all the samples of Mo coatings with a nominal thickness in the range of 6 – 10 nm could emit electrons at a field strength of less than 10 V/μm. Figure 2,a shows a typical AFM image of a Mo coating with an effective thickness of

6 nm. From its appearance, it can be concluded that the coating is heterogeneous, while the average lateral size of the elevated areas ("islands") is close to 20 nm at their height of 1 – 2 nm. The density of the islands is about 500 μm⁻².

The zirconium films were characterized by similar surface topography. In a typical AFM image (Fig. 2,b), grains with an average transverse size of about 30 nm and a height of up to 2 nm are distinguishable; their distribution density is about 400 per μm². The emissivity of such films was noticeable even before the thermal field ac-

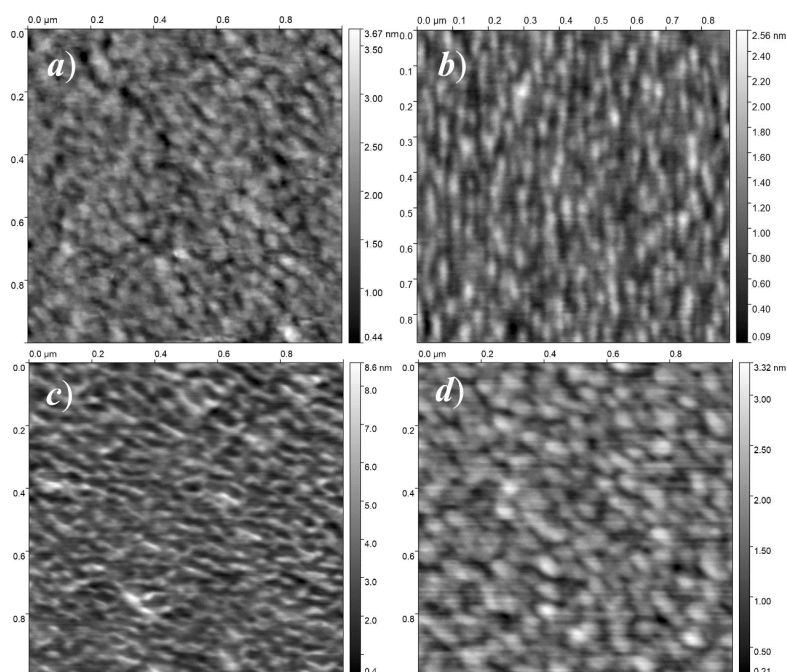


Fig. 2. AFM images of the surface of samples of metal coatings made of Mo (a), Zr (b), Ni (c), W (d) with an effective thickness of 6 nm

tivation procedure, and after the activation it was further improved (see Fig. 1, *b* and the table).

In terms of topography, the nickel film was markedly different from the metal films described above. The inhomogeneities present in the AFM images had a significantly larger vertical size and elongated shape. The length of the observed "elevations" for a typical case (see Fig. 2, *c*) reaches 60 – 100 nm at a height of up to 5 – 8 nm, and these elevations, as far as can be judged from the images, are assembled in a common network. Nickel films differed from those of molybdenum and zirconium in terms of their emission properties, and for the worse. After activation, they showed some emissivity, but the field emission current was extremely unstable. Upon reaching the value of 2 – 4 μA , the current irreversibly fell almost to zero; probably, a small number of emission centers on the surface were destroyed.

A typical AFM image of the surface of a tungsten film (Fig. 2, *d*) is similar in structure to images of molybdenum and zirconium. However, the topographical features here are somewhat larger: their transverse size is on average 80 nm, and their maximal height is about 3 nm. The emissivity of the tungsten films was worse than that

of the metals considered earlier. When heated to 500 °C during the activation process, an emission current of 100 nA could be obtained at a voltage of 3.5 kV (at an emission gap of 0.6 mm). However, after cooling the sample, the threshold voltage values were above 4 kV, which made it technically impossible to register the emission dependences.

When analyzing the above experimental data, it should be taken into account that AFM images do not allow us to unambiguously determine whether the observed inhomogeneities of the topography are isolated islands of metal. The results of SEM-EMF mapping carried out for several samples indicate that metal coatings with a nominal thickness of 6 nm (or more) in the areas that were not damaged during the emission testing by the action of electric discharges (they were located outside the actively emitting areas), were solid. Consequently, in many cases, the obtained AFM images revealed only a local inhomogeneity of the film thickness, but not their separation into isolated islands, which could be expected due to the available data for carbon coatings with similar emission properties [17 – 19]. Nevertheless, the comparison of the emissivity of metal coat-

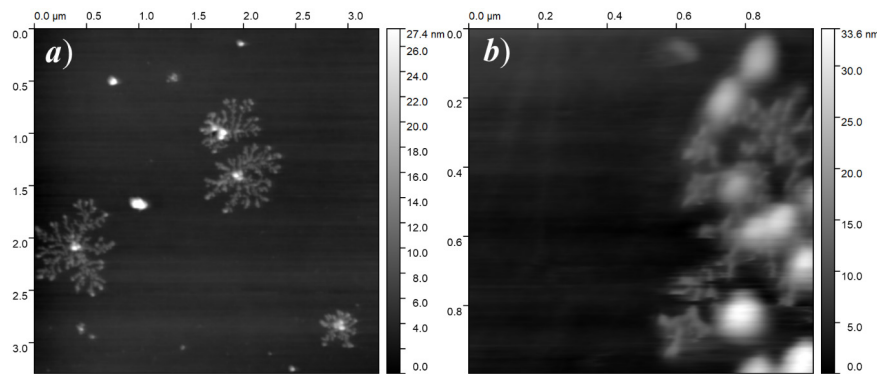


Fig. 3. AFM images of dendritic structures on the surfaces of two samples of coatings: Ti deposited on a Si plate without oxidation (*a*), and Mo deposited on a Si plate with a thick layer (about 200 nm) of oxide (*b*)

ings with the parameters of their AFM images revealed a significant correlation (confirmed by the results presented in the following sections): the best emissivity was possessed by the samples with the smallest scale of topographic surface heterogeneity.

The results of the experiment with titanium films deserve a separate discussion. They were distinguished by a complete lack of emissivity; the thermal field activation procedure also did not give the desired result. The image of the surface of one of the standard-made films of this metal is shown in Fig. 3,*a*. Here, the metal forms isolated islands of large size (in comparison with the grains of other coated films shown in Fig. 2), up to approximately 1 μm . The islands have a characteristic appearance of dendritic structures that "grow" from a central protrusion of considerable (tens of nanometers) height. There are no nanometer-sized islands here — this fact has been specially verified.

This morphology of the titanium film is unusual, since this metal is characterized in principle by high adhesion to silicon and its dioxide, which, in particular, allows the use of titanium layers as buffers when depositing films of other metals (see, for example, [25]). At the same time, it is known that the structure of titanium films significantly depends on the method and conditions of their applying [26]. The growth of dendrite-like ("fractal") clusters similar in shape and size to those found in our samples of titanium films (see Fig. 3), was observed and was theoretically described, for example, in [27]. To imple-

ment the mechanism of dendrite formation proposed there, it is required for the thin surface layer of the substrate to be non-conductive (usually the role of this layer is performed by the oxide), and for the deposited material to come in charged state. In this case, the field of accumulated surface charge prevents the deposition of new material in all areas, except for the vicinity of defects in the non-conducting layer, which defects allow the charge to "drain" into the volume of the substrate. This is just the place where the growth of the coating begins, spreading over the surface as a collection of dendritic structures that are electrically connected to the substrate through defects in the oxide layer.

For the conditions of applying titanium coating in this work, both criteria for the feasibility of the scenario described above could be met:

- the natural oxide layer was preserved on the silicon substrates used;

- when implementing the magnetron sputtering method, a significant part of the material comes to the substrate in the charged state [28].

The question of what particular features of the substrates, targets, or sputtering mode we used led to the formation of a titanium coating in the form of a set of dendrite-like islands requires further study. From the standpoint of the main goal of this study, the most important conclusion is that the titanium coating consisting of large dendrite clusters is not capable of low-threshold cold electron emission.

To test the assumption about the effect of the surface electric charging on the morphology

of the resulting films, a special experiment was performed (see experiment No. 2 in the table). The molybdenum films were deposited on silicon substrates with their own conductivity and on artificially oxidized surface. In the second case, the thickness of the oxide layer was 200 nm, which allowed us to expect an increase in the effects associated with surface charging, compared with the case of naturally oxidized substrates. Indeed, some areas of such coatings differed significantly in morphology from Mo films on silicon with a natural oxide layer (see Fig. 2,*a*) and were similar to Ti coatings (see Fig. 3,*a*): dendritic structures were formed on the surface, and they were "tied" to linear and point defects (see Fig. 3,*b*). Such samples showed no emissivity either before or during the thermal field activation procedure. In addition to the morphological features of the coatings, the absence of emission activity can also be attributed to the difficult transport of carriers to the emission centers through the thick oxide layer.

Dependence of the emission properties of coatings on the type of conductivity of the substrate

The nature of hot electron mechanism of emission suggests the possibility of a significant influence of the substrate properties on the emissivity. To assess experimentally the degree and nature of this effect, two molybdenum films with different values of effective thickness were grown on naturally oxidized substrates of *p*-type silicon of the KDB 10 brand and *n*-type silicon of the

KEF 7.5 brand. Here Russian abbreviation KDB means boron-doped, hole-conducting silicon; KEF stands for "phosphorus-doped silicon with electronic conductivity"; figures mean the resistivity of the substrate, expressed in ohms per centimeter.

Summary data on the emissivity of such samples are given in the table (experiment No. 3). In general, we can note a slightly higher emissivity of films grown on substrates with hole conductivity. In addition, the samples of *n*-silicon substrates lost their emission properties after a short time (14 days) after the activation procedure. The best parameters were obtained from a sample of Mo-coating on a KDB 10 substrate, which had an effective layer thickness of 6 nm. It was characterized not only by a high emissivity, but also by the "correct" response to the thermal field activation procedure. Due to these properties, it is the substrates with hole conductivity that were used in most of the experiments in this work.

At the same time, the observed difference in the emissivity of the samples of different substrates could be determined not by the type of their conductivity itself, but by the morphology of the films created. AFM images of the surface of molybdenum coated samples with the same effective thickness of 6 nm on the substrates of different types are shown in Fig. 4. The differences in the topography of the films are quite noticeable: the coating grains on the *p*-Si substrate have smaller lateral dimensions (30 – 50 nm). The structure of the films having a surface with such

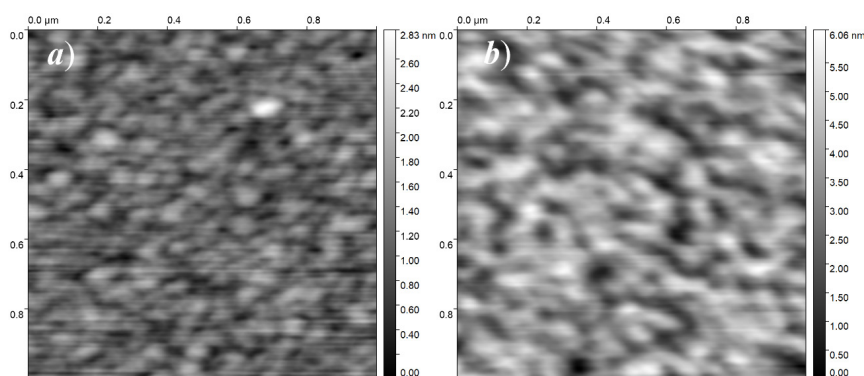


Fig. 4. AFM images of the surface of Mo films on KDB 10 (*a*) and KEF 7.5 (*b*) substrates. The effective thickness of the films is 6 nm



a topography was, in our conclusion, optimal in terms of their emissivity.

Dependence of the emission properties on the coating thickness

To clarify the relationship between the emission properties of coatings and their thickness, samples of molybdenum films with a nominal thickness of 2 to 20 nm were made on KDB 10 substrates. The summary of their best emission parameters is presented in the table (experiment No. 4).

For coatings with the thicknesses d_{nom} of 2 and 4 nm, stable low-threshold emission could not be obtained. In contrast, coatings with nominal thickness of 6 nm showed low switching thresholds and stable emission current. However, the maximum values of the obtained current for them were small, and this may indicate a small number of activated emission centers. The 8 nm films were characterized by slightly higher threshold values of the electric field, but the maximum values of the I_{max} increased by more than 5 times, compared to the 6 nm films. Films with a nominal thickness of 10 nm had an even higher turning on threshold, but the maximum

values of the obtained currents for them turned out to be the record for this type of structure studied by us. The sample with $d_{\text{nom}} = 20$ nm had no emission properties at all; the procedure for its thermal field activation also did not bring the required results.

AFM images of the surface of Mo coatings of different thicknesses on substrates of the same type (KDB 10) are shown in Fig. 4, *a* and Fig. 5 (for the coating thickness of 6 nm). The pattern of regular changes in the surface topography of samples with an increase in the amount of deposited material is also illustrated by the graph in Fig. 6, which shows the dependence on the effective thickness of coatings for the "normalized roughness" of images calculated using the Gwyddion package.

In Fig. 5, *a*, which represents the coating of the smallest thickness (2 nm), only a few prominent features (grains) are found on the area of $1 \mu\text{m}^2$ with a characteristic transverse size of up to 30 – 50 nm and the height of up to 1 – 2 nm. Approximately these are the dimensions of the islands, which, in accordance with the emission models used in the works [13 – 15, 20, 21], were associated with low-threshold field emission

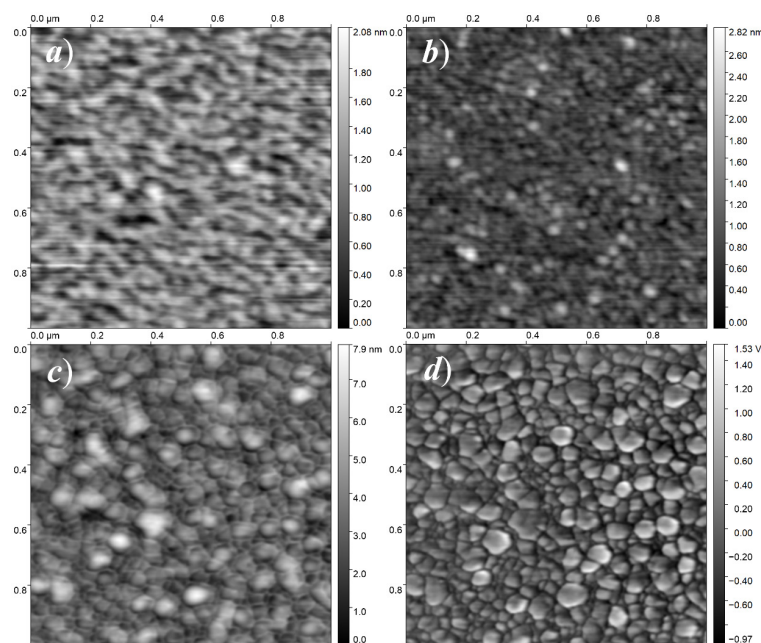


Fig. 5. AFM images of the surface topography of Mo films with different effective thicknesses, nm: 2 (*a*), 8 (*b*), 10 (*c*); *d* – "phase" image of the surface area (*c*). The films are grown on a KDB 10 substrate

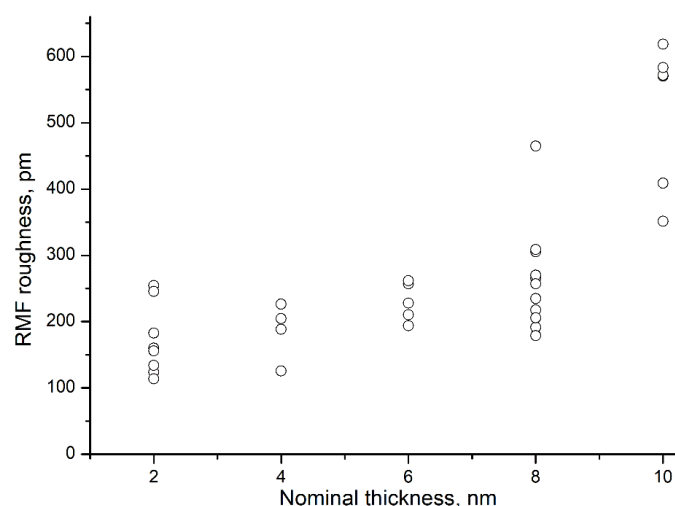


Fig. 6. Dependences of the root-mean-square parameter of the surface roughness of Mo films (according to AFM images) on the values of their effective thickness. Calculated using the Gwyddion package

centers. On the surfaces of $d_{nom} = 6$ nm and 8 nm (see Fig. 4,*a*, and 5,*b*, respectively) grains of the same size are present in much larger quantities, which may determine the high emissivity of such films. At the same time, AFM images of the 10 nm film (see the topography of the sample surface in Fig. 5,*c* and the corresponding "phase" distribution in Fig. 5,*d*) show a coating composed of contiguous domains of slightly larger transverse size and height. However, the grains of the size that we have defined as "optimal" are also present here. The smaller number of them can be responsible for the higher field emission threshold in such coatings, while the greater stability and endurance of the emission can be determined just by the presence of slightly larger islands. With further increase in the thickness of the Mo coating (sample 20 nm), the crystallites apparently formed a stable multilayer structure, and the film lost its emissivity.

Dependence of the emission properties on the parameters of the film deposition process

The experimental results described above indicate that the emission properties of coatings are related to their morphology. It is known that the morphology of coatings can change with varying conditions of their deposition. That is why in the course of this work, the coatings were compared,

which differed only in the features of the technology of their growing. For comparison, Mo films with $d_{nom} = 6$ nm grown on silicon substrates with hole conductivity were selected. The parameters of the manufacturing process of three such samples are given in the table (experiment No. 5). The topography of the surface of the obtained films is shown in the SEM images (Fig. 7).

On the surface of the sample No. 1 (see Fig. 7,*a*), formed at a temperature of 100 °C and the lowest growth rate (0.13 Å/s), grains with a typical transverse size of 20 nm were present. Their density can be estimated as approximately 500 μm^{-2} . In the image of sample No. 2 (Fig. 7,*b*), formed at the same temperature, but at a higher deposition rate, the grains have a larger average size: 30 – 40 nm; their number per unit area was approximately 300 μm^{-2} . Sample No. 3 (Fig. 7,*c*) was formed at an elevated substrate temperature (150 °C) and high film growth rate (1 Å/s). The average grain size here was the smallest one (about 15 – 20 nm) with a wide size distribution. The grain concentration was approximately 700 μm^{-2} .

Thus, it is obvious that there is a difference in the morphology of the coatings, and the grain variety, presumably associated with low-threshold emission centers, was present on the surface in all cases.

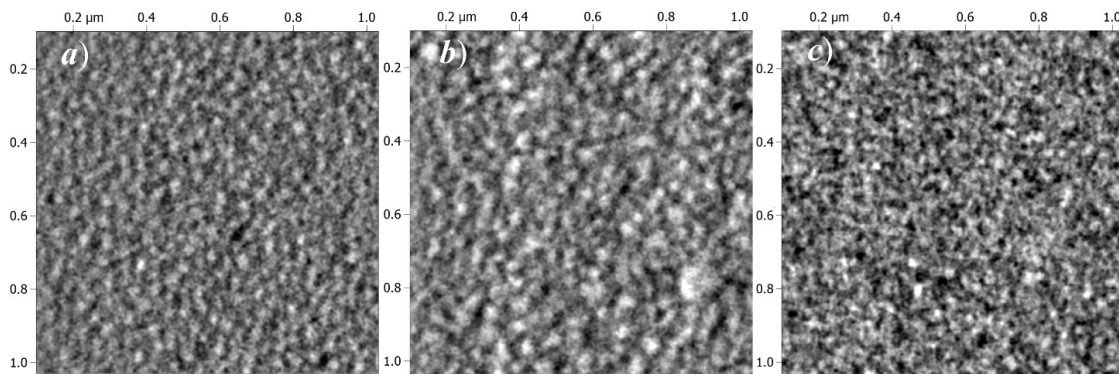


Fig. 7. SEM images (secondary electron detector) for samples No.1 (a), No.2 (b) and No.3 (c) made under different conditions (see experiment No. 5 in the table and description in the text)

In accordance with this, all three samples had the ability to emit electrons at low voltage with a noticeable quantitative difference in the emission parameters (see experiment No. 5 in the table). The correlation of the surface topography of the samples with their emissivity corresponded to the trends noted earlier.

The sample No. 1 with the smallest spatial scale of heterogeneity was characterized by the lowest emission threshold.

The threshold field for sample No. 2, with the largest grains, was the highest, but the maximum value of the sampled current I_{\max} was also the highest (the current-voltage characteristic of the emission is shown in Fig. 1,a).

Sample No. 3 demonstrated the lowest value of the permissible emission current and intermediate values of the threshold field.

Discussion of the results and conclusions

The main result of the presented work can be considered as the fact of detection of low-voltage electron emission by thin metal films formed on oxidized silicon.

Then, the correlation of the film's emissivity with its morphology (as far as it can be estimated through AFM data) is established. At the same time, the influence of other factors, namely, the type of metal and the type of conductivity of the substrate, was weaker.

In the experiments carried out, the effectiveness of thermopole activation of auto-emissivity was confirmed for the case of metal coat-

ings deposited on the semiconductor substrate. Just the same procedure was proposed earlier for carbon films [24]. This activation is largely analogous to the "electroforming" procedure required (according to the review [13] and the works mentioned there) to observe the emission of electrons from metal films when surface current flows through them. The physical content of this process is presumably metal atom migration, leading to the formation of isolated islands up to 100 nm in size, separated by gaps, on which, when a lateral potential difference appears, the electric field is concentrated. When electric current flows, the charge carriers cross the gaps between the islands by tunneling, which creates favorable conditions for the formation of population of hot electrons that can be emitted into vacuum. The effect is enhanced by the suppression of the electron-phonon interaction in nanoscale islands [13 – 15, 20, 21]. At the initial stages of the proposed thermal field activation procedure, the increased temperature accelerates the surface migration of atoms and promotes the formation of islands. It is known from the literature that thin solid metal films deposited on dielectric substrates at low temperature acquire an island structure as a result of heating to 300 – 600 °C [29]. In the presented experiments, to initiate the process of activating the emission properties of most coatings, they needed to be heated to a temperature from the same range. After the appearance of the emission current, the formation of the optimal coating structure can

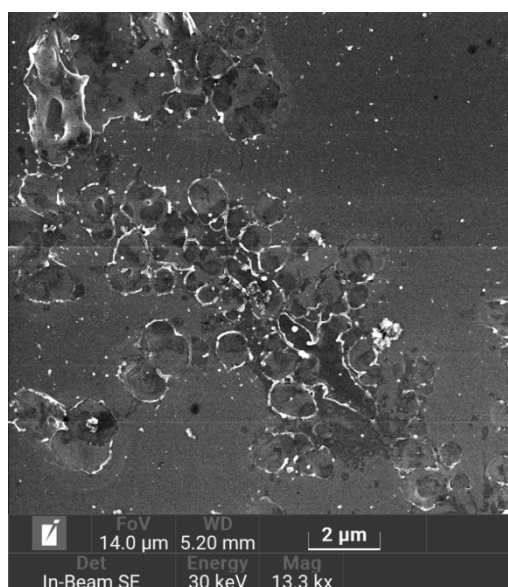


Fig. 8. SEM image of the surface of the Mo coating sample with the thickness of 10 nm after emission tests

be facilitated by additional factors caused by this current, namely, by local heating and ion bombardment of the surface; it was previously shown [30, 31] that irradiation with ion fluxes also contributes to the transformation of thin solid metal films into island films (dewetting). The possibility of forming coverage areas (emission centers) with a structure that is optimal in terms of the efficiency of heating the electronic subsystem of the islands and the emission of electrons into vacuum, should be determined, first of all, by the thickness of the metal film and its original morphology –

the size and concentration of the crystallites already present in the composition. This is exactly what was observed in the experiments.

Among other things, the above hypothesis about the mechanism of activation of the emissivity of the studied coatings explains the small values of obtained emission currents, which did not exceed tens of microamperes when the current was collected from an area of about 0.3 cm^2 . If the action of factors associated with the flow of the emission current causes an increase in the emission capacity of the local coating area, then a positive feedback between the emission current and the emission capacity is created, which should lead to the rapid destruction of most emission centers. (And indeed, the SEM images (Fig. 8) of the surface of the samples that had passed the emission tests often showed a large number of craters that can be identified with destroyed emission centers, even if no field gap breaks were recorded during testing.)

Due to the fact that the emerging emission centers are constantly activated until self-destruction, the lifetime of most of them is small. This limits the number of simultaneously functioning emission centers and the average value of the current density. Perhaps, the prospects for achieving high values of the average density of the emission current of cold film emitters should be associated with finding a way to control local emission currents – for example, with the introduction of microelectrode systems or resistive ballast layers.

REFERENCES

1. **Eletskii A.V.**, Carbon nanotube-based electron field emitters, *Physics–Uspekhi*. 53 (9) (2010) 863–892.
2. **Egorov N., Sheshin E.**, Field emission cathode-based devices and equipment. In: *Field Emission Electronics*. Springer Series in Advanced Microelectronics, Vol. 60. Springer, Cham, 2017.
3. **Egorov N.V., Sheshin E.P.**, On the current state of field-emission electronics, *J. Surf. Invest.: X-ray, Synchrotron Neutron Tech.* 11 (2) (2017) 285–294.
4. **Giubileo F., Di Bartolomeo A., Iemmo L., et al.**, Field emission from carbon nanostructures, *Appl. Sci.* 8 (4) (2018) 526.
5. **Fursey G.N.**, *Field emission in vacuum microelectronics*, Kluwer Academic–Plenum Publishers, New York, 2005.
6. **Fursey G.N., Polyakov M.A., Bagraev N.T., et al.**, Low-threshold field emission from carbon structures, *J. Surf. Invest.: X-ray, Synchrotron Neutron Tech.* 13 (5) (2019) 814–824.
7. **Kleshch V.I., Smolnikova E.A., Orekhov A.S.,**



et al., Nano-graphite cold cathodes for electric solar wind sail, *Carbon*. 81 (January) (2015) 132–136.

8. **Haque A., Narayan J.**, Electron field emission from Q-carbon, *Diam. Relat. Mater.* 86 (June) (2018) 71–78.

9. **Davidovich M.V., Yafarov R.K.**, Pulsed and static field emission VAC of carbon nanocluster structures: experiment and its interpretation, *Tech. Phys.* 64 (8) (2019) 1210–1220.

10. **Borzjak P.G., Sarbej O.G., Fedorowitsch R.D.**, Neue Erscheinungen in sehr dünnen Metallschichten, *Phys. Status Solidi, B.* 8 (1) (1965) 55–58.

11. **Nepijko S.A., Kutnyakhov D., Protsenko S.I., et al.**, Sensor and microelectronic elements based on nanoscale granular systems, *J. Nanopart. Res.* 13 (12) (2011) 6263–6281.

12. **Shen Z., Wang X., Wu S., Tian J.**, Numerical analysis of the surface-conduction electron-emitter with a new configuration, *Mod. Phys. Lett. B.* 30 (10) (2016) 1650137.

13. **Fedorovich R.D., Naumovets A.G., Tomchuk P.M.**, Electron and light emission from island metal films and generation of hot electrons in nanoparticles, *Phys. Rep.* 328 (2–3) (2000) 73–179.

14. **Bilotsky Y., Tomchuk P.M.**, Peculiarity of electron-phonon energy exchange in metal nanoparticles and thin films, *Surf. Sci.* 602 (1) (2008) 383–390.

15. **Tomchuk P., Bilotsky Y.**, New peculiarity in the temperature and size dependence of electron-lattice energy exchange in metal nanoparticles, *Int. J. Mod. Phys. B.* 28 (31) (2014) 1450220.

16. **Gloskovskii A., Valdaitsev D.A., Cinchetti M., et al.**, Electron emission from films of Ag and Au nanoparticles excited by a femtosecond pump-probe laser, *Phys. Rev. B.* 77 (19) (2008) 195427.

17. **Arkhipov A.V., Gabdullin P.G., Gordeev S.K., et al.**, Photostimulation of conductivity and electronic properties of field-emission nanocarbon coatings on silicon, *Tech. Phys.* 62 (1) (2017) 127–136.

18. **Andronov A., Budylna E., Shkitun P., et al.**, Characterization of thin carbon films capable of low-field electron emission, *J. Vac. Sci. Technol. B.* 36 (2) (2018) 02C108.

19. **Gabdullin P., Zhurkin A., Osipov V., et al.**, Thin carbon films: correlation between morphology and field-emission capability, *Diam. Relat. Mater.* 105 (May) (2020) 107805.

20. **Arkhipov A.V., Zhurkin A.M., Kvashenkina O.E., et al.**, Electron overheating during field emission from carbon island films due to phonon bottleneck effect, *Nanosystems: Physics, Chemistry, Mathematics.* 9 (1) (2018) 110–113.

21. **Arkhipov A.V., Eidelman E.D., Zhurkin A.M., et al.**, Low-field electron emission from carbon cluster films: combined thermoelectric/hot-electron model of the phenomenon, *Fuller. Nanotub. Car. N.* 28 (4) (2020) 286–294.

22. **Dubois S.M.-M., Zanolli Z., Declerck X., Charlier J.-C.**, Electronic properties and quantum transport in graphene-based nanostructures, *Eur. Phys. J., B.* 72 (1) (2009) 1–24.

23. **Varlamov A.A., Kavokin A.V., Luk'yanchuk I.A., Sharapov S.G.**, Anomalous thermoelectric and thermomagnetic properties of graphene, *Physics–Uspekhi.* 55 (11) (2012) 1146–1151.

24. **Bondarenko V.B., Gabdullin P.G., Gnuchev N.M., et al.**, Emissivity of powders prepared from nanoporous carbon, *Tech. Phys.* 49 (10) (2004) 1360–1363.

25. **Thomsen L.B., Nielsen G., Vendelbo S.B., et al.**, Electron emission from ultralarge area metal-oxide-semiconductor electron emitters, *J. Vac. Sci. Technol. B.* 27 (2) (2009) 562–567.

26. **Arshi N., Lu J., Lee C.G., et al.**, Thickness effect on properties of titanium film deposited by d.c. magnetron sputtering and electron beam evaporation techniques, *Bull. Mater. Sci.* 36 (5) (2013) 807–812.

27. **Mishin M.V., Zamotin K.Y., Protopopova V.S., Alexandrov S.E.**, Atmospheric pressure PECVD nanoparticles: Mechanism of nanoparticle self-organisation into micron sized fractal clusters on a solid surface, *Phys. Chem. Chem. Phys.* 17 (11) (2015) 7138–7148.

28. **Kashtanov P.V., Smirnov B.M., Hippler R.**, Magnetron plasma and nanotechnology, *Physics–Uspekhi.* 50 (5) (2007) 455–488.

29. **Niekiel F., Schweizer P., Kraschewski S.M., et al.**, The process of solid-state dewetting of Au thin films studied by in situ scanning transmission electron microscopy, *Acta Mater.* 90 (15 May) (2015) 118–132.

30. **Lo Savio R., Repetto L., Guida P., et al.**, Control of the micrometric scale morphology of silicon nanowires through ion irradiation-induced metal dewetting, *Solid State Commun.* 240 (Au-

gust) (2016) 41–45.

31. **Tuzhilkin M.S., Bessalova P.G., Mishin M.V., et al.**, Formation of Au nanoparticles and

features of etching of a Si substrate under irradiation with atomic and molecular ions, *Semiconductors*. 54 (1) (2020) 137–143.

Received 14.10.2020, accepted 24.11.2020.

THE AUTHORS

BIZYAEV Ivan S.

Peter the Great St. Petersburg Polytechnic University

29 Politechnicheskaya St., St. Petersburg, 195251, Russian Federation
ivanbiziaev@yandex.com

GABDULLIN Pavel G.

Peter the Great St. Petersburg Polytechnic University

29 Politechnicheskaya St., St. Petersburg, 195251, Russian Federation
gabdullin_pg@spbstu.ru

GNUCHEV Nikolay M.

Peter the Great St. Petersburg Polytechnic University

29 Politechnicheskaya St., St. Petersburg, 195251, Russian Federation
nmg@rphf.spbstu.ru

ARKHIPOV Alexander V.

Peter the Great St. Petersburg Polytechnic University

29 Politechnicheskaya St., St. Petersburg, 195251, Russian Federation
arkhipov@rphf.spbstu.ru

СПИСОК ЛИТЕРАТУРЫ

1. **Елецкий А.В.** Холодные полевые эмиттеры на основе углеродных нанотрубок // *УФН*. 2010. Т. 180. № 9. С. 897–930.

2. **Егоров Н.В., Шешин Е.П.** Автоэлектронная эмиссия. Принципы и приборы. М.: Интеллект, 2011. 704 с.

3. **Егоров Н.В., Шешин Е.П.** Современное состояние автоэмиссионной электроники // *Поверхность. Рентгеновские, синхротронные и нейтронные исследования*. 2017. № 3. С. 5–15.

4. **Giubileo F., Di Bartolomeo A., Iemmo L., Luongo G., Urban F.** Field emission from carbon nanostructures // *Applied Sciences*. 2018. Vol. 8. No. 4. P. 526.

5. **Fursey G.N.** Field emission in vacuum microelectronics. New York: Kluwer Academic–Plenum Publishers, 2005, 205 p.

6. **Фурсей Г.Н., Поляков М.А., Баграев Н.Т., Закиров И.И., Нащекин А.В., Бочаров В.Н.** Низкопороговая полевая эмиссия из углеродных структур // *Поверхность. Рентгеновские, синхротронные и нейтронные исследования*. 2019. № 9. С. 28–39.

7. **Kleshch V.I., Smolnikova E.A., Orekhov A.S., Kalvas T., Tarvainen O., Kauppinen J., Nuottajarvi A., Koivisto H., Janhunen P., Obratsov A.N.** Nano-graphite cold cathodes for electric solar wind sail // *Carbon*. 2015. Vol. 81. January. Pp. 132–136.

8. **Haque A., Narayan J.** Electron field emission from Q-carbon // *Diamond and Related Materials*. 2018. Vol. 86. June. Pp. 71–78.

9. **Давидович М.В., Яфаров Р.К.** Импульсные и статические автоэмиссионные ВАХ углеродных нанокластерных структур: эксперимент и



его интерпретация // Журнал технической физики. 2019. Т. 89. № 8. С. 1282–1293.

10. **Borzjak P.G., Sarbej O.G., Fedorowitsch R.D.** Neue Erscheinungen in sehr dünnen Metallschichten // *Physica Status Solidi*. B. 1965. Vol. 8. No. 1. Pp. 55–58.

11. **Nepijko S.A., Kutnyakhov D., Protsenko S.I., Odnodvoretz L.V., Schönhense G.** Sensor and microelectronic elements based on nanoscale granular systems // *Journal of Nanoparticle Research*. 2011. Vol. 13. No. 12. Pp. 6263–6281.

12. **Shen Z., Wang X., Wu S., Tian J.** Numerical analysis of the surface-conduction electron-emitter with a new configuration // *Modern Physics Letters*. B. 2016. Vol. 30. No. 10. P. 1650137.

13. **Fedorovich R.D., Naumovets A.G., Tomchuk P.M.** Electron and light emission from island metal films and generation of hot electrons in nanoparticles // *Physics Reports*. 2000. Vol. 328. No. 2–3. Pp. 73–179.

14. **Bilotsky Y., Tomchuk P.M.** Peculiarity of electron-phonon energy exchange in metal nanoparticles and thin films // *Surface Science*. 2008. Vol. 602. No. 1. Pp. 383–390.

15. **Tomchuk P., Bilotsky Y.** New peculiarity in the temperature and size dependence of electron-lattice energy exchange in metal nanoparticles // *International Journal of Modern Physics*. B. 2014. Vol. 28. No. 31. P. 1450220.

16. **Gloskovskii A., Valdaitsev D.A., Cinchetti M., et al.** Electron emission from films of Ag and Au nanoparticles excited by a femtosecond pump-probe laser // *Physical Review*. B. 2008. Vol. 77. No. 19. P. 195427.

17. **Архипов А.В., Габдуллин П.Г., Гордеев С.К., Журкин А.М., Квашенкина О.Е.** Фотостимуляция проводимости и электронные свойства автоэмиссионных наноуглеродных покрытий на кремнии // Журнал технической физики. 2016. Т. 86. № 12. С. 135–144.

18. **Andronov A., Budylna E., Shkitun P., Gabdullin P., Gnuchev N., Kvashenkina O., Arkhipov A.** Characterization of thin carbon films capable of low-field electron emission // *Journal of Vacuum Science and Technology*. B. 2018. Vol. 36. No. 2. P. 02C108.

19. **Gabdullin P., Zhurkin A., Osipov V., Besedina N., Kvashenkina O., Arkhipov A.** Thin carbon films:

correlation between morphology and field-emission capability // *Diamond and Related Materials*. 2020. Vol. 105. May. P. 107805.

20. **Arkhipov A.V., Zhurkin A.M., Kvashenkina O.E., Osipov V.S., Gabdullin P.G.** Electron overheating during field emission from carbon island films due to phonon bottleneck effect // *Наносистемы: физика, химия, математика*. 2018. Т. 9. № 1. С. 110–113.

21. **Arkhipov A.V., Eidelman E.D., Zhurkin A.M., Osipov V.S., Gabdullin P.G.** Low-field electron emission from carbon cluster films: combined thermoelectric/hot-electron model of the phenomenon // *Fullerenes, Nanotubes and Carbon Nanostructures*. 2020. Vol. 28. No. 4. Pp. 286–294.

22. **Dubois S.M.-M., Zanolli Z., Declerck X., Charlier J.-C.** Electronic properties and quantum transport in graphene-based nanostructures // *The European Physical Journal*. B. 2009. Vol. 72. No. 1. Pp. 1–24.

23. **Варламов А.А., Кавокин А.В., Лукьянчук И.А., Шарапов С.Г.** Аномальные термоэлектрические и термомагнитные свойства графена // *Успехи физических наук*. 2012. Т. 182. № 11. С. 1229–1234.

24. **Бондаренко В.Б., Габдуллин П.Г., Гнучев Н.М., Давыдов С.Н., Кораблёв В.В., Кравчик А.Е., Соколов В.В.** Эмиссионные характеристики порошков из нанопористого углерода // Журнал технической физики. 2004. Т. 74. № 10. С. 113–116.

25. **Thomsen L.B., Nielsen G., Vendelbo S.B., Johansson M., Hansen O., Chorkendorff I.** Electron emission from ultralarge area metal-oxide-semiconductor electron emitters // *Journal of Vacuum Science & Technology*. B. 2009. Vol. 27. No. 2. Pp. 562–567.

26. **Arshi N., Lu J., Lee C.G., Yoon J.H., Koo B.H., Ahmed F.** Thickness effect on properties of titanium film deposited by d.c. magnetron sputtering and electron beam evaporation techniques // *Bulletin of Materials Science*. 2013. Vol. 36. No. 5. Pp. 807–812.

27. **Mishin M.V., Zamotin K.Y., Protopopova V.S., Alexandrov S.E.** Atmospheric pressure PECVD nanoparticles: Mechanism of nanoparticle self-organisation into micron sized fractal clusters on a solid surface // *Physical Chem-*

istry, Chemical Physics. 2015. Vol. 17. No. 11. Pp. 7138–7148.

28. **Каштанов П.В., Смирнов Б.М., Хиплер Р.** Магнетронная плазма и нанотехнология // Успехи физических наук. 2007. Т. 177. № 5. С. 473–510.

29. **Niekiel F., Schweizer P., Kraschewski S.M., Butz B., Spiecker E.** The process of solid-state dewetting of Au thin films studied by in situ scanning transmission electron microscopy // Acta Materialia. 2015. Vol. 90. 15 May. Pp. 118–132.

30. **Lo Savio R., Repetto L., Guida P., Angeli E.,**

Firpo G., Volpe A., Ierardi V., Valbusa U. Control of the micrometric scale morphology of silicon nanowires through ion irradiation-induced metal dewetting // Solid State Communications. 2016. Vol. 240. August. Pp. 41–45.

31. **Тужилкин М.С., Беспалова П.Г., Мишин М.В., Колесников И.Е., Карабешкин К.В., Карасев П.А., Титов А.И.** Формирование наночастиц Au и особенности травления подложки Si после облучения атомарными и молекулярными ионами // Физика и техника полупроводников. 2020. Т. 54. № 1. С. 90–96.

Статья поступила в редакцию 14.10.2020, принята к публикации 24.11.2020.

СВЕДЕНИЯ ОБ АВТОРАХ

БИЗЯЕВ Иван Сергеевич — аспирант, научный сотрудник лаборатории «Самоорганизующиеся высокотемпературные наноструктуры» Санкт-Петербургского политехнического университета Петра Великого, Санкт-Петербург, Российская Федерация.

195251, Российская Федерация, г. Санкт-Петербург, Политехническая ул., 29
ivanbiziaev@yandex.com

ГАБДУЛЛИН Павел Гарифович — кандидат физико-математических наук, доцент Высшей инженерно-физической школы Санкт-Петербургского политехнического университета Петра Великого, Санкт-Петербург, Российская Федерация.

195251, Российская Федерация, г. Санкт-Петербург, Политехническая ул., 29
gabdullin_pg@spbstu.ru

ГНУЧЕВ Николай Михайлович — доктор физико-математических наук, профессор Высшей инженерно-физической школы Санкт-Петербургского политехнического университета Петра Великого, Санкт-Петербург, Российская Федерация.

195251, Российская Федерация, г. Санкт-Петербург, Политехническая ул., 29
nmg@rphf.spbstu.ru

АРХИПОВ Александр Викторович — доктор физико-математических наук, доцент Высшей инженерно-физической школы Санкт-Петербургского политехнического университета Петра Великого, Санкт-Петербург, Российская Федерация.

195251, Российская Федерация, г. Санкт-Петербург, Политехническая ул., 29
arkhipov@rphf.spbstu.ru



DOI: 10.18721/JPM.14109
UDC 533.9.01

MODERATE AND LOW PRESSURE GLOW DISCHARGE IN THE GAP BETWEEN TWO ECCENTRIC TUBES

A.P. Golovitskii, D.G. Korenyugin

Peter the Great St. Petersburg Polytechnic University,
St. Petersburg, Russian Federation

The paper considers the positive column of a low and moderate pressure glow discharge located between two dielectric cylindrical walls with noncoincident parallel axes, the discharge current being aligned along the axes. The electron temperature of such discharge plasma was shown to be higher than the one of traditional cylindrical geometry when the outer plasma radii are equal, but the spatial distribution of plasma density in the discharge cross-section can acquire strong inhomogeneity in the azimuthal direction.

Keywords: glow discharge, positive column, eccentric geometry, electron temperature

Citation: Golovitskii A.P., Korenyugin D.G., Moderate and low pressure glow discharge in the gap between two eccentric tubes, St. Petersburg Polytechnical State University Journal. Physics and Mathematics. 14 (1) (2021) 121–129. DOI: 10.18721/JPM.14109

This is an open access article under the CC BY-NC 4.0 license (<https://creativecommons.org/licenses/by-nc/4.0/>)

ТЛЕЮЩИЙ РАЗРЯД СРЕДНЕГО И НИЗКОГО ДАВЛЕНИЯ В ЗАЗОРЕ МЕЖДУ ДВУМЯ ЭКСЦЕНТРИЧНЫМИ ТРУБКАМИ

А.П. Головицкий, Д.Г. Кореньюгин

Санкт-Петербургский политехнический университет Петра Великого,
Санкт-Петербург, Российская Федерация

Рассмотрен положительный столб тлеющего разряда низкого и среднего давления в диффузионном режиме, в зазоре между двумя цилиндрическими диэлектрическими стенками с несовпадающими параллельными осями, причем ток разряда направлен вдоль этих осей. Показано, что электронная температура плазмы такого разряда выше, чем в традиционной цилиндрической геометрии при равных внешних радиусах плазмы, но пространственное распределение плотности плазмы в поперечном сечении разряда может приобретать сильную азимутальную неоднородность.

Ключевые слова: тлеющий разряд, положительный столб, эксцентричная геометрия, электронная температура

Ссылка при цитировании: Головицкий А.П., Кореньюгин Д.Г. Тлеющий разряд среднего и низкого давления в зазоре между двумя эксцентричными трубками // Научно-технические ведомости СПбГПУ. Физико-математические науки. 2021. Т. 14. № 1. С. 121–129. DOI: 10.18721/JPM.14109

Статья открытого доступа, распространяемая по лицензии CC BY-NC 4.0 (<https://creativecommons.org/licenses/by-nc/4.0/>)

Introduction

In papers [1, 2] we theoretically studied plasma of positive column of low and moderate pressure glow discharge located in the gap between two dielectric coaxial cylindrical tubes; in addition, the longitudinal field E_z and the discharge current were directed along the axis of the tubes. The authors showed that in such a discharge geometry, there is a considerable increase in electron temperature T_e in comparison with the cylindrical geometry even with a small (0.1 and less) ratio of the radii of the inner to the outer wall due to the additional channel of electron losses: electron diffusion to the inner wall. This result is important, in particular, for design of gas-discharge light and UV radiation sources, as it provides an opportunity to increase specific power of the radiation and its efficiency without any noticeable reduction in the discharge volume. All of this is possible by means of a transition from the traditional cylindrical to coaxial discharge geometry only. The results of [1, 2] make it possible to give a physical explanation to the experimental results obtained earlier in articles [3–7].

The results of papers [1, 2] were obtained under the assumption of strictly coaxial, concentric placement of tubes. However, such an ideal case is hard to translate into practice. Manufacturing errors often lead to an axial misalignment: eccentricity of the inner and outer tubes, i.e. to central asymmetry of both the device cross-section, and the profiles of charged particle densities as well.

This paper aimed to evaluate the quantitative influence the eccentricity of the discharge channel cross-section on the spatial distributions of plasma electron densities n and on the electron temperature T_e .

In this article we confine ourselves to the study of a simple case of a positive column of electropositive glow discharge in diffusion mode under low and moderate pressure: when the length of thermal diffusivity of the electrons is more than the outer plasma radius, and electron temperature T_e is constant inside the device cross-section. We assume the direct ionization by electron impact to be the main mechanism of charged particles production, while ambipolar

diffusion to the walls being the dominant mechanism of their decay.

Calculation methodology

Fig. 1 shows the discharge channel cross-section in eccentric geometry. The origin (point O) was chosen in the center of the inner circle with radius R_1 . The center of the outer circle with radius R (point O_R) is displaced from the origin by distance d . Angle φ is measured from the x axis. The discharge plasma is located between two said circles. The discharge current direction is perpendicular to xy plane.

The equation of spatial distribution of electrons density in the positive column under the conditions indicated above has the following form [8]:

$$D_A \Delta n + \nu_i n = 0,$$

where ν_i , Hz, is ionization frequency; D_A , cm²/s, is ambipolar diffusion coefficient; the values of ν_i and D_A do not depend on spatial coordinates due to assumed constancy of T_e .

Using a reduced coordinate $X = r / R$ and defining $\xi = R\sqrt{\nu_i / D_A}$, we obtain:

$$\frac{\partial^2 n}{\partial X^2} + \frac{1}{X} \frac{\partial n}{\partial X} + \frac{1}{X^2} \frac{\partial^2 n}{\partial \varphi^2} + \xi^2 n = 0. \quad (1)$$

We seek the solution of Eq. (1) as a product of two functions:

$$n = P(r)\Phi(\varphi).$$

Then Eq. (1) takes the form

$$\frac{X^2 P''}{P} + \frac{X P'}{P} + \xi^2 X^2 = -\frac{\Phi''}{\Phi} = k^2,$$

where k is a constant value.

Consequently, $\Phi'' = -k^2 \Phi$, or

$$\Phi(\varphi) = C_1^{(k)} \cos(k\varphi) + C_2^{(k)} \sin(k\varphi). \quad (2)$$

From a physical point of view, $\Phi(\varphi)$ is a periodic and even function by φ with the period of 2π . Therefore, k can have only integer values: $k = 0$,

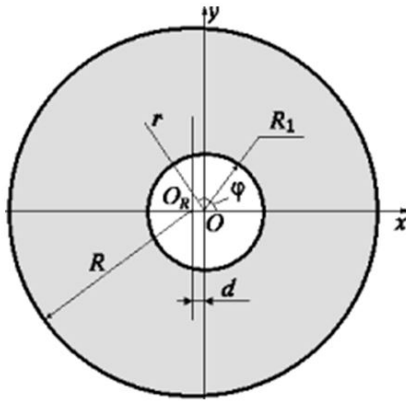


Fig. 1. Discharge channel cross-section (shaded area) in eccentric geometry: x, y and r, φ are Cartesian and cylindrical coordinate systems; d is eccentricity of the outer circle with respect to the inner one (their radii are equal to R and R_1 , respectively)

1, 2, ..., while $C_2^{(k)} = 0 \forall k$.

Function $P(r)$ satisfies the expression

$$P(r) = B_{k1} J_k(\xi X) + B_{k2} N_k(\xi X), \quad (3)$$

where $J_k(x)$, $N_k(x)$ — Bessel and Neumann functions of k^{th} order.

As general solution of Eq. (1) we obtain the following expression in the discharge cross-section:

$$n(X, \varphi) = \sum_{k=0}^{\infty} \{C_k \cos(k\varphi) \times [J_k(\xi X) + B_k N_k(\xi X)]\}, \quad (4)$$

where $B_{k1} = 1, B_{k2} \equiv B_k$ due to homogeneity of Eq.(1).

Boundary conditions on the inner circle correspond to the zero values:

$$n(\rho, \varphi) = 0 \forall \varphi, \quad (5)$$

where ρ is a reduced radius of the inner wall ($\rho = R_1 / R$); the boundary conditions on the outer wall are the same:

$$n(X_R, \varphi_R) = 0 \forall \varphi_R \in [0, 2\pi), \quad (6)$$

where X_R is the reduced radial coordinate of a point on the outer circle having the angle of its vision from the origin φ_R .

Values X_R and φ_R are connected by the relation (see Fig. 1):

$$X_R^2 + a^2 - 2X_R a \cos(\pi - \varphi_R) = 1,$$

where $a = d/R$, or

$$X_R = \sqrt{1 - a^2 \sin^2 \varphi_R} - a \cos \varphi_R. \quad (7)$$

The angle φ_R , like φ , is measured from x axis counterclockwise, and its angular point lies in the origin.

It follows from Eqs. (4) and (5) that

$$B_k = -\frac{J_k(\xi \rho)}{N_k(\xi \rho)} \forall k \in [0, 1, 2, \dots, \infty).$$

Then

$$n(X, \varphi) = \sum_{k=0}^{\infty} C_k \cos(k\varphi) \Omega_k(\xi, X), \quad (8)$$

where we have introduced a notation

$$\Omega_k(\xi, X) = J_k(\xi X) - \frac{J_k(\xi \rho)}{N_k(\xi \rho)} N_k(\xi X).$$

It follows from boundary conditions (6) that

$$\sum_{k=0}^{\infty} C_k \cos(k\varphi_R) \Omega_k(\xi, X_R) = 0, \quad (9)$$

where values φ_R and X_R are connected by the relation (7).

Eq. (8), provided we find coefficients C_k and eigenvalues ξ from Eq. (9), is an exact solution of problem (1) for the eccentric case. But if we set satisfaction of the boundary conditions (6) in all points of the outer circle, then to find coefficients C_k we need to solve a system of linear algebraic equations (9) of unlimited size.

Although, we should note that for $a \rightarrow 0$, when both the value of the gap between the walls and solution (8) do not depend on angle φ , and only one term remains in the sums (8) and (9) — namely by $k = 0$. In addition, Eq.(9) transforms

into a transcendental equation for eigenvalue ξ in the purely coaxial case:

$$\Omega_0(\xi, 1) = J_0(\xi) - \frac{J_0(\xi\rho)}{N_0(\xi\rho)} N_0(\xi) = 0, \quad (9a)$$

and expression (8) transforms into an equation

$$n(X, \varphi) \propto \Omega_0(\xi, X). \quad (9b)$$

Therefore, it is reasonable to assume that in the eccentric case for small deviations from the coaxial one, i.e., when a value is small, but finite ($a \ll 1$), we could take a finite number of terms M in the sums (8) and (9) to obtain an approximate solution of (1)¹:

$$n(X, \varphi) \approx \sum_{k=0}^{M-1} C_k \cos(k\varphi) \Omega_k(\xi, X), \quad (10)$$

$$\sum_{k=0}^{M-1} C_k \cos(k\varphi_R) \Omega_k(\xi, X_R) = 0. \quad (11)$$

Next, suppose M rays come from the origin O at angles

$$\varphi_j = \pi j / (M - 1), \quad j = 0, 1, \dots, (M - 1)$$

and divide the upper semi-circumference of the inner circle $X = \rho$ into $M - 1$ identical sectors. These rays cross the upper semi-circumference in the points with a reduced radial coordinates (see Eq. (7)):

$$X_j = \sqrt{1 - a^2 \sin^2\left(\frac{\pi j}{M - 1}\right)} - a \cos\left(\frac{\pi j}{M - 1}\right), \quad (12)$$

including the points on X axis for $\varphi = 0, \pi$.

To find an approximate solution, let us demand satisfaction of zero boundary conditions (6) not in all of points of the outer semi-cir-

cumference, but only in M of its upper points $\{X_j, \varphi_j\}$. Since the above boundary conditions are satisfied in its symmetrically located lower points by default, these zero conditions are finally satisfied in $(2M - 2)$ points on the entire outer semi-circumference. Then expression (11) transforms into the following:

$$\sum_{k=0}^{M-1} C_k \cos(k\varphi_j) \Omega_k(\xi, X_j) = 0; \quad j = 0, 1, \dots, M - 1, \quad (13)$$

which is a homogenous system of linear algebraic equations (linear system) having square matrix $M \times M$ with respect to a finite number M of coefficients C_k .

For the solution of system (13) to be non-trivial, its determinant must equal zero. From here we can find approximate values of the first M eigenvalues of problem (1). As function $n(X, \varphi)$ describing the density should never be less than zero between the circles (i.e. in the space occupied by the discharge plasma), only the eigenfunction corresponding to the smallest eigenvalue will have physical sense. It is the one we further substitute into Eq. (13).

Due to homogeneity of Eq. (1), its solution can be calculated up to a constant factor only. Therefore, we can compute coefficients C_k in relative units, assuming, for example, $C_0 = 1$. Then, the matrix column of linear system (13) that contains $C_0 = 1$ is moved to the right-hand side of the linear system. Thus, system (13) is transformed from a homogenous into an inhomogeneous, but overdetermined linear system containing M equations and $(M - 1)$ unknown coefficients C_1, C_2, \dots, C_{M-1} , which numerical values can be computed using the method of least squares.

The calculation showed that the values of coefficients C_k quickly decrease with the growth of k , so when $a \leq 0.2$ and $\rho \leq 0.5$, this proves the validity of the assumption that finiteness of the number of terms (10) and (11) brings no significant error in the solution of $n(X, \varphi)$. Fig. 2 demonstrates the quality of fulfillment of boundary conditions (9) for seven and two points of the upper semi-circumference and, re-

¹ The validity of this assumption is proved in further calculations.

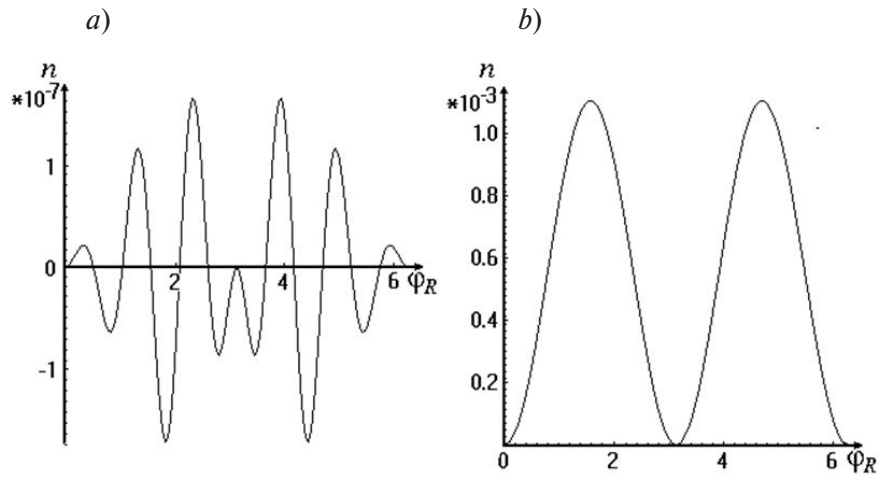


Fig. 2. Graphs of fulfillment of boundary conditions (9) at the outer circle if they are established exactly in $(2M - 2)$ points of the border; the cases presented are for $M = 7$ (a) and 2 (b); function $n(X, \varphi)$ at the maximum is assumed to be equal to 1

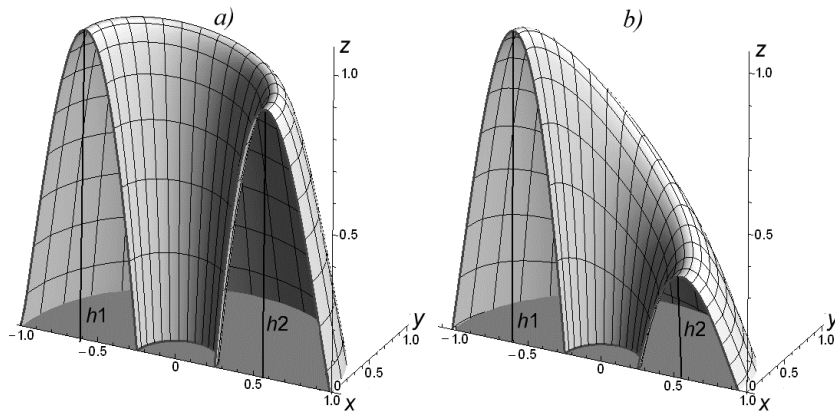


Fig. 3. 3D-distributions of function $n(X, \varphi)$ in the upper semi-circumference, i.e. when $y \geq 0$ (see Fig. 1) for the eccentricity values $a = 0.01$ (a) и 0.04 (b); reduced radius of the inner wall

spectively, for seven and two terms of sum (10). It can be seen that despite the small amount of points, boundary conditions (9) have satisfactory fulfillment at the entirety of the outer border: a difference in the solutions of $n(X, \varphi)$ for seven and two terms of (10) turns out to be inessential, and in the eigenvalues — in the third decimal place.

After calculating coefficients C_1, C_2, \dots, C_{M-1} variable $n(X, \varphi)$ is normalized to 1 at the maximum, while values C_0, C_1, \dots, C_{M-1} are recalculated once more.

Calculation results

Fig. 3 presents examples of solutions according to the described procedure.

We should note the high sensitivity of the form of $n(X, \varphi)$ to eccentricity: there is a considerable inhomogeneity of $n(X, \varphi)$ by the angle even at small values of a (see Fig. 3). The greater ρ , the stronger the inhomogeneity at the same value of a . Quantitatively it can be characterized by a ratio between the minimum and the maximum values of function $n(X, \varphi)$ on the “ridge” (see Fig. 3). A graph of this ratio h_2/h_1 vs a is shown on Fig. 4, a.

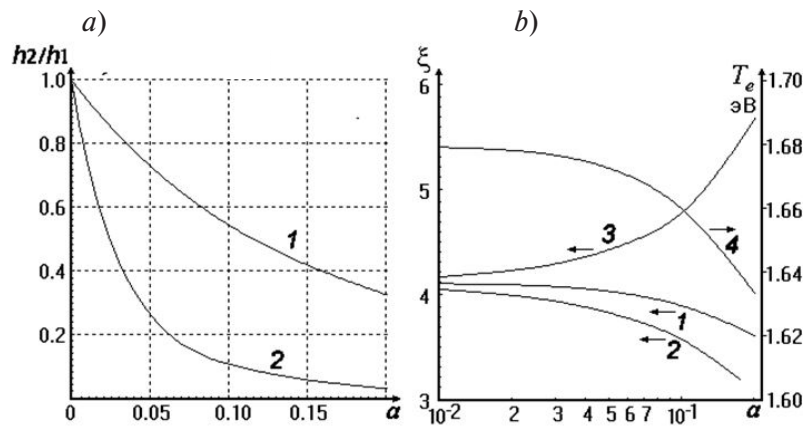


Fig. 4. Dependencies of the ratio h_2/h_1 (a), as well as eigenvalues ξ and plasma electron temperature T_e (b) on the eccentricity a of the gas-discharge tube.

Ratio h_2/h_1 (see Fig. 3) shows inhomogeneity of $n(X, \varphi)$ when $\rho = 0.05$ (1) and 0.25 (2). We also present diagrams of eigenvalues for eccentric (1) and coaxial (2, 3) cases with gaps $1 - \rho + a$ (2) and $1 - \rho - a$ (3); value of T_e (4) is calculated for Ar plasma at the pressure of 1 Torr and $R = 1$ cm for the eccentric case

Discussion of results

In the coaxial case, the width of the gap between the walls $b = 1 - \rho$ is constant and does not depend on φ . Due to central symmetry, in the coaxial case there is no other direction of the orthogonal to the current diffusion flow, except for the radial one.

The eigenvalue $\xi = R\sqrt{v_i/D_A}$ determines the value of temperature T_e , which in the case under consideration (low pressure) is constant across the whole positive column cross-section and corresponds to the equality of the rates of electrons production by direct ionization in the volume and their losses due to ambipolar diffusion to the walls in the radial direction [9, 10]. If we know the eigenvalue ξ , we can estimate the value of T_e both for the coaxial and eccentric discharge geometry using the following expression:

$$\xi = 8191 CpR \sqrt{1 + \frac{1}{2} \frac{W_i}{T_e}} \sqrt{\frac{T_e}{W_i}} \exp\left(-\frac{1}{2} \frac{W_i}{T_e}\right),$$

where W_i , eV, is ionization potential of gas atom; p , Torr, is gas pressure; R , cm, is radius of the outer wall; C is a constant, which values are tabulated in papers [9, 10] for various gases.

We deduced the presented expression in this paper using the relation obtained in papers [9,

10] which connects the value T_e with the tube radius and gas type for the cylindrical geometry of the positive column of glow discharge in diffusion mode.

For the eccentric case in the considered conditions of positive column, the value of T_e for small eccentricity has only weak deviation from the ideal coaxial case. An example of dependence of T_e on a for an Ar discharge at $p = 1$ Torr, $R = 1.00$ cm and $R_1 = 0.25$ cm is shown in Fig. 4, b (curve 4). The value of T_e decreases only insignificantly from 1.68 eV at $a = 0$ (coaxial geometry) down to 1.63 eV, when eccentricity $a = 0.2$. Let us note that, for the cylindrical geometry in the same conditions, the value of T_e would only amount to 1.51 eV.

In an eccentric discharge, the value of T_e also remains constant in the volume of positive column, which means that the ionization rate is constant in the entirety of the volume. However, the width of the gap between the walls b at $a > 0$ does not remain constant with the change of the angle φ . It changes from $b_{\min} = 1 - \rho - a$ at $\varphi = 0$ to $b_{\max} = 1 - \rho + a$ at $\varphi = \pi$ (see Fig. 1), therefore the rate of radial diffusive removing should depend on the angle φ : it should be maximal at b_{\min} and minimal at b_{\max} . The calculations show that the eigenvalue ξ for $a > 0$ (see Fig. 4, b, curve 1) has intermediate value between

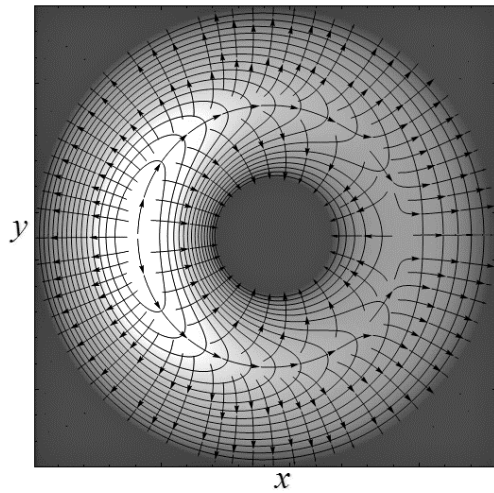


Fig. 5. Spatial distribution of $n(X, \varphi)$ (expressed by brightness and contours), as well as directions of electron flows in plasma cross-section (arrowhead lines) in eccentric discharge geometry for $\rho = 0.25$ and $a = 0.04$. The “compensating” flow goes in azimuthal direction over the ridge of the $n(X, \varphi)$ distribution

the ones for two control coaxial cases: with the gaps equal to b_{\max} and b_{\min} (curves 2 and 3, respectively). This means that for the eccentric case, in the neighborhood of angle $\varphi \approx 0$ (where the gap is the narrowest) the ionization rate turns out to be insufficient to compensate for the radial diffusive removing of the particles to the walls, while in the area of $\varphi \approx \pi$ (widest gap) it is excessive.

This result should lead to the following effects:

firstly, to increasing of electron (and ion) density and its gradient in the neighborhood of widest gap, and to decreasing of the said parameters in the narrowest gap in comparison with the coaxial case $a = 0$, i.e. to the occurrence of azimuthally inhomogeneous distribution of $n(X, \varphi)$ (see Fig. 3);

secondly, for the density distributed in this manner, there is an azimuthal gradient $\text{grad}_{\varphi}[n(X, \varphi)]$ and a corresponding diffusion

electron flow in the azimuthal direction that “pumps” the electrons from the wide gap into the narrow one on both sides of the inner wall (Fig. 5). This flow compensates for the excessive generation of electrons in the wide gap, as well as the extra electron losses due to diffusive removing to the walls in the narrow gap; by such a way the balance of charged particles can be throughout ensured. However, the inhomogeneity of $n(X, \varphi)$ from the angle φ still remains, since the said flow compensating for the imbalance of the rates of production and decay of charged particles in different areas of positive column cross-section can take place only in the presence of the azimuthal density gradient. It is necessary to note that the presence of a gradient of electron densities directed on average from the narrow gap to the wide one will cause a constant electric field directed on average along x axis. It should retard the described electron diffusion in the azimuthal direction to the ambipolar one.

Conclusion

Summing up, the absence of central symmetry of the spatial distribution of the positive column plasma density in the eccentric discharge geometry can be considered as a characteristic feature of plasma in this geometry, which is in fact responsible for maintaining the charged particles balance of plasma in the entire volume dedicated to it. Insignificant eccentricity has only little impact on the value of electron temperature T_e . However, to retain acceptable azimuthal homogeneity of the discharge after the transition from the cylindrical to coaxial geometry, it is necessary to provide good accuracy of the gas-discharge device manufacturing: the distance between the axes of the inner and the outer cylindrical walls should not exceed 1–2% of the width of the gap between the walls.

REFERENCES

1. Golovitskii A.P., Coaxial (tubular) glow discharge in electronegative gases, *Technical Physics*. 61 (7) (2016) 995–1003.
2. Golovitskii A.P., Remiga O.A., The electronegative glow discharge in the cylindrical and coaxial geometry: the comparison of optical radiation

emission ability, St. Petersburg State Polytechnical University Journal. Physics and Mathematics. 12 (3) (2019) 92–100.

3. **Panchenko A.N., Skakun V.S., Sosnin E.A., et al.**, High-power coaxial excilamps with an average power of over 100 Watts, Tech. Phys. Lett. 21 (10) (1995) 851–852.

4. **Lomaev M.I., Panchenko A.N., Skakun V.S. et al.**, Exilamps producing up to 130 W of output power and possibility of its applications, Laser and Particle Beams. 15 (2) (1997) 339–345.

5. **Panchenko A.N., Sosnin E.A., Tarasenko V.F.**, Improvement of output parameters of glow discharge UV exilamps, Optics Communications. 161 (4–6) (1999) 249–252.

6. **Golovitskii A.P.**, Low-pressure inductive rf discharge in a rare gas-halogen mixture for economical mercury-free luminescence light sources,

Tech. Phys. Lett. 24 (6) (1998) 233–234.

7. **Golovitskii A., Pelli A.**, Specific power of ultraviolet radiation from rf middle pressure discharge in a mixture of inert gas and chlorine, Proceedings of the 9th International Conference on Plasma Physics and Plasma Technology (PPPT-9), Minsk, Belarus, Sept. 17 – 21 (2018) 61–64.

8. **Golant V.E., Zhilinskii A.P., Sakharov I.E.**, Fundamentals of plasma physics, John Wiley & Sons, New York, 1980.

9. **Granovskii V.L.**, Elektricheskiy tok v gaze. Ustanovivshisya tok [Flow of electricity in the gas. The steady-state current], Edited by L.A. Sena, V.E. Golant, Nauka, Moscow, 1971 (in Russian).

10. **Von Engel A., Steenbeck M.**, Elektrische Gasentladungen: ihre Physik und Technik, Verlag von Julius Springer, Berlin, 1934.

Received 29.10.2020, accepted 02.11.2020.

THE AUTHORS

GOLOVITSKII Alexander P.

Peter the Great St. Petersburg Polytechnic University

29 Politechnicheskaya St., St. Petersburg, 195251, Russian Federation

alexandergolovitski@yahoo.com

KORENYUGIN Dmitry G.

Peter the Great St. Petersburg Polytechnic University

29 Politechnicheskaya St., St. Petersburg, 195251, Russian Federation

polarisdk@mail.ru

СПИСОК ЛИТЕРАТУРЫ

1. **Головицкий А.П.** Коаксиальный (трубчатый) тлеющий разряд в электроотрицательных газах // Журнал технической физики. 2016. Т. 86. № 7. С. 38–45.

2. **Головицкий А.П., Ремига О.А.** Сравнение способности испускания оптического излучения электроотрицательного тлеющего разряда в цилиндрической и коаксиальной геометрии // Научно-технические ведомости СПбГПУ. Физико-математические науки. 2019. Т. 12. № 3. С. 101–109.

3. **Панченко А.Н., Скакун В.С., Соснин Э.А., Тарасенко В.Ф., Ломаев М.И.** Мощные коак-

сиальные эксилампы со средней мощностью более 100 Вт // Письма в Журнал технической физики. 1995. Т. 21. Вып. 20. С. 77–80.

4. **Lomaev M.I., Panchenko A.N., Skakun V.S., Sosnin E.A., Tarasenko V.F., Adamson M.G., Myers B.R., Wanga F.T.** Exilamps producing up to 130 W of output power and possibility of its applications // Laser and Particle Beams. 1997. Vol. 15. No. 2. Pp. 339–345.

5. **Panchenko A.N., Sosnin E.A., Tarasenko V.F.** Improvement of output parameters of glow discharge UV exilamps // Optics Communications. 1999. Vol. 161. No. 4–6. Pp. 249–252.



6. Головицкий А.П. Индуктивный высоко-частотный разряд низкого давления в смеси инертных газов и галогенов для экономичных безртутных люминесцентных источников света // Письма в Журнал технической физики. 1998. Т. 24. Вып. 6. С. 63–67.
7. Golovitskii A., Pelli A. Specific power of ultra-violet radiation from rf middle pressure discharge in a mixture of inert gas and chlorine // Proceedings of the 9th International Conference on Plasma Physics and Plasma Technology (PPPT-9). Minsk, Belarus, Sept. 17 – 21, 2018. Pp. 61–64.
8. Голант В.Е., Жилинский А.П., Сахаров И.Е. Основы физики плазмы. М.: Атомиздат, 1977. 384 с.
9. Грановский В.Л. Электрический ток в газе. Установившийся ток. Под ред. Л.А. Сена и В.Е. Голанта. М.: Наука. Главная редакция физико-математической литературы, 1971. 544 с.
10. Von Engel A., Steenbeck M. Elektrische Gasentladungen: ihre Physik und Technik. Berlin: Verlag von Julius Springer, 1934. 352 S.

Статья поступила в редакцию 29.10.2020, принята к публикации 02.11.2020.

СВЕДЕНИЯ ОБ АВТОРАХ

ГОЛОВИЦКИЙ Александр Петрович — доктор физико-математических наук, профессор Высшей инженерно-физической школы Санкт-Петербургского политехнического университета Петра Великого, Санкт-Петербург, Российская Федерация.

195251, Российская Федерация, г. Санкт-Петербург, Политехническая ул., 29
alexandergolovitski@yahoo.com

КОРЕНЮГИН Дмитрий Геннадиевич — старший преподаватель Высшей инженерно-физической школы Санкт-Петербургского политехнического университета Петра Великого, Санкт-Петербург, Российская Федерация.

195251, Российская Федерация, г. Санкт-Петербург, Политехническая ул., 29
polarisdsk@mail.ru

COPPER-64 ISOTOPE PRODUCTION THROUGH THE CYCLOTRON PROTON IRRADIATION OF THE NATURAL-NICKEL TARGET

A. Tiba, A.Yu. Egorov, Ya.A. Berdnikov, V.N. Lomasov

Peter the Great St. Petersburg Polytechnic University,
St. Petersburg, Russian Federation

A method of calculation has been developed as well numerical simulation have been performed for a production process of ^{64}Cu isotope by the ^{64}Ni (p, n) ^{64}Cu nuclear reaction. The required radionuclide applicable in the nuclear medicine is produced through irradiating a cyclotron target of natural nickel with a proton beam. The process conditions were dictated by the capabilities of the cyclotron; the initial kinetic energy of 17 MeV (at a current of 10 μA) was fed into computation. As a result, dependencies of the ^{64}Cu isotope production on the target thickness and on the irradiation time were obtained. The target depth of proton penetration was investigated, and it was established where the peak of radionuclide concentration was produced. An analysis of the obtained data allowed us to find the optimal thickness of the nickel target, which is 0.54 mm.

Keywords: copper-64, natural nickel, yield calculation, target thickness, proton beam

Citation: Tiba A., Egorov A.Yu, Berdnikov Ya.A., Lomasov V.N., Copper-64 isotope production through the cyclotron proton irradiation of the natural-nickel target, St. Petersburg Polytechnical State University Journal. Physics and Mathematics. 14 (1) (2021) 130–137. DOI: 10.18721/JPM.14110

This is an open access article under the CC BY-NC 4.0 license (<https://creativecommons.org/licenses/by-nc/4.0/>)

ПРОИЗВОДСТВО ИЗОТОПА МЕДИ-64 ПУТЕМ ОБЛУЧЕНИЯ ЦИКЛОТРОННОЙ МИШЕНИ ИЗ ПРИРОДНОГО НИКЕЛЯ ПУЧКОМ ПРОТОНОВ

А. Тиба, А.Ю. Егоров, Я.А. Бердников, В.Н. Ломасов

Санкт-Петербургский политехнический университет Петра Великого,
Санкт-Петербург, Российская Федерация

Разработана методика расчета и выполнено численное моделирование процесса получения изотопа меди-64 по ядерной реакции ^{64}Ni (p, n) ^{64}Cu . Требуемый радионуклид, применяемый в ядерной медицине, производится путем облучения мишени из природного никеля пучком протонов, получаемым на циклотроне. Условия проведения процесса диктовались возможностями циклотрона. В расчеты закладывалась начальная кинетическая энергия протонов 17 МэВ (ток равен 10 мкА). В результате получены зависимости наработки изотопа меди-64 от толщины мишени и от времени облучения, изучена глубина проникновения протонов в мишень, установлено, где концентрация ядер наработанного радионуклида максимальна. Анализ полученных данных позволил определить оптимальную толщину никелевой мишени, она составила 0,54 мм.

Ключевые слова: медь-64, природный никель, расчет выхода, толщина мишени, пучок протонов

Ссылка при цитировании: Горобей Н.Н., Лукьяненко А.С., Гольцев А.В. Собственная масса Вселенной // Научно-технические ведомости СПбГПУ. Физико-математические науки. 2021. Т. 14. № 1. С. 130–137. DOI: 10.18721/JPM.14110



Introduction

As known, radiology and radiation therapy are based on the use of various radiopharmaceuticals containing radioactive isotopes. Among the radionuclides belonging to different elements, Cu-64 isotope is unique due to its capability to emit β^+ -, β^- particles (their energies equal 0.65 and 0.57 MeV, and their yield values are 17.5 and 38.5%, respectively) and Auger electrons as a result of its radioactive decay. Therefore, this isotope is applicable in both positron emission tomography (PET), as well as in theranostics (theranostics focuses on producing pharmaceuticals which can be simultaneously applied as a means of early diagnosis and as a therapeutic agent) [1, 2]. The isotope's considerable advantages over others lie not only in its chemical properties, but also in its long half-life (12.7 h) allowing simplification of production, transportation and application of Cu-64 labeled radiopharmaceuticals in comparison with those in common use nowadays.

The possibility of reduction of cupric Cu^{2+} to cuprous Cu^+ is used in molecular imaging and targeted radiotherapy of hypoxic tissues, including tumors [3, 4].

Clinical trials of ^{64}Cu based pharmaceuticals showed copper uptake only in hypoxic heart and brain cells. Peptides and antibodies radiolabeled with this isotope can also be applied in medical radiology [5–8].

A comparison of ^{64}Cu labeled radiopharmaceuticals and those based on ^{111}In -Octreoscan which is currently in use showed the advantage of the former as a positron-emitter for it allowed imaging even for some unpredicted metastatic growth [9]. Clinical testing of the ^{64}Cu -TETA-mab1A3 conjugate (applied in colorectal cancer detection) demonstrated the advantage of PET with ^{64}Cu over the similarly ^{111}In labeled conjugate [10–12].

The ^{64}Cu radionuclide can be produced in reactors by means of capturing either $^{63}\text{Cu}(n, \gamma)^{64}\text{Cu}$ thermal neutrons or $^{64}\text{Zn}(n, p)^{64}\text{Cu}$ fast neutrons (n, p are neutrons and protons, γ are gamma rays).

The isotope can be produced in a cyclotron by the $^{64}\text{Ni}(p, n)^{64}\text{Cu}$ nuclear reaction [13].

However, the ^{64}Cu production yield in reactors is low, while their radionuclidic purity is often unsatisfactory [13]. Therefore, the use of cyclotrons in the ^{64}Cu production becomes necessary since they support charged particles induced reactions. Both natural and enriched (by 99.6%) nickel can serve as a target for the ^{64}Cu production in cyclotrons.

The purpose of this article is to develop a method of calculation, and the corresponding algorithm and program, as well as to conduct a numerical simulation of the ^{64}Cu production by means of irradiating a natural nickel target with a proton beam.

Numerical parameters of the model were determined by the characteristics of the MGC-20 cyclotron located in Peter the Great St. Petersburg Polytechnic University: proton energy of 17 MeV at a current of 10 μA . The numerical simulation allowed us to determine the optimal target thickness for the maximum yield of the desired isotope.

Method of calculation

As it was noted before, for the ^{64}Cu production, we used a proton beam with the initial energy of 17 MeV (current of 10 μA). A natural ^{64}Ni isotopic mixture (the percentage of ^{64}Ni isotope in the natural nickel amounts to 0.926%) serves as the target.

The computations allow for proton energy losses due to excitation and ionization resulting from the passage through of the target substance [14]:

$$\left\langle -\frac{dE}{dx} \right\rangle = \frac{Kz^2Z\rho}{A\beta^2} \left[\frac{1}{2} \ln \left(\frac{2m_e c^2 \beta^2 \gamma^2 W_{\max}}{I^2} \right) - \beta^2 - \frac{\delta(\beta_\gamma)}{2} \right], \quad (1)$$

where $-dE/dx$, MeV/cm, are specific ionization losses (x is the depth of proton penetration); z , Z are charge numbers of the projectile particle and the target respectively; A , g/mol, is atomic mass; ρ , g/cm³, is the target density; m_e , g, electron mass; c , cm/s, – the speed of light; β is a ratio of the projectile particle velocity to the speed of light ($\beta = v/c$); γ is the Lorentz factor; W_{\max} , MeV, is maximum energy transfer in a unit collision; I , eV, is mean ionization potential; $\delta(\beta\gamma)$ is a correction factor allowing for the influence of the target density on the ionization potential.

The K coefficient is calculated by the formula

$$K = 4\pi N_A r_e^2 m_e c^2 = 0.307 \text{ MeV/mol},$$

where N_A is the Avogadro constant; r_e , cm, is the classical electron radius.

The maximum energy transfer is expressed as

$$W_{\max} = \frac{2m_e c^2 \beta^2 \gamma^2}{\left[1 + \frac{2\gamma m_e}{M} + \left(\frac{m_e}{M}\right)^2\right]},$$

where M , g, is the mass of the projectile particle.

The Ni mean ionization potential is equal to (just as for other elements) $I = 311 \pm 10$ eV [15].

We should note that in a nonrelativistic case $\beta^2 \ll 1$; furthermore, a proton ($z = 1$, $M \gg m_e$) is the projectile particle, the energy loss occurs at all Ni isotope electron shells in natural nickel, i.e., $\rho = \rho_{\text{Ni}} = 8.908$ g/cm³; $A = \langle A \rangle = 58.6934$ g/mol. Then, Eq. (1) is simplified:

$$\left\langle -\frac{dE}{dx} \right\rangle = \left(\frac{KZ\rho}{A\beta^2} \right) \ln \left[\frac{2m_e c^2 \beta^2}{I} \right]. \quad (2)$$

The solution to Eq. (2) gives a dependence $E(x)$ of the mean proton energy on the depth of proton penetration.

The Cu⁶⁴ isotope is produced by means of the Ni⁶⁴ (p, n) Cu⁶⁴ reaction. Energy dependence of this reaction cross section $\sigma(E)$ was measured in many experiments. This article used the results of the combined data presented in paper [16].

Using the solution to Eq. (2), let us determine the dependence of the reaction cross section on the depth of proton penetration $\sigma(x)$. The Cu⁶⁴ production at different depths of target penetration is then determined by the formula:

$$\frac{dN_{\text{Cu}64}}{dx} = \left(\frac{J n_{\text{Ni}64}}{\lambda e} \right) \times (1 - \exp(-t \lambda_{\text{rad}})) \sigma(x), \quad (3)$$

where $N_{\text{Cu}64}$ is the number of ⁶⁴Cu isotope nuclides; J , A, is the cyclotron current; $n_{\text{Ni}64}$ is ⁶⁴Ni nuclides concentration in the natural nickel; λ is the ⁶⁴Cu decay constant; e , C, is the electron charge; t_{rad} , s, is the time of the target irradiation.

By integrating Eq. (3) from zero to the target thickness τ , we obtain a distribution of the ⁶⁴Cu production with respect to the isotope penetration:

$$N_{\text{Cu}64}(\tau, t_{\text{rad}}) = \int_0^\tau dx \left\{ \frac{dN_{\text{Cu}64}}{dx} \right\}, \quad (4)$$

In this case, we can disregard a decrease in intensity of the proton beam with the increasing of the target depth, as well other processes resulting in proton loss. The obtained formula does not consider the cooling time of the target which can be allowed for by multiplying it by an exponential factor of the $\exp(-\lambda t_{\text{cool}})$ form. It can be seen from Eq. (3) that at $t_{\text{rad}} \approx 3/\lambda$, there is no point in any further irradiation as the accumulation curve reaches a plateau.

Such a behavior of the dependence is due to a gradual appearance of commensurability of the isotope production and its decay rates. However, the value of $1/\lambda$ for ⁶⁴Cu equals to 18.3 h, which significantly exceeds the real time of irradiation. At $t_{\text{rad}} \ll 1/\lambda$ the factor

$$[1 - \exp(-\lambda t_{\text{rad}})]/\lambda \approx t_{\text{rad}},$$

i.e., the production is proportional to time.

Results of the used method and discussion

The solution to Eq. (2) is presented in Fig. 1, *a* for the protons of the initial kinetic en-

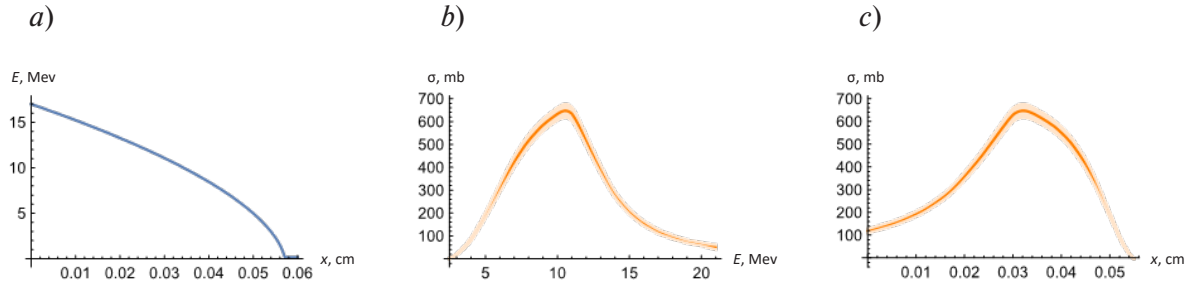


Fig. 1. Proton energy distribution throughout the depth of the natural nickel target (solution to Eq. (2)) (a) and dependence of the $^{64}\text{Ni}(p, n)^{64}\text{Cu}$ reaction cross section on the proton energy (b) and on the target depth (c). Initial kinetic proton energy is 17 MeV; in Fig. b) and c), the lines show the “cross section” curves behavior, while the bands correspond to the cross section error [16]

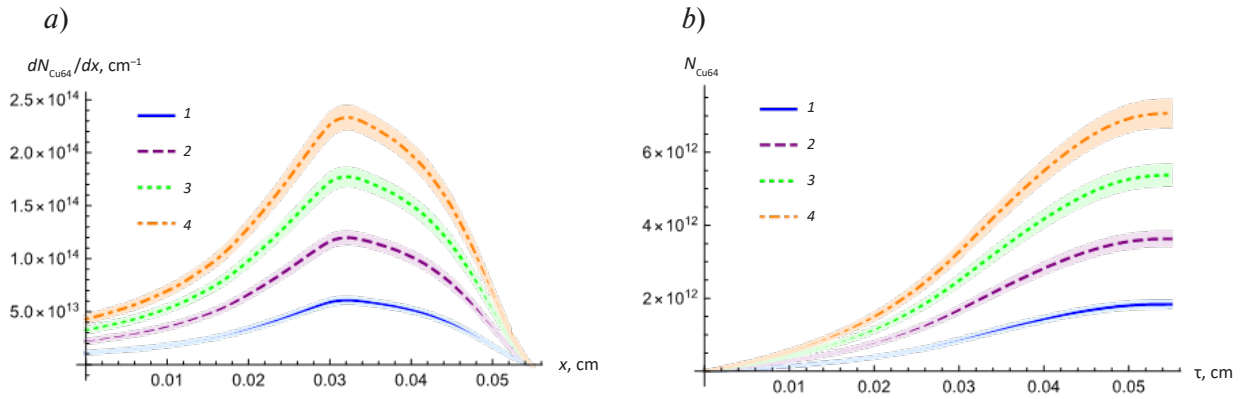


Fig. 2. Ionization loss distribution of ^{64}Cu nuclides throughout the depth of target penetration (a) and dependencies of the number of the produced nuclides on the target thickness (b) for different irradiation intervals, h : 0.5 (1), 1.0 (2), 1.5 (3), 2.0 (4). The lines show the dependencies curves, while the bands correspond to their error (connected with the reaction cross section errors)

ergy of 17 MeV and the natural nickel target. We can see that the protons lose all of their energy at the 0.56 mm target depth.

Fig. 1,b shows the result of interpolating the reaction cross section (3), obtained in paper [16]. By processing this dependence and using the solution of Eq. (2) we found a dependence of the cross section on the target depth (Fig. 1,c). It is clear that the cross section is maximal at the proton energy of approximately 10 MeV, which is reached at the depth of around 0.32 mm. At the same depth, we also observe the peak concentration of the produced ^{64}Cu radionuclides.

Fig. 2,a shows the computational results of ^{64}Cu number distribution throughout the depth for various irradiation intervals (we took a range

from 0.5 to 2 h, see Eq. (3)). Fig. 2,b presents the results of integrating dependence (4) with respect to the target thickness τ for the same irradiation intervals.

Fig. 3 shows the results of computing the number of the produced ^{64}Cu nuclides depending on two irradiation intervals (5 and 50 h) for four values of the target thickness. We can see that for the 5 h irradiation interval the number of the produced nuclides grows in a linear manner and with a fair degree of accuracy, while for the longer period of time the growth levels off after the saturation point.

An analysis of the obtained data allows us to conclude that the peak ^{64}Cu production is achieved at the target thickness of 0.545 ± 0.006 mm. The error is primarily due to the equivocation arising

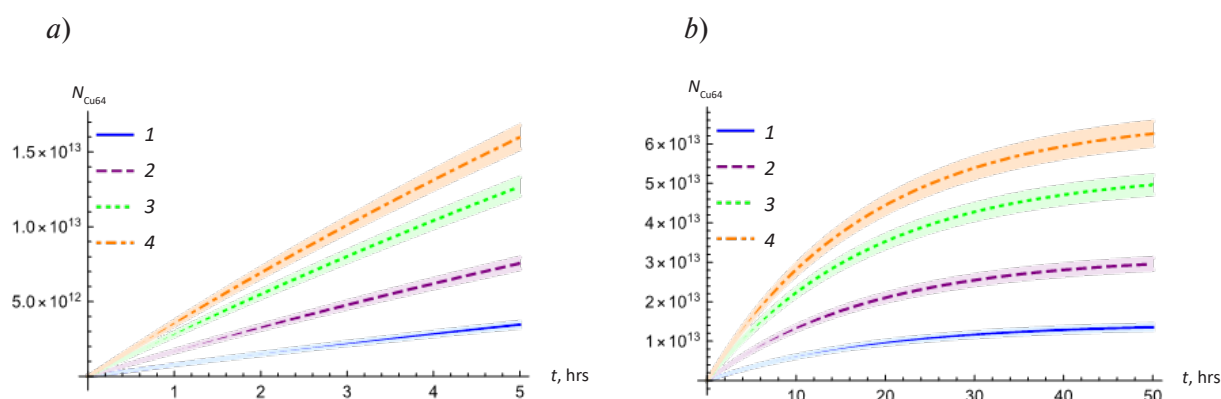


Fig. 3. Dynamics of the number of accumulated ^{64}Cu nuclides in 5 h (a) and 50 h (b) of irradiating the target of different thickness τ , mm: 0.2 (1), 0.3 (2), 0.4 (3), 0.5 (4). The lines show the dependencies curves, while the bands correspond to their error (connected with the reaction cross section errors)

from measuring the cross section $\sigma(E)$ [16] at the reaction energy threshold of 2.5 MeV (we allowed for the equivocation from using the simplified Eq. (2) instead of the complete Eq. (1)). Any further increase of the target thickness should not lead to an increase in the production as at greater thickness values the mean proton energy falls below the reaction energy threshold. The peak ^{64}Cu nuclide concentration lies at the target depth from 0.20 to 0.49 mm.

Thus, we can consider the identified target thickness value, i.e. 0.545 ± 0.006 mm, optimal for the maximum production number of the ^{64}Cu isotope.

Conclusion

This article developed a design procedure and numerical simulation of a production process

for ^{64}Cu isotope important for application in the nuclear medicine. The process of the ^{64}Cu isotope through irradiating a target of natural nickel with a proton beam obtained in a cyclotron. The initial kinetic energy of protons was 17 MeV at a current of 10 μA .

By means of computations we obtained dependencies of the ^{64}Cu isotope production on the target thickness and on the time of irradiation. We identified the depth of target penetration at which the nuclide concentration of the produced isotope reaches its peak.

As a result of the conducted simulation of the process, we found the optimal target thickness, which is 0.54 mm, to produce the maximum number of the ^{64}Cu isotope. The obtained result is essential for diagnostics and therapy of various diseases applied in nuclear medicine.

REFERENCES

1. Fujibayashi Y., Taniuchi H., Wada K., et al., Differential mechanism of retention of Cu-pyruvaldehyde-bis(N4-methylthiosemicarbazone) (Cu-PTSM) by brain and tumor: A novel radiopharmaceutical for positron emission tomography imaging, *Annals of Nuclear Medicine*. 9 (1) (1995) 1–5.
2. Philpott G.W., Schwarz S.W., Anderson C.J., et al., Radioimmuno PET: Detection of colorectal carcinoma with positron-emitting copper-64-labeled monoclonal antibody, *Journal of Nuclear Medicine*. 36 (10) (1995) 1818–1824.
3. Blower P.J., Lewis J.S., Zweit J., Copper radionuclides and radiopharmaceuticals in nuclear medicine, *Nuclear Medicine and Biology*. 23 (8) (1996) 957–980.
4. Bass L.A., Wang M., Welch M.J., Anderson C.J., In vivo transchelation of copper-64 from TE-



TA-octreotide to superoxide dismutase in rat liver, *Bioconjugate Chem.* 11 (4) (2000) 527–532.

5. **Sprague J.E., Peng Y., Sun X., et al.**, Preparation and biological evaluation of copper-64-labeled tyr3-octreotate using a cross-bridged macrocyclic chelator, *Clinical Cancer Research*. 10 (24) (2004) 8674–8682.

6. **Oh M., Tanaka T., Kobayashi M., et al.**, Radio-copper-labeled Cu-ATSM: an indicator of quiescent but clonogenic cells under mild hypoxia in a Lewis lung carcinoma model, *Nuclear Medicine and Biology*. 36 (4) (2009) 419–426.

7. **Boswell C.A., Regino C.A.S., Baidoo K.E., et al.**, A novel side-bridged hybrid phosphonate/acetate pendant cyclam: Synthesis, characterization, and ^{64}Cu small animal PET imaging, *Bioorganic & Medicinal Chemistry*. 17 (2) (2009) 548–552.

8. **Holland J.P., Ferdani R., Anderson C.J., Lewis J.S.**, Copper-64 radiopharmaceuticals for oncologic imaging, *PET Clinics*. 4 (1) (2009) 49–67.

9. **Hoffman T.J., Smith C.J.**, True radiotracers: Cu-64 targeting vectors based upon bombesin peptide, *Nuclear Medicine and Biology*. 36 (6) (2009) 579–585.

10. **Kiani S., Staples R.J., Treves S.T., Packard A.B.**, Synthesis and characterization of a tetramethyl furanone functionalized diiminedioxime, a potential ligand for ^{64}Cu radiopharmaceuticals, and its copper(II) and nickel(II) complexes, *Polyhedron*. 28 (4) (2009) 775–785.

11. **Matarrese M., Bedeschi P., Scardaoni R., et al.**, Automated production of copper radioisotopes and preparation of high specific activity [^{64}Cu]Cu-ATSM for PET studies, *Applied Radiation and Isotopes*. 68 (1) (2010) 5–13.

12. **Pfeifer A., Knigge U., Mortensen J., et al.**, Clinical PET of neuroendocrine tumors using ^{64}Cu -DOTATATE: First-in-humans study, *Journal of Nuclear Medicine*. 53 (8) (2012) 1207–1215.

13. **Zweit J., Smith A.M., Downey S., Sharma H.L.**, Excitation functions for deuteron induced reactions in natural nickel: Production of no-carrier-added ^{64}Cu from enriched ^{64}Ni targets for positron emission tomography, *International Journal of Radiation Applications and Instrumentation, Part A. Applied Radiation and Isotopes*. 42 (2) (1991) 193–197.

14. **Tanabashi M., Hagiwara K., Hikasa K., et al.**, (Particle Data Group), Review of particle physics, *Physical Review, D*. 98 (3) (2018) 030001.

15. **Seltzer S.M., Berger M.J.**, Evaluation of the collision stopping power of elements and compounds for electrons and positrons, *The International Journal of Applied Radiation and Isotopes*. 33 (11) (1982) 1189–1218.

16. **Aslam M.N., Sudár S., Hussain M., et al.**, Charged particle induced reaction cross section data for production of the emerging medically important positron emitter ^{64}Cu : A comprehensive evaluation, *Radiochimica Acta*. 97 (12) (2009) 669–686.

Received 19.10.2020, accepted 09.02.2021.

THE AUTHORS

TIBA Ali

Peter the Great St. Petersburg Polytechnic University

29 Politechnicheskaya St., St. Petersburg, 195251, Russian Federation
alitiba1991@gmail.com

EGOROV Anatoliy Yu.

Peter the Great St. Petersburg Polytechnic University

29 Politechnicheskaya St., St. Petersburg, 195251, Russian Federation
egorov.a@spbstu.ru

BERDNIKOV Yaroslav A.

Peter the Great St. Petersburg Polytechnic University

29 Politechnicheskaya St., St. Petersburg, 195251, Russian Federation
berdnikov@spbstu.ru

LOMASOV Vladimir N.

Peter the Great St. Petersburg Polytechnic University

29 Politechnicheskaya St., St. Petersburg, 195251, Russian Federation

lomasov_vn@spbstu.ru

СПИСОК ЛИТЕРАТУРЫ

1. **Fujibayashi Y., Taniuchi H., Wada K., Yonekur Y., Konishi J., Yokoyama A.** Differential mechanism of retention of Cu-pyruvaldehyde-bis(N4-methylthiosemicarbazone) (Cu-PTSM) by brain and tumor: A novel radiopharmaceutical for positron emission tomography imaging // *Annals of Nuclear Medicine*. 1995. Vol. 9. No. 1. Pp. 1–5.
2. **Philpott G.W., Schwarz S.W., Anderson C.J., Dehdashti F., Connett J.M., Zinn K., Meares C.F., Cutler P.D., Welsh M.J., Siegel B.A.** Radioimmuno PET: Detection of colorectal carcinoma with positron-emitting copper-64-labeled monoclonal antibody // *Journal of Nuclear Medicine*. 1995. Vol. 36. No. 10. Pp. 1818–1824.
3. **Blower P.J., Lewis J.S., Zweit J.** Copper radionuclides and radiopharmaceuticals in nuclear medicine // *Nuclear Medicine and Biology* 1996. Vol. 23. No. 8. Pp. 957–980.
4. **Bass L.A., Wang M., Welch M.J., Anderson C.J.** In vivo transchelation of copper-64 from TE-TA-octreotide to superoxide dismutase in rat liver // *Bioconjugate Chemistry*. 2000. Vol. 11. No. 4. Pp. 527–532.
5. **Sprague J.E., Peng Y., Sun X., Weisman G.R., Wong E.H., Achilefu S., Anderson C.J.** Preparation and biological evaluation of copper-64-labeled tyr3-octreotate using a cross-bridged macrocyclic chelator // *Clinical Cancer Research*. 2004. Vol. 10. No. 24. Pp. 8674–8682.
6. **Oh M., Tanaka T., Kobayashi M., Furukawa T., Mori T., Kudo T., Fujieda S., Fujibayashi Y.** Radio-copper-labeled Cu-ATSM: an indicator of quiescent but clonogenic cells under mild hypoxia in a Lewis lung carcinoma model // *Nuclear Medicine and Biology*. 2009. Vol. 36. No. 4. Pp. 419–426.
7. **Boswell C.A., Regino C.A.S., Baidoo K.E., Wong K.J., Milenic D.E., Kelley J.A., Lai C.C., Brechbiel M.W.** A novel side-bridged hybrid phosphonate/acetate pendant cyclam: Synthesis, characterization, and ^{64}Cu small animal PET imaging // *Bioorganic & Medicinal Chemistry*. 2009. Vol. 17. No. 2. Pp. 548–552.
8. **Holland J.P., Ferdani R., Anderson C.J., Lewis J.S.** Copper-64 radiopharmaceuticals for oncologic imaging // *PET Clinics*. 2009. Vol. 4. No. 1. Pp. 49–67.
9. **Hoffman T.J., Smith C.J.** True radiotracers: Cu-64 targeting vectors based upon bombesin peptide // *Nuclear Medicine and Biology*. 2009. Vol. 36. No. 6. Pp. 579–585.
10. **Kiani S., Staples R.J., Treves S.T., Packard A.B.** Synthesis and characterization of a tetramethyl furanone functionalized diiminedioxime, a potential ligand for ^{64}Cu radiopharmaceuticals, and its copper(II) and nickel(II) complexes // *Polyhedron*. 2009. Vol. 28. No. 4. Pp. 775–785.
11. **Matarrese M., Bedeschi P., Scardaoni R., et al.** Automated production of copper radioisotopes and preparation of high specific activity [^{64}Cu] Cu-ATSM for PET studies // *Applied Radiation and Isotopes*. 2010. Vol. 68. No. 1. Pp. 5–13.
12. **Pfeifer A., Knigge U., Mortensen J., et al.** Clinical PET of neuroendocrine tumors using ^{64}Cu -DOTATATE: First-in-humans study // *Journal of Nuclear Medicine*. 2012. Vol. 53. No. 8. Pp. 1207–1215.
13. **Zweit J., Smith A.M., Downey S., Sharma H.L.** Excitation functions for deuteron induced reactions in natural nickel: Production of no-carrier-added ^{64}Cu from enriched ^{64}Ni targets for positron emission tomography // *International Journal of Radiation Applications and Instrumentation. Part A. Applied Radiation and Isotopes*. 1991. Vol. 42. No. 2. Pp. 193–197.
14. **Tanabashi M., Hagiwara K., Hikasa K., et al.** (Particle Data Group). Review of Particle Physics // *Physical Review. D*. 2018. Vol. 98. No. 3. P. 030001.
15. **Seltzer S.M., Berger M.J.** Evaluation of

the collision stopping power of elements and compounds for electrons and positrons // The International Journal of Applied Radiation and Isotopes. 1982. Vol. 33. No. 11. Pp. 1189–1218.

16. **Aslam M.N., Sudár S., Hussain M., Ma-**

lik A.A., Shah H.A., Qaim S.M. Charged particle induced reaction cross section data for production of the emerging medically important positron emitter ^{64}Cu : A comprehensive evaluation // Radiochimica Acta. 2009. Vol. 97. No. 12. Pp. 669–686.

Статья поступила в редакцию 19.10.2020, принята к публикации 09.02.2021.

СВЕДЕНИЯ ОБ АВТОРАХ

ТИБА Али — аспирант Высшей инженерно-физической школы Санкт-Петербургского политехнического университета Петра Великого, Санкт-Петербург, Российская Федерация.

195251, Российская Федерация, г. Санкт-Петербург, Политехническая ул., 29
alitiba1991@gmail.com

ЕГОРОВ Анатолий Юрьевич — ассистент Высшей инженерно-физической школы Санкт-Петербургского политехнического университета Петра Великого, Санкт-Петербург, Российская Федерация.

195251, Российская Федерация, г. Санкт-Петербург, Политехническая ул., 29
egorov.a@spbstu.ru

БЕРДНИКОВ Ярослав Александрович — доктор физико-математических наук, профессор Высшей инженерно-физической школы Санкт-Петербургского политехнического университета Петра Великого, Санкт-Петербург, Российская Федерация.

195251, Российская Федерация, г. Санкт-Петербург, Политехническая ул., 29
berdnikov@spbstu.ru

ЛОМАСОВ Владимир Николаевич — кандидат физико-математических наук, старший научный сотрудник, руководитель лабораторий научно-технологического комплекса «Ядерная физика» Санкт-Петербургского политехнического университета Петра Великого, Санкт-Петербург, Российская Федерация.

195251, Российская Федерация, г. Санкт-Петербург, Политехническая ул., 29
lomasov_vn@spbstu.ru

DOI: 10.18721/JPM.14111

UDC 530.12:517.988.38(075.8)

THE PROPER MASS OF THE UNIVERSE

N.N. Gorobey¹, A.S. Lukyanenko¹, A.V. Goltsev²

¹ Peter the Great St. Petersburg Polytechnic University,
St. Petersburg, Russian Federation;

² Ioffe Institute of the Russian Academy of Sciences,
St. Petersburg, Russian Federation

A modification of the covariant theory based on the concept of the proper mass (mass distribution) of the system is proposed. The proper mass is a special dynamic quantity that forms a fundamental frame of reference for measuring proper time and spatial shifts without violating the theory's covariance. A simple model of an inhomogeneous system (universe, string) with two proper time parameters, whose constraint algebra is isomorphic to SL_2 , is considered.

Keywords: universe, time, mass, covariance, reference frame, algebra of constraints

Citation: Gorobey N.N., Lukyanenko A.S., Goltsev A.V., The proper mass of the universe, St. Petersburg Polytechnical State University Journal. Physics and Mathematics. 14 (1) (2021) 138–145. DOI: 10.18721/JPM.14111

This is an open access article under the CC BY-NC 4.0 license (<https://creativecommons.org/licenses/by-nc/4.0/>)

СОБСТВЕННАЯ МАССА ВСЕЛЕННОЙ

Н.Н. Горобей¹, А.С. Лукьяненко¹, А.В. Гольцев²

¹ Санкт-Петербургский политехнический университет Петра Великого,
Санкт-Петербург, Российская Федерация;

² Физико-технический институт им. А.Ф. Иоффе РАН,
Санкт-Петербург, Российская Федерация

Предложена модификация ковариантной теории, основанная на понятии собственной массы (распределение масс) системы. Собственная масса является особой динамической величиной, которая образует фундаментальную систему отсчета для измерения собственного времени и пространственных сдвигов без нарушения ковариантности теории. Рассмотрена простая модель неоднородной системы (Вселенная, струна) с двумя параметрами собственного времени, алгебра связей которой изоморфна SL_2 .

Ключевые слова: Вселенная, время, масса, ковариантность, система обсчета, алгебра связей

Ссылка при цитировании: Горобей Н.Н., Лукьяненко А.С., Гольцев А.В. Собственная масса Вселенной // Научно-технические ведомости СПбГПУ. Физико-математические науки. 2021. Т. 14. № 1. С. 138–145. DOI: 10.18721/JPM.14111

Статья открытого доступа, распространяемая по лицензии CC BY-NC 4.0 (<https://creativecommons.org/licenses/by-nc/4.0/>)

Introduction

The quantization of covariant theories, to which we include gauge theories with constraints linear in momenta, as well as the theory of grav-

ity and string theory with quadratic in momenta (Hamiltonian) constraints, makes it necessary to expand their phase space by including Lagrange multipliers and ghosts along with the correspond-



ing canonical momenta [1 – 6]. However, in the simplest case of the reparametrization-invariant theory of a relativistic particle, all this construction is reduced to introducing the particles proper time parameter into the initial action, followed by integrating the wave function over this parameter within $[0, \infty)$ [7]. The result is a representation of the Feynman propagator of a particle, which was first proposed by V.A. Fock [8] and J. Schwinger [9]. Based on this, a simplified procedure for quantizing the covariant theory was proposed in Ref. [10], in which the parameters of finite symmetry transformations (including the proper time in reparameterization-invariant theories) are introduced into the classical theory as additional coordinates.

The equations of constraints in quantum theory with this modification take the form of evolution equations on a group space, and the invariant propagator is obtained after integrating the wave function over the group parameters over the entire area of their variation (for proper time, these are the functional space (FS) integrals within $[0, \infty)$ with a simple measure equal to 1. However, in contrast to gauge theories with linear momentum constraints, FS integrals are not removed by delta functions from Hamiltonian constraints. This means that in quantum theory there is no time parameter. In Ref. [11], to solve the problem of time in the case of a homogeneous isotropic model of the universe, the second stage of modification is proposed, in which an additional condition is imposed on the dynamics of proper time as an independent dynamic variable. It consists in adding to the initial action its small variation generated by the infinitesimal shift of proper time. As a result, a new quantity arises in the theory – mass-energy, which corresponds to its own time. In a homogeneous universe, this quantity is an integral of motion and must be added to the original set of constants of the universe. In Ref. [11], it was also suggested that the mass of the universe, taking into account the multi-turnaround of time in the general case [12], will have the character of a distribution, which should be supplemented by the corresponding mass flux density. The purpose of this work is to substantiate this assumption by the example of a simple dynamical system with

two proper time parameters and with the algebra of constraints identical to $SL(2, R)$. In this case, we will have two components of its own mass and a flow between them. These three parameters are not integrals of motion. They are present in the energy-momentum balance of the system (constraint equations), and should be considered as observable quantities. Their equations of motion, together with the equations of constraints, make it possible to remove integration over the parameters of proper time and thereby solve the problem of time in the quantum theory.

The first stage of modification of $SL(2, R)$ -model

The initial Lagrange function of the considered dynamic system has the form:

$$L = \frac{1}{2N_1}(\dot{u} - N_3 u)^2 + \frac{1}{2N_3}(\dot{v} + N_3 v)^2 + \frac{N_1}{2}v^2 + \frac{N_2}{2}u^2, \quad (1)$$

where the dot denotes derivatives with respect to an arbitrary parameter τ ; N_1, N_2 are the lapse functions, N_3 is the shift function [12].

Minkowski indices $u_\mu, v_\nu, \mu, \nu = 0, 1, 2, 3$ are implied and abbreviated notation for the invariants of the Minkowski space are used.

Hamilton's function is reduced to a linear combination of constraints

$$h = N_1 H_1 + N_2 H_2 + N_3 D, \quad (2)$$

where

$$H_1 = \frac{1}{2}(p^2 - v^2), \quad H_2 = \frac{1}{2}(\pi^2 - u^2), \quad (3)$$

$$D = pu - \pi v.$$

The Poisson brackets of these constraints form the algebra $SL(2, R)$ [13]:

$$\begin{aligned} \{D, H_1\} &= 2H_1, \quad \{D, H_2\} = -2H_2, \\ \{H_1, H_2\} &= D. \end{aligned} \quad (4)$$

This algebra will serve us as the simplest analogue of the algebra of constraints of the theory of gravity (and string [14]). The constraints are generators of infinitesimal symmetry transformations of the canonical variables, which are compensated by the transformation of the lapse and shift functions [1],

$$\delta N_\alpha = \dot{\varepsilon}_\alpha - C_{\beta\gamma\alpha} N_\beta \varepsilon_\gamma, \quad (5)$$

which ensures the invariance of the action (in this case $C_{311} = 2$, $C_{322} = -2$, $C_{123} = 1$).

At the first stage of the modification of the dynamic theory, as additional generalized coordinates, we introduce the parameters of finite symmetry transformations that arise as a result of the integration of the system of functional differential equations:

$$N_\beta = \dot{s}_\alpha \Lambda_{\alpha\beta}, \quad (6)$$

where the functions $\Lambda_{\alpha\beta}$ obey the system of differential equations [10]:

$$\begin{aligned} & \frac{\partial \Lambda_{\alpha\beta}}{\partial s_\gamma} - \frac{\partial \Lambda_{\gamma\beta}}{\partial s_\alpha} + \\ & + \Lambda_{\alpha\delta} \Lambda_{\gamma\omega} C_{\delta\omega\beta} = 0. \end{aligned} \quad (7)$$

The modified theory is obtained by substituting (6) into the original Lagrange function (1).

The modified Hamilton function reduces to a linear combination of modified constraints

$$\begin{aligned} & p_{s_\alpha} - \Lambda_{\alpha 1} H_1 - \\ & - \Lambda_{\alpha 2} H_2 - \Lambda_{\alpha 3} D = 0, \end{aligned} \quad (8)$$

which form a closed algebra with trivial Poisson brackets.

It is these constraints, in quantum theory that have the form of evolution equations on a group space with coordinates s_α . Since these coordinates are not observable, one should take additional integrals over them of the wave function over the entire range of their variation on the manifold of the group. For the parameters of proper time, these are the integrals of the FS within $[0, \infty)$. As

a result of this integration, the wave function loses its dynamic meaning. It is necessary to take the next step in modifying the original theory [11], which will remove additional integrals.

Second stage of the theory modification

Considering the coordinates on the group space as independent dynamic variables, we take their classical equations of motion as additional conditions. The latter are obtained as a result of the infinitesimal shift of these variables $s_\alpha \rightarrow s_\alpha + \varepsilon_\alpha$ in the action.

Thus, the finally modified Lagrange function takes the form:

$$\begin{aligned} \tilde{L} = & \frac{1}{2} \left[\frac{(\dot{u} - N_3 u)^2}{N_1} + v^2 N_1 \right]^2 + \\ & + \frac{1}{2} \left[\frac{(\dot{v} + N_3 v)^2}{N_2} + u^2 N_2 \right]^2 - \\ & - \frac{1}{2} \left[\frac{(\dot{u} - N_3 u)^2}{N_1^2} + v^2 \right] \delta N_1 - \\ & - \frac{1}{2} \left[\frac{(\dot{v} + N_3 v)^2}{N_2^2} + u^2 \right] \delta N_2 - \\ & - \left[u \frac{(\dot{u} - N_3 u)}{N_1} - v \frac{(\dot{v} + N_3 v)}{N_2} \right] \delta N_3. \end{aligned} \quad (9)$$

Below we will see that this modification significantly changes the theory in the right direction – the removal of the integrals of the FS over its group evolution parameters.

We turn to the Hamiltonian form of the modified theory. Let's find the canonical momenta:

$$p = \frac{(\dot{u} - N_3 u)}{N_1} \left(1 - \frac{\delta N_1}{N_1} \right) - u \frac{\delta N_3}{N_1}, \quad (10)$$

$$\pi = \frac{(\dot{v} + N_3 v)}{N_2} \left(1 - \frac{\delta N_2}{N_2} \right) + v \frac{\delta N_3}{N_2}, \quad (11)$$

$$p_{s_\alpha} = -H_1 \Lambda_1^\beta - H_2 \Lambda_2^\beta -$$



$$\begin{aligned}
 & -H_1 \frac{\partial \Lambda_1^\beta}{\partial s_\gamma} \varepsilon_\gamma - H_2 \frac{\partial \Lambda_2^\beta}{\partial s_\gamma} \varepsilon_\gamma - \\
 & -D \frac{\partial \Lambda_3^\beta}{\partial s_\gamma} \varepsilon_\gamma + \\
 & + \frac{(\dot{u} - N_3 u)^2}{N_1^2} \frac{\delta N_1}{N_1} \Lambda_1^\beta + \\
 & + \frac{(\dot{v} + N_3 v)^2}{N_2^2} \frac{\delta N_2}{N_2} \Lambda_2^\beta + \\
 & + u \frac{(\dot{u} - N_3 u)}{N_1} \frac{\delta N_3}{N_1} \Lambda_1^\beta - \\
 & - v \frac{(\dot{v} + N_3 v)}{N_2} \frac{\delta N_3}{N_2} \Lambda_2^\beta, \\
 P_{\varepsilon_\beta} = & -H_1 \Lambda_1^\beta - H_2 \Lambda_2^\beta - D \Lambda_3^\beta.
 \end{aligned} \quad (12)$$

The Hamilton function, as expected, is reduced to a linear combination of new constraints, which are here used by Eqs. (12).

In these equations, velocities should be eliminated by expressing them in terms of canonical momenta. First, eliminate the variation $\delta N_1, \delta N_2, \delta N_3$. To do this, we use the old constraints that are contained in Eqs. (13) together with the new dynamic variables, which are the two components of the mass distribution in our model universe and the mass flow. We express the old connections through new dynamic variables by solving Eqs. (13) using a triple of 3-vectors $\Omega_\beta^1, \Omega_\beta^2, \Omega_\beta^3$, each of which is orthogonal to the corresponding additional pair of column vectors $\Lambda_1^\beta, \Lambda_2^\beta, \Lambda_3^\beta$:

$$\begin{aligned}
 H_1 = & -\frac{(P_\varepsilon, \Omega^1)}{(\Omega^1, \Lambda_1)}, \quad H_2 = -\frac{(P_\varepsilon, \Omega^2)}{(\Omega^2, \Lambda_2)}, \\
 D = & -\frac{(P_\varepsilon, \Omega^3)}{(\Omega^3, \Lambda_3)}.
 \end{aligned} \quad (14)$$

We find the variations $\delta N_1, \delta N_2$ from the Hamiltonian constraints:

$$\begin{aligned}
 1 - \frac{\delta N_1}{N_1} = & \frac{\sqrt{\left(p + u \frac{\delta N_3}{N_1}\right)^2}}{\sqrt{H_1 + v^2}}, \\
 1 - \frac{\delta N_2}{N_2} = & \frac{\sqrt{\left(\pi - v \frac{\delta N_3}{N_2}\right)^2}}{\sqrt{H_2 + u^2}},
 \end{aligned} \quad (15)$$

and for the variations δN_3 the momentum constraint remains:

$$\begin{aligned}
 D = & \frac{u \left(p + u \frac{\delta N_3}{N_1} \right)}{1 - \frac{\delta N_1}{N_1}} - \\
 & - \frac{v \left(\pi - v \frac{\delta N_3}{N_2} \right)}{1 - \frac{\delta N_2}{N_2}}.
 \end{aligned} \quad (16)$$

which we cannot solve explicitly.

We only note that the variation δN_3 is a homogeneous function of the first degree of the canonical momenta, as well as Eqs. (15), which contain square roots. After that, we can substitute the velocities (10), (11) in Eqs. (12) and obtain the required equations of new constraints.

Leaving these constraints in the same implicit form, we write the modified action in the canonical form:

$$\begin{aligned}
 \tilde{I} \doteq & \int d\tau \left[p\dot{u} + \pi\dot{v} + p_{s_\alpha} \dot{s}_\alpha - \right. \\
 & \left. - \dot{P}_{\varepsilon_\alpha} \varepsilon_\alpha - \tilde{N}_\alpha \left(p_{s_\alpha} - \tilde{h}_\alpha \right) \right],
 \end{aligned} \quad (17)$$

where \tilde{h}_α denotes the right hand side of the Eqs. (12).

Here we consider infinitesimal shifts as canonical momenta. We will see the solution to the problem of time in our “universe” when we exclude momenta in this canonical form of action and write it again in Lagrangian form. We can do this explicitly.

Proper time

We will be the first to exclude the momenta p_{s_α} conjugated to the group parameters s_α . As a result, we get $\tilde{N}_\alpha = \dot{s}_\alpha$. Next we exclude infinitesimal shifts. This gives the equations of motion in the form of the law of the change in time of new dynamic variables:

$$\begin{aligned} Q_\gamma = \dot{P}_{\varepsilon_\alpha} + \\ + \frac{(P_\varepsilon, \Omega^1)}{(\Omega^1, \Lambda_1)} \frac{\partial \Lambda_1^\beta}{\partial s_\gamma} \dot{s}_\beta + \frac{(P_\varepsilon, \Omega^2)}{(\Omega^2, \Lambda_2)} \frac{\partial \Lambda_2^\beta}{\partial s_\gamma} \dot{s}_\beta + \\ + \frac{(P_\varepsilon, \Omega^3)}{(\Omega^3, \Lambda_3)} \frac{\partial \Lambda_3^\beta}{\partial s_\gamma} \dot{s}_\beta = 0. \end{aligned} \quad (18)$$

The last ones we exclude the canonical momenta corresponding to the "physical" degrees of freedom – the Minkowski coordinates u_μ , v_ν . Here the difficulty remains associated with the absence of an explicit solution of the constraint equations with respect to variations δN_1 , δN_2 , δN_3 . However, it is easy to see that the resulting dependence of the modified Hamiltonian on the canonical momenta is a homogeneous function of the first degree. The consequence is that all terms in the canonical action (17), depending on the canonical momenta, disappear.

Thus, the dependence of the modified action on all velocities disappears, except for the one contained in the equations of motion (18), as well as in the old constraints (4), which we must now remember and add to the action as additional conditions. We also recall that the implicit solution of these constraints involves the operation of extracting a square root with a choice of the sign of this root. We must perform the same operation under additional conditions, writing down the Hamiltonian constraints with square roots of the kinetic energies of the physical degrees of freedom. As a result, we get the modified action in the form

$$\tilde{I} \doteq \int d\tau \times$$

$$\begin{aligned} \times \left\{ \varepsilon_\beta Q_\beta + \lambda_1 \left[\sqrt{(\dot{u} - N_3 u)^2} - N_1 \sqrt{v^2 - \frac{(P_\varepsilon, \Omega^1)}{(\Omega^1, \Lambda_1)}} \right] + \right. \\ + \lambda_2 \left[\sqrt{(\dot{v} + N_3 v)^2} - N_2 \sqrt{u^2 - \frac{(P_\varepsilon, \Omega^2)}{(\Omega^2, \Lambda_2)}} \right] + \\ + \lambda_3 \left[\sqrt{\frac{N_2}{N_1}} u (\dot{u} - N_3 u) - \right. \\ \left. - \sqrt{\frac{N_1}{N_2}} v (\dot{v} + N_3 v) - \sqrt{N_1 N_2} \frac{(P_\varepsilon, \Omega^3)}{(\Omega^3, \Lambda_3)} \right] + \\ \left. + N_1 \left[\frac{(P_\varepsilon, \Omega^1)}{(\Omega^1, \Lambda_1)} - v^2 \right] + N_2 \left[\frac{(P_\varepsilon, \Omega^2)}{(\Omega^2, \Lambda_2)} - u^2 \right] \right\}, \end{aligned} \quad (19)$$

where additional conditions are included with the corresponding Lagrange multipliers λ_1 , λ_2 , λ_3 . Infinitesimal shifts ε_β also fulfill their original function of the Lagrange multipliers.

Note that the modified Lagrange function is a homogeneous first-order velocity function, so that the theory remains explicitly reparameterization-invariant.

In the quantum theory, in the representation of a propagator in the form of a functional integral, integration over the Lagrange multipliers gives the product of the corresponding functional delta functions that remove functional integration over group parameters s_α , as well as over additional parameters P_{ε_α} . The dynamics of the latter, considered by us as observables, serves to measure their proper time in the universe. If we do not allow the introduction of new observables and set $P_\varepsilon = 0$, the additional equations of motion for them also disappear. Then the FS integrals are removed by δ -functions from the initial constraints, which have the same meaning as the first integral,

$$\int \frac{dq}{\sqrt{E - U(q)}} = t, \quad (20)$$



defining time in mechanics.

Any physical degree of freedom can play the role of proper time in this case.

Conclusions

A modification of the covariant dynamical theory with constraint algebra SL_2 is inspired by the problem of time in quantum theory. The usual practice in this case of imposing additional gauge conditions violating the covariance has been replaced by a modification of the original theory at the classical level, which does not violate the covariance of the dynamics of the physical degrees of freedom. Additional conditions in it are imposed on the physically unobserva-

ble parameters of symmetry transformations – proper time (for each point of the "universe" its own) and the spatial shift between points. However, the modification turns out to be deeper, adding new dynamical variables to the balance of energy and momentum of physical degrees of freedom, which should be considered observable. The dynamics of these observables can serve to measure proper time and spatial shifts, forming the fundamental frame of reference in the universe.

Acknowledgement

The authors thank V.A. Franke for useful discussions.

REFERENCES

1. **Faddeev L.D., Slavnov A.A.**, Gauge fields: An introduction to quantum theory, 2nd edition, Westview Press, 1993.
2. **Fradkin E.S., Vilkovisky G.A.**, Quantization of relativistic systems with constraints, Phys. Lett. B. 55 (2) (1975) 224–226.
3. **Batalin I.A., Vilkovisky G.A.**, Relativistic S -matrix of dynamical systems with boson and fermion constraints, Phys. Lett. B. 69 (3) (1977) 309–312.
4. **Henneaux M.**, Hamiltonian form of the path integral for theories with a gauge freedom, Phys. Rep. 126 (1) (1985) 1–66.
5. **Kugo T., Ojima I.**, Local covariant operator formalism of non-Abelian gauge theories and quark confinement problem, Progr. Theor. Phys. Suppl. 66 (February) (1979) 1–130.
6. **Ore F.R., van Nieuwenhuisen P.**, Local {BRST} symmetry and the geometry of gauge-fixing, Nucl. Phys. B. 204 (2) (1982) 317–332.
7. **Govaerts J.**, A note on the Fradkin – Vilkovisky theorem, CERN-TH 5010/88 (1988).
8. **Fock V.A.**, The eigen-time in classical and quantum mechanics, Phys. Zs. Sowjet. 12 (4) (1937) 404–425 (in German).
9. **Schwinger J.**, On gauge invariance and vacuum polarization, Phys. Rev. 82 (5) (1951) 664–679.
10. **Gorobey N., Lukyanenko A.**, Time and observables in covariant quantum theory, arXiv:2001.09003[gr-qc], 2020.
11. **Gorobey N., Lukyanenko A., Goltsev A.**, Feynman propagator for a system of interacting scalar particles in the Fokker theory, arXiv:2002.03607v1[quant-ph], 2020.
12. **Misner C.W., Thorne K. S., Wheeler J.A.**, Gravitation, Princeton University Press, New Jersey, USA, 2017.
13. **Montesions M., Rovelli C., Thiemann T.**, $SL(2, \mathbb{R})$ model with two Hamiltonian constraints, Phys. Rev. D. 60 (4) (1999) 044009.
14. **Green M.B., Schwarz J.H., Witten E.**, Superstring theory, Vol. 1: Introduction, Cambridge University Press, 1987.

Received 03.08.2020, accepted 23.10.2020.

THE AUTHORS

GOROBEY Natalia N.

Peter the Great St. Petersburg Polytechnic University

29 Politechnicheskaya St., St. Petersburg, 195251, Russian Federation

n.gorobey@mail.ru

LUKYANENKO Alexander S.

Peter the Great St. Petersburg Polytechnic University

29 Politechnicheskaya St., St. Petersburg, 195251, Russian Federation

alex.lukyan@rambler.ru

GOLTSEV Alexander V.

Ioffe Institute of RAS

26, Politekhnikeskaya, St. Petersburg, 195251, Russian Federation

gorobej_nn@spbstu.ru

СПИСОК ЛИТЕРАТУРЫ

1. **Славнов А.А., Фаддеев Л.Д.** Введение в квантовую теорию калибровочных полей. 2-е изд. М.: Наука. 1988. 272 с.
2. **Fradkin E.S., Vilkovisky G.A.** Non-perturbation methods in 2 dimensional quantum field theory // Phys. Lett. B. 1975. Vol. 55. No. 2. Pp. 224–226.
3. **Batalin I.A., Vilkovisky G.A.** Relativistic S-matrix of dynamical systems with boson and fermion constraints // Phys. Lett. B. 1977. Vol. 69. No. 3. Pp. 309–312.
4. **Henneaux M.** Hamiltonian form of the path integral for theories with a gauge freedom // Phys. Rep. 1985. Vol. 126. No. 1. Pp. 1–66.
5. **Kugo T., Ojima I.** Local covariant operator formalism of non-Abelian gauge theories and quark confinement problem // Progr. Theor. Phys. Suppl. 1979. Vol. 66. February. Pp. 1–130.
6. **Ore F.R., van Nieuwenhuisen P.** Local {BRST} symmetry and the geometry of gauge-fixing // Nucl. Phys. B. 1982. Vol. 204. No. 2. Pp. 317–332.
7. **Govaerts J.** A note on the Fradkin – Vilkovisky theorem // CERN-TH 5010/88, 1988. 21 p.
8. **Фок В.А.** Собственное время в классической и квантовой механике // Известия АН СССР. Серия физическая. 1937. № 4–5. С. 551–568.
9. **Schwinger J.** On gauge invariance and vacuum polarization // Phys. Rev. 1951. Vol. 82. No. 5. Pp. 664–679.
10. **Gorobey N., Lukyanenko A.** Time and observables in covariant quantum theory// arXiv:2001.09003 [gr-qc] (2020).
11. **Gorobey N., Lukyanenko A.** Feynman propagator for a system of interacting scalar particles in the Fokker theory // arXiv:2002.03607v1 [quant-ph] (2020).
12. **Misner C.W., Thorne K.S., Wheeler J.A.** Gravitation. New Jersey, USA: Princeton University Press, 2017. 1279 p.
13. **Montesions M., Rovelli C., Thiemann T.** SL(2, R) model with two Hamiltonian constraints // Phys. Rev. D. 1999. Vol. 60. No. 4. P. 044009.
14. **Green M.B., Schwarz J.H., Witten E.** Superstring theory. Vol. 1. Introduction. Cambridge: Cambridge University Press, 1987. 469 p.

Статья поступила в редакцию 03.08.2020, принята к публикации 23.10.2020.

СВЕДЕНИЯ ОБ АВТОРАХ

ГОРОБЕЙ Наталья Николаевна — доктор физико-математических наук, профессор кафедры физики Санкт-Петербургского политехнического университета Петра Великого, Санкт-Петербург, Российская Федерация.

195251, Российская Федерация, г. Санкт-Петербург, Политехническая ул., 29

n.gorobey@mail.ru

ЛУКЬЯНЕНКО Александр Сергеевич — доктор физико-математических наук, профессор кафедры физики Санкт-Петербургского политехнического университета Петра Великого, Санкт-Петербург, Российская Федерация.

195251, Российская Федерация, г. Санкт-Петербург, Политехническая ул., 29
alex.lukyan@rambler.ru

ГОЛЫЦЕВ Александр Викторович — доктор физико-математических наук, профессор, старший научный сотрудник Физико-технического института им. А.Ф. Иоффе, Санкт-Петербург, Российская Федерация.

195251, Российская Федерация, г. Санкт-Петербург, Политехническая ул., 26
golysev@ua.pt

DOI: 10.18721/JPM.14112
UDC 519.816

MAKING A COLLECTIVE EXPERT DECISION BASED ON THE NEUMANN – PEARSON ALGORITHM

V.I. Antonov¹, V.V. Garbaruk², V.N. Fomenko²

¹ Peter the Great St. Petersburg Polytechnic University,
St. Petersburg, Russian Federation;

² Petersburg State Transport University,
St. Petersburg, Russian Federation

In the article, we consider the possibility of processing voting results in the case of a team of experts with different efficiency in assessing the situation. The experts were expected to decide whether or not a patient is suffering from a specific disease. The most intelligent combination of the individual expert's votes into a collective council's decision was required. Our algorithm was based on the Neumann – Pearson principle of minimizing the type II error probability at the fixed type I error probability. The team of experts with different qualifications was shown to be able to draw a correct conclusion with high probability.

Keywords: team of experts, assessment efficiency, Neumann and Pearson method

Citation: Antonov V.I., Garbaruk V.V., Fomenko V.N., Making a collective expert decision based on the Neumann – Pearson algorithm, St. Petersburg Polytechnical State University Journal. Physics and Mathematics. 14 (1) (2021) 146–154. DOI: 10.18721/JPM.14112

This is an open access article under the CC BY-NC 4.0 license (<https://creativecommons.org/licenses/by-nc/4.0/>)

ПРИНЯТИЕ КОЛЛЕКТИВНОГО ЭКСПЕРТНОГО РЕШЕНИЯ НА ОСНОВЕ АЛГОРИТМА НЕЙМАНА – ПИРСОНА

В.И. Антонов¹, В.В. Гарбарук², В.Н. Фоменко²

¹ Санкт-Петербургский политехнический университет Петра Великого,
Санкт-Петербург, Российская Федерация;

² Петербургский государственный университет путей сообщения
Императора Александра I, Санкт-Петербург, Российская Федерация

В статье рассмотрена возможность обработки результатов голосования в случае коллектива экспертов с различной эффективностью оценки ситуации. Предполагалось, что эксперты должны решить вопрос о наличии или отсутствии у пациента конкретного заболевания. Требовалось наиболее разумно объединить голоса отдельных экспертов в коллективное решение консилиума. В основу построения такого алгоритма был положен метод минимизации вероятности ошибки второго рода при фиксированной вероятности ошибки первого рода (алгоритм Неймана – Пирсона). Показано, что совет, состоящий из экспертов с различной квалификацией, может с большой вероятностью приходить к правильному выводу.

Ключевые слова: коллектив экспертов, эффективность оценки, метод Неймана и Пирсона

Ссылка при цитировании: Антонов В.И., Гарбарук В.В., Фоменко В.Н. Принятие коллективного экспертного решения на основе алгоритма Неймана – Пирсона // Научно-технические ведомости СПбГПУ. Физико-математические науки. 2021. Т. 14. № 1. С. 146–154. DOI: 10.18721/JPM.14112

Статья открытого доступа, распространяемая по лицензии CC BY-NC 4.0 (<https://creativecommons.org/licenses/by-nc/4.0/>)



Introduction

Drawing a difficult and non-standard conclusion, as a rule, requires an opinion supplied by a group of experts. In case of selecting several decisions, to arrange the possible options provided by the experts, paired comparison method, ranking, and other methods are used [1, 2]. When choosing a single solution, it is assumed that all experts are equally professional, and an option is considered accepted if it received the maximum number of votes. Many papers [3 – 8] consider the features and drawbacks of such a manner of votes processing.

In the article, we consider the possibility of processing voting results in the case of a team of experts with different efficiency in the situation assessment. It is also implied that the experts need to choose only one of two options. Such an alternative is common, for example, in the course of a medical council when deciding on a certain diagnosis. Using their experience and the data on a certain patient available, the experts attempt to identify which of the two situations they are dealing with: whether a patient is suffering from a specific disease or not.

A necessity of such a choice occurs not only in the medical field. Expert experience is in demand in consulting companies [9], academic and work councils. There is a binary choice, for example, when assigning a candidate to the head position in a company, when there is a need for a decision on whether the candidate has all the essential leader qualities and whether he or she is effective in the future. The experts can also participate in decision making concerning the feasibility of revolutionary enterprise reforming, involvement in a certain investment project, etc.

Application of optimal

Neumann – Pearson algorithm to make a collective expert decision

Assume that an expert team consists of G homogenous groups with N_g number of experts in each group. The experts are believed to make decisions independently, including the cases inside one group. Homogenous group can be formed on the basis of their previous work in different medical councils. These groups can be represented by

various healthcare facility departments, in each of which voting takes place. The employees of one department may have similar views on the disease symptoms.

Let us denote the a $p_A^{(g)}$ probability that an expert doctor of a g group takes a healthy patient for a healthy one, and a $p_B^{(g)}$ probability that the expert doctor takes an ill patient for a healthy one. Those are conditional probabilities that the expert says “healthy” in situations A and B , respectively. The experts are united in one g group because they have the same probability values $p_A^{(g)}$ and $p_B^{(g)}$. Then the probabilities that the expert is right equal $p_A^{(g)}$ and $1 - p_B^{(g)}$. The probabilities of the right choice may be equal to or satisfy either a $p_A^{(g)} > 1 - p_B^{(g)}$ inequality or a $p_A^{(g)} < 1 - p_B^{(g)}$ inequality. The latter inequality in the medical field, for instance, characterizes a doctor who is apt to overdiagnosis, i.e. misdiagnosing a patient with a disease.

Further, let us denote the number of votes supporting A in the g group using n_g . Unite those values into a voting vector

$$\mathbf{n} = (n_1, n_2, \dots, n_G).$$

The number of different results of the voting equals

$$M = \prod_{g=1}^G (N_g + 1).$$

If we consider that the experts decide independently of each other, then the \mathbf{n} result possibility in the A and B options is expressed as

$$P_A(\mathbf{n}) = \prod_{g=1}^G C_{N_g}^{n_g} (p_A^{(g)})^{n_g} (1 - p_A^{(g)})^{N_g - n_g}, \quad (1)$$

$$P_B(\mathbf{n}) = \prod_{g=1}^G C_{N_g}^{n_g} (p_B^{(g)})^{n_g} (1 - p_B^{(g)})^{N_g - n_g}. \quad (2)$$

Statistics play the key role in building the optimal Neumann – Pearson criterion:

$$K(\mathbf{n}) = \frac{P_B(\mathbf{n})}{P_A(\mathbf{n})}. \quad (3)$$

Let us arrange the possible voting results in $K(\mathbf{n})$ ascending order:

$$K(\mathbf{n}_1) \leq K(\mathbf{n}_2) \leq \dots \leq K(\mathbf{n}_M). \quad (4)$$

Introduce a cross section of sequence (4) by means of

$$K_0 = K(\mathbf{n}_{k_0}),$$

where k_0 is the sequence number of the K_0 value in sequence (4).

The choice of the k_0 value is discussed below. A collective decision, according to the Neumann – Pearson criterion, is made depending on which of the following conditions is satisfied for the voting $\mathbf{n} = \mathbf{n}_k$:

$$k < k_0, \quad (5)$$

$$k = k_0, \quad (6)$$

$$k > k_0. \quad (7)$$

In case (5), the A hypothesis is supported, i.e. according to the nomenclature accepted in Mathematical Statistics, the population of such \mathbf{n}_k voting vectors falls to the admissible domain. In case (7), the hypothesis is rejected (\mathbf{n}_k belongs to the critical domain). In borderline case (6), the decision is made statistically: the A hypothesis is rejected with the ε probability, and is supported with the probability of $1 - \varepsilon$.

For this algorithm, the probability of the type I error equals

$$\alpha = \sum_{k=k_0+1}^M P_A(\mathbf{n}_k) + P_A(\mathbf{n}_{k_0})\varepsilon. \quad (8)$$

The probability of the type II error is given by an expression

$$\beta = \sum_{k=1}^{k_0-1} P_B(\mathbf{n}_k) + P_B(\mathbf{n}_{k_0})(1 - \varepsilon). \quad (9)$$

In the Neumann – Pearson algorithm, the probability of the type I error can be set arbitrarily, while the algorithm provides the minimal probability of the type II error with the set value of the type I error probability.

Then, the k_0 and ε parameters are chosen with such a condition in mind according to which the type I error probability α takes the set value. From relation (8), we obtain:

$$\begin{aligned} k_0 &= \max k, \quad \sum_{l=k}^M P_A(\mathbf{n}_l) \geq \alpha; \\ \varepsilon &= 1 - \frac{\sum_{l=k_0}^M P_A(\mathbf{n}_l) - \alpha}{P_A(\mathbf{n}_{k_0})}. \end{aligned} \quad (10)$$

Let us explain the meaning behind the Neumann – Pearson criterion optimality. Consider a certain arbitrary criterion of making a collective decision defined by a function

$$\varphi_1(\mathbf{n}_k) \quad (0 \leq \varphi_1(\mathbf{n}_k) \leq 1). \quad (11)$$

This function equals the probability of the A hypothesis being rejected, and respectively, with the probability of $1 - \varphi_1(\mathbf{n}_k)$ being supported in case of the \mathbf{n}_k voting result. The corresponding function for the optimal criterion according to Eqs. (5) – (7) has the form

$$\varphi(\mathbf{n}_k) = \begin{cases} 0, & k < k_0; \\ \varepsilon, & k = k_0; \\ 1, & k > k_0. \end{cases}$$

Assume that α_1 and β_1 are the probabilities of the type I and type II errors for criterion (11). The Neumann – Pearson criterion is optimal in a sense that at any choice of function (11) the condition

$$\alpha_1 \leq \alpha \Rightarrow \beta_1 \geq \beta.$$

is satisfied.

This excludes a case when some criterion has the type II error probability lower than the optimal criterion has at the same or lower levels of the type I error probability.

The optimality can be formulated more graphically, if we introduce a notion of comparable criteria with respect to accuracy. Let us assume that two criteria are comparable if the probabilities of type I and II errors of one of them deviate from



the respective probabilities of the other criterion in one way. We can naturally call the criterion with lower error probabilities more accurate. In these terms, the optimal criterion is more accurate than any comparable criterion or both criteria have the same accuracy.

Eqs. (10) and (9) allow us to construct the function

$$\beta = \beta(\alpha).$$

The choice of the type I error probability α is arbitrary, and using the Neumann – Pearson algorithm for each of its value we obtain the minimum possible probability of the type II error.

If we know the a priori probability of the A option (let us denote it as P_A), then we can set the following task: to select α in such a way, as to obtain the minimum possibility of the total error in making the decision

$$\gamma(\alpha) = P_A \alpha + (1 - P_A) \beta(\alpha). \quad (12)$$

This value of α_{opt} is determined by the formula

$$\alpha_{opt} = \arg \min_{\alpha} \gamma(\alpha). \quad (13)$$

Example of calculation with the optimal algorithm

Let us present an actual example of calculations based on the optimal criterion. Consider a medical council consisting of two groups. The council parameters are given in Table 1. The results of applying the optimal criterion to the process collective decision making of this council are

displayed in Table 2.

The second Table shows various voting results ranked by the value of (3). The rightmost column presents the $K(\mathbf{n})$ values. The second and the third columns (on the left) give the number of votes supporting the A option in each of the two groups: values n_1 and n_2 , respectively.

The fourth column on the left shows the probability of the respective voting result in an assumption that the experts are presented with the A option. The fifth column on the left includes a cumulative probability: the probability of this result or any other (it is located below). The second and the third columns on the right contain similar information, but the experts are considering the B option. Moreover, the cumulative probability is calculated for the voting results located above the one under consideration. The cumulative probabilities serve for the purpose of calculating the statistical errors (see the text below).

Assume that the sequence of the voting results given in Table 2 is arbitrarily divided into the upper and the lower parts. The Table demonstrates the division at the state with the sequence number $k = k_0 = 4$. According to the optimal criteria, the states located below the border, i.e. the numbers of the line put in bold red type, belong to the critical domain, while the states above the border fall into the admissible domain. If a voting result falls into the critical domain, then the experts support the B option. If a voting result is located in the admissible domain, then the decision is made in favor of the A option. If the voting ends in the borderline case, then the B option is supported with the ε probability and the A option is supported with the $1 - \varepsilon$ probability.

Medical council parameters

Table 1

Group number	Number, people	p_A	p_B
1	3	0.90	0.20
2	2	0.95	0.10

The possibilities that an expert doctor takes a healthy patient for an ill patient (p_A) and an ill person for a healthy one (p_B) are presented.

Table 2

Council voting results and their probability parameters

Seq. number k	Vector of voting for option A $\mathbf{n} = (n_1, n_2)$		Option A		Option B		$K(\mathbf{n})$
1	3	2	0.658	1.00	0.00008	0.00008	0.000122
2	2	2	0.219	0.342	0.00096	0.00104	0.00438
3	3	1	0.0693	0.123	0.00144	0.00248	0.0208
4	1	2	0.0244	0.0535	0.00384	0.00632	0.158
5	2	1	0.0231	0.0291	0.0173	0.0236	0.749
6	3	0	0.00182	0.00606	0.00648	0.0301	3.56
7	0	2	0.000902	0.00424	0.00512	0.0352	5.67
8	1	1	0.00257	0.00334	0.06912	0.104	26.9
9	2	0	0.000608	0.000773	0.0778	0.182	128
10	0	1	0.000095	0.000165	0.0922	0.274	970
11	1	0	0.0000675	0.00007	0.311	0.585	4610
12	0	0	0.0000025	0.0000025	0.0415	1.00	166000

Thus, the border is statistically blurred: with the probability of ε it falls into the critical domain, while it belongs to the admissible one with the $1 - \varepsilon$ probability. It is clear from the above that after the choice of the values

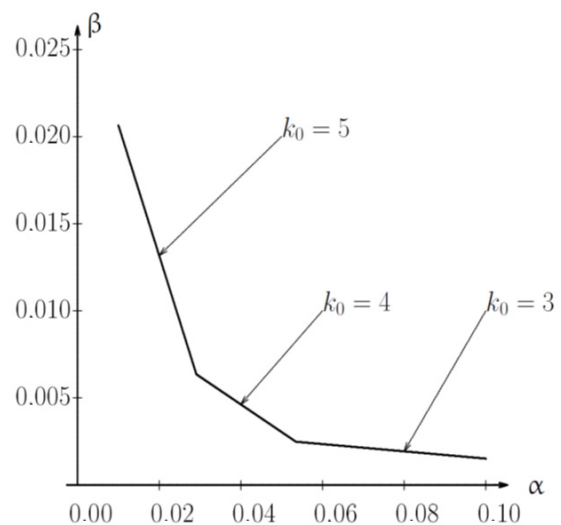
$$k_0 \text{ and } \varepsilon (1 \leq k_0 \leq 12, 0 < \varepsilon \leq 1)$$

the type I and II error probabilities are equal to:

$$\begin{aligned} \alpha &= \sum_{k_0+1}^{(A)} + \varepsilon \cdot P_{k_0}^{(A)}, \\ \beta &= \sum_{k_0-1}^{(B)} + (1 - \varepsilon) \cdot P_{k_0}^{(B)}, \end{aligned} \quad (14)$$

which is in agreement with Eqs. (8) and (9).

The Figure shows a fragment of the $\beta(\alpha)$ function graph for the α values of interest and model parameters presented in Table 1. Note that the dependence of β on α is piecewise linear which results from Eq. (14). Indeed, with a continuous increase in α , at first the ε value grows at the constant value of k_0 . Then, when ε reaches its maximum value of $\varepsilon = 1$, the k_0 value drops by one, the cumulative probability $\sum_{k_0+1}^{(A)}$ increases by $P_{k_0}^{(A)}$, while the ε value becomes zero. With the further



Example of a dependence of the type II error probability on the type I error probability (model parameters are given in Table 1)

growth of α the ε value increases again, and the whole process repeats itself. We can see from Eq. (14) that the β value has a linear dependence on ε . Therefore, at the regions where α changes, while k_0 is fixed, β a linear dependence on α . The

Figure shows three of such linear dependence regions. At the peaks of the broken line the value $\varepsilon = 1$, which means the stochastic element of the optimal criterion disappears at such values of α .

It follows from the piecewise linear nature of the $\beta(\alpha)$ function that the probability of the total error $\gamma(\alpha)$ has the same property (see Eq. (12)). But then the task of minimizing the $\gamma(\alpha)$ function (see Eq. (13)) as its solution has a value of α corresponding to one of the peaks. At those peaks, $\varepsilon = 1$ and the criterion is stochastic. Thus, in the frame of a rather generalized task setting, the Neumann – Pearson criterion does not contain a randomized element. If we take into account the fact that in case of continuous distribution the randomization is missing entirely [11], we can say that the optimal criterion in practice is often deterministic.

The method presented in this paper allows rational combination of votes of individual expert doctors into a collective conclusion of the council. This algorithm of collective decision making is optimal in the sense described above. The previous paragraph shows that even a council consisting of the experts of different qualification can make the right decision with high probability. This situation is akin to lowering the computational error by means of their independence and massive character. Similarly, in case of collective decision making, it is critical that the experts providing their conclusions are independent of each other. This condition may be subject to a breach in real life due to various reasons. For example, in the course of collective discussion of a diagnosis, each specialist might be inclined to unify the opinions of the council members. Some experts might exert unintentional pressure (for instance, due to their authority) on other specialists. All of these factors may contribute to both an increase

or a decrease of the probability of the right collective decision.

Some misconception widely spread among the specialists of these group might be another possible cause for a deviation from independent reasoning of an expert. This may lead to emergence of a statistical dependence (correlation) between opinions of some experts, although in this case they do not interact with each other directly.

Let us note that the independence of the expert decision making is not an essential precondition to the use of the optimal criterion. If there is a correlation, Eqs. (1) and (2) become invalid. However, if there are sufficient data on the dependence, we can write the corresponding formulae even in the presence of the correlation instead.

Conclusion

We studied a possibility of processing voting results in case of a team consisting of experts with different qualification. As an example, we considered a case in medical sphere when a medical council was expected to decide whether or not a patient is suffering from a specific disease. The most intelligent combination of the individual expert's votes into a collective council's decision was required. Our algorithm was based on the Neumann – Pearson principle of minimizing the type II error probability at the fixed type I error probability. We tested the developed algorithm by using a simple example: two councils that included 2 and 3 experts. The team of experts with different qualifications was numerically shown to be able to draw a correct conclusion with high probability. The considered methods are recommended for application both in medical personnel training [15, 16], as well as in similar situations demanding an expert group conclusion.

REFERENCES

1. **David H.A.**, The method of paired comparisons, 2nd edition, Lubrecht & Cramer, Ltd., London, 1969.
2. **Kendall M.G.**, Ranks of correlation methods, 4th edition, Charles Griffin and Co., London, 1970.
3. **Gibbard A.**, Manipulation of voting schemes: general result, *Econometrica*. 41 (4) (1973) 587–601.
4. **Tyushnyakov V.N., Chelashov D.A.**, Issledovaniye paradoksa tsiklicheskogo golosovaniya pri prinyatii kollektivnykh resheniy [Investigation

of the paradox of cyclic voting in collective decision-making], *Modern Problems of Science and Education. Surgery.* (7–3) (2014) 91–92 (in Russian).

5. **Malyshev V.A., Chebotarev P.Yu.**, On optimal group claims at voting in a stochastic environment, *Avtomatika i Telemekhanika.* (6) (2017) 157–172 (in Russian).

6. **Bulatnikova I.N., Fedorova O.I., Chuyan S.G.**, Prinyatiye resheniya putyom golosovaniya [Decision-making by voting], *Innovation Science.* 3 (4–3) (2015) 169–172 (in Russian).

7. **Volsky V.I., Lezina Z.M.**, Golosovaniye v mal'kch gruppakh. Protsedury i metody sravnitel'nogo analiza [Small group voting. Comparative analysis procedures and methods]. Nauka, Moscow, 2001 (in Russian).

8. **Arrow K.J.**, Social choice and individual values, John Wiley & Sons, Inc., New York, 1963.

9. **Nesterenko I.N., Saradzhishvili V.M., Zaitseva Yu.Yu.**, Upravlencheskiy konsalting: problemy i perspektivy razvitiya na otechestvennom rynke [Management consulting: problems and development prospects in the domestic market], *Young Scientist.* 260 (22) (2019) 560–562 (in Russian).

10. **Neyman J., Pearson E.S.**, On the problem of the most efficient tests of statistical hypotheses,

Philosophical Transactions of Royal Society of London. A. 231 (694–706) (1933) 289–337.

11. **Sevastianov B.A.**, Kurs teorii veroyatnostey i matematicheskoy statistiki [The course of probability theory and mathematical statistics], Nauka, Moscow, 1982 (in Russian).

12. **Nathan A.A., Guz S.A., Gorbachev O.G., et al.**, Matematicheskaya statistika, 3-ye izdaniye [Mathematical statistics, 3rd edition], MIPT Publishing, Moscow, 2011 (in Russian).

13. **Smorkalova V.M.**, Zadachy proverki statisticheskikh gipotez [Tasks of testing the statistical hypotheses], Nizhny Novgorod State University, Nizhny Novgorod, 2015 (in Russian).

14. **Korosteleva O.N.**, The assessment of efficiency of expert groups at conducting examination of scientific qualification works, *Sociology of Science & Technology.* 8 (3) (2017) 89–98 (in Russian).

15. **Causer J., Barach P., Williams A.M.**, Expertise in medicine: using the expert performance approach to improve simulation training, *Medical Education.* 48 (2) (2014) 115–123.

16. **Altman D.G., Goodman S.N., Schroter S.**, How statistical expertise is used in medical research, *Journal of the American Medical Association.* 2002. Vol. 287 (21) (2002) 2817–2820.

Received 21.12.2020, accepted 01.02.2021.

THE AUTHORS

ANTONOV Valerii I.

Peter the Great St. Petersburg Polytechnic University

29 Politechnicheskaya St., St. Petersburg, 195251, Russian Federation
antonovvi@mail.ru

GARBARUK Victor V.

Petersburg State Transport University

9 Moskovsky Ave., St. Petersburg, 190031, Russian Federation
vigarb@mail.ru

FOMENKO Viktor N.

Petersburg State Transport University

9 Moskovsky Ave., St. Petersburg, 190031, Russian Federation
vfomenko1943@gmail.com

СПИСОК ЛИТЕРАТУРЫ

1. **David H.A.** The method of paired comparisons. 2nd edition. London: Lubrecht & Cramer, Ltd., 1969. 124 p.
2. **Kendall M.G.** Ranks of correlation methods. 4th edition. London: Charles Griffin and Co., 1970. 202 p.
3. **Gibbard A.** Manipulation of voting schemes: general result // *Econometrica*. 1973. Vol. 41. No. 4. Pp. 587–601.
4. **Тюшняков В.Н., Челашов Д.А.** Исследование парадокса циклического голосования при принятии коллективных решений // *Современные наукоемкие технологии*. 2014. № 7 (часть 3). С. 91–92.
5. **Мальшев В.А., Чеботарев П.Ю.** Об оптимальном пороге притязаний группы при голосовании в стохастической среде // *Автоматика и телемеханика*. 2017. № 6. С. 157–172.
6. **Булатникова И.Н., Федорова О.И., Чуян С.Г.** Принятие решений путем голосования // *Инновационная наука*. 2015. Т. 3. № 4 (часть 3). С. 169–172.
7. **Вольский В.И., Лезина З.М.** Голосование в малых группах. Процедуры и методы сравнительного анализа. М.: Наука, 2001. 192 с.
8. **Arrow K.J.** Social choice and individual values. New York: John Wiley & Sons, Inc., 1963. 90 p.
9. **Нестеренко И.Н., Сараджишвили В.М., Зайцева Ю.Ю.** Управленческий консалтинг: проблемы и перспективы развития на отечественном рынке // *Молодой ученый*. 2019. Т. 260. № 22. С. 560–562.
10. **Neyman J., Pearson E.S.** On the problem of the most efficient tests of statistical hypotheses // *Philosophical Transactions of Royal Society of London. A*. 1933. Vol. 231. No. 694–706. Pp. 289–337.
11. **Севастьянов Б.А.** Курс теории вероятностей и математической статистики. М.: Наука, 1982. 256 с.
12. **Натан А.А., Гуз С.А., Горбачев О.Г., Гасников А.В., Черноусова Е.О.** Математическая статистика. Изд. 3-е, испр. и доп. М: Изд-во МФТИ, 2011. 32 с.
13. **Сморкалова В.М.** Задачи проверки статистических гипотез. Нижний Новгород: Нижегородский госуниверситет, 2015. 23 с.
14. **Коростелева О.Н.** Оценка эффективности экспертных групп при проведении экспертизы научно-квалификационных работ // *Социология науки и технологий*. 2017. Т. 8. № 3. С. 89–98.
15. **Causer J., Barach P., Williams A.M.** Expertise in medicine: using the expert performance approach to improve simulation training // *Medical Education*. 2014. Vol. 48. No. 2. Pp. 115–123
16. **Altman D.G., Goodman S.N., Schroter S.** How statistical expertise is used in medical research // *Journal of the American Medical Association*. 2002. Vol. 287. No. 21. Pp. 2817–2820.

Статья поступила в редакцию 21.12.2020, принята к публикации 01.02.2021.

СВЕДЕНИЯ ОБ АВТОРАХ

АНТОНОВ Валерий Иванович — доктор технических наук, заведующий кафедрой высшей математики Санкт-Петербургского политехнического университета Петра Великого, Санкт-Петербург, Российская Федерация.

195251, Российская Федерация, г. Санкт-Петербург, Политехническая ул., 29
antonovvi@mail.ru

ГАРБАРУК Виктор Владимирович — кандидат технических наук, профессор кафедры высшей математики Петербургского государственного университета путей сообщения Императора Александра I, Санкт-Петербург, Российская Федерация.

190031, Российская Федерация, г. Санкт-Петербург, Московский пр., 9
vigarb@mail.ru

ФОМЕНКО Виктор Николаевич — доктор физико-математических наук, профессор кафедры высшей математики Петербургского государственного университета путей сообщения Императора Александра I, Санкт-Петербург, Российская Федерация.

190031, Российская Федерация, г. Санкт-Петербург, Московский пр., 9
vfomenko1943@gmail.com

DOI: 10.18721/JPM.14113
UDC 517.938:070

MATHEMATICAL MODELING OF INFORMATION CONFRONTATION

S.V. Timofeev, A.V. Baenkhaeva

Baikal State University,
Irkutsk, Russian Federation

The article continues our studies in the previously constructed mathematical model of dissemination of new information in the society. The model is a system of four ordinary differential equations with quadratic nonlinearity in the right parts. Two fundamental domains have been taken in the parameter space of the model and they may be of interest in application. In some sense, these domains provide two diametrically opposite and essentially different scenarios of new information dissemination. In every case, the global properties of the phase pattern of the constructed dynamic system were investigated using qualitative methods of the theory of differential equations. Both conceptual and geometric interpretations of the obtained results were given.

Keywords: differential equation, stationary solution of system, invariant set, asymptotic stability

Citation: Timofeev S.V., Baenkhaeva A.V., Mathematical modeling of information confrontation, St. Petersburg Polytechnical State University Journal. Physics and Mathematics. 14 (1) (2021) 155–166. DOI: 10.18721/JPM.14113

This is an open access article under the CC BY-NC 4.0 license (<https://creativecommons.org/licenses/by-nc/4.0/>)

МАТЕМАТИЧЕСКОЕ МОДЕЛИРОВАНИЕ ИНФОРМАЦИОННОГО ПРОТИВОБОРСТВА

С.В. Тимофеев, А.В. Баенхаева

Байкальский государственный университет,
г. Иркутск, Российская Федерация

В статье излагается продолжение исследований построенной ранее базовой математической модели распространения в обществе новой информации. Данная модель представляет собой автономную систему четырех обыкновенных дифференциальных уравнений с квадратичной нелинейностью в правых частях. В пространстве параметров системы выделены две важные области, представляющие интерес для приложений. В определенном смысле в этих областях реализуются два диаметрально противоположных и принципиально разных сценария распространения новой информации в обществе. С помощью качественных методов теории дифференциальных уравнений в каждом случае изучены глобальные свойства фазового портрета построенной динамической системы. Даны содержательная и графическая интерпретации полученных результатов.

Ключевые слова: дифференциальное уравнение, стационарное решение системы, инвариантное множество, асимптотическая устойчивость

Ссылка при цитировании: Тимофеев С.В., Баенхаева А.В. Математическое моделирование информационного противоборства // Научно-технические ведомости СПбГПУ. Физико-математические науки. 2021. Т. 14. № 1. С. 155–166. DOI: 10.18721/JPM.14113

Статья открытого доступа, распространяемая по лицензии CC BY-NC 4.0 (<https://creativecommons.org/licenses/by-nc/4.0/>)

Introduction

In paper [1], we presented a constructed mathematical model of dissemination of new information in the society:

$$\begin{aligned}\frac{dN}{dt} &= \beta N - \gamma AN, \\ \frac{dC}{dt} &= \alpha AN - \mu(C - C_*), \\ \frac{dA}{dt} &= \rho C - \eta \gamma AN - \lambda A, \\ \frac{di}{dt} &= \sigma N - \omega i.\end{aligned}\quad (1)$$

While constructing, it was considered that the main factors for the dissemination of new information were the following values, depending on the time t :

$N(t)$ (after “News”) is a quantitative characteristic of information related to news which corresponds to promotion of new views in the information space;

$C(t)$ (after “Censorship”) is a number of censor bodies with a certain resource base which aim to maintain the previously established concepts;

$A(t)$ (after “Alternative view”) is a quantitative characteristic of information flow (probably initiated by censor bodies) which opposes the dissemination of a new concept in the information space;

$i(t)$ (after “index”) is a parameter of a share of population favorably disposed towards to new ideas emerging in mass media at the time of occurrence:

$$i = 1 - \frac{I^*}{I},$$

where I , %, corresponds to complete acceptance of conventional statements before the beginning of observations; I^* , %, is a respective characteristic of acceptance of conventional statements with new views disseminating in mass media.

Parameters $\beta \geq 0$, $\gamma \geq 0$ respectively shows the capacity of new information dissemination via

mass media and probabilistic characteristic of the effect neutralized by means of stating the opposite opinion. In turn, coefficient $\alpha \geq 0$ shows the intensity of the reaction to the confrontation of opposite views, parameter $\mu > 0$ is inversely related to the time of operation of additionally formed bodies (let us assume that a society always has some special resource available in the number of C_* in order to protect the previous concept).

Average velocity of news generated by one body of information C is characterized by parameter $\rho \geq 0$, while $\eta \geq 0$ is the amount of information A aimed at neutralizing the impact of messages N . Coefficient $\lambda > 0$ is inversely related to the time the information A is forgotten.

Parameters $\sigma > 0$, $\omega \geq 0$ characterize respectively the acceptance rate of the new idea and return to the former concept due to inertia of mentality.

Undoubtedly, the proposed mathematical model does not account for all the subtle features and details while describing the process of new information dissemination via mass media in the society. However, this generalized form of the model allows binding main factors dedicated to this action into a system and deeper understanding of the process of information confrontation.

Previously, using the methods described in papers [2–5], we showed that system (1) has characteristics that allow studying global properties of its solutions: uniqueness, continuous dependence on parameters, their unlimited extendibility. In addition, for this system, we proved invariance of the set

$$\begin{aligned}R_+^4 &= \\ &= \{(N, C, A, i) \in R^4 : N \geq 0, C \geq 0, A \geq 0, i \geq 0\}.\end{aligned}$$

We also found two stationary solutions which have rather clear interpretation [1]:

$$\begin{aligned}X_{1st} &= (N_{1st}, C_{1st}, A_{1st}, i_{1st}) = \\ &= (0, C_*, \rho C_*/\lambda, 0),\end{aligned}$$

$$X_{2st} = (N_{2st}, C_{2st}, A_{2st}, i_{2st}),$$



where

$$\begin{aligned} N_{2st} &= \frac{\mu(\lambda\beta - \gamma\rho C_*)}{\beta(\alpha\rho - \mu\eta\gamma)}, \\ C_{2st} &= \frac{\alpha\lambda\beta - \eta\mu\gamma^2 C_*}{\gamma(\alpha\rho - \mu\eta\gamma)}, \\ A_{2st} &= \frac{\beta}{\gamma}, \\ i_{2st} &= \frac{\sigma\mu(\lambda\beta - \gamma\rho C_*)}{\omega\beta(\alpha\rho - \mu\eta\gamma)}. \end{aligned}$$

In the space of system parameters, we indicated two domains in which $X_{ist} \in R_+^4$, $i = 1, 2$, but with properties significantly different from each other:

$$\Omega_1 : \begin{cases} \gamma\rho C_* > \lambda\beta \\ \mu\eta\gamma > \alpha\rho \end{cases}, \quad \Omega_2 : \begin{cases} \gamma\rho C_* < \lambda\beta \\ \mu\eta\gamma < \alpha\rho \end{cases}.$$

By means of using qualitative methods of studying differential equations, we studied global properties of the phase pattern of the constructed dynamic system. This allowed us to identify several possible scenarios of dissemination of new information in the society.

This paper investigates the solution properties of system (1) in parameter domains

$$\begin{aligned} \Lambda_1 : & \begin{cases} \gamma\rho C_* < \lambda\beta \\ \mu\eta\gamma > \alpha\rho \end{cases}, \\ \Lambda_2 : & \begin{cases} \gamma\rho C_* > \lambda\beta \\ \mu\eta\gamma < \alpha\rho \end{cases}, \end{aligned}$$

which may be of interest in application.

In these domains, set R_+^4 contains only one stationary solution:

$$\begin{aligned} X_{1st} &= (N_{1st}, C_{1st}, A_{1st}, i_{1st}) = \\ &= (0, C_*, \rho C_*/\lambda, 0). \end{aligned}$$

Before the study, one comment should be made. Since in system (1), a variable $i(t)$ is present only in the last equation, a further investiga-

tion may be conducted for a system of lesser dimension which is expedient to present in a form more suitable for the studies:

$$\begin{aligned} \frac{dC}{dt} &= \alpha AN - \mu(C - C_*), \\ \frac{dA}{dt} &= \rho C - (\lambda + \eta\gamma N)A, \\ \frac{dN}{dt} &= (\beta - \gamma A)N. \end{aligned} \quad (2)$$

The obtained results can be then easily extended to the variable $i(t)$.

It is easy to show that the set

$$\begin{aligned} R_+^3 &= \\ &= \{(C, A, N) \in R^3 : C \geq 0, A \geq 0, N \geq 0\} \end{aligned}$$

for this set is invariant and contains only one stationary solution

$$\begin{aligned} X_{st} &= (C_{st}, A_{st}, N_{st}) = \\ &= (C_*, \rho C_*/\lambda, 0). \end{aligned}$$

Note that in Λ_1 this stationary solution is unstable, while in Λ_2 it is stable.

The conceptual meaning of the stationary solution X_{st} was formulated in paper [1] as a system of views predominant in a society, for the support of which administrative resource in the number of C_* employs a sufficient (from the point of view of this resource) amount of information $\rho C_*/\lambda$ in mass media.

Due to autonomy of system (2), initial conditions can be written as follows:

$$\begin{aligned} C(0) &= C_0 \geq 0, \\ A(0) &= A_0 \geq 0, N(0) = N_0 \geq 0. \end{aligned} \quad (3)$$

Analysis of models (2), (3) in the parameter domain

A reduced two-dimensional system of differential equations

$$\begin{aligned}\frac{dA}{dt} &= \rho C - (\lambda + \eta\gamma N)A, \\ \frac{dN}{dt} &= (\beta - \gamma A)N,\end{aligned}\quad (4)$$

obtained from system (2) at $\alpha = 0$ and $C(t) = C_*$ when $t \geq 0$ gives a better understanding of the behavior of solutions to three-dimensional system (2), (3) in the Λ_1 domain.

We should explain that system (4) describes a situation when the bodies of information protection due to various reasons do not react to targeted media “injections” of data that contradict the accepted opinions of the society.

System (4) in the parameter domain Λ_1 in the invariant set

$$R_+^2 = \{(A, N) \in R^2 : A \geq 0, N \geq 0\}$$

has only one stationary solution:

$$X_{st} = (A_{st}, N_{st}) = (\rho C_*/\lambda, 0),$$

which is a saddle.

Known techniques of qualitative analysis of two-dimensional differential equations systems [6] allow constructing a phase pattern and investigating the behavior of system (4) trajectories (Fig. 1). As seen from the Figure, all trajectories of system (4) with initial conditions

$$A(0) = A_0 \geq 0, N(0) = N_0 > 0$$

when $t \rightarrow +\infty$ have the same behavior:

$$A(t) \rightarrow 0, N(t) \rightarrow +\infty.$$

We show that in

$$\begin{aligned}R_+^3 &= \\ &= \{(C, A, N) \in R^3 : C \geq 0, A \geq 0, N \geq 0\}\end{aligned}$$

system (2), (3) has a qualitatively similar phase pattern.

Let

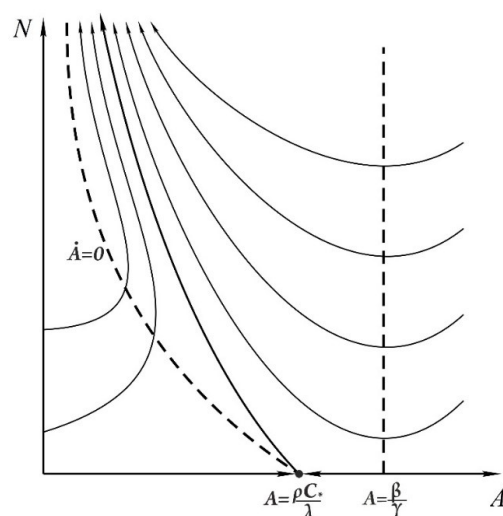


Fig. 1. Phase pattern of system (4) in the R_+^2 set

$$R^+ = \{(C, A, N) \in R_+^3 : N > 0\},$$

$$\partial R^+ = \{(C, A, N) \in R_+^3 : N = 0\}.$$

For an arbitrary solution of system (2), (3), specifically for

$$X(t) = (C(t), A(t), N(t)),$$

let us denote $\Lambda^+(X)$ as a ω -bounding set of this solution [7].

Lemma. For all trajectories of system(2), originating in the R^+ set, $\Lambda^+ \cap \partial R^+$ is an empty set.

P r o o f. The set ∂R^+ is invariant due to system (2), (3). Indeed, if

$$X_0 = (C_0, A_0, N_0) \in \partial R^+,$$

then system (2) is determined by linear equations

$$\begin{aligned}\frac{dC}{dt} &= -\mu(C - C_*), \\ \frac{dA}{dt} &= \rho C - \lambda A, \\ N(t, X_0) &\equiv 0,\end{aligned}\quad (5)$$

For which a special X_{st} point has global, uniform, asymptotic stability in ∂R^+ .



Assume that the $\Lambda^+ \cap \partial R^+$ set is not empty. Then there is such a trajectory $X(t, X_0)$ of system (2), (3), that from $X(t, X_0) \in R^+$ it follows that $X(t, X_0) \rightarrow \partial R^+$. Based on the theorem of continuous dependence of system (2), (3) solutions on the initial data [8], $X(t, X_0) \rightarrow X_{st}$ when $t \rightarrow +\infty$. Which is impossible, as X_{st} is an unstable stationary solution to system (2), (3).

Thus, the lemma is proved.

Theorem 1. *All trajectories of system (2), originating in the R^+ set, are not bounded.*

P r o o f. Assume the converse. Let there be such a trajectory $X(t, X_0)$ which is bounded when

$$X_0 = (N(0), C(0), A(0), i(0)) \in R^+$$

Introduce Lyapunov's function into consideration

$$V(X, t) = \gamma AN - \beta N - \gamma \int_0^t \dot{A} N d\tau,$$

and find its derivative due to system (1):

$$\begin{aligned} \dot{V}(X, t) &= \gamma \dot{N} A + \gamma \dot{A} N - \\ &- \beta \dot{N} - \gamma \dot{A} N = \dot{N}(\gamma A - \beta) = \\ &= -(\beta - \gamma A)^2 N \leq 0. \end{aligned}$$

This derivative is locally Lipschitzian along X and continuous. The $V(X, t)$ function itself is bounded from below. Let us show this:

The boundedness from below of the difference $\gamma AN - \beta N$ is obvious given the boundedness of the $X(t, X_0)$ trajectory. The third summand of the presented function is also bounded from below. Indeed, it is positive in a set, where $\dot{A} < 0$. In a set, where $\dot{A} > 0$, it can be estimated as follows:

$$\begin{aligned} -\gamma \int_0^t \dot{A} N d\tau &\geq -\gamma \int_0^t \dot{A} N_{\max} d\tau = \\ &= -\gamma N_{\max} [A(t) - A(0)] \geq \\ &\geq -\gamma N_{\max} A_{\max} + \gamma N_{\max} A(0). \end{aligned}$$

The second derivative $\ddot{V}(X, t)$, due to system (1), is obviously bounded from below as well. Consequently (see [7], statement VIII.4.7),

$$\dot{V}(X, t) \rightarrow 0 \text{ at } t \rightarrow +\infty.$$

This fact ensures that the trajectory is approaching to its ω -bounding set

$$\begin{aligned} \Lambda^+ \subset M = \\ = \left\{ (N, C, A, i) \in R_+^4 : A = \frac{\beta}{\gamma} \vee N = 0 \right\}. \end{aligned}$$

Since system (1) is autonomous, this set is invariant due to the system.

Consider an Λ^+ set.

In the R^+ set, a plane $A = \beta/\gamma$ does not contain sets invariant due to system (2). Therefore, the trajectory of system (1) cannot approach this plane when $t \rightarrow +\infty$. The plane $N = 0$, according to lemma, can also not contain the points of ω -bounding set. Consequently, the system trajectory cannot approach the $N = 0$ plane when $t \rightarrow +\infty$ as well. We arrived at a contradiction.

This proves the theorem.

Let us select two subsets in the R^+ set (Fig. 2):

$$\begin{aligned} H_1 &= \left\{ (C, A, N) \in R^+ : A \leq \frac{\beta}{\gamma} \right\}, \\ H_2 &= \left\{ (C, A, N) \in R^+ : A > \frac{\beta}{\gamma} \right\}. \end{aligned} \quad (6)$$

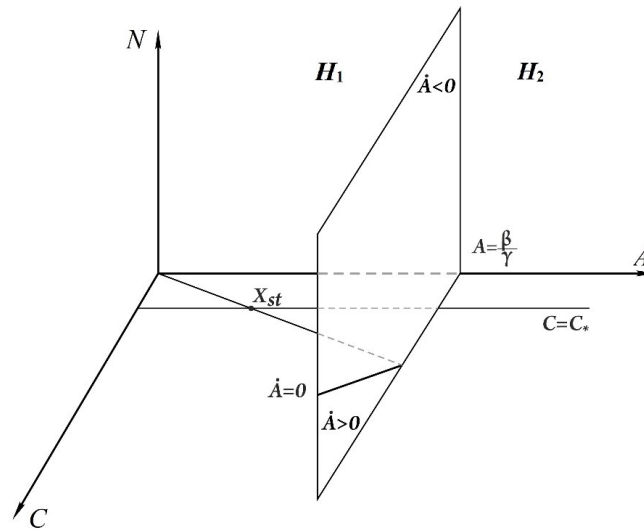
In the H_1 subset, consider such surfaces, on which values $C(t)$, $A(t)$, $N(t)$ respectively equal zero:

$$N = \frac{\mu(C - C_*)}{\alpha A}, \quad (7)$$

$$N = \frac{\rho C}{\eta \gamma A} - \frac{\lambda}{\eta \gamma}, \quad (8)$$

$$A = \frac{\beta}{\gamma}. \quad (9)$$

Let us estimate the mutual arrangement of surfaces (7) and (8) by prior determination of their intersection with the plane $N = 0$ (see Fig. 2): $C = C_*$ and $C = \lambda A / \rho$ for Eqs. (7) and (8) respectively.


 Fig. 2. Two selected subsets (6) in the R^+ set

At the intersection of these lines, there is a stationary solution

$$X_{st} = (C_{st}, A_{st}, N_{st}) = (C_*, \rho C_*/\lambda, 0).$$

At any intersection with a plane $A = \tilde{A}$, surfaces (7) and (8) respectively have the form:

$$N = \frac{\mu C}{\alpha \tilde{A}} - \frac{\mu C_*}{\alpha \tilde{A}}, \quad (10)$$

$$N = \frac{\rho C}{\eta \gamma \tilde{A}} - \frac{\lambda}{\eta \gamma}. \quad (11)$$

For the Λ_1 domain parameters, the coefficient of C in the expression for line (10) turns out to be greater than the respective coefficient for line (11), as it results from inequality $\mu\eta\gamma > \alpha\rho$ after dividing by $\alpha\eta\gamma\tilde{A}$ that

$$\frac{\mu}{\alpha \tilde{A}} > \frac{\rho}{\eta \gamma \tilde{A}}.$$

Note here, that a diagram of the considered problem (Fig. 3) allows graphical estimation of the mutual arrangement of surfaces (7), (8) in the H_1 subset. This representation will be used to prove the following theorem.

Theorem 2. Assume that in the R^+ set of the parameter domain H_1 ,

$$X(t, X_0) = (C(t, X_0), A(t, X_0), N(t, X_0))$$

is the solution of system (2), (3). Then, at $t \rightarrow +\infty$, a component of this solution $A(t) \rightarrow 0$, while $N(t) \rightarrow +\infty$.

P r o o f. Let us prove the theorem in three steps.

Step 1. Let us show that any solution $X(t) = (C(t), A(t), N(t))$ from the H_2 subset of the R^+ set after a finite time falls into the H_1 subset. Indeed, if $A > \beta/\gamma$, it follows from the third equation of system (2) that $\dot{N}(t) < 0$. Then, still in H_2 , the $X(t)$ solution in finite time falls in a rather close neighborhood of plane $N = 0$. However, in this plane, all solutions of system (2) at $t \rightarrow +\infty$ approach the stationary solution of X_{st} , for which

$$A_{st} = \rho C_*/\lambda < \beta/\gamma$$

in Λ_1 . Therefore, the theorem of continuous dependence on the initial data [8] guarantees that any solution to system (2) out of the H_2 subset falls into the H_1 subset in finite time.

Step 2. It is clear that solutions of $X(t)$ fall from H_2 into H_1 , where $\dot{N}(t) > 0$, through a part of plane (9) $A = \beta/\gamma$, in which $\dot{A} < 0$ (see Fig. 2). Now, let us show that from the part of the H_1 set, where $\dot{A} < 0$, at $t \rightarrow +\infty$, the component

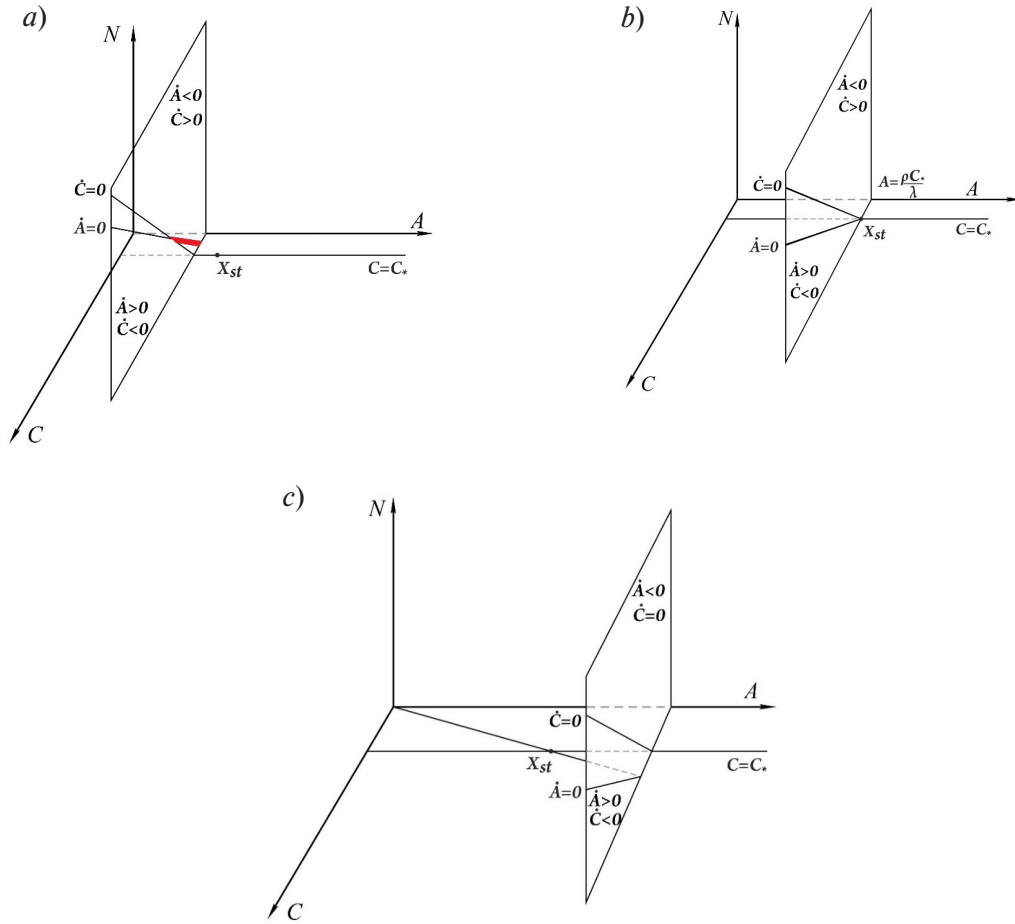


Fig. 3. Surface (7), (8) for various values of A :
 $0 < A < A_{st}$ (a), $A = A_{st}$ (b), $A_{st} < A < \beta/\gamma$ (c)

$A(t) \rightarrow 0$, and $N(t) \rightarrow +\infty$.

Let us introduce two functions: $V_1(X) = \dot{A}$ and $V_2(X) = \dot{C}$. Using the relations (7), (8), it is easy to verify that in the H_1 subset on the surface $V_1(X) = 0$, when

$$A_{st} < A \leq \beta/\gamma$$

$V_2(X) < 0$ (see Fig. 3,b,c). Therefore, due to system (2),

$$\begin{aligned} \dot{V}_1(X) \Big|_{X: V_1(X)=0} &= \\ &= \dot{A} = \rho \dot{C} - \eta \gamma \dot{N} A < 0. \end{aligned}$$

Consequently, the system solution from the surface $\dot{A} = 0$ falls into the domain, where $\dot{A} < 0$. Only for a few values $0 < A < A_{st}$, indicated in Fig. 3,a (red line segment), the solution may fall

from the surface $\dot{A} = 0$ into a domain, where $\dot{A} > 0$. When it starts to go up, the $A(t)$ component can grow up to value $A = A_{st}$ only under the condition that $\dot{C} < 0$ at $A = A_{st}$ (Fig. 3,b). For this, we need to cross the surface $V_2(X) = \dot{C} = 0$. But on this surface due to system (2)

$$\dot{V}_2(X) = \ddot{C} = \alpha \dot{A} N + \alpha A \dot{N} > 0.$$

Therefore, as $\dot{N} > 0$ in the H_1 subset, then $A(t)$ through surface (8) again falls into the domain, where $\dot{A} < 0$, and consequently starts to drop. Thus, when $t \rightarrow +\infty$ the component $A(t) \rightarrow 0$, while $N(t) \rightarrow +\infty$.

Step 3. Solution $X(t, X_0)$, starting in the H_1 part, where $\dot{A} > 0$ and $\dot{C} < 0$, falls either through the surface $A = \beta/\gamma$ into the H_2 subset or into the surface $\dot{A} = 0$, where $V_1(X) = 0$. Although, in the first case, as it was shown in the previous steps,

$A(t) \rightarrow 0$, and $N(t) \rightarrow +\infty$ at $t \rightarrow +\infty$. In the second case, due to system (2), we have

$$\begin{aligned} \dot{V}_1(X) \Big|_{X: V_1(X)=0} &= \\ &= \ddot{A} = \rho \dot{C} - \eta \gamma \dot{N} A < 0. \end{aligned}$$

Thus, we find ourselves in the part of the H_1 domain, in which $\dot{A} < 0$, where due to $\dot{N} > 0$, $A(t) \rightarrow 0$ again, and $N(t) \rightarrow +\infty$ at $t \rightarrow +\infty$. Which is what we set out to prove.

This proves Theorem 2.

Interpretation. With this ratio of parameters of system (2), the results of the mathematical studies allow us to make a conclusion on the preparedness of the society to accept new ideas and opinions. Any appearance of views and opinions in mass media that do not coincide with the traditional ones will find support of the society members. In this case, the recipients replace the previously dominating concept completely.

Analysis of models (2), (3) in the parameter domain Λ_2

It is easy to show (see paper [1], statement 2) that in the parameter domain Λ_2 , a stationary solution

$$\begin{aligned} X_{st} &= (C_{st}, A_{st}, N_{st}) = \\ &= (C_*, \rho C_*/\lambda, 0) \end{aligned}$$

of system (2), (3) has asymptotic stability. Let us study its domain of attraction.

Note that the right part of the equation for $C(t)$ of system (2) ensures the trajectory under the initial conditions falls from the R_+^3 set into a subset, where $C(t) \geq C_*$, which is invariant. Therefore, we will study only this part of R_+^3 . In addition, from the equation for $A(t)$ of system (2) we can see that plane $A = \beta/\lambda$ divides this subspace into two sets (Fig. 4):

$$R_+^N = \{(C, A, N) \in R_+^3 : C \geq C_*, \dot{N} \geq 0\},$$

$$R_-^N = \{(C, A, N) \in R_+^3 : C \geq C_*, \dot{N} \leq 0\},$$

in which X_{st} is located.

Theorem 3. Assume that for systems (2), (3) in the parameter domain Λ_2 , a condition

$$\beta\eta\gamma + \mu\eta\gamma < \rho\alpha. \quad (12)$$

is satisfied. Then the entirety of the space

$$\begin{aligned} R_+^3 &= \\ &= \{(C, A, N) \in R^3 : C \geq 0, A \geq 0, N \geq 0\} \end{aligned}$$

is a part of the attraction domain of asymptotically stable stationary solution X_{st} .

P r o o f. Take an arbitrary trajectory $X(t, X_0)$ of system (2), (3) originating in the R_+^3 set. As we noted in the beginning of the section, in finite time, it either end up in R_+^N or in R_-^N . Let's employ further reasoning in three steps as well.

Step 1. Let us show that any solution

$$X(t) = (C(t), A(t), N(t))$$

out of the R_+^N set in finite time falls into the R_-^N set.

Consider surface (8) (Fig. 4), where $\dot{A} = 0$, and function $V_1(X) = \dot{A}$. In the Λ_2 parameter domain, keeping in mind Eq. (8), if condition (12) is satisfied, for a certain positive volume δ we have:

$$\begin{aligned} \dot{V}_1(X) \Big|_{X: V_1(X)=0} &= \\ &= \ddot{A} = \rho \dot{C} - \eta \gamma \dot{N} A = \\ &= \left(\frac{\rho C - \lambda A}{\eta \gamma} \right) (\rho \alpha - \mu \eta \gamma - \beta \eta \gamma + \\ &\quad + \eta \gamma^2 A) + \rho \mu C_* - \lambda \mu A \geq \\ &\geq \left(\frac{\rho C_* - \lambda \frac{\beta}{\lambda}}{\eta \gamma} \right) (\rho \alpha - \mu \eta \gamma - \\ &\quad - \beta \eta \gamma + \eta \gamma^2 A) + \rho \mu C_* - \lambda \mu \frac{\beta}{\gamma} = \\ &= \left(\frac{\rho \gamma C_* - \lambda \beta}{\eta \gamma^2} \right) (\rho \alpha - \mu \eta \gamma - \end{aligned}$$

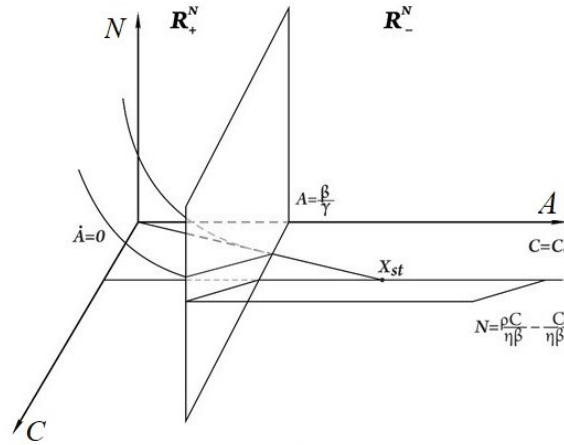


Fig. 4. Key surfaces (8) and (13) in sets R_+^N and R_-^N respectively

$$-\beta\eta\gamma + \eta\gamma^2 A) + \frac{\rho\mu\gamma C_* - \lambda\mu\beta}{\gamma} > \delta > 0.$$

Thus, the trajectory $X(t)$ falls into the domain, where $\dot{A} > 0$, from surface (8), and, respectively,

$$N < \frac{\rho C}{\eta\gamma A} - \frac{\lambda}{\eta\gamma}.$$

If $V_1(X) < 0$ in a certain part of the R_+^N space, then the search for derivative $V_1(X)$ sign, due to system (2), comes down to calculating the sign of a derivative on the surface $V_1(X) = 0$, since

$$\begin{aligned} \dot{V}_1(X)_{X:V_1(X)=0} &= \\ &= \ddot{A} = \rho\dot{C} - \lambda\dot{A} - \eta\gamma\dot{N}A - \eta\gamma\dot{A}N \geq \\ &\geq \rho\dot{C} - \eta\gamma\dot{N}A = \dot{V}_1(X)_{X:V_1(X)=0} > 0. \end{aligned}$$

This means that all trajectories out of the R_+^N set fall in the part, where $\dot{A} > 0$.

Due to smoothness of function $V_1(X)$, we can find such a positive number ε , so that the component $N(t)$ from some finite point of time starts satisfying a relation

$$N < \frac{\rho C}{\eta\gamma A} - \frac{\lambda}{\eta\gamma} - \varepsilon,$$

only if the $X(t)$ trajectory is in the R_+^N set.

Next, for the component $A(t) > 0$, we have:

$$\begin{aligned} \dot{A} &= \rho C - \eta\gamma A N - \lambda A > \rho C - \\ &- \eta\gamma A \left(\frac{\rho C}{\eta\gamma A} - \frac{\lambda}{\eta\gamma} - \varepsilon \right) - \lambda A = \\ &= \eta\gamma A \varepsilon > 0. \end{aligned}$$

The last inequality ensures that any $X(t)$ trajectory of system (2) after finite time falls into R_-^N , where $A > \beta/\gamma$ and, consequently, $\dot{N} < 0$.

Step 2. Let us prove that falling from the R_+^N set into the R_-^N set, the $X(t)$ trajectory at $t \rightarrow +\infty$ approaches the stationary solution X_{st} .

Let us set a direction for a vector field at the surface

$$N = \frac{\rho}{\eta\beta} (C - C_*) + q, \quad q - \text{const.} \quad (13)$$

Scalar product of vectors

$$\begin{aligned} \mathbf{n} &= \left(\frac{\partial N}{\partial C}; \frac{\partial N}{\partial A}; -1 \right) = \\ &= \left(\frac{\rho}{\eta\beta}; 0; -1 \right), \end{aligned}$$

$$\frac{dX}{dt} = \left(\frac{dC}{dt}; \frac{dA}{dt}; \frac{dN}{dt} \right)$$

has the following form:

$$\frac{\rho}{\eta\beta}(C - C_*) \times \\ \times \left[\left(\alpha \frac{\rho}{\eta\beta} + \gamma \right) A - (\mu + \beta) \right].$$

This expression is positive when

$$A > \frac{\mu + \beta}{\alpha \frac{\rho}{\eta\beta} + \gamma} = \frac{(\mu + \beta)\eta\beta}{\alpha\rho + \gamma\eta\beta} = \bar{A}.$$

Because of the fact that in the Λ_2 parameter domain $\bar{A} < \beta/\gamma$, the $X(t)$ trajectory, falling from the R_+^N set into R_-^N (see Fig. 4), can no longer go back from R_-^N to R_+^N . And since in R_-^N $\dot{N} < 0$, after finite time, the $X(t)$ trajectory of system (2) arrives in the arbitrarily small neighborhood of plane $N = 0$. For system (2), this plane is invariant, and according to system of equations (5), all trajectories on it approach the stationary X_{st} . Therefore, based on the theorem of continuous dependence of system (2), (3) solutions on the initial data [8], the $X(t)$ trajectory of this system from the small neighborhood of plane $N = 0$ also approaches the stationary X_{st} , when $t \rightarrow +\infty$.

Step 3. Take the $X(t, X_0)$ trajectory of system (2), (3), originating in the R_-^N set. At any t moment of time, a point of this trajectory is located on surface (13) for some $q = q_0$. But in R_-^N , as shown in the second step of the proof, with the growth of time t , $X(t, X_0)$ “descends” onto a surface, where $q < q_0$. Therefore, the $X(t, X_0)$ solution originating in the R_-^N set arrives either in the R_+^N set via the plane $A = \beta/\gamma$ or on surface (13), where $q \leq 0$. In both cases, this guarantees, in line with the reasoning of the previous steps of the proof, that $X(t, X_0) \rightarrow X_{st}$, when $t \rightarrow +\infty$.

Thus, Theorem 3 is proved.

The phase pattern of system (2), (3) is shown in Fig. 5.

The interpretation of the obtained results is of interest. They show that with the indicated relations of system (2) parameters the society (or its segment) is completely dominated by a certain concept (for example, ideological or technological). The cause of this might be full acceptance of the processes occurring in the society or a failure

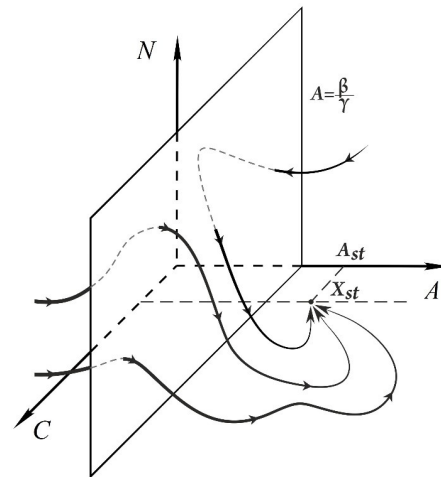


Fig. 5. Phase pattern of system (2), (3) in the parameter domain Λ_2

to change the established views. This could also happen due to high efficiency of the censor bodies which do not allow new information to fully fill the information space.

Conclusion

The study performed in this paper significantly expands the domain of investigated system characteristics which allows predicting the behavior of solutions depending on the initial data.

1. In the parameter space, we identified two important domains Λ_1 and Λ_2 , in which we mathematically justified certain global properties of the phase pattern of the studied dynamic system.

2. For each case, we provide an interpretation of the obtained results. In one instance, it is preparedness of the society to replace the dominating concept completely (for example, ideological or technological). In another case, on the contrary, it is a failure to accept new provisions due to various reasons.

The authors consider the results obtained in this article to be a continuation of the system research presented in papers [1, 9–11]. This project is aimed at studying mass media as a dynamic system with a high velocity of changes. The use of the methods of non-linear dynamics allows most complete and thorough investigation of the structure and properties of the processes unfolding in such a system.

REFERENCES

1. **Timofeev S.V., Sukhodolov A.P.**, A model of new information dissemination in the society, St. Petersburg Polytechnical State University Journal. Physics and Mathematics. 12 (4) (2019) 119–134.
2. **Pontryagin L.S.**, Obyknoennyye differentsialnyye uravneniya [Ordinary differential equations], Nauka, Moscow, 1974.
3. **Erugin N.P.**, Kniga dlya chteniya po obshchemu kursu differentsialnykh uravneniy [The book for reading on the general course of differential equations], Nauka i Tekhnika, Minsk, 1972.
4. **Cesari L.**, Asymptotic behavior and stability problems in ordinary differential equations, Inbunden Engelska, 1971.
5. **Ladas G.E., Lakshmikantham V.**, Differential equations in abstract spaces, Academic Press, New York, 1972.
6. **Bautin N.N., Leontovich E.A.**, Metody i priemy kachestvennogo issledovaniya dinamicheskikh sistem na ploskosti [Methods and technique of qualitative study of dynamical systems on the plane], Nauka, Moscow, 1990.
7. **Rouche N., Habets P., Laloy N.**, Stability theory by Liapunov's direct method, Springer-Verlag 1977.
8. **Fedoryuk M.V.**, Obyknoennyye differentsialnyye uravneniya [Ordinary differential equations], Nauka, Moscow, 1985.
9. **Bayenkhayeva A.V., Timofeev S.V.**, The evolutionary approach to development of mass media: construction of a mathematical model, Izvestiya Baykalskogo Gosudarstvennogo Universiteta [News of Baikal State University]. 26 (5) (2016) 825–833.
10. **Sukhodolov A.P., Kuznetsova I.A., Timofeev S.V.**, The analysis of approaches in modelling of mass media, Theoretical and Practical Issues of Journalism. 6 (3) (2017) 287–305.
11. **Sukhodolov A.P., Timofeev S.V.**, Mass media and virtual reality: new opportunities and prospects, Theoretical and Practical Issues of Journalism. 7 (4) (2018) 567–580.

Received 09.12.2020, accepted 24.12.2020.

THE AUTHORS

TIMOFEEV Sergey V.

Baikal State University

11, Lenin St., Irkutsk, 664003, Russian Federation
timofeevsv12@gmail.com

BAENKHAIEVA Ayuna V.

Baikal State University

11, Lenin St., Irkutsk, 664003, Russian Federation
ayunab2000@mail.ru

СПИСОК ЛИТЕРАТУРЫ

1. **Тимофеев С.В., Суходолов А.П.** Модель распространения новой информации в обществе // Научно-технические ведомости СПб-ГПУ. Физико-математические науки. 2019. Т. 12. № 4. С. 119–134.
2. **Понтрягин Л.С.** Обыкновенные дифференциальные уравнения. М.: Наука, 1974. 332 с.
3. **Еругин Н.П.** Книга для чтения по общему курсу дифференциальных уравнений. Минск: Наука и техника, 1972. 664 с.
4. **Чезаре Л.** Асимптотическое поведение и устойчивость решений обыкновенных дифференциальных уравнений. М.: Мир, 1964. 478 с.
5. **Lakshmikantham V., Ladas G.E.** Differential equations in abstract spaces. New-York: Academic Press, 1972. 231 p.

6. **Баутин Н.Н., Леонтович Е.А.** Методы и приемы качественного исследования динамических систем на плоскости. М.: Наука, 1990. 486 с.
7. **Руш Н., Абетс П., Лалуа М.** Прямой метод Ляпунова в теории устойчивости. М.: Мир, 1980. 300 с.
8. **Федорюк М.В.** Обыкновенные дифференциальные уравнения. М.: Наука, 1985. 448 с.
9. **Баенхаева А.В., Тимофеев С.В.** Эволюционный подход к развитию средств массовой информации: построение математической модели // Известия Байкальского государственного университета. 2016. Т. 26. № 5. С. 825–833.
10. **Суходолов А.П., Кузнецова И.А., Тимофеев С.В.** Анализ подходов в моделировании средств массовой информации // Вопросы теории и практики журналистики. 2017. Т. 6. № 3. С. 287–305.
11. **Суходолов А.П., Тимофеев С.В.** СМИ и виртуальная реальность: новые возможности и перспективы // Вопросы теории и практики журналистики. 2018. Т. 7. № 4. С. 567–580.

Статья поступила в редакцию 09.12.2020, принята к публикации 24.12.2020.

СВЕДЕНИЯ ОБ АВТОРАХ

ТИМОФЕЕВ Сергей Викторович — кандидат физико-математических наук, доцент кафедры математических методов и цифровых технологий Байкальского государственного университета, г. Иркутск, Российская Федерация.

664003, Российская Федерация, г. Иркутск, ул. Ленина, 11
timofeevsv12@gmail.com

БАЕНХАЕВА Аюна Валерьевна — кандидат технических наук, старший преподаватель кафедры математических методов и цифровых технологий Байкальского государственного университета, г. Иркутск, Российская Федерация.

664003, Российская Федерация, г. Иркутск, ул. Ленина, 11
ayunab2000@mail.ru

DOI: 10.18721/JPM.14114
UDC 539.3

CROSS-PROPERTY CONNECTIONS BETWEEN YOUNG'S MODULUS AND DIFFUSION COEFFICIENT OF TWO-PHASE COMPOSITE

K.P. Frolova

Institute for Problems in Mechanical Engineering RAS,
St. Petersburg, Russian Federation;
Peter the Great St. Petersburg Polytechnic University,
St. Petersburg, Russian Federation

The paper interrelates changes in the effective elastic and diffusion properties of a two-phase composite using microstructural parameters. It is suggested that there are some inhomogeneities identical in shape in the material. The development of the cross-property connections in the explicit tensor form has been presented. The segregation effect, being a constant jump in concentration of particles of the solute flux at the matrix/inhomogeneity interface, was taken into account. It is a good practice to apply the derived cross-property relations to finding some effective properties of material using others when the material's microstructure is unknown. The obtained expressions were put to the test for isotropic material with pores; the approximate correlations were compared with exact ones found for the specific microstructure.

Keywords: effective Young's modulus, effective diffusion coefficient, cross-property connection, segregation effect

Citation: Frolova K.P., Cross-property connections between Young's modulus and diffusion coefficient of two-phase composite, St. Petersburg Polytechnical State University Journal. Physics and Mathematics. 14 (1) (2021) 167–178. DOI: 10.18721/JPM.14114

This is an open access article under the CC BY-NC 4.0 license (<https://creativecommons.org/licenses/by-nc/4.0/>)

СООТНОШЕНИЯ МЕЖДУ МОДУЛЕМ ЮНГА И КОЭФФИЦИЕНТОМ ДИФфуЗИИ ДВУХФАЗНОГО МАТЕРИАЛА

К.П. Фролова

Институт проблем машиноведения РАН,
Санкт-Петербург, Российская Федерация;
Санкт-Петербургский политехнический университет Петра Великого,
Санкт-Петербург, Российская Федерация

В работе устанавливается взаимосвязь между изменениями эффективных упругих и диффузионных свойств двухфазного композита через микроструктурные параметры. Предполагается, что в материале присутствуют одинаковые по форме неоднородности. Представлен вывод соотношений в явном тензорном виде. При установлении взаимосвязи между эффективными свойствами учитывается эффект сегрегации, заключающийся в скачке концентрации растворенного вещества на границе раздела матрица/неоднородность. Полученные соотношения целесообразно использовать для определения одних эффективных свойств через другие, когда микроструктура материала неизвестна. Установленная взаимосвязь проверена для изотропного материала с порами. Найденные приближенные соотношения сравниваются с точными, полученными для конкретной микроструктуры.

Ключевые слова: эффективный модуль Юнга, эффективный коэффициент диффузии, взаимосвязь между свойствами композита

Ссылка при цитировании: Фролова К.П. Соотношения между модулем Юнга и коэффициентом диффузии двухфазного материала // Научно-технические ведомости СПбГПУ. Физико-математические науки. 2021. Т. 14. № 1. С. 167–178. DOI: 10.18721/JPM.14114

Статья открытого доступа, распространяемая по лицензии CC BY-NC 4.0 (<https://creativecommons.org/licenses/by-nc/4.0/>)

Introduction

Finding connections between various effective properties of heterogeneous materials is a fundamental problem of mechanics [1, 2]. These mathematical expressions interrelate the changes in different physical properties caused by a certain microstructure. The significance of this problem is defined by the fact that it allows one to determine certain effective properties by means of others in the absence of exhaustive information on the composite microstructure.

The search for various cross-property connections have been a topic for studies in literature since 1960s. An in-depth review of this problem is presented in [3]; according to the data presented the published studies may be conditionally divided into four directions:

- qualitative research;
- establishment of empirical dependencies;
- determination of the ranges of material characteristic changes;
- finding connections for materials with isolated inhomogeneities in explicit form.

There are currently a limited number of the published works devoted to the fourth direction. Explicit connections between effective elastic and conductive properties of materials were established in [4, 5]. These expressions describe anisotropic material with an isotropic matrix; the accuracy of the proposed connections depends on the shape of the inhomogeneities and the difference in the elastic properties of the constituents. Equations connecting strength characteristics of metal composite with graphite flakes to its thermal conductivity were obtained in [6]. Connections between effective thermal expansion and effective thermal conductivity were presented in [7, 8]. The accuracy of these correlations depends on the shape of inhomogeneities and the difference in the thermal

conductivity of the constituents. Mutual dependencies between effective diffusion coefficient and thermal conductivity of a metal-diamond composite were presented in [7, 8]. Explicit connections between thermal and electrical properties of a composite were obtained in [11].

A significant difference between the problems of diffusion and thermal conductivity considered in [4, 5] is that temperature is a continuous function across the interface of two phases (matrix/inhomogeneity) while concentration is usually not [12]. This phenomenon of the diffusing particles accumulating at the phase interface or inside inhomogeneities is known as the segregation effect [13].

This work is devoted to establishing explicit connections between effective elastic and diffusion properties of a two-phase composite with inhomogeneities identical in shape while taking the segregation effect into account.

The obtained connections are tested for a case of isotropic porous material while interrelating the changes in Young's modulus and diffusion coefficient.

Connections between effective elastic and diffusion properties of a two-phase composite

The connections between effective elastic and conductive properties obtained in papers [4, 5] are based on the fact that the changes in these properties different in nature are under control of the same microstructural parameters. Two main assumptions were used in the course of deriving the connections:

- inhomogeneities are spheroidal;
- effective properties are determined in the framework of the non-interaction approximation (NIA).



However, papers [4, 5] show that the obtained connections are valid for materials with differently shaped inhomogeneities and at greater concentrations than the NIA permits. This is due to the fact that the shape and concentration of inhomogeneities influence the elastic and conductive properties to the same extent.

Based on an analogy between diffusion and conductivity equations, let us use a methodology described in papers [4, 5] to establish connections between effective elastic and diffusion properties. According to this methodology, property contribution tensors are introduced to describe the effect of an inhomogeneity on the properties of interest, they act as primary microstructural parameters [3].

We introduce the fourth-rank compliance contribution tensor \mathbf{H} describing extra strain occurring over a reference volume due to the presence of the isolated inhomogeneity. The indicated tensor depends on the shape of the inhomogeneity and the difference in the elastic properties of the matrix and the inhomogeneity. In case the inclusion is spheroidal, tensor \mathbf{H} is transversely-isotropic (the symmetry axis coincides with the symmetry axis of the spheroid) and can be presented as a linear combination of $\mathbf{T}_1, \mathbf{T}_2, \dots, \mathbf{T}_6$ tensor basis elements:

$$\mathbf{H} = \sum_{k=1}^6 h_k \mathbf{T}_k, \quad (1)$$

where

$$\begin{aligned} \mathbf{T}_1 &= \boldsymbol{\theta}\boldsymbol{\theta}, \\ \mathbf{T}_2 &= \frac{1}{2} \left((\boldsymbol{\theta}\boldsymbol{\theta})_{(1,4)}^T + (\boldsymbol{\theta}\boldsymbol{\theta})_{(2,4)}^T - \boldsymbol{\theta}\boldsymbol{\theta} \right), \\ \mathbf{T}_3 &= \boldsymbol{\theta}\mathbf{nn}, \quad \mathbf{T}_4 = \mathbf{nn}\boldsymbol{\theta}, \\ \mathbf{T}_5 &= \frac{1}{4} \left(\mathbf{n}\boldsymbol{\theta}\mathbf{n} + (\mathbf{n}\boldsymbol{\theta}\mathbf{n})_{(1,2)(3,4)}^T + \right. \\ &\quad \left. + (\boldsymbol{\theta}\mathbf{nn})_{(1,4)}^T + (\boldsymbol{\theta}\mathbf{nn})_{(2,3)}^T \right), \\ \mathbf{T}_6 &= \mathbf{nnnn}, \end{aligned}$$

$\boldsymbol{\theta}$ is a projection tensor; $\boldsymbol{\theta} = \mathbf{I} - \mathbf{nn}$ (\mathbf{I} is the second-rank unit tensor).

Effective compliance tensor can be deter-

mined in the frame of the NIA in the following way:

$$\mathbf{S}^{eff} = \mathbf{S}^0 + \frac{1}{V} \sum_k V_k \mathbf{H}_k, \quad (2)$$

where \mathbf{S}^0 is a matrix compliance tensor, V is a reference volume, V_k is the volume of the k^{th} inhomogeneity.

When calculating effective elastic properties of the materials with inhomogeneities identical in shape, expression (2) can be rewritten in a form:

$$\begin{aligned} \mathbf{S}^{eff} &= \mathbf{S}^0 + \rho (\mathbf{W}_1 \boldsymbol{\Pi} + \mathbf{W}_2 \mathbf{J}) + \\ &+ \mathbf{W}_3 (\mathbf{I}\boldsymbol{\omega} + \boldsymbol{\omega}\mathbf{I}) + \mathbf{W}_4 (\mathbf{J} \cdot \boldsymbol{\omega} + \boldsymbol{\omega} \cdot \mathbf{J}) + \\ &+ \mathbf{W}_5 \boldsymbol{\Omega}, \end{aligned} \quad (3)$$

where

$$\mathbf{J} = \frac{1}{2} \left((\boldsymbol{\Pi})_{(1,4)}^T + (\boldsymbol{\Pi})_{(2,4)}^T \right)$$

is the fourth-rank unit tensor; parameters W_i ($i = 1, 2, \dots, 5$) are expressed by means of h_i coefficients as

$$\begin{aligned} W_1 &= h_1 - h_2/2, \quad W_2 = h_2, \\ W_3 &= -2h_1 + h_2 + 2h_3, \\ W_4 &= -2h_2 + h_5, \\ W_5 &= h_1 + \frac{h_2}{2} - 2h_3 - h_5 + h_6, \end{aligned}$$

while

$$\begin{aligned} \boldsymbol{\Omega} &= \frac{1}{V} \sum_k V_k (\mathbf{nnnn})^{(k)}, \\ \boldsymbol{\omega} &= \frac{1}{V} \sum_k V_k (\mathbf{nn})^{(k)}, \\ \rho &= \text{tr} \boldsymbol{\omega} = \frac{1}{V} \sum_k V_k; \end{aligned} \quad (4)$$

ρ is a volume fraction of the inhomogeneities.

One can determine the effective diffusion properties of the material consisting of a matrix with an isotropic diffusivity tensor $\mathbf{D}_0 = D_0 \mathbf{I}$ and inhomogeneities with $\mathbf{D}_1 = D_1 \mathbf{I}$ in a sim-

ilar way [14]. Either a second-rank diffusivity contribution tensor \mathbf{H}^D which determines additional mass flux caused by the presence of the inhomogeneity in the material, or a second-rank diffusion resistivity contribution tensor \mathbf{H}^{DR} ($\mathbf{H}^{DR} = -\mathbf{H}^D/D_0^2$), is introduced.

Both the matrix and the inhomogeneity obey linear Fick's law. The normal component of the flux is deemed to be continuous at the interface of the matrix (denoted by "+") and the inhomogeneity (denoted by "-"), while the concentration is subject to a jump

$$c(x)\Big|_{x \rightarrow \partial V^+} = sc(x)\Big|_{x \rightarrow \partial V^-}, \quad (5)$$

where s is the segregation factor.

The presence of the segregation effect leads to a fundamental distinction of the diffusion process from that of thermal conductivity considered in papers [4, 5]. The segregation factor shows a ratio of the concentrations at the inhomogeneity's interface and inside of it; it equals one in case of a continuous concentration function at the matrix/inhomogeneity interface. A case of $s > 1$ corresponds to a material in which the diffusing particles accumulate at the interface of two phases, while the $s < 1$ case corresponds to trapping of particles inside the inhomogeneities [14]. In studies of matrices with pores, only the $s \leq 1$ case is of interest from the physical point of view.

In case of the spheroidal inhomogeneity, the contribution tensors are determined in the following matter:

$$\begin{aligned} \mathbf{H}^D &= D_0 [B_1 (\mathbf{I} - \mathbf{nn}) + B_2 \mathbf{nn}], \\ \mathbf{H}^{DR} &= -\frac{1}{D_0} [B_1 (\mathbf{I} - \mathbf{nn}) + B_2 \mathbf{nn}], \end{aligned} \quad (6)$$

while the B_1 and B_2 coefficients depend on the shape of the inhomogeneities, the difference in the diffusion coefficients of the matrix and the inhomogeneity, as well as the segregation factor.

The effective diffusivity tensor is introduced in the frame of the NIA as

$$\mathbf{D}^{eff} = D_0 \mathbf{I} + \frac{1}{V} \sum_k V_k \mathbf{H}_k^D, \quad (7)$$

while the effective resistivity tensor has a form

$$(\mathbf{D}^{eff})^{-1} = \frac{1}{D_0} \mathbf{I} + \frac{1}{V} \sum_k V_k \mathbf{H}_k^{DR}. \quad (8)$$

Effective diffusion properties of the material with the inhomogeneities identical in shape can be expressed using the ρ volume fraction of the inhomogeneities and the second-rank tensor $\boldsymbol{\omega}$ determined by expressions (4) in the following manner:

$$\begin{aligned} \frac{1}{D_0} \mathbf{D}^{eff} - \mathbf{I} &= \mathbf{I} - D_0 (\mathbf{D}^{eff})^{-1} = \\ &= B_1 \rho \mathbf{I} + (B_2 - B_1) \boldsymbol{\omega}. \end{aligned} \quad (9)$$

Establishing explicit connections between the effective elastic and diffusion properties is possible if they are expressed in terms of the same microstructural parameters, i.e. the ρ scalar parameter and $\boldsymbol{\omega}$ tensor parameter. Therefore, to obtain the cross-property connections, we need to eliminate the summand containing the fourth-rank $\boldsymbol{\Omega}$ tensor in effective compliance tensor expression (3). According to statements in papers [4, 5], this is possible by means of correcting W_1, W_2, W_3, W_4 coefficients:

$$\begin{aligned} \mathbf{S}^{eff} &= \mathbf{S}^0 + \frac{1}{E_0} [\rho (s_1 \mathbf{I} \cdot \mathbf{I} + s_2 \mathbf{J}) + \\ &+ \frac{s_3}{2} (\mathbf{I} \cdot \boldsymbol{\omega} + \boldsymbol{\omega} \cdot \mathbf{I}) + \frac{s_4}{2} (\mathbf{J} \cdot \boldsymbol{\omega} + \boldsymbol{\omega} \cdot \mathbf{J})], \end{aligned} \quad (10)$$

where E_0 is Young's modulus of the matrix, s_i ($i = 1, 2, 3, 4$) coefficients are determined as

$$\begin{aligned} s_1 &= E_0 (\hat{h}_1 - \hat{h}_2 / 2), \\ s_2 &= E_0 \hat{h}_2, \\ s_3 &= E_0 (-2\hat{h}_1 + \hat{h}_2 + 2\hat{h}_3), \\ s_4 &= E_0 (-2\hat{h}_2 + \hat{h}_5), \end{aligned}$$

and \hat{h}_i ($i = 1, 2, \dots, 5$) coefficients are expressed through h_i as follows:

$$\begin{aligned}
 \hat{h}_i &= h_i (1 - \delta \operatorname{sign} h_i) \\
 &\text{at } i = 1, 2, 6; \\
 \hat{h}_i &= h_i (1 + \delta \operatorname{sign} h_i) \\
 &\text{at } i = 3, 5; \\
 \delta &= \\
 &= \frac{h_1 + h_2 / 2 - 2h_3 - h_5 + h_6}{|h_1| + |h_2| / 2 + 2|h_3| + |h_5| + |h_6|}.
 \end{aligned}$$

$$\begin{aligned}
 &\times (\operatorname{tr} \mathbf{D}^{eff} / D_0 - 3) + \\
 &+ \alpha_3 \left[(\mathbf{D}^{eff} / D_0 - \mathbf{I}) \mathbf{I} + \right. \\
 &\quad \left. + \mathbf{I} (\mathbf{D}^{eff} / D_0 - \mathbf{I}) \right] + \\
 &+ \alpha_4 \left[(\mathbf{D}^{eff} / D_0 - \mathbf{I}) \mathbf{J} + \right. \\
 &\quad \left. + \mathbf{J} (\mathbf{D}^{eff} / D_0 - \mathbf{I}) \right]
 \end{aligned} \tag{13}$$

To derive the connections between the effective elastic and diffusion properties of the material for a general case of orientation distribution of inhomogeneities, let us express the $\mathbf{\omega}$ tensor and the ρ parameter using the \mathbf{D}^{eff} and $(\mathbf{D}^{eff})^{-1}$ tensors, respectively:

$$\begin{aligned}
 \mathbf{\omega} &= \\
 &= \frac{1}{(B_2 - B_1)} \left(\frac{1}{D_0} \mathbf{D}^{eff} - \mathbf{I} \right) - \\
 &\quad - \frac{B_1}{(B_2 - B_1)} \rho \mathbf{I}, \\
 \rho &= \frac{\operatorname{tr} \mathbf{D}^{eff} - 3D_0}{D_0 (2B_1 + B_2)};
 \end{aligned} \tag{11}$$

$$\begin{aligned}
 \mathbf{\omega} &= \\
 &= \frac{1}{(B_2 - B_1)} \left(\mathbf{I} - D_0 (\mathbf{D}^{eff})^{-1} \right) - \\
 &\quad - \frac{B_1}{(B_2 - B_1)} \rho \mathbf{I}, \\
 \rho &= \frac{3 - D_0 \operatorname{tr} (\mathbf{D}^{eff})^{-1}}{2B_1 + B_2}.
 \end{aligned} \tag{12}$$

As a result of substituting these expressions in Eq. (10), we can obtain two correlations establishing an explicit connection between the effective compliance and the effective diffusion properties:

$$\begin{aligned}
 E_0 (\mathbf{S}^{eff} - \mathbf{S}^0) &= \\
 &= (\alpha_1 \mathbf{I} \cdot \mathbf{I} + \alpha_2 \mathbf{J}) \times
 \end{aligned}$$

while using relations (11) and

$$\begin{aligned}
 E_0 (\mathbf{S}^{eff} - \mathbf{S}^0) &= \\
 &= (\alpha_1 \mathbf{I} + \alpha_2 \mathbf{J}) \times \\
 &\quad \times (3 - D_0 \operatorname{tr} (\mathbf{D}^{eff})^{-1}) + \\
 &+ \alpha_3 \left[\left(\mathbf{I} - D_0 (\mathbf{D}^{eff})^{-1} \right) \mathbf{I} + \right. \\
 &\quad \left. + \mathbf{I} \left(\mathbf{I} - D_0 (\mathbf{D}^{eff})^{-1} \right) \right] + \\
 &+ \alpha_4 \left[\left(\mathbf{I} - D_0 (\mathbf{D}^{eff})^{-1} \right) \mathbf{J} + \right. \\
 &\quad \left. + \mathbf{J} \left(\mathbf{I} - D_0 (\mathbf{D}^{eff})^{-1} \right) \right]
 \end{aligned} \tag{14}$$

while using relations (12);
here

$$\begin{aligned}
 \alpha_1 &= \frac{s_1 (B_2 - B_1) - s_3 B_1}{(B_2 - B_1) (2B_1 + B_2)}, \\
 \alpha_2 &= \frac{s_2 (B_2 - B_1) - s_4 B_1}{(B_2 - B_1) (2B_1 + B_2)}, \\
 \alpha_3 &= \frac{s_3}{2(B_2 - B_1)}, \\
 \alpha_4 &= \frac{s_4}{2(B_2 - B_1)}.
 \end{aligned}$$

Cross-property connections between effective Young's modulus and effective diffusion coefficient of a porous material

To derive connections between effective elastic moduli and effective diffusion coefficients,

we need to use a component representation of Eqs. (13) and (14). In case of isotropic material, the following connections are in effect:

$$\frac{E^{eff}}{E_0} = \left[1 + (3\alpha_1 + 3\alpha_2 + 2\alpha_3 + 2\alpha_4) \left(\frac{D^{eff}}{D_0} - 1 \right) \right]^{-1} \quad (15)$$

while using tensor expression (13) and

$$\frac{E^{eff}}{E_0} = \left[1 + (3\alpha_1 + 3\alpha_2 + 2\alpha_3 + 2\alpha_4) \left(1 - \frac{D_0}{D^{eff}} \right) \right]^{-1} \quad (16)$$

while using tensor expression (14).

Connections (15) and (16) express a dependence of one effective modulus on the other at the macro level. The necessary information on the microstructure is reduced to determining the shape of an individual inhomogeneity as α_i coefficients depend on it; in addition, there is no need to analyze the orientation distribution of inhomogeneities. In the general case, connections (15) and (16) are approximate, since they are obtained based on the approximate expression for effective compliance tensor (10).

Two cases correspond to the isotropic material containing inhomogeneities:

- they have spherical shape,
- they have arbitrary orientation distribution.

Connections (15) and (16) are exact in the first case as $\delta = 0$ and consequently the approximate expression for effective compliance tensor (10) coincides with the exact one. In the second case, $\delta \neq 0$ and expressions (15), (16) are approximate.

Let us investigate two these cases and evaluate the accuracy of the obtained approximate connections.

Using Eqs. (15), (16), let us determine the connection between effective Young's modulus and the effective diffusion coefficient of the ma-

terial with spherical pores and compare the obtained expression and a direct calculation.

In case of the matrix with pores, the components of inhomogeneity's compliance contribution tensor h_i have the form

$$\begin{aligned} h_1 &= \frac{q_6}{2\Delta}, \quad h_2 = \frac{1}{q_2}, \quad h_3 = -\frac{q_3}{\Delta}, \\ h_4 &= -\frac{q_4}{\Delta}, \quad h_5 = \frac{4}{q_5}, \quad h_6 = \frac{2q_1}{\Delta}, \end{aligned} \quad (17)$$

where $\Delta = 2(q_1 q_6 - q_3 q_4)$ and

$$\begin{aligned} q_1 &= \mu [4\kappa - 1 - 2(3\kappa - 1)f_0 - 2\kappa f_1], \\ q_2 &= 2\mu [1 - (2 - \kappa)f_0 - \kappa f_1], \\ q_3 &= q_4 = 2\mu [(2\kappa - 1)f_0 + 2\kappa f_1], \\ q_5 &= 4\mu [f_0 + 4\kappa f_1], \\ q_6 &= 8\mu \kappa [f_0 - f_1], \\ \kappa &= (1 - \nu)/2; \end{aligned}$$

μ – shear modulus of the matrix; ν – Poisson's ratio of the matrix; f_0, f_1 – functions depending on the shape of the spheroidal inhomogeneity, i.e. on the aspect ratio $\gamma = a_3/a$ (a_3 – semiaxis of rotation) as

$$\begin{aligned} f_0 &= \frac{1 - g}{2(1 - \gamma^{-2})}, \\ f_1 &= \frac{1}{4(1 - \gamma^{-2})^2} [(2 + \gamma^{-2})g - 3\gamma^{-2}], \end{aligned}$$

where

$$g = \begin{cases} \frac{1}{\gamma\sqrt{1-\gamma^2}} \arctan \frac{\sqrt{1-\gamma^2}}{\gamma}, & \gamma \leq 1 \\ \frac{1}{2\gamma\sqrt{\gamma^2-1}} \ln \left(\frac{\gamma + \sqrt{\gamma^2-1}}{\gamma - \sqrt{\gamma^2-1}} \right), & \gamma \geq 1. \end{cases}$$

Diffusivity tensor coefficients have the form



$$B_1 = \frac{1-\lambda}{s\lambda + (1-s\lambda)f_0}, \quad (18)$$

$$B_2 = \frac{1-\lambda}{1-2(1-s\lambda)f_0},$$

where $\lambda = D_0/D_1$.

Then Eqs. (15) and (16) are reduced respectively to equalities

$$\begin{aligned} \frac{E^{eff}}{E_0} &= \left[1 + \frac{(1-\nu)(9+5\nu)}{2(7-5\nu)} \times \right. \\ &\quad \left. \times \frac{1+2s\lambda}{1-\lambda} \left(\frac{D}{D_0} - 1 \right) \right]^{-1}, \\ \frac{E^{eff}}{E_0} &= \left[1 + \frac{(1-\nu)(9+5\nu)}{2(7-5\nu)} \times \right. \\ &\quad \left. \times \frac{1+2s\lambda}{1-\lambda} \left(1 - \frac{D_0}{D} \right) \right]^{-1}. \end{aligned} \quad (19)$$

To obtain explicit cross-property connections, let us express the volume fraction of the inhomogeneities directly through the effective diffusion coefficient determined within the framework of the NIA and substitute it into the exact expression for the effective compliance tensor determined within the NIA as well.

Thus, the diffusivity and resistivity contribution tensors of the inhomogeneity are determined by expressions

$$\begin{aligned} \mathbf{H}_p^D &= \frac{3(1-\lambda)}{2s\lambda + 1} D_0 \mathbf{I}, \\ \mathbf{H}_p^{DR} &= -\frac{3(1-\lambda)}{(2s\lambda + 1)D_0} \mathbf{I}. \end{aligned} \quad (20)$$

Substitution of first and second Eqs. (20) respectively into Eq. (7) for the effective diffusivity tensor and Eq. (8) for the effective resistivity tensor allows expressing the volume fraction of the inhomogeneities through effective diffusion properties.

Subsequent substitution of the obtained expression for ρ in effective compliance tensor giv-

en by Eq. (2) taking into account the formula for isotropic compliance contribution tensor of the spherical pore

$$\begin{aligned} \mathbf{H}_p &= \frac{15(1-\nu)}{2\mu} \left[\frac{1}{10(1+\nu)} \frac{1}{3} \mathbf{I} \cdot \mathbf{I} + \right. \\ &\quad \left. + \frac{1}{7-5\nu} \left(\mathbf{J} - \frac{1}{3} \mathbf{I} \cdot \mathbf{I} \right) \right], \end{aligned} \quad (21)$$

leads to a result that completely coincides with expressions (19).

Thus, we tested the obtained approximate connections for a case of microstructure in which they are exact.

In the second case corresponding to the isotropic material (the arbitrary orientation distribution of the inhomogeneities), connections (15) and (16) are approximate. At the same time, we can establish connections between the effective elastic and diffusion properties for the case of arbitrary orientation distribution of spheroids independently by analogy with the method used above for the case of the spherical inhomogeneities.

For a quantitative and qualitative evaluations of the obtained approximate connections, let us compare them with the exact ones determined for this exact microstructure.

To establish exact connections, let us determine the volume fraction of the inhomogeneities using the effective diffusion coefficient of the isotropic material and then substitute the obtained expression in the equation determining effective Young's modulus. This approach is adequate due to the isotropy of the effective tensors. Therefore, the scalar parameter ρ is the only common microstructural parameter determining the effective properties of the material. When we use the NIA in terms of diffusivity contribution tensors, we obtain the following expression, which connects effective Young's modulus to the effective diffusion coefficient:

$$\frac{E^{eff}}{E_0} = \left[1 + \frac{E_0 h_\Sigma}{15\eta} \left(\frac{D^{eff}}{D_0} - 1 \right) \right]^{-1}, \quad (22)$$

and when we use the same method in terms

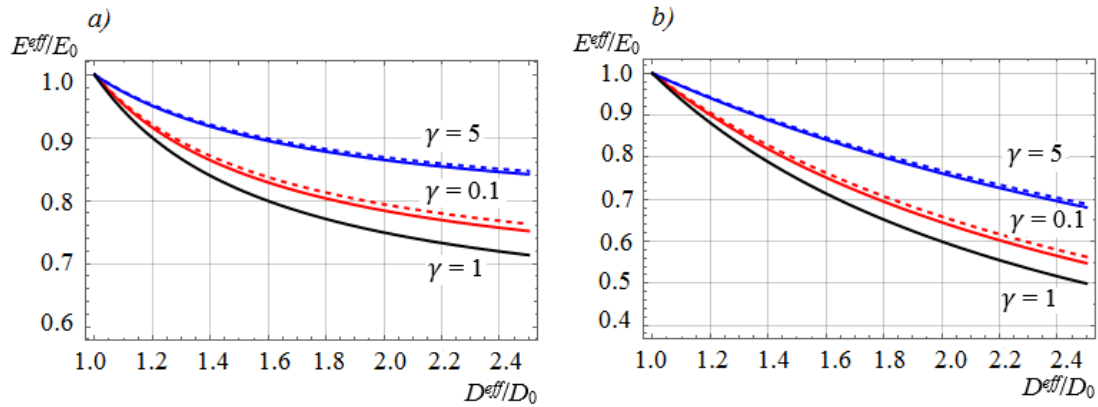


Fig. 1. Dependencies of relative effective Young's modulus on the relative effective diffusion coefficient while using compliance/resistivity (a) and compliance/diffusivity (b) cross-property connections for various values of the γ aspect ratios. Approximate connections (solid lines) are compared to exact ones (dashed lines)

of resistivity contribution tensors the expression has a form:

$$\frac{E^{eff}}{E_0} = \left[1 + \frac{E_0 h_\Sigma}{15\eta} \left(1 - \frac{D_0}{D^{eff}} \right) \right]^{-1}, \quad (23)$$

where $h_\Sigma = 8h_1 + 4h_2 + 4h_3 + 2h_5 + 3h_6$, $\eta = 2B_1/3 + B_2/3$.

Fig. 1 presents a comparison of the results obtained on the basis of approximate connections (15), (16) with the results obtained based on exact connections (22) and (23) respectively for the case of $\lambda = 0$, which corresponds to $D_1 \rightarrow \infty$ (in this case the segregation factor, as it follows from connection (18), is of no importance), $E_0 = 208$ GPa.

It is clear that connections (15) and (16) describe the relation between the effective properties at the macro level with sufficient accuracy. However, the effective values obtained using the resistivity tensors (Fig. 1, a) and the diffusivity tensors (Fig. 1, b) are different. This is due to the fact that the interaction of the inhomogeneities was neglected.

To obtain exact connection taking into account this interaction, let us employ Maxwell's homogenization scheme [3]. A result obtained using this scheme in terms of the diffusivity contribution tensors coincides with the result obtained in terms of the resistivity contribution tensors, and therefore the result is unambiguous as

opposed to the NIA.

The author has already determined Young's modulus of the material with spheroidal pores in paper [15], and the effective diffusion coefficient of such material in paper [16]. To obtain exact connections, we need to substitute the expression of the volume fraction of the inhomogeneities

$$\rho = 3 \frac{D^{eff} - D_0}{(D^{eff} + 2D_0)\eta}$$

into the expression for effective Young's modulus.

Fig. 2 presents a comparison of the approximate connections established in this work with the exact ones obtained using Maxwell's scheme for $\lambda = 0$, $E_0 = 208$ GPa.

An analysis of plots shown in Fig. 2 allows us to conclude that it is a good practice to use the connections obtained in terms of the diffusivity contribution tensors as they display better coincidence with the exact connections obtained within the Maxwell's scheme.

While studying the influence of segregation on the material cross-property connections, let us take into account that the diffusion coefficient of the pores is much greater than that of the matrix ($D_1 \gg D_0$), but at the same time it is finite; such an assumption corresponds to a real material. To be specific, let us assume that $\lambda = 0.01$, $E_0 = 208$ GPa. A dependence on the segregation

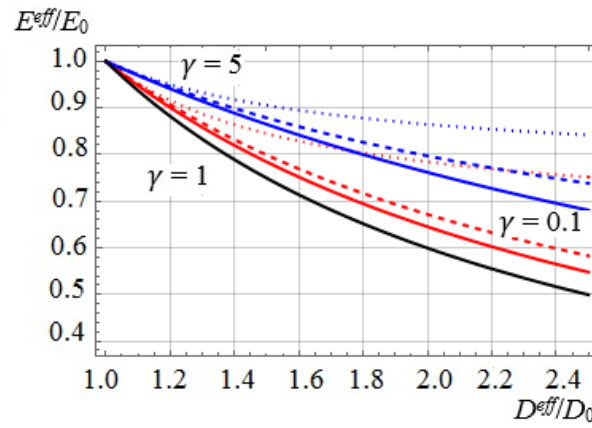


Fig. 2. Comparison of approximate compliance/diffusivity (solid lines) and compliance/resistivity (dashed lines) cross-property connections with exact connections (Maxwell's scheme, dashed lines)

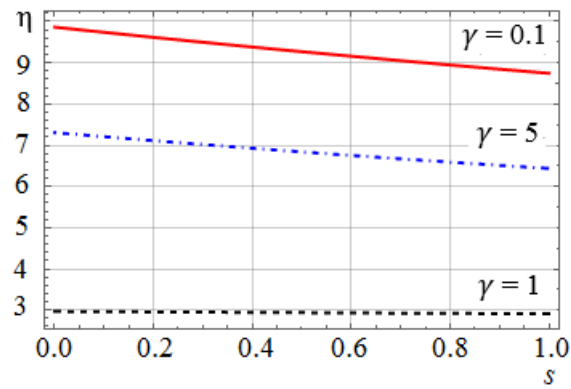


Fig. 3. Dependence of the η coefficient on the segregation factor at various aspect ratios γ

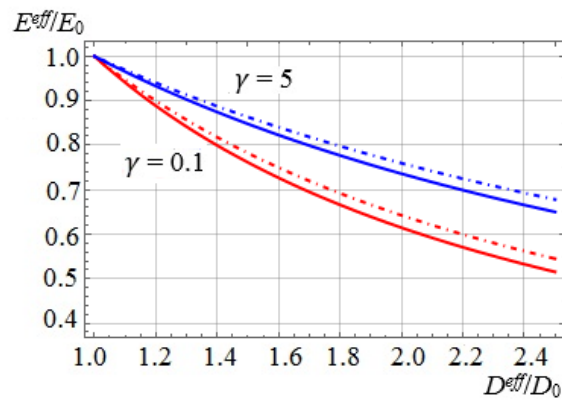


Fig. 4. Dependence of effective Young's modulus on the effective duffusion coefficient at two aspect ratios γ and the segregation parameter: $s = 1.00$ (solid line) and $s = 0.01$ (dash and dot line)

factor is implicitly present in expressions (15), (16) only in the η coefficient, since

$$\begin{aligned} 3\alpha_1 + 3\alpha_2 + 2\alpha_3 + 2\alpha_4 = \\ = \frac{3(s_1 + s_2) + s_3 + s_4}{3\eta}, \end{aligned}$$

the same coefficient can be derived in the effective diffusivity tensor.

The dependence of the η coefficient on the segregation factor at various aspect ratios of the spheroid is presented in Fig. 3.

We can see that the segregation has no significant influence in the presence of spherical pores. In case of oblate and prolate spheroidal pores, the segregation influence is stronger, which affects the effective diffusion coefficients as well [14, 16]. However, according to the dependencies shown in Fig. 4, the segregation has no significant impact directly on the cross-property relations (the dependencies are based on compliance/diffusivity cross-property connection). Thus, another advantage of using the established cross-property connections in the explicit form consists in no dependence on whether or not the diffusing particles are trapped inside the pores: all we need is the information on the effective material properties (elastic or diffusion).

Conclusion

The paper provides explicit cross-property connections between effective elastic and diffusion properties of the material. The obtained de-

pendencies can be applied to determine changes in certain effective properties by means of others in the absence of exhaustive information on the composite microstructure.

The cross-property connections were derived on the basis of a known (from literature) methodology described in terms of contribution tensors to determine a correlation between effective elastic and thermal conductivity properties. The dependencies take the segregation effect into account, which makes the diffusion problem fundamentally different from the thermal conductivity problem.

The case of isotropic material with containing trapped particles was detailed. The established cross-property connections describe the dependence of the effective Young's modulus of such material on the effective diffusion coefficient with sufficient accuracy.

Comparison of the results with the ones obtained within the Maxwell's scheme accounting for interaction between inhomogeneities shows that compliance/diffusivity connections are more preferable.

The paper analyzed the influence of segregation on the effective cross-property connections. It is shown, that accounting for segregation has no significant impact. This proves the advantage of applying the obtained connections when determining certain properties using the others at the macro level, since there is no need to estimate the segregation factor.

The study was supported by the Russian Foundation for Basic Research (grant No. 20-08-01100).

REFERENCES

1. **Berryman J.G., Milton G.W.**, Microgeometry of random composites and porous media, *Journal of Physics D: Applied Physics*. 21(1) (1988) 87–94.
2. **Gibiansky L.V., Torquato S.**, Connection between the conductivity and bulk modulus of isotropic composite materials, *Proceedings of the Royal Society of London. Series A: Mathematical, Physical and Engineering Sciences*. 452 (1945) (1996) 253–283.
3. **Kachanov M., Sevostianov I.**, *Micromechanics of materials, with applications*, Vol. 249, Springer, Berlin, Germany, 2018.
4. **Sevostianov I., Kachanov M.**, Explicit cross-property correlations for anisotropic two-phase composite materials, *Journal of the Mechanics and Physics of Solids*. 50 (2) (2002) 253–282.
5. **Sevostianov I., Kachanov M.**, Connections between elastic and conductive properties of het-

erogeneous materials, In the book: *Advances in Applied Mechanics*, Edited by H. Aref, E. van der Giessen, Elsevir, USA. 42 (2009) 69–252.

6. **Mazloun A., Oddone V., Reich S., Sevostianov I.**, Connection between strength and thermal conductivity of metal matrix composites with uniform distribution of graphite flakes, *International Journal of Engineering Science*. 139 (June) (2019) 70–82.

7. **Sevostianov I.**, On the thermal expansion of composite materials and cross-property connection between thermal expansion and thermal conductivity, *Mechanics of Materials*. 45 (February) (2012) 20–33.

8. **Mazloun A., Sevostianov I.**, Connections between anisotropic tensors of thermal conductivity and thermal expansion coefficients, *International Journal of Engineering Science*. 122 (January) (2018) 1–13.

9. **Anisimova M.A., Knyazeva A.G., Sevostianov I.**, Connection between diffusion coefficient and thermal conductivity of a metal matrix composite, *IOP Conference Series: Materials Science and Engineering*. 175 (1) (2017) 012051.

10. **Anisimova M., Knyazeva A., Sevostianov I.**, Effective thermal properties of an aluminum matrix composite with coated diamond inhomogeneities, *International Journal of Engineering Science*. 106 (September) (2016) 142–154.

11. **Mazloun A., Kováčik J., Emmer Š., Sevostianov I.**, Copper-graphite composites: Thermal expansion, thermal and electrical conductivities, and cross-property connections, *Journal of Materials Science*. 51 (17) (2016) 7977–7990.

12. **Zhang Y., Liping L.**, On diffusion in heterogeneous media, *American Journal of Science*. 312 (9) (2012) 1028–1047.

13. **Kaur I., Mishin Y., Gust W.**, *Fundamentals of grain and interphase boundary diffusion*, 3rd revised and enlarged edition, John Wiley & Sons. Inc., 1995.

14. **Knyazeva A.G., Grabovetskaya G.P., Mishin I.P., Sevostianov I.**, On the micromechanical modelling of the effective diffusion coefficient of a polycrystalline material, *Philosophical Magazine*. 95 (19) (2015) 2046–2066.

15. **Frolova K.P.**, Determination of the effective Young's modulus of medium with microstructure typical for hydrogen degradation, *St. Petersburg Polytechnical State University Journal. Physics and Mathematics*. 13 (2) (2020) 160–174.

16. **Frolova K.P., Vilchevskaya E.N.**, Effective diffusion coefficient of a porous material applied to the problem of hydrogen damage, Ch. 7, In the book: *Polyansky V.A., Belyaev A.K. (Eds.). Advances in Hydrogen Embrittlement Study*, Springer, Cham., 2021, *Advanced Structured Materials*, Vol. 143, Pp. 113–130.

Received 19.01.2021, accepted 01.02.2021.

THE AUTHOR

FROLOVA Ksenia P.

Institute for Problems in Mechanical Engineering RAS

Peter the Great St. Petersburg Polytechnic University

29 Politechnicheskaya St., St. Petersburg, 195251, Russian Federation

kspfrolova@gmail.com

СПИСОК ЛИТЕРАТУРЫ

1. **Berryman J.G., Milton G.W.** Microgeometry of random composites and porous media // *Journal of Physics D: Applied Physics*. 1988. Vol. 21. No. 1. Pp. 87–94.

2. **Gibiansky L.V., Torquato S.** Connection between the conductivity and bulk modulus of isotropic composite materials // *Proceedings of the Royal Society of London. Series A: Mathematical,*

Physical and Engineering Sciences. 1996. Vol. 452. No. 1945. Pp. 253–283.

3. **Kachanov M., Sevostianov I.** Micromechanics of materials, with applications. Berlin, Germany: Springer, 2018. Vol. 249. 712 p.

4. **Sevostianov I., Kachanov M.** Explicit cross-property correlations for anisotropic two-phase composite materials // Journal of the Mechanics and Physics of Solids. 2002. Vol. 50. No. 2. Pp. 253–282.

5. **Sevostianov I., Kachanov M.** Connections between elastic and conductive properties of heterogeneous materials // Advances in Applied Mechanics. Vol. 42. Edited by H. Aref, E. van der Giessen. USA: Elsevir, 2009. Pp. 69–252.

6. **Mazloun A., Oddone V., Reich S., Sevostianov I.** Connection between strength and thermal conductivity of metal matrix composites with uniform distribution of graphite flakes // International Journal of Engineering Science. 2019. Vol. 139. June. Pp. 70–82.

7. **Sevostianov I.** On the thermal expansion of composite materials and cross-property connection between thermal expansion and thermal conductivity // Mechanics of Materials. 2012. Vol. 45. February. Pp. 20–33.

8. **Mazloun A., Sevostianov I.** Connections between anisotropic tensors of thermal conductivity and thermal expansion coefficients // International Journal of Engineering Science. 2018. Vol. 122. January. Pp. 1–13.

9. **Anisimova M.A., Knyazeva A.G., Sevostianov I.** Connection between diffusion coefficient and thermal conductivity of a metal matrix composite // IOP Conference Series: Materials Science and Engineering. 2017. Vol. 175. No. 1. P. 012051.

10. **Anisimova M., Knyazeva A., Sevostianov I.** Effective thermal properties of an aluminum matrix composite with coated diamond inhomogeneities // International Journal of Engineering Science. 2016. Vol. 106. September. Pp. 142–154.

11. **Mazloun A., Kováčik J., Emmer Š., Sevostianov I.** Copper-graphite composites: Thermal expansion, thermal and electrical conductivities, and cross-property connections // Journal of Materials Science. 2016. Vol. 51. No. 17. Pp. 7977–7990.

12. **Zhang Y., Liping L.** On diffusion in heterogeneous media // American Journal of Science. 2012. Vol. 312. No. 9. Pp. 1028–1047.

13. **Kaur I., Mishin Y., Gust W.** Fundamentals of grain and interphase boundary diffusion. 3rd revised and enlarged edition. John Wiley & Sons. Inc., 1995. 528 p.

14. **Knyazeva A.G., Grabovetskaya G.P., Mishin I.P., Sevostianov I.** On the micromechanical modelling of the effective diffusion coefficient of a polycrystalline material // Philosophical Magazine. 2015. Vol. 95. No. 19. Pp. 2046–2066.

15. **Фролова К.П.** Определение эффективного модуля Юнга среды с микроструктурой, характерной для водородной деградации // Научно-технические ведомости СПбГПУ. Физико-математические науки. 2020. Т. 13. № 2. С. 160–174.

16. **Frolova K.P., Vilchevskaya E.N.** Effective diffusion coefficient of a porous material applied to the problem of hydrogen damage (Chapter 7) // Polyanskiy V.A., Belyaev A.K. (Eds.). Advances in Hydrogen Embrittlement Study. Springer, Cham., 2021. Advanced Structured Materials. Vol. 143. Pp. 113–130.

Статья поступила в редакцию 19.01.2021, принята к публикации 01.02.2021.

СВЕДЕНИЯ ОБ АВТОРЕ

ФРОЛОВА Ксения Петровна — младший научный сотрудник Института проблем машиноведения РАН, Санкт-Петербург, Российская Федерация; ассистент Высшей школы теоретической механики Санкт-Петербургского политехнического университета Петра Великого, Санкт-Петербург, Российская Федерация.

199178, Российская Федерация, г. Санкт-Петербург, Большой проспект В.О., 61
kspfrolova@gmail.com